CORA Cork Open Research Archive
Cartlann Taighde Oscailte Chorcaí

Title	Theory of radiative and nonradiative recombination processes in nitride-based heterostructures
Authors	McMahon, Joshua M.
Publication date	2023
Original Citation	McMahon, J. M. 2023. Theory of radiative and nonradiative recombination processes in nitride-based heterostructures. PhD Thesis, University College Cork.
Type of publication	Doctoral thesis
Rights	© 2023, Joshua Malachy McMahon. - https://creativecommons.org/licenses/by-nc-nd/4.0/
Download date	2026-11-16 09:54:30
Item downloaded from	https://hdl.handle.net/10468/15954



UCC
University College Cork, Ireland
Coláiste na hOllscoile Corcaigh

Theory of radiative and nonradiative recombination processes in nitride-based heterostructures

Joshua Malachy McMahon
B.A. (Mod)
118226696



NATIONAL UNIVERSITY OF IRELAND, CORK

School of Physics

Thesis submitted for the degree of Doctor of Philosophy

October 2023

Head of School: Prof. Paul Callanan

Supervisors: Dr. Stefan Schulz
Prof. Eoin P. O'Reilly

Research supported by the Sustainable Energy Authority of Ireland and Science Foundation Ireland

Contents

Abstract . . . iv
Publications, presentations and posters . . . xii
Acknowledgements . . . xiv

Prologue **1**

1 Light-Emitting Diodes **14**
1.1 Introduction . . . 14
1.2 Principles of operation . . . 16
1.2.1 Double heterostructures and quantum wells . . . 18
1.3 Quantifying and modelling efficiency in LED devices . . . 21
1.3.1 ABC model . . . 22
1.4 III-nitride materials and derived heterostructures . . . 25
1.4.1 Wurtzite crystal structure . . . 25
1.4.2 Polarisation . . . 28
1.4.2.1 Piezoelectric polarisation and strain . . . 29
1.4.3 Impact of polarisation on III-N quantum wells . . . 30
1.4.4 Alloy disorder and carrier localisation in III-nitrides . . . 36

2 Electronic structure theory **43**
2.1 Introduction . . . 43
2.2 Basic considerations . . . 44
2.2.1 Reciprocal space . . . 44
2.2.2 Electronic band structures . . . 46
2.3 *Ab initio* methods . . . 49
2.3.1 Density functional theory . . . 50
2.4 Semi-empirical methods . . . 53
2.4.1 Effective mass approximation and $\mathbf{k} \cdot \mathbf{p}$ theories . . . 54
2.4.2 Modified continuum-based approaches . . . 59
2.4.3 Tight-binding . . . 62
2.4.3.1 Basic considerations . . . 63
2.4.3.2 Including strain effects . . . 67
2.4.3.3 Including polarisation field effects . . . 72

3 Calculating radiative and Auger recombination rates in a tight-binding framework **76**
3.1 Calculation of the radiative recombination rate . . . 76
3.2 Calculation of Auger recombination rate . . . 83
3.3 Polarisation field screening . . . 87

4 Temperature dependent recombination in InGaN QWs **90**
4.1 Introduction . . . 90
4.1.1 QW model systems . . . 91
4.2 Results . . . 93
4.2.1 Impact of localisation on optical properties . . . 93

4.2.2 Radiative recombination 97
4.2.3 Auger recombination 100
4.2.4 Competition between radiative and Auger recombination 110
4.3 Conclusion 115

5 Carrier density dependent recombination in InGaN QWs 118
5.1 Introduction 118
5.2 Results 120
5.2.1 Impact of polarisation field screening on electronic structure 120
5.2.2 Auger recombination 124
5.2.3 Competition between radiative and Auger recombination - theory experiment comparison 128
5.3 Conclusion 137

6 Temperature dependent radiative and Auger recombination in AlGaN/AlN QWs 139
6.1 Introduction 139
6.1.1 Theoretical framework and quantum well model systems 143
6.2 Results 145
6.2.1 Electronic structure 146
6.2.2 Radiative recombination 152
6.2.3 Auger recombination 157
6.2.4 Competition between radiative and Auger recombination 163
6.3 Conclusion 165

7 Concluding Remarks 168
7.1 Summary 168
7.2 Outlook 174

8 Bibliography 177

Appendices 209

A Determination of on-site energies 210

I, Joshua Malachy McMahon, certify that this thesis is my own work and I have not obtained a degree in this university or elsewhere on the basis of the work submitted in this thesis.

Joshua Malachy McMahon

Abstract

Most modern blue-violet short wavelength visible light-emitting diodes (LEDs) incorporate group III-nitride (III-N) semiconductor quantum wells (QWs), and ultraviolet (UV) LEDs could be developed using similar materials and heterostructures. Relative to filament and fluorescent bulb technologies, modern blue-violet short wavelength emitting III-N QW-based devices are significantly more efficient. However, they suffer from efficiency "droop" effects, the fundamental causes of which are under debate. For example, the efficiency of III-N LEDs drops with increasing *drive current*, and thus increased carrier density in the well, an effect known as "current droop". Furthermore, even at fixed drive current, when the *temperature* of the device rises, there is a corresponding drop in device efficiency, the so-called "thermal droop". On top of current and temperature dependent droop, III-N QW-based light emitting devices also suffer significant reductions in efficiency at longer (green to red) and shorter (deep UV) wavelengths. The reduction in efficiency as III-N devices are engineered to emit at longer wavelengths is a major contributor to the so-called "green gap" phenomenon, wherein neither III-N nor other III-V heterostructure-based devices (such as those based on phosphides or arsenides emitting in the red to infrared spectral range) can be designed to emit efficiently in the green to yellow spectral range.

Input from theory is important for understanding the fundamental origins of these droop phenomena, as well as to guide device design to improve the efficiency of not only blue-violet visible wavelength emitters that suffer from droop, but also devices emitting at the shorter and longer wavelengths mentioned above. However, theoretical results obtained for other semiconductor structures (such as those based on II-VI and other III-V heterostructures) cannot be carried over to III-N systems due to significant differences in the fundamental material properties. For instance, alloy disorder causes strong carrier localisation in III-N semiconductor alloys, which can significantly alter the electronic and optical properties of III-N heterostructures. Although experimental data indicates the importance of such effects, only very recently have they been accounted for in theoretical studies, as they present a significant modelling challenge. The aim of this thesis is to address this challenge using atomistic modelling.

Auger recombination has been discussed in the literature as an important nonradiative process in c-plane InGaN/GaN QWs in which an electron

recombines with a hole, but instead of a photon being emitted (as in radiative recombination) another carrier is excited. If the rate of Auger recombination grows faster than the rate of radiative recombination as temperature or carrier density increases, overall, there will be a negative impact on device performance. For instance, there is much evidence that Auger recombination plays a significant role in carrier density dependent droop, but the exact nature of the Auger process underlying this droop phenomenon is still under debate, and several Auger recombination mechanisms have been suggested, including a defect-assisted process as well as alloy disorder enhanced Auger recombination. Auger recombination has also been explored as a possible cause of thermal droop but there is still much debate over its relevance to this droop phenomenon. Despite experimentally established links between Auger recombination and these droop phenomena, on the theoretical side the impact of alloy disorder on the Auger recombination process in III-N *QW* systems is widely unexplored.

Our theoretical framework is based on a nearest neighbour sp^3 tight-binding model, which takes input from a valence force field model to determine the equilibrium lattice positions of the alloy disordered QW structures studied. On top of this, local variations in strain and polarisation fields are accounted for in the framework, along with polarisation field screening effects at high carrier densities in the well. The tight-binding energies and wave functions are then used to calculate the radiative and Auger recombination rates.

For InGaN/GaN QW systems, our predicted values for radiative and Auger recombination rates lie within the wide range of experimentally reported values, and confirm that the coefficient of Auger recombination is not as small as one may expect from the expected dependence of Auger coefficient on band gap. To study the thermal droop, we have evaluated the radiative and Auger recombination rates at a fixed carrier density but as a function of temperature. Our results reflect the unconventional but experimentally observed increase of the radiative recombination rate with increasing temperature. When focusing on the competition between radiative and alloy-enhanced Auger effects, neglecting, e.g., defect-related processes such as Shockley-Read-Hall recombination, our results indicate an improvement of device performance with increasing temperature, in contrast to experimentally determined efficiency data. Thus, we expect that alloy-enhanced Auger recombination, intrinsic to InGaN-based QWs, is not responsible for thermal droop. As a result, efficiency improvement strategies that target, for instance, factors

extrinsic to the well, such as reducing defect densities, should be considered.

Turning to the carrier density dependent droop (i.e. the current droop), the competition between radiative and Auger rates as a function of carrier density (but at fixed temperatures) was determined. In InGaN/GaN QW systems, already at low carrier densities our model predicts Auger recombination rates large enough to be considered significant contributors to this droop phenomenon (based on expectations from the literature). When investigating the carrier density dependence of the recombination rates, we find that the Auger rate grows faster than the radiative rate as carrier density increases in the c-plane InGaN/GaN QWs studied here. Working within a commonly used model of efficiency in LEDs, we compared the theoretically determined carrier density dependent efficiency data to experimental results from collaborators at the Universities of Manchester and Cambridge for samples with varying defect densities. We found a good agreement between theory and experiment at carrier densities where this droop phenomenon is observed; the temperature is kept constant in the experiments and calculations. Furthermore, the drop in efficiency with increasing carrier density was essentially independent of sample, and thus independent of defect density. Overall, these results indicate that defect-assisted Auger processes may be of secondary importance, and alloy-enhanced Auger recombination can be sufficient to explain the current droop. Moreover, despite the large Auger coefficients, the green emitting samples studied in our theory experiment comparison were found to have relatively high internal quantum efficiencies, suggesting that Auger recombination may not be limiting the performance of longer wavelength visible light-emitting devices.

Lastly, UV LEDs based on AlGaN QW systems have attracted significant attention in recent years for the potential development of more efficient and environmentally friendly UV emitters. Despite this, and despite the experimental observation of both thermal and current droop in AlGaN-based QWs, Auger recombination and carrier localisation have also been widely unexplored in these systems, particularly from a theoretical perspective. Thus, we applied our theoretical framework to determine the radiative and Auger recombination rates at a fixed carrier density but as a function of temperature in c-plane AlGaN/AlN QWs, thus providing insight into the thermal droop of such emitters. We found Auger recombination rates on the same order of magnitude as those determined for the InGaN/GaN QWs studied above. Based on our results, we expect that Auger recombination is not the driving cause of

thermal droop in AlGaN/AlN QWs. However, based on expectations from the literature, the values calculated here suggest that Auger recombination could be a significant contributor to current droop in AlGaN QWs.

Overall, our calculations show that alloy-enhanced Auger recombination is indeed strongly contributing to nonradiative recombination processes in III-N heterostructures. However, the thermal droop does not seem to be driven by this intrinsic nonradiative process. Instead, other factors, such as defect-assisted Auger recombination or carrier injection deficiencies, may be responsible. Thus, device optimisation strategies that target these extrinsic effects may still improve efficiency. With regard to the current density dependent droop, our calculations indicate that alloy-enhanced Auger recombination plays a significant role. Efforts to mitigate the impact of alloy-enhanced Auger recombination on the internal quantum efficiency could consider targeting larger active regions to reduce current density, or improved current spreading through the multiple QWs employed in LEDs. Although alloy-enhanced Auger recombination may present an intrinsic roadblock to reducing current droop, our results suggest that the reduction in efficiency of longer wavelength III-N devices emitting in the visible range (i.e. green) is not driven by this Auger process. Thus, device performance optimisation may still be achievable by targeting extrinsic factors such as carrier injection efficiency and homogeneity.

To my parents, and my grandparents.

To Pip and Colin.

In loving memory of Niamh Lynch, Conor King and Cian Nugent.

Ar dheis Dé go raibh a n-anamacha.

“Results! Why, man, I have gotten a lot of results! I know several thousand things that won’t work.”

- T. Edison (allegedly)

From “Edison: His Life and Inventions” by Frank Lewis Dyer and Thomas Commerford Martin, Volume 2, Chapter 24, p. 616, Harper & Brothers, New York (1910)

Publications, presentations and posters

Journal publications

- [1] "Carrier density dependent Auger recombination in c-plane (In,Ga)N/GaN quantum wells: Insights from atomistic calculations," J. M. McMahon, E. Kioupakis, and S. Schulz, *J. Phys. D: Appl. Phys.* vol. 57, p. 125102, 2024
- [2] "Disentangling the Impact of Point Defect Density and Carrier Localization-Enhanced Auger Recombination on Efficiency Droop in (In,Ga)N/GaN Quantum Wells," R. M. Barrett, J. M. McMahon, R. Ahumada-Lazo, J. A. Alanis, P. Parkinson, S. Schulz, M. J. Kappers, R. A. Oliver, and D. Binks, *ACS Photonics* vol. 10, no. 8, pp. 2632-2640, 2023
- [3] "Atomistic analysis of Auger recombination in c-plane (In,Ga)N/GaN quantum wells: Temperature-dependent competition between radiative and nonradiative recombination," J. M. McMahon, E. Kioupakis, and S. Schulz, *Physical Review B* vol. 105, p. 195307, 2022
- [4] "Atomistic analysis of radiative recombination rate, Stokes shift, and density of states in c-plane InGaN/GaN quantum wells," J. M. McMahon, D. S. P. Tanner, E. Kioupakis, and S. Schulz, *Applied Physics Letters* vol. 116, p. 181104, 2020
- [5] "Interface roughness, carrier localization, and wave function overlap in c-plane (In,Ga)N/GaN quantum wells: interplay of well width, alloy microstructure, structural inhomogeneities, and Coulomb effects," D. S. P. Tanner, J. M. McMahon, and S. Schulz, *Physical Review Applied* vol. 10, 034027, 2018

Conference talks

- "Atomistic study of radiative and Auger recombination rates in c-plane InGaN/GaN quantum wells", J. McMahon, E. Kioupakis, and S. Schulz, at the *International Workshop on Nitride Semiconductors*, Berlin, October 2022
- "Theoretical study of the carrier density dependence of Auger recombination in polar (In,Ga)N/GaN quantum wells", J. M. McMahon, E. Kioupakis, and S. Schulz, at the *UK Nitride Consortium Winter Meeting*,

Online, January 2022

- "Temperature dependence of radiative and non-radiative recombination rates in c-plane InGaN/GaN quantum wells", J. M. McMahon, D. S. P. Tanner, E. Kioupakis, and S. Schulz, at the *UK Nitride Consortium Winter Meeting*, Online, January 2021
- "Carrier localization in polar InGaN QWs: Consequences for the temperature dependence of the radiative recombination", J. M. McMahon, D. S. P. Tanner, E. Kioupakis, and S. Schulz, at the *UK Nitride Consortium Winter Meeting*, Cardiff, January 2020

Conference posters

- "Influence of temperature on the radiative and non-radiative recombination rates in c-plane InGaN/GaN quantum wells", J. M. McMahon, E. Kioupakis, and S. Schulz, at *Photonics Ireland*, Online, June 2021
- "Atomistic analysis of radiative and nonradiative recombination in InGaN quantum wells", Joshua McMahon and Stefan Schulz, at the *IPIC Industry Workshop*, March 2020

Contributions to invited talks

- "Carrier transport, radiative and non-radiative recombination in (In,Ga)N heterostructures: Insights from atomistic and multi-scale simulations," Stefan Schulz, at *Applied Mathematics and Simulation for Semiconductors and Electrochemical Systems*, Weierstrass Institute for Applied Analysis and Stochastics, Berlin, September, 2021

Acknowledgements

This research would not have been possible without the support of Science Foundation Ireland and the Sustainable Energy Authority of Ireland.

This research would also not have been possible without the inexhaustible, always helpful and supportive guidance and encouragement of Dr Stefan Schulz. My sincerest thanks must go to him first and foremost for believing in me and giving me this opportunity all those years ago. And doubly so for continuing to support and guide me even through the tumultuous times since then.

The unwavering support of Prof. Eoin O'Reilly as well, from my first time stepping foot in Tyndall in 2012 up to now, has been a consistent source of comfort and inspiration. It is an honour to be able to say that I worked with both Dr. Schulz and Prof. O'Reilly.

To complete the excellent supervision team for my time in Tyndall, I am so grateful to Dr. Farzan Gity in his role as monitor. Despite the stress of preparing for yearly reviews I can safely say I looked forward to them knowing that Dr. Gity's presence would only have a positive impact, along with his willingness to help and curiosity for the work we were doing.

A huge thank you to our collaborators, Prof. Manos Kioupakis in the US and Dr. Dave Binks and Dr. Rachel Barrett in the UK for the consistently incredibly insightful conversations. It was a pleasure to work with ye.

I do not think I can convey how thankful I am to my parents, Chris and Miriam, for supporting me every step of the way, from the first time I said I wanted to study theoretical physics to today. I owe them everything. This work is as much the fruit of their labour, as it is mine. As they say; "all that is good in me, began with you".

To my grandparents too, I don't think I can properly convey how thankful I am to them. I will always remember the times I stayed far too late drinking tea and chatting and venting about PhD stress. I will also always remember discussing the mystifying nature of how magnets work with Grandad driving home from school one afternoon. Trying to get to the bottom of that question played an important role in my burgeoning interest in physics at the time.

To Denis, Dave and Hank, yere company got me through some of the hardest times in the last five years and I am so grateful for yere friendship. I am looking forward to our adventures in the future.

To Sinéad, Ciaran, Kate, Niall, Jamesy and Clara, I am so glad our friendships continue despite the distance between us. I am so looking forward to seeing ye more often. Yere support has always been such a massive comfort, especially through COVID but, really, every day.

Thank you to everyone I've crossed paths with in the office too. I know I didn't

spend much time in there after COVID but it was always a nice treat to see ye. To Daniel and Rob, it was a pleasure working with ye, I wish ye all the best in the future. To Noor and Saroj, thank you for yere company on those late evenings, it would've been a very lonely office otherwise. And particularly, thank you to Michael. I sometimes forget how wild it is that we've known each other for 23 of the last 27 years, going from playschool to PhD. I am also so glad that despite the distance between us as well, our friendship is one that we can always pick up from where we left off.

A big, general thank you to everyone in UCC Ultimate, Rebel Ultimate and XVI Ultimate. Frisbee has always been a wonderful escape. I also want to briefly look further back, and acknowledge the support of everyone I was close with when I started this journey. To the theoretical physics class of 2018, although it was intimidating at times, ultimately yere intelligence and, more importantly, hard work was always an inspiration. To Jess and Danny, Kevin B and Kevin Q, Sean B and Ruairí (this is all your fault), a huge thank you for being wonderful friends. I have such fond memories of our times together. I would not have walked this path without yere support, as well as the support of Rory, Chloe, Ailne and Seamus, and especially, for your constant encouragement and belief in me, Christina.

Lastly, I cannot forget the unwavering support of Pip and Colin, and Inca now too, reminding me to relax, and teaching me how as well.

Ar scáth a chéile a mhaireann na daoine.

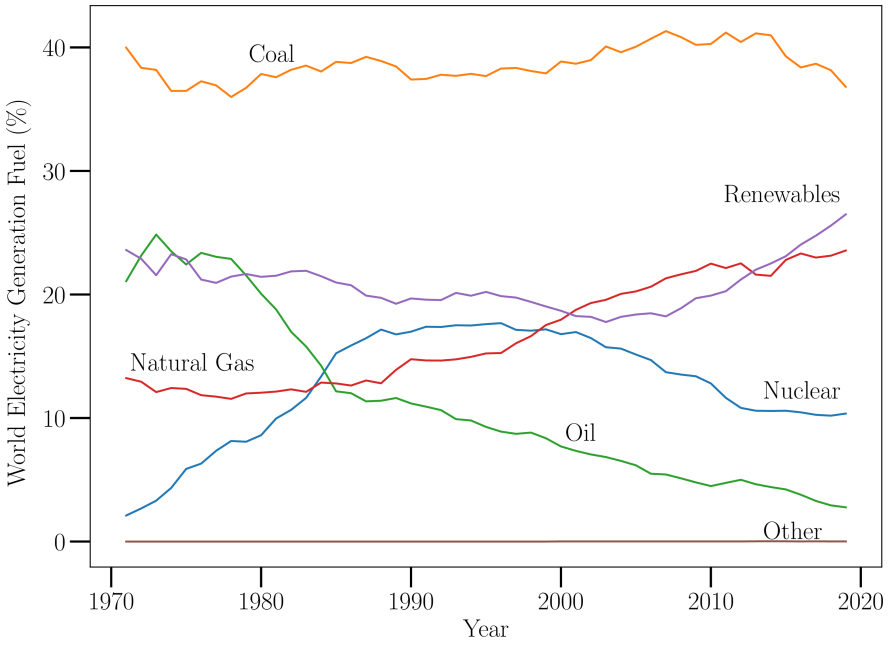


Figure 1: Breakdown of fuel types used to generate electricity between 1971 and 2019. Data available under Creative Commons license CC BY 4.0 from Ref. [6].

Prologue

From the use of primitive animal fat candles to light caves for painting by prehistoric humans [7], to the mass production of extremely precisely engineered nanoscale light emitters in modern times, human civilisations have always sought innovative ways to dispel darkness. Nowhere is this innovation more evident than in the vast efforts of the past century to develop solid state lighting (SSL) technologies.

SSL technologies hold many advantages over conventional filament and fluorescent bulb-based technologies. They are generally less fragile, more environmentally friendly and more efficient [8]. Indeed, efficiency has always been one of the most important metrics by which the development of not only SSL, but all lighting, has been measured [9].

Now, more than ever, developing more efficient lighting technologies is crucial. Energy consumption due to lighting demands continues to grow, and is expected to continue further. Global electricity consumption due to lighting grew to over 1700 TWh in the years leading up to 2020, and has grown year on year since then [10]. This increasing usage is directly linked to significant greenhouse gas emissions [8]. Figure 1 shows the fuels used to generate electricity from 1971 to 2019. Although the use of renewable energy sources has increased, still, nearly two thirds of electricity generation is facilitated by fossil fuel-based technologies [6]. In order to accelerate the crucial reduction of carbon emissions to avoid global warming of more than 2°C, all feasible paths to mitigating energy consumption must be explored.

Although improvements to the efficiencies of filament and fluorescent bulbs continue, in 2010, Humphreys [8] reported that "incandescent light bulbs convert about 5% of the electricity they use into visible light" and "energy saving compact fluorescent lamps ... are only about 20% efficient." SSL technologies, in the form of light-emitting diodes (LEDs), can achieve electricity to light conversion efficiencies of over 90% in certain applications and at certain wavelengths [11] and are generally more efficient than filament or fluorescent bulbs due to the direct emission of light from the material [8]. Furthermore, both filament and fluorescent technologies suffer from short lifetimes relative to SSL technologies. Filament bulbs generally have lifetimes of approximately 1000 hours, and although fluorescent bulbs can last longer, poor usage practises can significantly shorten their lifetime [8]. LEDs can have lifetimes on the order of 100 times longer than filament bulbs, and are generally far more robust.

Despite their greater operational efficiencies, the potential for larger energy expenditure during the manufacturing, transportation and disposal of an LED lamp, in comparison to filament of fluorescent technologies, has led to recent "life-cycle" analyses [12, 13]. For instance, in the analysis of Ref. [12], it was reported that, in 2011, fluorescent technologies and LED-based lamps had similar average life-cycle energy consumption values, which were both approximately a quarter of the value for filament-based lamps. However, the report also concluded that "energy-in-use", i.e., the energy used when the lamp is switched on, is the dominant contribution to the average life-cycle energy consumption for both technologies. Thus, although fluorescent lamps are slightly less energy intensive in the manufacturing, transport and disposal phases than LEDs, these processes contribute less than 10% of the overall

average life-cycle energy consumption for both technologies. As a result, improvements to LED operational efficiencies (i.e. that reduce the "energy-in-use") would significantly reduce the overall average life-cycle energy consumption of LEDs. It was estimated that these improvements would halve the overall average life-cycle energy consumption of LEDs by 2015 [13]. On top of this, improvements to manufacturing and disposal/recycling techniques could also be realised, reducing the overall energy consumption further. Although beyond the scope of this thesis, we also note that there is much debate over the potential for a so-called "rebound effect". The rebound effect refers to the increased adoption and usage of LED-based lamps due to their lower initial purchasing costs and, in particular, due to their lower related energy-in-use costs. As a result, in the short term, the introduction of a more efficient LED technology may lead to an overall reduction in energy consumption for lighting, but there may be a subsequent increase to a level of energy consumption larger than the value before the efficiency was improved. Thus, any overall energy saving due to improved efficiency may be negated [14]. Regardless of whether such a rebound effect will occur, reducing the rate of increase of energy usage and connected carbon output remains crucial, with SSL technologies providing the best path forward.

Given the advantages SSL technologies hold over conventional lighting technologies, in terms of pathways to improve efficiency and overall life-cycle energy consumption, along with commercial interests and interest in the fundamental physics of these devices, huge research efforts have gone into understanding the materials and heterostructures that underlie LEDs. Furthermore, optimisations of the designs of LED-based light emitting devices continue to attract huge interest. In this chapter we will briefly recap the major milestones in the development of LED technologies before discussing some of the current bottlenecks to increasing the efficiency of these devices further and theoretical efforts to understand and predict solutions to these bottlenecks. Finally, we will lay out the structure of this thesis.

A brief history of solid state lighting

The first documented observation of the direct emission of light from a material, called electroluminescence (EL), is credited to H. J. Round when he observed a weak form of EL from SiC in 1907 [9]. However, the significance of this discovery was essentially lost until the early 1920s when O. Losev

independently rediscovered the phenomenon in the semiconductor materials SiC and ZnO. Losev suggested that the phenomenon may be an inverse of the photoelectric effect, as he was able to relate the emission wavelength to the voltage he applied to the material. Interest in EL continued but efficiency did not significantly improve despite extensive research efforts. Losev had originally identified two forms of EL, which depended on the bias of the applied voltage (types I and II). One of these Losev identified as occurring under high reverse bias (type I), and the other required a smaller forward bias (type II). It was suggested by Destriau in 1955 that only type II EL would be able to achieve efficiencies required for lighting applications. Indeed, type II EL forms the basis of light emission from almost all modern LEDs, as we will see [9].

Nowadays we understand that the structures investigated by Round, Losev and Destriau were examples of Schottky barrier diodes, in which there is a contact (also called a junction) between a metal and a semiconductor. The invention of the p-n junction and so-called double heterostructures (DHs), such as quantum wells (QWs), heralded the era of modern LED devices in subsequent decades [9]. In the 1970s and 1980s much work was carried out to develop DHs based on alloys of AlAs and GaAs, in part due to the relative ease in creating high quality DHs made of those materials. These devices mainly emitted in the red-infrared spectral range.

AlAs and GaAs are examples of III-V semiconductors, i.e., they are compounds of group III and group V elements of the periodic table. In the search for materials that could be used in devices that emit over a wider visible spectral range, many compounds and alloys were investigated including II-VI and other III-V semiconductors. III-V semiconductors based on phosphorus containing compounds (phosphides, e.g., InP, GaP) also found significant use in red-infrared wavelength devices. However, when targeting shorter wavelength emission (i.e. from red to green), the efficiency of these devices deteriorated significantly. This was in part due to the incorporation of Al containing alloys such as AlAs or AlP to increase the band gap. Both AlAs and AlP, as well as GaP, are indirect gap semiconductors [15], which exhibit inherently reduced radiative efficiencies. In ternary and quaternary alloys of the indirect semiconductors mentioned above with direct gap materials, such as GaAs, InAs or InP, the band gap of the resulting alloy will switch from direct to indirect once the concentration of indirect gap material reaches a critical level. Thus, when targeting larger band gaps (and smaller wavelengths) by including

larger AlAs, AlP or GaP contents, the band gap becomes indirect and the radiative efficiency of the materials is reduced.

III-V materials based on nitrogen containing compounds (nitrides, e.g., InN, GaN, AlN) had been explored as early as the 1960s. III-N alloys differ significantly from arsenide and phosphide-based semiconductors. For instance, III-N alloys remain direct gap semiconductors over the entire visible wavelength range. However, III-N systems suffered from issues with crystal quality and difficulties in doping (a technique used to increase conductivity), thus the direct gap II-VI semiconductor ZnSe became the front-runner for short wavelength, blue spectral range applications [9]. III-N semiconductors overtook ZnSe as the material of choice when Amano, Akasaki and Nakamura overcame the poor crystal qualities and issues with p-doping GaN [9]. These breakthroughs paved the way for Amano, Akasaki and Nakamura to develop the first efficient blue LEDs, for which they were awarded the Nobel prize in 2014 [16, 17]. III-N systems are now the material of choice for blue LEDs, having outperformed ZnSe [8].

III-nitrides

III-N semiconductors have attracted massive amounts of research attention for a variety of reasons, one of which is the possibility of creating LEDs emitting across a much wider range than the blue section of the visible spectrum [8]. Figure 2 shows the range of theoretically possible emission energies of III-N alloys. The variation in the band gap between InN, AlN and GaN essentially arises from the differences in the interatomic spacings of these materials, which lead to different interactions between atomic orbitals localised on the constituent cation and anion sites. When semiconductors of differing band gaps are alloyed, the band gap of the resulting material lies, in general, somewhere between the two constituent materials. With the band gaps of GaN ($E_g \approx 3.51$ eV [18]) and InN ($E_g \approx 0.69$ eV [18]) lying on either side of the visible spectrum, in principle, alloys of these semiconductors (InGaN) could emit across that entire wavelength range. Furthermore, the band gap of AlN ($E_g \approx 6.0$ eV [19]) lies in the deep ultraviolet (UV) spectral window, thus allowing for the potential creation of LEDs with wavelengths spanning from the infrared to the deep UV. Although work on AlGaN-based UV LEDs has picked up in recent years, current state-of-the-art deep UV LEDs still suffer from relatively poor efficiencies [22].

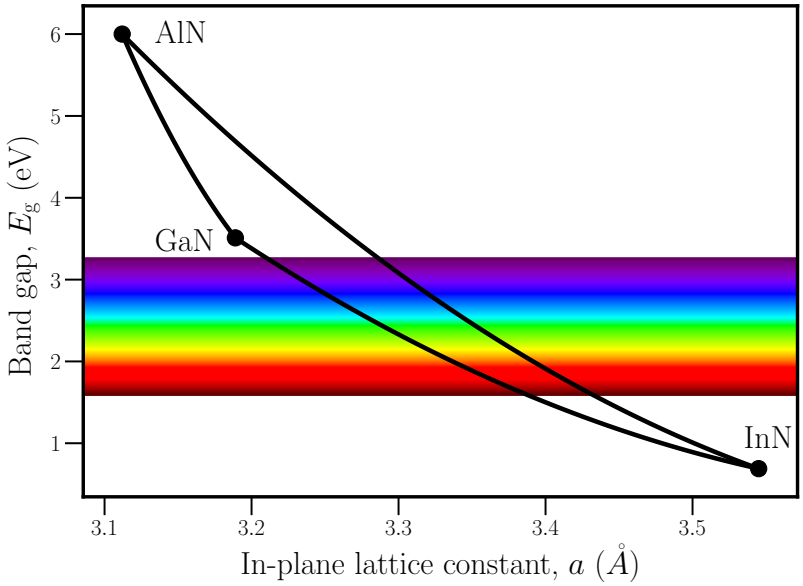


Figure 2: Band gap, E_g, as a function of the in-plane lattice constant, a, for the commonly used wurtzite III-N semiconductors, InN, GaN and AlN. The solid lines represent the range of emission energies from alloys of the III-N semiconductors, which are represented by black filled circles. Photon energies corresponding to the visible spectrum are represented appropriately. Binary III-N band gap values are taken from Ref. [18] (InN and GaN) and Ref. [19] (AlN) with band gap bowing parameters to describe the variation of the band gap as a function of the alloy composition from Ref. [20]. Lattice constants are taken from Ref. [21].

The realisation of efficient blue LEDs allowed not only for the implementation of efficient blue light emitters, but also for their use as the blue component of red-green-blue (RGB) displays, as well as for their use in white light sources [8]. RGB LEDs can be used to generate white light but there are a number of issues that arise. For instance, in practice, realising efficient InGaN-based LEDs with wavelengths in the red-green spectral range has proven extremely challenging [23]. Recalling from above that arsenide and phosphide-based emitters also suffer from poor efficiencies when targeting green wavelengths, the generally much lower efficiency of green LEDs when compared to red and blue emitters is referred to as the so-called “green gap”. Generally, arsenide-based LED technologies are used to produce efficient red light emitters, but integrating different material systems on the same chip raises further challenges [24].

InGaN-based LEDs operating at the blue end of the visible spectrum have found many applications, aided by their relatively high efficiencies, and make

up a significant portion of the lighting market [25]. Thus, given the large historical investment in the methods, expertise and equipment needed to mass produce InGaN-based LEDs, developing established III-N LED technology is more desirable for manufacturers in the short to medium term. Although, work on semiconductor LED alternatives such as organic and polymer-based LEDs continues [8, 25].

Initially, ZnSe was the front-runner for visible blue wavelength range LEDs due to the much higher dislocation densities found in GaN and InGaN. Although the crystal growth methods developed by Amano *et al.* and Nakamura *et al.* allowed the growth of much higher quality GaN crystals, the density of dislocation defects remained much higher ($\approx 10^6$ cm^{-2}) than in other III-V semiconductors such as arsenides and phosphides ($\approx 10^3$–10^5 cm^{-2}), and was even higher still in InGaN ($\approx 10^9$ cm^{-2}). Even though growth techniques have improved since the initial breakthroughs of Amano *et al.* and Nakamura *et al.*, modern GaN and InGaN QW-based LEDs still exhibit higher dislocation densities than other III-V materials, and also, counter-intuitively, higher efficiencies.

The prevailing theory used to explain this is that charge carriers become localised, and as such are prevented from diffusing to defects, where they might recombine nonradiatively (i.e. without the emission of a photon). Carrier localisation has been shown to have a significant impact on the optical and electronic properties of InGaN-based LEDs and we will discuss it in more detail later, but the exact origin of this effect and the length-scale over which it occurs is still debated [26]. As mentioned above, III-N semiconductors differ significantly from "conventional" semiconductor systems, such as those based on arsenides or phosphides. For example, in semiconductor materials, band structures are often characterised by their so-called effective mass. The effective mass is a key ingredient in understanding the electronic properties of a semiconductor and is usually given in units of the free electron mass, m_0. When electrons are excited from the valence band to the conduction band, the "missing" electron in the valence band can also be described by a positively charged quasi-particle, a so-called hole. As in the case of the electrons, an effective mass can also be assigned to a hole. The effective mass of holes in III-N semiconductors ($m^*_{\text{InN}} = 1.61$, $m^*_{\text{GaN}} = 1.87$ and $m^*_{\text{InN}} = 2.68$) is significantly larger than in III-As ($m^*_{\text{InAs}} = 0.26$, $m^*_{\text{GaAs}} = 0.45$ and $m^*_{\text{AlAs}} = 0.51$) or III-Ps ($m^*_{\text{InP}} = 0.46$ and $m^*_{\text{GaP}} = 0.79$). Due to these higher effective masses in III-N systems, small variations in the confining energy landscape of an alloy

disordered crystal or heterostructure may already lead to carrier localisation effects. On top of this, III-Ns tend to crystallise in the wurtzite phase, in contrast to III-As and III-P systems, which tend to crystallise in the zinc blende phase. Due to the nature of the wurtzite crystal structure, which will be discussed in more detail in Sec. 1.4, semiconductor materials in this phase exhibit stronger electrostatic built-in fields. The result of this is that in III-N alloys, where there is a varying local environment of In, Ga or Al ions, the energy landscape is further locally affected when compared to III-V alloys crystallising in the zinc-blende phase. Coupled with the larger hole effective masses, the local polarisation field fluctuations can further enhance carrier (hole) localisation in III-N alloys. Thus, it is an important aspect of the physics of III-N emitters and requires careful consideration. Furthermore, a gain in our understanding of carrier localisation and its impact on optical and electronic properties may also provide insight into how it affects efficiency. Significant efforts have been undertaken to understand the properties of III-N systems generally, and especially the factors that limit the efficiency of such devices. Efforts to further understand and improve the efficiency of III-N LEDs continue, as several bottlenecks have arisen.

Efficiency bottlenecks

Previously we mentioned the green gap, partly caused by the reduction in the efficiency of InGaN-based LEDs as the band gap of the active (light emitting) region of the device is tailored to lower values by increasing the In content in InGaN, in order to emit longer wavelengths in the yellow-green visible spectral range. The causes of the green gap, from the perspective of InGaN-based emitters, are still under debate, but it has been attributed to, for instance, the formation of defects [27, 28] or the increase in the strength of the built-in piezoelectric polarisation fields found in III-N QWs as In content increases, which tends to separate electrons and holes, hampering radiative recombination [29]. The latter aspect is also known as the quantum confined Stark effect (QCSE). Indeed, the theoretical work in Ref. [29] suggests that carrier localisation effects lead to a larger reduction in efficiency as In content increases.

Although the green gap has been attributed to material/active region specific issues, generally there are a number of factors that affect overall device efficiency, such as the efficiency of “injecting” electrons into the active region

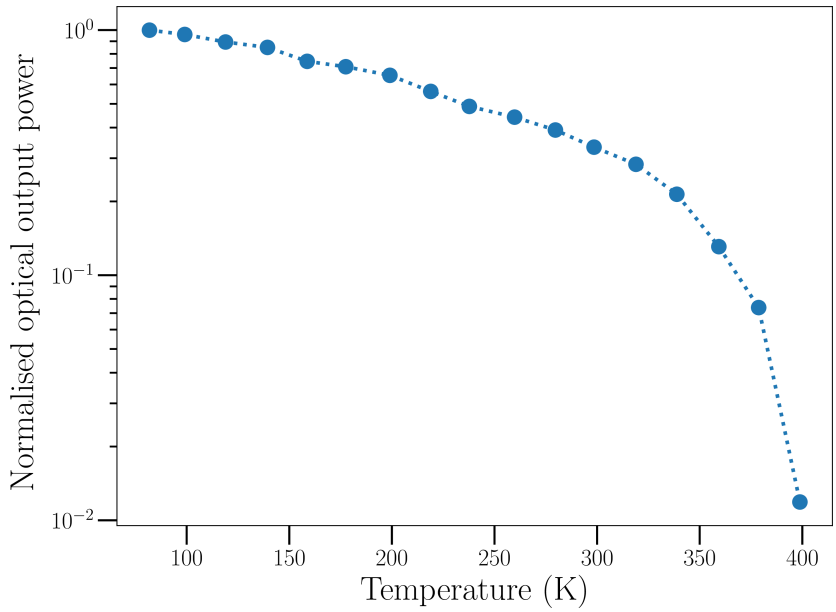


Figure 3: Experimentally determined normalised optical output power as a function of temperature for an InGaN/GaN QW. Adapted from data in Ref. [30]. Note: data is normalised to the output power at low temperatures, hence, it reflects efficiency.

or extracting light out of the device. There are two main efficiency bottlenecks affecting overall device performance that will be focus of this thesis, thermal "droop" and current "droop" [9, 31, 32, 33]. Thermal droop is the reduction in the efficiency of both InGaN and AlGaN QW-based LEDs at elevated temperatures [31, 32]. Figure 3 shows experimental data adapted from Ref. [30] on the (normalised) optical output power as a function of temperature in an InGaN/GaN QW-based LED at a fixed current. Generally, for LED devices, at room temperatures, $\sim 25°C$ (~ 300 K), the efficiency of the device will have already dropped, but there will further heating of the device from electrical energy that is not converted to light, leading to common device temperatures around $80°C$ (~ 350 K), with commercial devices rated up to even higher maximum junction temperatures of $175°C$ (~ 450 K) [30, 32]. In general, in semiconductor materials, Auger recombination is an important (nonradiative) process that can negatively affect device performance. It has been found experimentally in InGaN/GaN QWs that the rate of Auger recombination may increase with increasing temperature [34] and thus the Auger process could be connected to thermal droop. However, other factors such as defect related processes have also been suggested, along with inefficiencies in injecting current into the QW [31].

Current droop (often simply, but confusingly referred to as efficiency droop) is

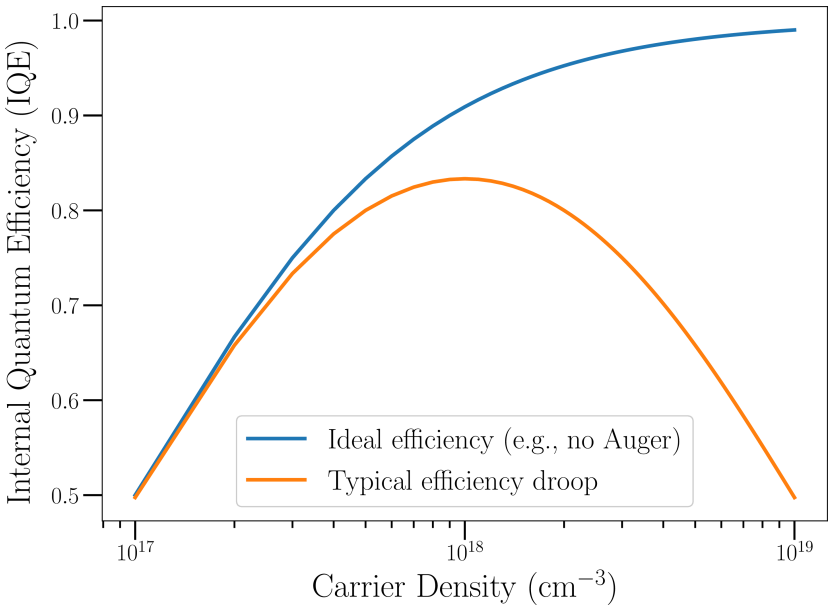


Figure 4: Theoretical IQE as a function of carrier density in a typical droop scenario and in an illustrative ideal scenario in which there is no Auger recombination. For the typical scenario, IQE coefficients of $A = 1 \times 10^{6}$ s^{-1} [2], $B = 1 \times 10^{-11}$ cm^3/s [4] and $C = 1 \times 10^{-30}$ cm^6/s [3] have been used in the ABC model. For the ideal scenario the C coefficient has been set to zero.

the reduction in the efficiency of both InGaN and AlGaN QW-based LEDs as the current density through the LED is increased [33]. Specifically, it is the reduction in the internal quantum efficiency (IQE), essentially the efficiency with which electrons are converted to photons, in the light emitting region of the structure (active region). Ideally, when the current passed through the LED is increased it will lead to an increase in the amount of light emitted. However, it is found that above a threshold current density the efficiency of light conversion decreases. These two scenarios (ideal and "drooped") are depicted in Figure 4, which shows the IQE as a function of carrier density (which is proportional to current density). To combat this, most commercial LEDs are operated at current densities lower than required for high brightness applications [9]. This has limited the use of InGaN-based visible LEDs in applications such as vehicle headlights and may become a significant issue for the use of AlGaN-based UV LEDs in future applications such as large scale water disinfection treatments [22].

Much effort has been directed towards understanding the origin of current droop both experimentally and theoretically. Commonly, the carrier density dependence of the IQE is investigated in terms of the so-called ABC model, in which there are three recombination pathways governed by three coefficients,

A, B and C: the A coefficient describes the Shockley-Read-Hall recombination, B, the radiative recombination and C is the Auger recombination coefficient. However, experimental studies that target the determination of these coefficients are required to make significant assumptions about the coefficients and the IQE in order to disentangle the different pathways. For instance, it is often assumed that the IQE is perfect at low temperatures, but this has been questioned in III-N systems [35]. Furthermore, there is often much uncertainty in the extracted values, and fitting the data for C, for example, may require the assumption of a value for B. It has also been found that parameters obtained via fitting procedures for one sample may not be transferable to other samples. Significant uncertainty remains, and although the role of Auger recombination has received much attention, other causes such as carrier leakage have also been suggested [9, 36].

To support the experimental studies, theoretical work has also targeted the determination of the recombination parameters entering the ABC model. To this end, theoretical frameworks that had been successfully applied to other III-V materials were employed to analyse III-N systems, but provided conflicting results [37, 38, 39]. However, in those analyses alloy disorder and carrier localisation effects were largely neglected, despite the fact that these phenomena were thought to be the primary cause of the high efficiencies of III-N emitters despite their high defect densities. The impact of alloy disorder was largely neglected as it presents a significant modelling challenge. Carrier localisation can occur in InGaN QWs, for example, on the length scale of 2 – 3 atoms [26]. Thus, ideally, an electronic structure theory with an atomistic resolution of the system is required. Simultaneously, while some carriers may be localised on atomistic length scales, others may be more extended, on the length scale of 2 – 3 nm [26]. To account for this, again ideally, a simulation that can be scaled up to these length scales is required. On top of this, including realistic QW widths and the barrier material, along with the polarisation fields mentioned above, presents a unique modelling challenge in nitride-based systems, which may not be present for III-As or III-P systems.

Although there have been some "state-of-the-art" *ab initio* studies of Auger recombination in bulk InGaN [40], modelling heterostructures, such as QWs, is generally beyond the scope of first principles frameworks [37]. Instead, continuum-based models based on, for instance, $\mathbf{k} \cdot \mathbf{p}$ theories, or virtual crystal approximations are often used [29, 37, 38, 39, 41, 42, 43, 44]. Many of these continuum-based models provide a good description of the electronic

structure in a restricted energy range and region of the first Brillouin zone (FBZ), but as we will see, calculating the Auger recombination rate requires an accurate description of the electronic structure in a wider energy range, and potentially over the entire FBZ. Continuum-based models can be extended to accurately describe the full FBZ and larger energy ranges but doing so increases the computational cost [44]. Furthermore, issues can arise in the application of $\mathbf{k} \cdot \mathbf{p}$ -based models to systems with interfaces, such as QWs [39]. Perhaps most importantly though, all of the approaches mentioned above require some spatial averaging of the alloy composition, which reduces the resolution of the simulation and may thus underestimate the impact of carrier localisation. For example, recent results have suggested that the coefficients of radiative and nonradiative Auger recombination in InGaN QWs are not carrier density independent, as is often assumed [2], and experimental reports of the temperature dependence of the radiative recombination rate stand in stark contrast to expectations based on fundamental theory and analysis in modified continuum-based frameworks [4].

Due to the fundamentally atomistic nature of alloy disorder, the intrinsically atomistic tight-binding model represents a natural approach to tackling this problem [45]. However, including effects such as the polarisation fields discussed above or deformations of the semiconductor crystal due to the presence of a heterostructure, present further challenges. So far, there have been very few theoretical studies of carrier recombination in III-N QWs (including InGaN-based QWs emitting in the visible spectral window, despite their technological importance) in an atomistic framework, with the work in Refs. [29], [46] and [47] being the exceptions. For instance, the focus of the studies in Refs. [29] and [46] is the impact of carrier localisation on the radiative recombination rate in InGaN QWs. In this thesis we aim to develop a model that accounts for alloy fluctuations and carrier localisation effects to gain insight into the radiative and Auger recombination rates of realistic InGaN and AlGaN QW structures.

Thesis overview

In Chapter 1 we will discuss some preliminary information on LEDs and how their efficiency is quantified, as well as the III-N heterostructures that form the light-emitting structures at the heart of LEDs. The wurtzite crystal structure of the relevant III-N materials will be introduced as well as some of the properties

unique to III-N systems, such as the previously mentioned polarisation fields and carrier localisation effects.

In order to capture these unique features, in Chapter 2, we will discuss electronic structure theories such as the *ab initio* and continuum-based models mentioned above, as well as the advantages and disadvantages of these methods. Subsequently we will introduce the tight-binding model used in the rest of this thesis to investigate the electronic and optical properties of III-N QWs.

Building on this electronic structure theory, in Chapter 3 we will discuss the determination of the radiative and Auger recombination rates in III-N QWs in general, and how these calculations are carried out within the established tight-binding framework. Subsequently, we will introduce modifications to the electronic structure to account for changes in carrier density.

With the theoretical framework established, in Chapter 4 we will primarily focus on the phenomenon of thermal droop in InGaN/GaN QWs by investigating the temperature dependence of the radiative and Auger recombination rates. This analysis is carried out for three different In contents in the well, allowing us to also comment on the impact of Auger recombination on the green gap.

In Chapter 5 the carrier density dependence of the radiative and Auger recombination rates will be analysed in order to gain insight into the current droop in InGaN/GaN QWs. Here, we will also compare our theoretical results to experimental data extracted by collaborators at the University of Manchester on samples grown at the University of Cambridge.

Lastly, we will target an investigation of thermal droop in UV emitting AlGaN-based systems in Chapter 6. We will discuss modifications to the theoretical framework developed here to determine the temperature dependence of the radiative and Auger rates in AlGaN/AlN QWs, giving insight into the role of Auger recombination in thermal droop.

To conclude, we will summarise the main results of the thesis and discuss open questions and potential future research topics in the outlook in Chapter 7.

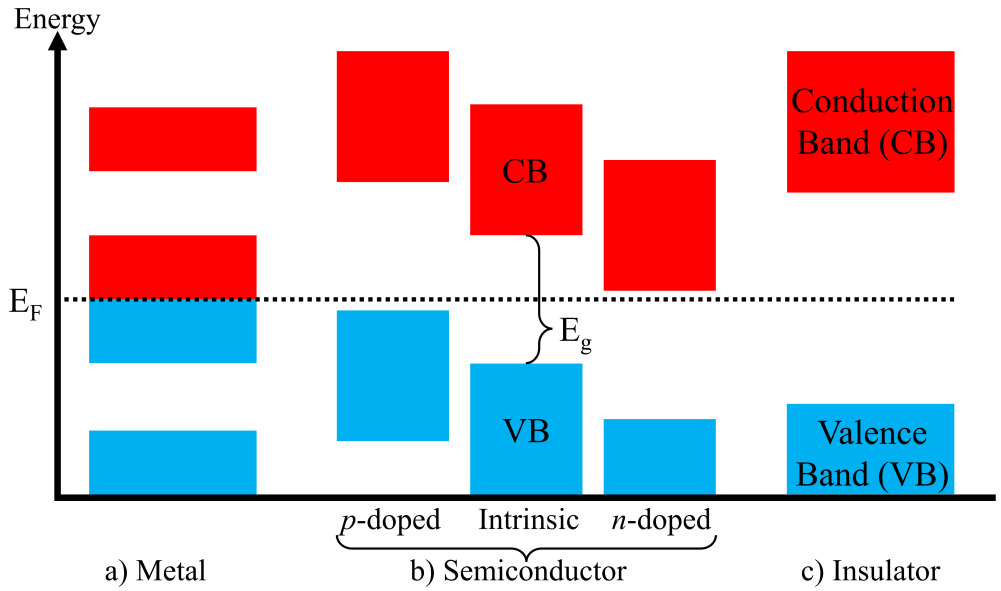


Figure 1.1: Schematic band diagram of a) a metal, b) a p-doped, intrinsic and n-doped semiconductor and c) an insulator. The range of energies that form the conduction (valence) band in a semiconductor and insulator are indicated by red (blue) boxes. Red (blue) energy ranges also represent unoccupied (occupied) electron states at 0 K. The Fermi level, E_F, is represented by a black dashed line. The band gap, E_g, is the difference in energy between the conduction band and valence band edges.

Chapter 1

Light-Emitting Diodes

1.1 Introduction

In the Prologue we mentioned that the advent of p-n junctions paved the way for efficient modern LEDs. All p-n junctions are formed from semiconducting materials. A semiconductor is a crystalline material with an electrical conductivity between that of a metal (which freely conducts charge) and an insulator (which does not freely conduct charge). To understand the categorisation of materials into metals, semiconductors and insulators, we

must first discuss the idea of energy "bands" and the Fermi level.

From fundamental solid state physics, electrons in a crystal may only occupy certain allowed energy states, but these states can be closely spaced in certain energy ranges called "bands", depicted in Figs. 1.1 a), b) and c) [48]. For a system of allowed electron energy states, the Fermi level, E_F, marks the midway point between occupied and unoccupied states (blue and red energy ranges in Fig. 1.1, respectively). In other words, it is the energy at which there is a probability of 1/2 of occupation, even if there is no allowed state at that energy. In a metal, the Fermi level lies within a band, for example in Fig. 1.1 a), thus, electrons are easily excited into unoccupied states by the thermal energy of the system, allowing charge to freely move in the material. In an insulator, the Fermi level lies in the "forbidden energy gap" or "band gap", and there is a large energy separation between bands, for example in Fig. 1.1 c), thus charge does not easily flow. In a semiconductor, the Fermi level also lies in the band gap, but the energy separation between conduction and valence bands is smaller than in an insulator. In this case, the thermal energy of the system is sufficient to excite a small number (i.e. a smaller number than in a metal) of electrons across the band gap into unoccupied states, for example in Fig. 1.1 b).

When an electron is excited into an unoccupied state, it leaves behind a vacant state. Electron vacancies can be thought of as positively charged quasi-particles called *holes*. The unoccupied states above the band gap in a semiconductor are usually referred to as the conduction band, in contrast to the occupied valence band states below the band gap. If an electron that has been excited to the conduction band loses its energy and recombines with a hole in the valence band, a photon of light with energy equal to (or greater than) the band gap of the material can be emitted. In a "direct" band gap material, electron hole pairs recombine and emit a photon as described. In an "indirect" band gap material, the electron must also interact with the underlying crystal lattice in order for the recombination to occur. This reduces the probability of light emission in indirect gap materials compared to direct gap materials.

A p-n junction consists of two regions in a semiconductor with a metallurgic interface between them, an n-doped region and a p-doped region. In an n-doped material, impurities (called dopants) have been added that introduce excess electrons. In this case they are called "donor" atoms as they "donate" extra electrons. In a p-doped material, the dopants have a deficit of electrons

and so introduce vacant sites for electrons to occupy, as such, they are called "acceptor" dopants. In other words, p-doped materials have an excess of holes.

The introduction of dopants to the semiconductor also affects the Fermi level in the system. In intrinsic semiconductors the Fermi level usually sits near the middle of the band gap (see "Intrinsic" in Fig. 1.1 b)). Introducing donor atoms into the system moves the Fermi level towards the conduction band edge (CBE) energy (see "n-doped" in Fig. 1.1 b)) and introducing acceptor atoms moves the Fermi level towards the valence band edge (VBE) energy (see "p-doped" in Fig. 1.1 b)). The energy levels of the n-dopants (E_D for donors) or p-dopants (E_A for acceptors) ideally are near the conduction or valence band edge energies, respectively. These energy levels are indicated by red (E_D) and blue (E_A) dashed lines in Fig. 1.2. The closer these levels are to the relevant band edge energies, the easier it is to excite the excess electrons or holes from the dopants to the band. If the n and p-doped regions consist of the same semiconductor material, and thus have the same band gap, the junction is called a homojunction. In a heterojunction, different semiconductors (which can have different band gaps) are used. When multiple heterojunctions are combined, a heterostructure is formed. The inclusion of heterostructures was a major step in the development of modern efficient LEDs [9]. We will return to the discussion of heterostructures below.

In this chapter we will discuss the general underlying principle of operation of most modern LEDs, i.e., the injection of charge carriers across a p-n junction. The quantum well (QW) double heterostructures which are crucial to the efficiency of LED devices will also be introduced. Subsequently, we will turn to the parameters and ABC model of efficiency often employed in the analysis of LED devices. Having discussed some key concepts pertaining to LEDs in general, lastly, the peculiarities of III-N systems, including their crystal structure, the impact of strain in III-N heterostructures, related polarisation fields, and carrier localisation effects will be discussed.

1.2 Principles of operation

As mentioned, before the introduction of double heterostructures (DHs), the p-n junctions used in LEDs were homojunctions. For the purpose of discussion, if we assume that there is a discrete, step-like change in the concentration of dopants across the interface between the n- and p-doped regions, and no

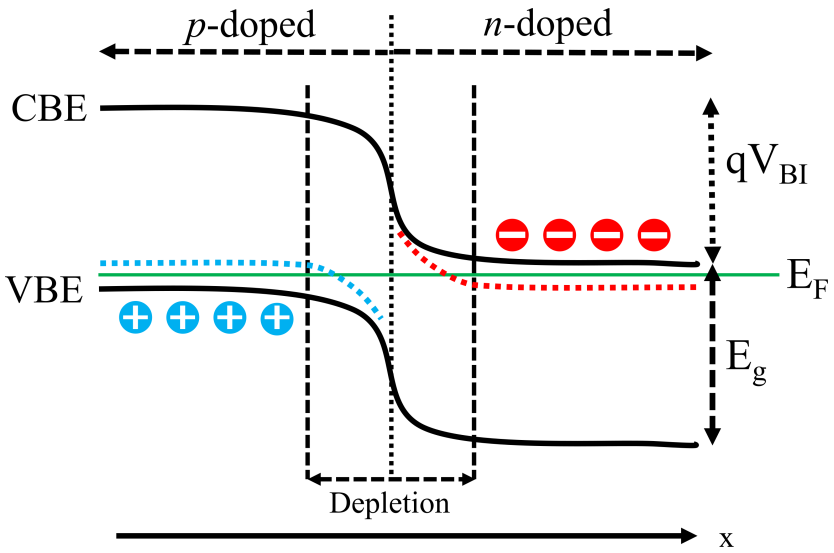


Figure 1.2: Conduction (CBE) and valence band edge (VBE) energies as a function of position along the growth direction of a p-n junction. Electrons in the n-doped region see a potential barrier due to the bending of bands by the built-in potential, similarly for holes in the p-doped region. The potential barrier is indicated by qV_{BI}. The depletion region forms around the interface between the n- and p-doped regions. Donor impurities in the n-doped (p-doped) region move the Fermi level, E_F towards the CBE (VBE). Dopant energies are indicated by red (blue) dashed lines for donors (acceptors). The built-in potential ensures that there is no discontinuity in the Fermi level.

external voltage applied to the junction, then there will be a region with a high concentration of electrons (the n-doped region) next to a region with a low concentration of electrons (the p-doped region), and vice versa for holes. Furthermore, due to the alteration of the Fermi level of the system with the introduction of n- and p-dopants, there will a discontinuity of the Fermi level across the interface. Charge will flow from a region of higher Fermi level to lower Fermi level [49].

Fick's law describes the tendency of particles to diffuse from regions of high to low concentration, thus electrons from the n-doped region will diffuse into the p-doped region and holes into the n-doped region. Electrons diffusing into the p-doped region will recombine with the excess of holes, and similarly for holes diffusing into the n-doped region. On either side of the interface a region of low electron and hole concentration will form called the depletion region.

Furthermore, as electrons diffuse from the n-doped region, positively charged donors remain. Similarly for holes, negatively charged acceptors remain in the p-doped region. The resulting net positive and negative charges in the n- and p-doped regions induce an electric field that opposes the diffusion process.

Associated with this field is a potential drop, V_{BI}, that will align the Fermi levels in the n- and p-doped regions, bringing the system into equilibrium, and resulting in a "band bending" effect, shown above in Fig. 1.2. Thus, for instance, electrons in the n-doped region see an energy barrier preventing their movement to the p-side of the junction.

If we apply a voltage across the junction that pulls carriers away from the depletion region (i.e. so that electrons are pulled to the right and holes to the left in Fig. 1.2, called reverse bias) the width of the depletion region and the magnitude of the potential energy barrier will increase. Conversely, applying a forward bias will reduce the width of the depletion region and magnitude of the potential barrier which will allow current to flow.

When current flows, electrons and holes cross the depletion region and may then recombine radiatively. This is depicted schematically below in Fig. 1.3 a). As we will see in more detail in the next section, the rate of radiative recombination depends on the concentration of charge carriers, thus increasing the carrier concentration would ideally lead to an increased rate of radiative recombination. This can be achieved by the inclusion of a double heterostructure.

1.2.1 Double heterostructures and quantum wells

Double heterostuctures (DHs) offer a number of advantages. The DHs targeted during the development of modern LEDs consisted of a material with a band gap that was lower than the band gap of the surrounding (barrier) material. One major advantage of this is that the light emitted by recombination in the lower band gap material (the so-called "active layer"/"active region") would not be absorbed by the barrier material, improving efficiency [9]. Furthermore, due to the lower energy in the active layer depicted in Fig. 1.3 b), charge carriers become confined in the DH. A schematic of the impact of the inclusion of a DH on the electrons and holes in a p-n junction is shown in Fig. 1.3 b). The confinement of electrons and holes in the active layer leads to a much higher rate of light emission from this region.

When first developed, DHs consisted of active layers with widths of $\sim$ 10 – 100 nm (e.g. the first nitride DHs developed by Nakamura *et al.* included an InGaN active layer 45 nm thick [50]). These improved device performance significantly, increasing light output power from 42 μW for a GaN

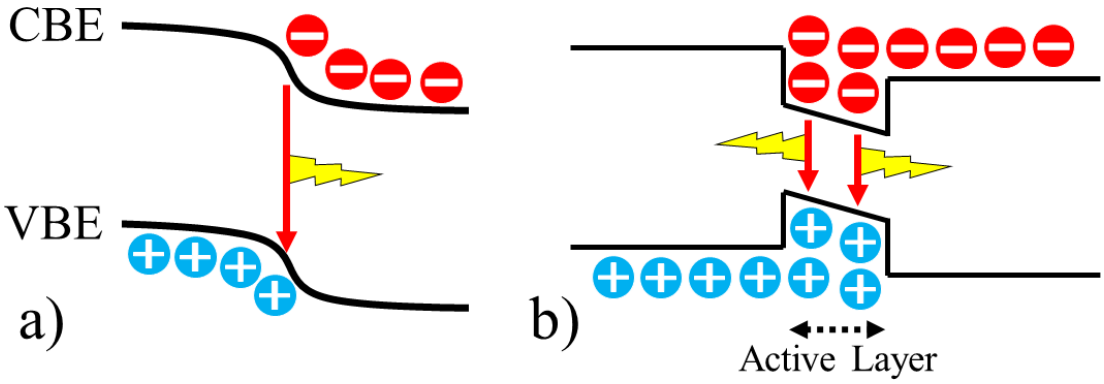


Figure 1.3: a) Under forward bias, the built-in potential and depletion region width in the p-n junction reduce, allowing carriers to enter. Carriers can undergo recombination, potentially resulting in the emission of a photon. b) Introduction of a double heterostructure confines carriers in the same spatial region, increasing the likelihood of recombination occurring.

homojunction (i.e. a homojunction consisting simply of n- and p-doped GaN) to 1.5 mW when including an InGaN DH [50]. Further improvements to growth techniques allowed the realisation of DHs with much narrower widths, increasing the concentration of charge carriers and thus the amount of light emitted [50].

Semiconductor QWs are DHs that are so thin ($\sim$ a few nanometres) that quantum confinement effects begin to manifest, bringing further advantages, such as the possibility to tailor the emission wavelength. By changing the band gap of the material in the active layer (using, for instance, alloys such as InGaN) and also the width of the active layer [51], QWs can be engineered to emit light at a specific wavelength. Modern blue LEDs often include QWs with widths of around 2 – 3 nm. The variation of the conduction and valence bands form a confining potential. A simple approximation of this situation is as a 1D particle in a box problem, schematic solutions of which are shown in Fig.1.4.

Figure 1.4 depicts the change in conduction band edge energy (CBE) and valence band edge energy (VBE) as a function of position along the direction of quantum confinement, when a material of lower band gap is embedded in a material of higher band gap. The QW shown in Fig. 1.4 is an example of a type I heterostructure (or type I band alignment), in which both electrons and holes are confined in the active layer (i.e. the CBE of the well material is lower in energy than the barrier material, and the VBE of the well material is higher in energy than the barrier material). In type II heterostructures, only one type of carrier is confined, for instance, the CBE of the well may be lower in energy

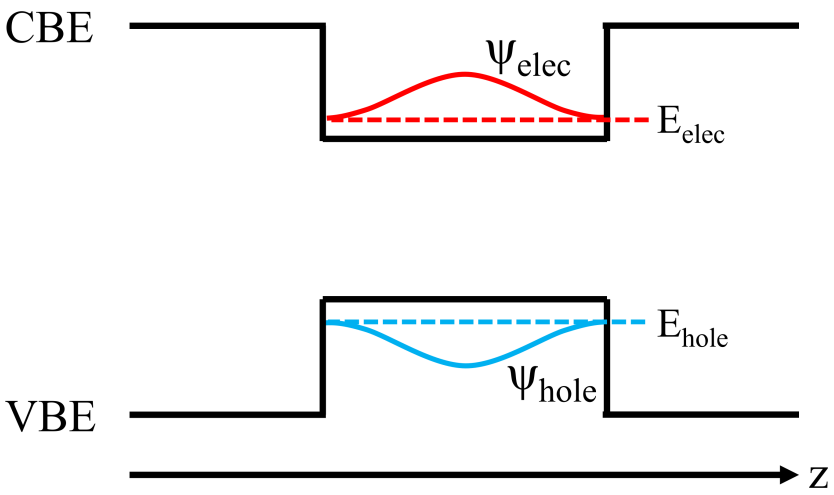


Figure 1.4: Type I band alignment of a typical QW showing variation of band edges as a function of position along the direction of quantum confinement. Carriers are confined in the region of lower band gap. Schematic solutions to a 1D particle in a box problem are represented by the carrier wave functions, Ψ, and lowest energy levels, E.

than the CBE of the barrier, but the VBE of the well may also be lower in energy than the VBE of the barrier, in which case only electrons would be confined in the QW, and vice versa.

As discussed above, confining both electrons and holes in the active layer leads to increased carrier concentration in the same spatial region and thus an increased rate of radiative recombination. For this reason, type I band alignments are desirable in optoelectronic applications. Further details on band alignments in type I and II heterostructures can be found in Ref. [52]. From a fundamental physics perspective the band alignment is determined by the band gap and the valence band offset, which can be determined theoretically or experimentally [20, 53, 54]. For example, for InN and GaN, the valence band offset (i.e. the difference in energy between the top of the valence band edges) has been determined to be approximately 0.62 eV [53, 54] (with the VBE of InN siting at higher energies than the VBE of GaN), and, as we saw above, the band gap of InN (and InGaN alloys) is smaller than that of GaN.

So far, we have discussed radiative recombination a number of times, as well as the efficiency of LEDs. We return now to the common measures of efficiency in LEDs in more detail, as well as quantifying the relationship between radiative (and nonradiative) recombination and efficiency.

1.3 Quantifying and modelling efficiency in LED devices

Throughout the history of the development of light-emitting diodes (LEDs) efficiency has been a key parameter since the optimisation of energy conversion is desirable for many reasons (e.g. commercial interests, pure scientific curiosity and, more recently, carbon output mitigation) [55]. However, in an LED device there are a number of parameters that are used to characterise the efficiency, the product of which gives the overall LED efficiency, known as the wall-plug efficiency (WPE) [9]. The following definitions are presented in Ref. [56] and only summarised here. A very thorough discussion of measures of efficiency, as well as factors that can affect efficiency in LEDs, can also be found in Ref. [9]. The WPE (η_{WPE}, also known as power efficiency) is the overarching measure of the total light output of an LED compared to the total electrical input to the LED, and accounts for all energy losses in the structure. WPEs can then be broken down into two contributions, the voltage efficiency (VE, η_{VE}, also known as feeding efficiency or electrical efficiency) and the external quantum efficiency (EQE, η_{EQE}) such that

$$\eta_{\text{WPE}} = \eta_{\text{VE}} \times \eta_{\text{EQE}} \ .$$

VE is defined as the fraction of electrical power supplied to injected electron hole pairs in the active region (e.g. in the QW). Losses measured by this parameter are mainly attributed to Ohmic heating of the contacts between the device power supply and the p-n junction. Another contributing factor to the VE is the injection efficiency (IE, η_{IE}). The IE is the ratio of the number of electrons injected into the active layer (shown in Fig. 1.3 b) above) to the number of electrons injected into the overall LED structure. IE can then take into account losses due to, for instance, carrier overshoot, where an electron or hole does not become confined in the active region.

EQE is defined as the ratio of the number of photons emitted from the device to the number of electrons injected into the active region. However, some photons produced in the active region of the device will not be emitted, for instance, they may be reabsorbed by free carriers in the barriers or in the metal contacts, or may be emitted in the wrong direction, e.g., towards the underlying substrate on which the LED is grown. There, in the substrate, they may also undergo absorption [9]. Thus, EQE can be further broken down into

two contributions, the light extraction efficiency (LEE, η_{LEE}) and the internal quantum efficiency (IQE, η_{IQE}) such that

$$\eta_{\text{EQE}} = \eta_{\text{LEE}} \times \eta_{\text{IQE}} \ .$$

LEE is a measure of the ability of photons to be extracted from the device and is a significant limiting factor in, for instance, the efficiency of deep UV emitting LEDs [22, 57, 58].

Furthermore, in III-N-based LEDs, as mentioned above in the Prologue, the IQE has been shown to "droop" with increasing carrier density. The IQE is defined as the ratio of the rate of photon generation to the total rate of recombination (including radiative and nonradiative processes) in the active region. The IQE allows us to quantify the efficiency of the active region in converting recombining electrons to photons. However, experimentally determining the IQE can prove challenging, due to the challenge of disentangling the measurements of the parameters described above [9]. Regardless, efforts have been made that rely on the so-called ABC model, that we will discuss in the following section, to shed light onto the droop effect and the IQE in general.

1.3.1 ABC model

In the ABC model [9, 33, 59], three major recombination pathways are usually considered:

- A nonradiative Shockley-Read-Hall (SRH) [60, 61, 62] recombination process that scales linearly with electron carrier density, n ($R_{\text{SRH}} \propto n$),
- a radiative recombination process proportional to the product of electron, n, and hole, p, carrier densities ($R_{\text{rad}} \propto np$),
- a nonradiative Auger recombination process involving three carriers ($R_{\text{Auger}} \propto n^2p$ or np^2).

The coefficients of proportionality are then the A, B and C recombination coefficients such that $R_{\text{SRH}} = An$, $R_{\text{rad}} = Bnp$ and $R_{\text{Auger}} = C_{nnp}n^2p + C_{npp}np^2$. The C_{nnp} and C_{npp} Auger coefficients are also often referred to as C_{eeh} and C_{hhe}, respectively. One of the main assumptions of the ABC model is that these proportionality coefficients are constants and thus independent of carrier density or temperature. Furthermore, in experimental reports of recombination coefficients, the coefficients can often be considered as

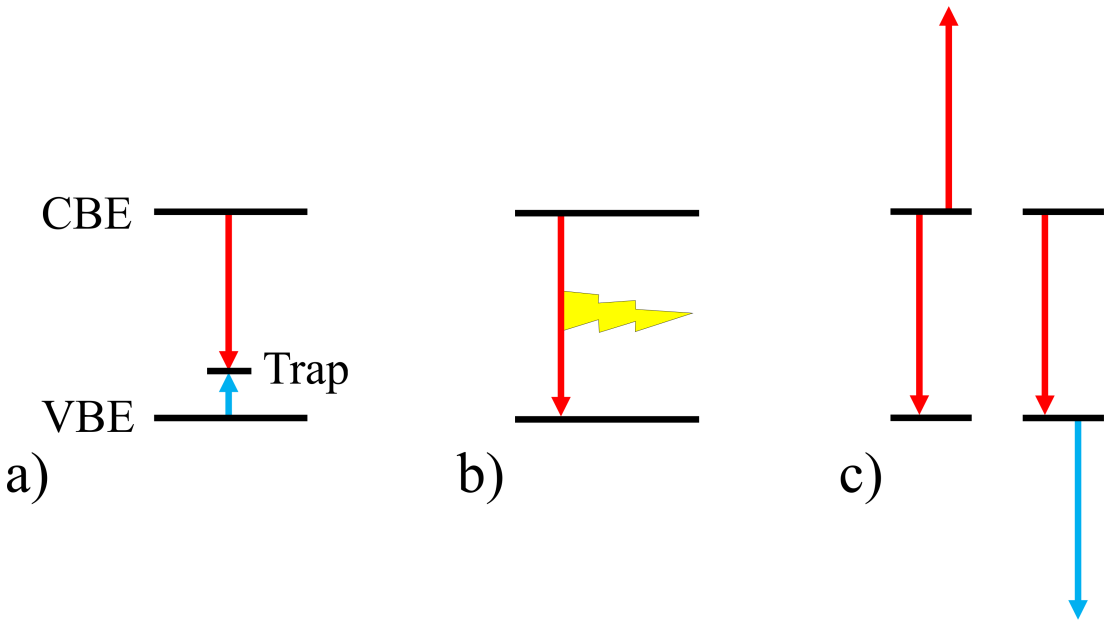


Figure 1.5: Schematic representations of the three recombination pathways in conventional ABC models. Changes in electron energy are represented by red arrows, changes in hole energy are represented by blue arrows. a) Shockley-Read-Hall recombination at a defect (trap) state is nonradiative. b) Radiative recombination results in the emission of a photon. c) Auger recombination is a three particle process. An electron hole pair recombine and interact with either another electron (eeh Auger) or another hole (hhe Auger) as shown.

"effective" parameters that include contributions from many processes. For instance, values of C reported in the literature may include contributions from different Auger-type processes, such as those enhanced by phonons or defects, or even other nonradiative processes. On top of this, when extracting coefficient values experimentally, often some assumptions about the value of, for instance, the B coefficient is required in order to determine C. Also, the coefficients extracted for a given experimental sample might not be transferable to other samples, given the empirical nature of the fitting. Thus, targeting a direct calculation of the coefficients may allow us to gain insight into the relative importance of different recombination processes, both radiative and nonradiative.

Figure 1.5 shows schematic depictions of the a) SRH, b) radiative and c) Auger recombination processes. The SRH model of recombination in semiconductors involves the recombination of an electron hole pair via an intermediate state (called a "trap" state), with an energy that lies in the band gap [60, 61, 62]. The intermediate state is generally associated with defects in the material,

such as impurities or threading dislocations [26]. Radiative recombination refers to a recombination event in which a photon is emitted. Auger recombination, also referred to as Auger-Meitner recombination [63, 64], is a three carrier process independently discovered by Pierre Auger and Lise Meitner in the mid-1920s. In an Auger recombination event, an electron hole pair recombines and interacts with either an electron or a hole via the Coulomb interaction. Thus, there are two distinct Auger processes, namely electron-electron-hole (eeh, sometimes called nnp) and hole-hole-electron (hhe, also called npp), depicted in Fig. 1.5 c). The total Auger rate is the sum of the eeh and hhe rates, and here the coefficient of total Auger recombination, C_{tot}, is the sum of C_{eeh} and C_{hhe}. Auger recombination is a nonradiative recombination process as it produces "hot" Auger carriers instead of photons.

In general, from the definition of the IQE;

$$\begin{aligned} \text{IQE} &= \frac{\#\left(\text{radiative recombinations}\right)}{\#\left(\text{recombinations in total}\right)} \\ &= \frac{R_{\text{radiative}}}{R_{\text{radiative}} + R_{\text{nonradiative}}} \\ &= \frac{Bnp}{Bnp + An + (C_{eeh}n^2p + C_{hhe}np^2)} \ . \end{aligned} \tag{1.1}$$

Here we have made the assumption that every electron injected into the active region undergoes one of the above recombination processes. Different approaches to determining A, B and C experimentally have been discussed in the literature but often require significant assumptions. For instance, as mentioned, it is often assumed that these coefficients do not vary with temperature or carrier density [65], or these approaches require some *a priori* knowledge of the B coefficient in order to determine A and C [65]. Accurately determining the carrier density in the active layer can also present another challenge.

The ABC model was, in the context of III-Ns, first invoked by Shen *et al.* to explain the observation of current droop. They reported that the droop was related to an internal loss process, and not, for instance, injection efficiency [66]. Although debate over the applicability of the ABC model to nitrides continues [59], this approach remains (sometimes with modifications) one of the primary methods used to quantify the IQE, as well as the radiative and nonradiative recombination rates both experimentally and theoretically [67, 68, 69, 70]. Often, experimental determinations of IQE take

a "top-down" approach, by fitting the expression for IQE in Eq. (1.1) to experimental data with A, B and C being free parameters.

Theoretically, however, it is possible to attempt a "bottom-up" analysis, determining the recombination coefficients (and thus the IQE) from the electronic structure. In order to gain this information about the electronic structure, we must account for material specific aspects, for instance, the underlying crystal structure and QW properties (e.g. well width, alloy composition, etc.). Although the ABC model is generally applicable to semiconductor LEDs [9], as discussed in the Prologue, III-N materials differ from "conventional" semiconductor materials in several ways, with these peculiarities, to a large extent, stemming from their crystal structure, material properties and growth direction. To obtain a detailed understanding of the IQE, we must gain insight into the electronic structure, which is tightly linked to the underlying crystal structure and resulting and connected properties of III-N materials. In the next section we discuss these features as well as the resulting impact on heterostructures consisting of these materials.

1.4 III-nitride materials and derived heterostructures

In general, when referring to III-N semiconductors, we are referring to the binary alloys InN, GaN and AlN, along with ternary alloys derived from these such as InGaN and AlGaN. One feature of the binary III-Ns that sets them apart from conventional III-V semiconductors is that they are thermodynamically stable in the wurtzite crystal structure, instead of the zinc-blende crystal structure [71, 72, 73]. So, we begin by examining features of a wurtzite crystal structure. In this analysis we assume the material is perfectly crystalline and does not contain defects.

1.4.1 Wurtzite crystal structure

Figure 1.6 shows an overview of the wurtzite unit cell. Features of this crystal structure are well documented and here we mainly summarise the discussion in Refs. [71] and [74]. The wurtzite crystal structure has C_{6v} symmetry [75]. In contrast to cubic systems, this hexagonal system is characterised by two lattice constants, a and c (see Fig. 1.6). If one makes an observation of the

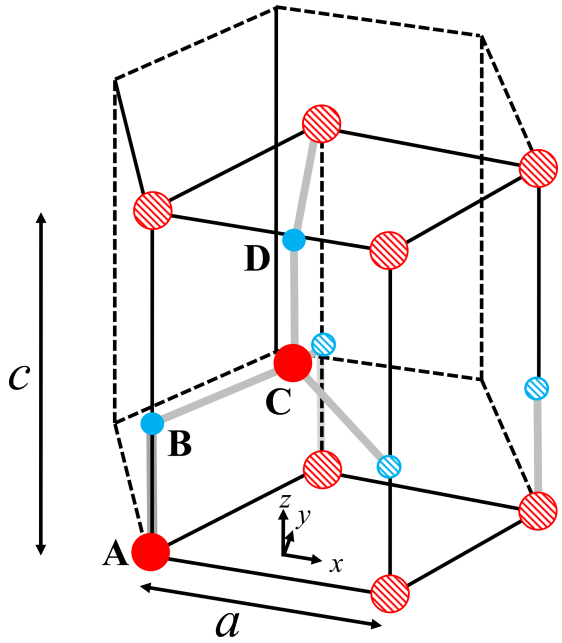


Figure 1.6: Representation of the wurtzite crystal structure (not to scale). The ions of the unit cell are labeled **A** to **D** and represented by the filled coloured circles, red circles representing cations (positively charged) such as In, Ga and Al, and blue representing anions (negatively charged), in this case N. The hatched circles represent periodic replicas of the ions of the unit cell. Cartesian x, y and z axes are presented relative to the lattice. The in-plane (x-y-plane), a, and out-of-plane (z-direction), c, lattice constants are also shown. Adapted from Ref. [72].

layout of atoms in the wurtzite lattice at a certain point, and then translates by a distance c along the $\hat{z}$-direction, the new atomic configuration will be indistinguishable. This direction is also called the c-axis/c-direction. The ideal wurtzite structure is formed by two interpenetrating hexagonal close-packed sub-lattices, offset by $(5/8)c$ in the z-direction. Similar translational invariances hold in the plane defined by x and y, which is called the c-plane, as it is normal to the c-axis.

Along with c, along the base of the structure there is the in-plane lattice constant a. Often, we will refer to in-plane (x-y plane, a lattice constant) and out-of-plane (z-direction, c lattice constant) directions, which correspond to directions in and perpendicular to the c-plane, respectively. Translations of the lattice that result in an indistinguishable lattice are defined by the primitive

lattice vectors:

$$\begin{aligned}\mathbf{a} &= (a, 0, 0) \ , \\ \mathbf{b} &= ((1/2)a, (\sqrt{3}/2)a, 0) \ , \\ \mathbf{c} &= (0, 0, c) \ .\end{aligned}$$

In Fig. 1.6, the ions of the unit cell are denoted by the coloured circles, red circles denoting cations (positively charged) such as In, Ga and Al, and blue denoting anions (negatively charged), in this case N. The anions and cations form alternating layers. The filled circles represent atoms of the primitive unit cell, i.e., the group of ions that generate the entire crystal when translated by the primitive lattice vectors. Shaded circles represent atoms in neighbouring periodic replicas of the unit cell. Often, the positions of ions in the lattice are given in terms of a, c and the internal parameter u. The internal parameter is defined to be the length of the cation-anion bond divided by c. In an ideal wurtzite structure $u = 3/8$ [76]. Within the primitive unit cell, atomic sites are located at the following positions [76]:

$$\begin{aligned}\mathbf{r_A} &= (0, 0, 0) \ , \\ \mathbf{r_B} &= (0, 0, uc) \ , \\ \mathbf{r_C} &= ((1/2)a, (1/(2\sqrt{3}))a, c/2) \ , \\ \mathbf{r_D} &= ((1/2)a, (1/(2\sqrt{3}))a, (u + 1/2)c) \ .\end{aligned}$$

Above, we defined the c-plane as the plane normal to the c-axis. In general, crystallographic directions and planes can be defined by Miller indices; h, k and l [48]. These indices are the reciprocal of the point of intersection of the plane of interest with the axes defined by the primitive lattice vectors, and negative values are identified by a bar above the index, e.g., $\bar{h}$. In general, a crystallographic *plane* is labelled with round brackets, (hkl), thus, in our example above, the c-plane would be denoted by (001). Square brackets are used to denote a *direction*, thus, above, the associated c-direction would be [001]. However, in hexagonal lattices a modified version called Miller-Bravais indices are used where the index $i = -h - k$ is introduced. The modified label is then $(hkil)$. This allows for quick identification of equivalent directions in hexagonal lattices. In Miller-Bravais notation, the wurtzite c-plane above becomes the (0001)-plane, and the c-direction is the [0001]-direction.

Although the definition of the Miller and Miller-Bravais indices may seem unusual, it allows for easier identification of crystallographic planes during experimental investigations of these crystals via measurements of the diffraction of, for instance, X-rays through the material [77]. In fact, the concept of the reciprocal of a real space length is key to investigating not only crystal structures, but also the nature of the quantum mechanical states of charge carriers. We will return to this idea of a "reciprocal space" below when we discuss the electronic structure. In general, the c-direction is the most common growth direction of III-N semiconductors, with layers deposited throughout the growth process on the c-plane. As we will be primarily discussing c-plane III-N QWs, we will often refer to the c-plane as the growth plane, and the c-direction as the growth direction. It is possible to grow III-Ns on other planes such as the $(1\bar{1}00)$-plane (m-plane) and the $(11\bar{2}0)$-plane (a-plane), however, it is more difficult to grow high quality crystals in these directions [78].

Furthermore, as mentioned previously, the atomic positions in a wurtzite crystal structure are often expressed in terms of the internal parameter, u. In an *ideal* structure, $u = 3/8$. However, in *realistic* wurtzite III-Ns u deviates from this value [79, 80, 81, 82]. The consequence of this deviation is that wurtzite systems exhibit a built-in electric polarisation, $\mathbf{P}$. From electrostatics we know that any discontinuity in $\mathbf{P}$ will lead to bound polarisation induced charges and built-in electrostatic fields [83, 84]. Although growth along other directions may be targeted to avoid the formation of polarisation fields, c-plane growth is the most common. Thus, the electric polarisation is the subject of our next discussion, as it can have a strong impact on the optical and electronic properties of c-plane III-N heterostructures.

1.4.2 Polarisation

Wurtzite III-N heterostructures have been shown experimentally to contain strong built-in electrostatic fields, stronger than those found in conventional III-V and II-VI semiconductors [85, 86]. As mentioned above, due to the deviation of the internal parameter from ideal in real wurtzite III-Ns, there will be a built-in polarisation. This deviation gives rise to a net dipole moment in each primitive unit cell along the vector from ion **D** to **C** in Fig. 1.6 above, $\mathbf{d_{DC}}$, i.e., the $-z$ direction. The net dipole moment per volume is defined to be the spontaneous polarisation vector field, $\mathbf{P}_{\text{SP}}$. In unstrained systems, spontaneous

polarisation is not found in zinc-blende materials due to reasons of symmetry [87, 88]. Furthermore, it has been observed that the magnitude of the spontaneous polarisation in wurtzite III-Ns is much larger than in wurtzite II-VI materials such as ZnO or BeO [85]. Further discussion can be found in Refs. [75] and [87].

In III-N heterostructures, on top of the spontaneous polarisation, $\mathbf{P}_{\text{SP}}$, there is also the possibility of a strain induced piezoelectric polarisation vector field, $\mathbf{P}_{\text{PZ}}$. It has been found experimentally that III-N materials exhibit significantly higher piezoelectric responses compared to other semiconductors given their high bond ionicity, and can be up to ten times larger in wurtzite III-N materials when compared to, for instance, zinc-blende arsenides [85, 86]. We now turn to discuss the piezoelectric polarisation in more detail.

1.4.2.1 Piezoelectric polarisation and strain

Deformations of a material cause strain to arise. In semiconductor crystals that lack inversion symmetry, strain can result in the formation of a net dipole moment [89]. This phenomenon, known as the piezoelectric effect, is strongly linked to the symmetry of the underlying crystal structure, the applied strain (hydrostatic, biaxial compressive, shear strain) and the growth direction. In general, we can relate the piezoelectric polarisation field, $\mathbf{P}_{\text{PZ}}$, in a material to an applied strain, ε, via the components of the strain tensor, ε_{jk}, and the components of the piezoelectric tensor, e_{ijk}, such that

$$P_{\text{PZ},i} = \sum_{j=1}^{3} \sum_{k=1}^{3} e_{ijk} \varepsilon_{jk} \ ,$$

where the indices i, j and k ($\in \{1, 2, 3\}$) run over the three Cartesian directions x, y and z of 3D space. This formalism, and the discussion below, broadly follow the approach set out in Ref. [87].

In linear elasticity theory, the strain tensor, ε, is of the form [87]

$$\varepsilon = \begin{pmatrix} \varepsilon_{xx} & \varepsilon_{yx} & \varepsilon_{zx} \\ \varepsilon_{xy} & \varepsilon_{yy} & \varepsilon_{zy} \\ \varepsilon_{xz} & \varepsilon_{yz} & \varepsilon_{zz} \end{pmatrix} \ ,$$

however, it can be shown [87] that three of the nine entries are redundant as the j and k indices are interchangeable due to symmetries of ε_{jk} [89]. This

simplification, due to Voigt [87], is often employed. If we describe pairs of indices as $xx = 1$, $yy = 2$, $zz = 3$, $yz = 4$, $xz = 5$, $xy = 6$, the strain tensor becomes

$$\varepsilon = \begin{pmatrix} \varepsilon_1 & \varepsilon_2 & \varepsilon_3 & \varepsilon_4 & \varepsilon_5 & \varepsilon_6 \end{pmatrix}^T \ .$$

It is also noted in Ref. [87] that in this convention $\varepsilon_\alpha = \varepsilon_{jk} + \varepsilon_{kj} = 2\varepsilon_{jk}$ with $j \neq k$, and the inclusion or exclusion of the factor of two has been inconsistent in the literature. Regardless, in Voigt notation the piezoelectric tensor becomes

$$e = \begin{pmatrix} e_{11} & e_{12} & e_{13} & e_{14} & e_{15} & e_{16} \\ e_{21} & e_{22} & e_{23} & e_{24} & e_{25} & e_{26} \\ e_{31} & e_{32} & e_{33} & e_{34} & e_{35} & e_{36} \end{pmatrix} \ .$$

However, some of these components can be shown to be either zero, or equal to other components, depending on the symmetry of the crystal structure of the material being described [87]. In a system with wurtzite symmetry, the piezoelectric tensor is

$$e = \begin{pmatrix} 0 & 0 & 0 & 0 & e_{15} & 0 \\ 0 & 0 & 0 & e_{15} & 0 & 0 \\ e_{31} & e_{31} & e_{33} & 0 & 0 & 0 \end{pmatrix} \ . \tag{1.2}$$

Overall then, for instance, in Voigt notation, the component of the piezoelectric polarisation vector field in the z-direction is given by

$$P_{\text{PZ},3} = \sum_{\alpha=1}^{6} e_{3\alpha}\varepsilon_\alpha \ . \tag{1.3}$$

The expression in Eq. (1.3) illustrates that strain in the growth plane of c-plane III-Ns will lead to a piezoelectric response. In III-N QWs, in-plane strain arises when III-N alloys with different in-plane lattice constants are grown on top of each other. We now look at the consequences this has for c-plane III-N QWs.

1.4.3 Impact of polarisation on III-N quantum wells

Most modern short-wavelength visible spectral range LEDs incorporate QWs consisting of thin (2 – 3 nm) c-plane InGaN layers in the active region, surrounded by, for instance, c-plane GaN barriers [67, 68, 69, 70]. Thus, already we expect that the discontinuity in spontaneous polarisation will lead to the formation of a polarisation field across the well. Furthermore, the

in-plane lattice constant mismatch between, for example, InN and GaN is approximately 11% ($a(\text{InN}) = 3.545$ Å and $a(\text{GaN}) = 3.189$ Å [21]) and so will lead to a significant strain in the system. As discussed above, this strain will lead to a piezoelectric contribution to the polarisation field in the well. In order to discuss the impact of the polarisation field on the electronic and optical properties of III-N QWs, as an illustration, we will focus on a simplified, 1D description of an InGaN/GaN QW.

In order to investigate the built-in polarisation field we require some knowledge of the strain that will arise from the lattice mismatch between GaN and the InGaN alloy in the well. To do this, we need to determine the lattice constants of the bulk (i.e. not in a QW) InGaN alloy. However, due to the distribution of In in the alloy it is not immediately clear how to do so, as the value will vary between areas of higher and lower In content. One approximation commonly used in this situation is the virtual crystal approximation (VCA). In a VCA various physical parameters of the bulk alloy are approximated as being weighted averages of the parameters of the constituent materials (such as the lattice constants, elastic constants, band gaps, etc. [21, 79]). This approach works remarkably well when describing, for example, the lattice constants of bulk InGaN alloys [90]. We denote InGaN alloys with specific InN contents by $\text{In}_x\text{Ga}_{1-x}\text{N}$, where x is the fractional molar InN content in the alloy. We can apply this approach to determine the a lattice constant of an $\text{In}_x\text{Ga}_{1-x}\text{N}$ alloy by using the following interpolation due to Végard (called Végard's law) [21];

$$a(\text{In}_x\text{Ga}_{1-x}\text{N}) = xa(\text{InN}) + (1-x)a(\text{GaN}) \ . \tag{1.4}$$

For instance, using parameters from Ref. [21], for a typical InN content of 10%, i.e., $x = 0.1$, with the in-plane lattice constants for InN and GaN given above, the resulting in-plane lattice constant for a $\text{In}_{0.1}\text{Ga}_{0.9}\text{N}$ alloy is $a(\text{In}_{0.1}\text{Ga}_{0.9}\text{N}) = 3.225$ Å. For the lattice parameters, Eq. (1.4) is often employed [21, 79], but for other material parameters, for instance band gaps, Eq. (1.4) needs to be modified to include a quadratic dependence of parameter on composition. The quadratic dependence is characterised by the so-called bowing parameter, which describes the deviation from a linear dependence. The bowing parameter can be determined by fitting experimental or theoretical data [20, 53, 82].

When such an $\text{In}_x\text{Ga}_{1-x}\text{N}$ alloy is grown on a GaN substrate, the mismatch in

the lattice constants will lead to a compressive strain in the $In_xGa_{1-x}N$ alloy in the growth plane if pseudomorphic growth is assumed. In such a case, the strain is constant in the QW region, but to minimise the elastic energy of the system, the InGaN "expands" along the growth direction. This assumption will generally be reasonable as long as the well width is below the critical thickness of an InGaN layer [91, 92, 93]. Thus, the in-plane lattice constants of the $In_xGa_{1-x}N$ layer will be the same as the in-plane lattice constants of the GaN substrate and the in-plane strain will be isotropic, i.e., $\varepsilon_1 = \varepsilon_2$. In terms of the a lattice constants of the well (a_{W}) and barrier (a_{B}) materials, $\varepsilon_1 = (a_{\text{B}} - a_{\text{W}})/a_{\text{W}}$. With the structure relaxed in the growth direction, there will be no stress in the c-direction, and we can relate the growth direction strain to the in-plane strain via [79]

$$\varepsilon_3 = -2\frac{C_{13}}{C_{33}}\varepsilon_1 \ ,$$

where the factor $2C_{13}/C_{33}$ is proportional to the Poisson ratio for the material [38]. The C_{ij} values are the elastic constants of the well material, which may be estimated by a linear interpolation using Végard's law, in a first approximation [21].

Given our assumption of pseudomorphic growth of the QW structure, we expect that shear stresses are absent [87]. Expanding the sum in Eq. (1.3) for the z component of the piezoelectric polarisation vector field, the magnitude of the resulting polarisation in the well in the z/c-direction is [79]

$$\begin{aligned} P_{\text{PZ},3} &= \varepsilon_1 e_{31} + \varepsilon_2 e_{32} + \varepsilon_3 e_{33} \\ &= 2\varepsilon_1 e_{31} + \varepsilon_3 e_{33} \\ &= 2\varepsilon_1 \left(e_{31} - e_{33}\frac{C_{13}}{C_{33}} \right) \ , \end{aligned}$$

where $e_{i\alpha}$ are the piezoelectric coefficients (see Eq. (1.2) above).

In order to see the consequences of the presence of this polarisation, we note that in general, in a dielectric material, there will be a charge density (called the bound charge, ρ_{bound}) associated with a polarisation field, $\mathbf{P}$, such that [38, 83, 84]

$$\rho_{\text{bound}}(\mathbf{r}) = -\nabla \cdot \mathbf{P}(\mathbf{r}) \ . \tag{1.5}$$

Thus, if there is no change in $\mathbf{P}(\mathbf{r})$, there will be no bound charge. For c-plane InGaN/GaN QWs, there will be a discontinuity in the polarisation field,

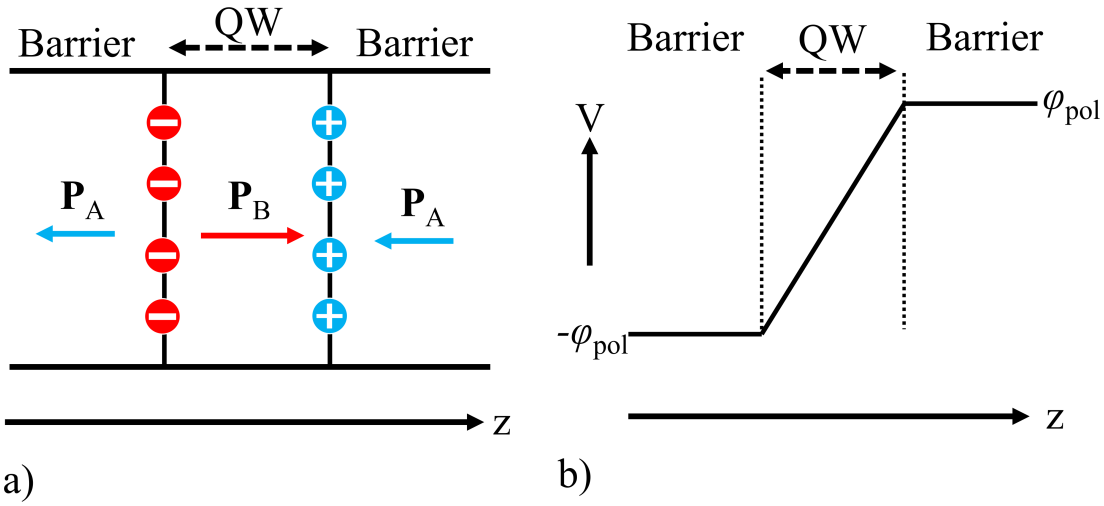


Figure 1.7: a) Formation of bound charges on the interfaces of a QW consisting of a material with polarisation $\mathbf{P}_B$, embedded in a material of polarisation $\mathbf{P}_A$. Negative (positive) charge is represented by red circles with negative symbols (blue circles with positive symbols). b) Resulting potential, φ_{pol}, across the well. Position along the growth direction is denoted by z.

$\mathbf{P} = (P_{SP} + P_{PZ})\hat{\mathbf{z}}$, at the interfaces, which will give rise to bound surface charges, depicted in Fig. 1.7 a). These bound charges generate an electric field, with an associated potential across the well of a similar form to the potential between two capacitor plates, depicted in Fig. 1.7 b). It is possible to determine this "built-in" potential, φ_{pol}, by combining Gauss's law;

$$\nabla \cdot \mathbf{D}(\mathbf{r}) = \rho_{total}(\mathbf{r}) = \rho_{free}(\mathbf{r}) + \rho_{bound}(\mathbf{r}) \ ,$$

with the constitutive relation between the displacement, $\mathbf{D}$, and electric, $\mathbf{E}$, fields [83, 84];

$$\mathbf{D}(\mathbf{r}) = \epsilon(\mathbf{r})\mathbf{E}(\mathbf{r}) \ .$$

Assuming there is only the polarisation induced bound charge, i.e., that no free charge exists in the system ($\rho_{free}(\mathbf{r}) = 0$) [38, 84], and bearing in mind the relationship between electric field and potential,

$$\mathbf{E}(\mathbf{r}) = -\nabla\varphi_{pol}(\mathbf{r}) \ ,$$

we find that

$$-\nabla\left(\epsilon(\mathbf{r})\nabla\varphi_{pol}(\mathbf{r})\right) = \rho_{bound}(\mathbf{r}) = -\nabla \cdot \mathbf{P}(\mathbf{r}) \ , \tag{1.6}$$

where $\epsilon(\mathbf{r})$ is the position dependent permittivity of the system. Returning to a

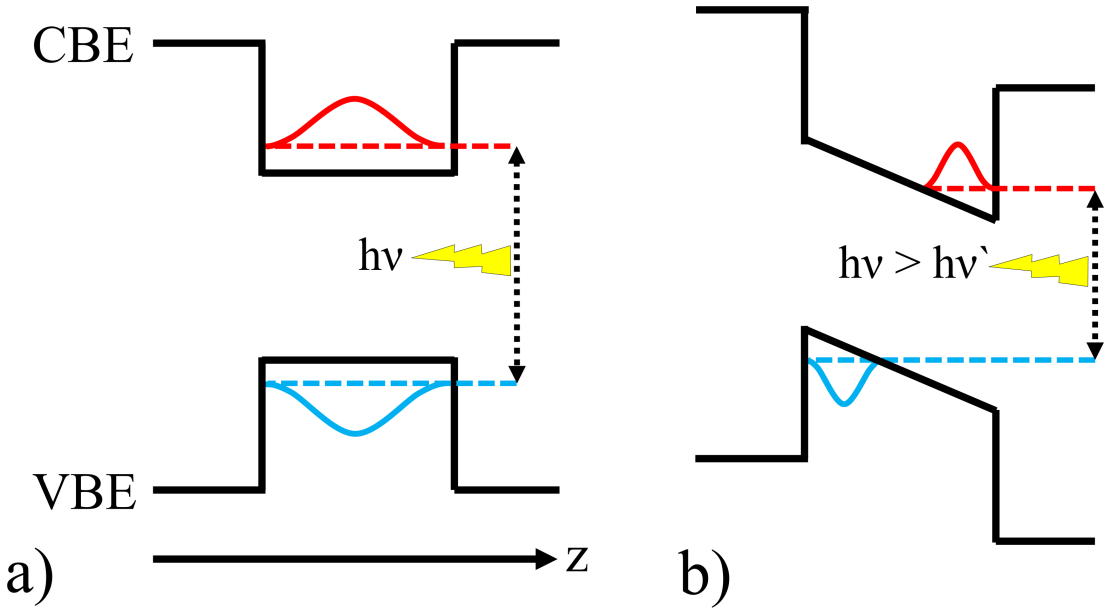


Figure 1.8: Conduction (CBE) and valence band edge (VBE) energies as a function of position along the growth direction, z, through a c-plane III-N QW a) without and b) with the presence of the built-in polarisation field. When the polarisation field is present, the carriers are separated along the growth direction. The red-shift of the emission energy is a signature of the quantum confined Stark effect [95].

1D model as an illustration, we must solve

$$-\frac{d}{dz}\left(\epsilon(z)\frac{d}{dz}\varphi_{\text{pol}}(z)\right) = \rho_{\text{pol}}(z) = -\frac{d}{dz}P(z) \ .$$

The resulting potential for a QW embedded in an unstrained barrier material of spontaneous polarisation P_{SP}^{B} is [21]

$$\varphi_{\text{pol}}(z) = \left(\frac{P_{\text{SP}}^{\text{W}} - P_{\text{SP}}^{\text{B}} + P_{\text{PZ}}^{\text{W}}}{2\epsilon_0\epsilon_r^{\text{W}}}\right)(|z| - |z-h|) \ .$$

Here, h is the QW width, ϵ_r^{W} is the relative permittivity in the well, P_{SP}^{W} is the spontaneous polarisation in the well and P_{PZ}^{W} is the piezoelectric polarisation in the well [86]. This potential will modify the electronic and optical properties of the QW, causing the tilting of bands shown above in Fig. 1.8. This effect can be quite large in III-N QWs with electric field strengths on the order of MV/cm reported in InGaN/GaN QWs [86, 94].

Figures 1.8 a) and b) show schematics of the conduction and valence band edge energy profiles along with the electron and hole ground states in a

c-plane III-N QW a) in the absence of and b) in the presence of the built-in polarisation field. Due to the tilting of the bands the difference in energy between the lowest conduction band state and highest valence band state decreases. As electrons and holes occupy their respective ground states, the energy of photons emitted when electron hole pairs recombine radiatively will reduce, causing a red-shift of the emission [95]. Furthermore, the charge carriers will become separated along the growth direction. In Fig. 1.8 b), the holes are confined at the left side of the well, and electrons on the right. The spatial separation of charge carriers and associated red-shift of emission wavelength are referred to as the quantum confined Stark effect (QCSE) [95]. This spatial separation may also impact the recombination rates in III-N QWs. Larger separation between carriers leads to smaller interactions, as the wave function overlap will also be reduced. The result of this will be smaller radiative and Auger rates, which, as we will see below in Chapter 3, depend on the overlap of carrier wave functions.

In this section we saw that the piezoelectric polarisation is strain dependent, thus large fluctuations in strain can lead to large fluctuations in piezoelectric polarisation field. In a realistic III-N alloy there is a random distribution of cation species throughout the well [96]. Due to the differences in lattice constant/bond length between III-N materials, this will lead to fluctuations in strain even within a given unit cell, when there are different cation species present. In the case of InN and GaN the difference in lattice constant is quite large (approximately 10%) and so the deformations of the four bonds surrounding a given atom can lead to significant "local" fluctuations in strain. Consequently, not only is the macroscopic piezoelectric field (described above in a 1D model) present, but also large 3D local fluctuations in strain and piezoelectric field must be accounted for as they will have a significant impact on the carrier wave functions, potentially enhancing carrier localisation. In fact, experimental studies suggest that InGaN and AlGaN systems exhibit strong carrier localisation effects [9, 97].

However, simulating alloy disorder effects has proven to be a unique challenge. In order to fully capture these effects, as discussed in the Prologue, we require an approach that is fully three dimensional, and is ideally atomistic in nature, i.e., an approach that takes into account atom by atom variations in material parameters. In the following section we discuss some general consequences of alloy disorder in III-N semiconductors, particularly InGaN systems. As has been mentioned previously, InGaN systems have received far

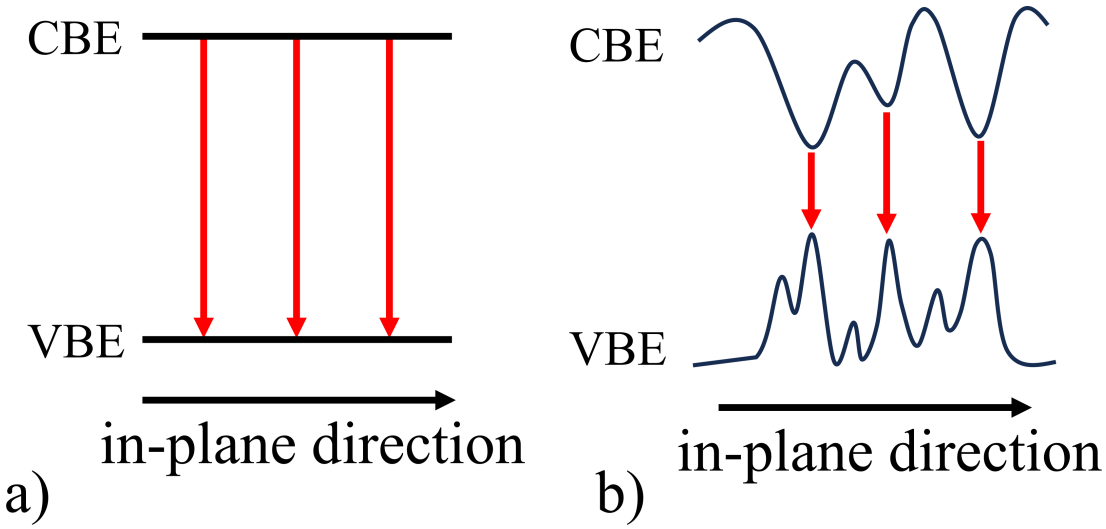


Figure 1.9: Conduction (CBE) and valence band edge (VBE) energies as a function of position in the growth plane in a) a perfect semiconductor (homogeneous emission energy) and b) a disordered semiconductor (inhomogeneous emission energies).

more attention than AlGaN systems, but recent work suggests similar effects may be present in both.

1.4.4 Alloy disorder and carrier localisation in III-nitrides

Above we discussed that alloy disorder can lead, for instance, to local fluctuations in strain and polarisation fields [98]. Moreover, given the relatively large difference in the band gaps of, for instance, InN and GaN ($E_g(\text{InN}) \approx 0.69$ eV compared to $E_g(\text{GaN}) \approx 3.51$ eV [18]), variations in alloy content will also lead to significant local fluctuations in confining potential and thus regions of lower (In rich) and higher (Ga rich) energy [36]. A similar situation arises for AlGaN-based QWs ($E_g(\text{AlN}) \approx 6.0$ eV [19]). These local variations in confining potential, coupled with the local variations in polarisation field, can lead to strong carrier localisation effects. As already mentioned above, experimental studies give clear indications of such carrier localisation effects.

A strong indication of carrier localisation is the broadening of low temperature photoluminescence (PL) peaks observed experimentally in InGaN and AlGaN QWs [99]. During PL studies a sample is illuminated by light with energy above the band gap of the well material which leads to photoexcitation of carriers, i.e., electrons are excited from the valence to the conduction band.

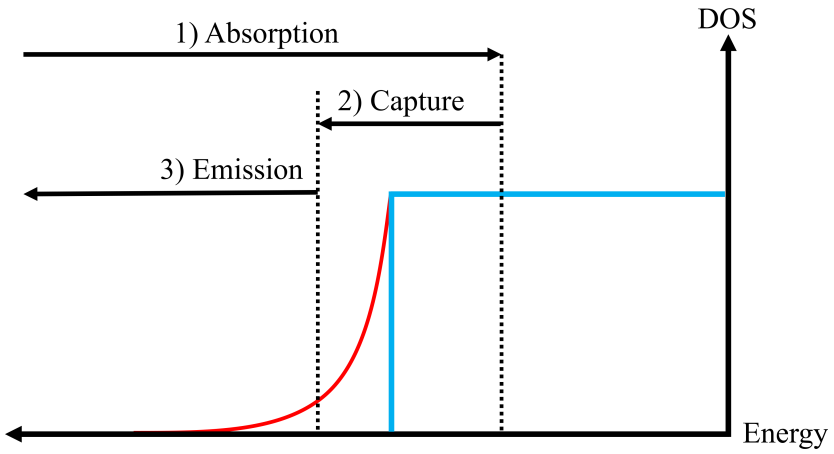


Figure 1.10: Energy dependence of the density of states (DOS) of a QW structure with (red) and without (blue) carrier localisation effects. The "step-function"-like DOS of an ideal QW structure with two degrees of freedom from fundamental quantum mechanical considerations is given by the blue solid line. In a QW system experiencing carrier localisation effects, the DOS is broadened by "tail states" with energies in the band gap, characterised by the exponential DOS tail (red solid line). The Stokes shift is the difference in energy between 1) Absorption and 3) Emission, due to 2) Capture, indicated by the different arrow lengths, see main text for details. After Ref. [104].

The carriers then relax to the lowest energy state in the region they were excited in, and then recombine, emitting light.

If the energy potential across the well was similar to that in Fig. 1.9 a) above, at low temperatures, due to the locally flat band edge profile, radiative recombinations would result in emitted photons of a single energy. Such a PL spectrum would then show a single, narrow peak at that energy. For example, "conventional" III-V InGaAs/GaAs QWs have been shown to have very narrow peaks, characterised by full width at half maximum (FWHM) values of < 10 meV [100, 101, 102]. However, alloy disorder can lead to very strong fluctuations in the potential energy landscape, as depicted schematically in Fig. 1.9 b). Thus, at low temperatures the carriers will be confined in local "pockets", or "valleys", and when recombining, will emit photons in a range of energies. For example, typical c-plane InGaN/GaN QW FWHM are found to be $\approx 20 - 80$ meV [103].

Another experimentally observable result of carrier localisation is the relatively large Stokes shift, E_S, which is defined as the difference in PL peak energy and absorption edge energy, in III-N QWs [9]. The Stokes shift arises from the broadening of the density of states (DOS) in an alloy disordered QW. The DOS in a homogeneous QW system, in contrast, will correspond to that of a system

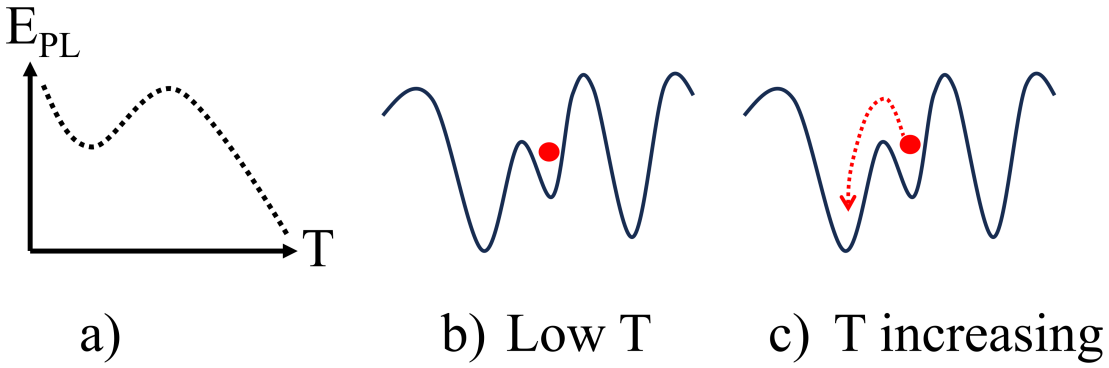


Figure 1.11: a) Schematic of the evolution of PL peak energy, E_{PL}, with temperature, T, in c-plane InGaN/GaN QWs, see, for example Ref. [112]. b) Potential energy landscape in a disordered QW at low temperatures. A carrier, represented by a red circle, is localised in a local energy minimum ("pocket"). c) As temperature increases the carrier gains energy and can "hop" to lower energy pockets.

with two degrees of freedom. From fundamental quantum mechanics, it can be shown that the DOS of such a system is "step-function"-like in character, a schematic of which is shown by the blue line in Fig. 1.10. However, the alloy disordered confinement potential in InGaN systems, coupled with local fluctuations in strain and polarisation field, leads to the confinement of states with a range of energies near the "band" edge and into the band gap, introducing the exponential "tail" represented by the red line in Fig. 1.10.

The presence of tail states due to alloy disorder can contribute to the Stokes shift for the following reasons. Absorption processes are generally dominated by the excitation of carriers into unoccupied states higher into the band (see step 1 in Fig. 1.10). In contrast, during PL studies, after absorption, carriers are "captured" and relax down in energy to localised band edge states (see step 2 in Fig. 1.10). Finally, emission is dominated by carriers recombining from localised band edge states, emitting photons with lower energies than were initially absorbed (see step 3 in Fig. 1.10). In a homogeneous QW the there would be no difference between the absorption and emission energies. Although the Stokes shift can also be affected by structural properties such as the built-in field and fluctuations in the width of the well, generally it is found to be significantly larger in InGaN/GaN QWs (up to $E_S \approx 500 - 800$ meV [103, 105, 106]) compared to, for instance, arsenide QWs ($E_S < 30$ meV [107, 108, 109, 110]) or CdSe/CdS systems ($E_S < 100$ meV [111]).

The description of the locally fluctuating potential landscape has also been

applied to the explanation of the temperature dependence of the PL peak energy, which exhibits a characteristic "S-shape". A schematic of the evolution of PL peak energy with temperature for a typical c-plane InGaN QW is depicted in Fig. 1.11 a). At low temperatures, as temperature initially increases, the PL peak red-shifts to lower energies, before blue-shifting as temperature continues to increase, and finally begins to red-shift again. An example of this can be seen in the experimental work of Ref. [112].

Figures 1.11 b) and c) present a schematic representation of how carriers distribute in a fluctuating energy landscape at low temperature, and as temperature initially increases. The initial decrease in PL peak energy is attributed to the population of states in regions of higher local energy minima (maxima for holes), depicted in Fig. 1.11 b). These carriers may "hop" between local potential minima and reach lower energy valleys, indicated in Fig. 1.11 c). As temperature continues to increase the carriers can occupy states with higher energies, up to and above the fluctuations, thus the PL peak will increase. Subsequently, the band gap of the system begins to decrease, which is the so-called Varshni shift [113, 114], hence the PL peak energy also decreases [115].

A further consequence of alloy disorder is that localised carriers trapped in regions of higher In content are less likely to diffuse through the well and interact with nonradiative (defect-related) recombination centres. Overall, this may lead to an increase in the LED efficiency [26]. Thus, as mentioned in the Prologue, carrier localisation is often assumed to be a key ingredient in the remarkably high efficiencies of InGaN QW-based devices despite their large defect densities [9, 26]. However, there is still some uncertainty in the exact origin and length scale of carrier localisation in III-N QWs [26]. For example, on the nanometre scale, the suggestion of non-random indium "clustering" was made by Narukawa *et al.* [116], when they reported In rich regions of the well, which would facilitate hole localisation. However, it was found subsequently that the In rich regions were an artefact of the experimental transmission electron microscopy (TEM) method used to investigate the In distribution, and subsequent studies using atom probe tomography (APT) to avoid similar artefacts found a random distribution of In atoms throughout the well [26, 96, 117]. Indeed, theoretical studies suggested that single In-N-In chain are sufficient to localise carriers, particularly holes [118, 119], with experimental results supporting this [120].

The method widely adopted in the literature for studying the impact of alloy disorder on the electronic structure is to assume randomly distributed Ga and In atoms in a given supercell [121, 122, 123, 124]. This is often done by generating a special quasi-random structure that mimics the correlation function of a random alloy, in the case of density functional theory studies [125], or considering a large number of different alloy configurations in the case of empirical atomistic models. The benefit of the latter approach is that it allows for the impact of the microstructure on the results to be studied, such as the potential broadening of the transition energies, which can then be compared to experimental data on the broadening of the PL structure [122]. Given the broad PL linewidth of these structures, this indicates that already the local alloy configuration plays an important role for optical properties of InGaN heterostructures. We follow this widely adopted method of assuming a random alloy distribution as input to our atomistic theoretical model. To do so, when distributing cation sites, no statistical preference is given to assigning In atoms to sites that already neighbour In sites. This approach is then consistent with, for instance, atom probe tomography measurements that indicate a random distribution of In atoms in InGaN QWs [96].

However, explanations of experimental data generally expected that not only holes, but also electrons are localised, and prevented from diffusing to nonradiative recombination sites [26]. It was expected that electrons would form bound ("excitonic") states with the holes that were localised on In-N-In chains, and thus be localised in a similar manner [118, 119, 120]. Excitonic effects occur due to the interaction of the electron and hole via the Coulomb force. The related quasi-particle (exciton) can, for example, have different electronic energy levels. However, Kalliakos *et al.* [126] found that the excitonic model could not explain their experimental data on low temperature PL spectra, and suggested that a so-called "donor-acceptor" pair (DAP) model (similar to the picture of dopants above in Sec. 1.1) was more suitable [126]. Morel *et al.* expanded on this suggestion with their pseudo-DAP model, which takes into account the differences between actual dopant atoms and the so-called "isoelectronic traps" that arise in regions of higher In content [127].

In the pseudo-DAP picture, not only are the electrons and holes spatially separated in the growth direction due to the built-in polarisation field, but the carriers are also separated in the growth plane due to fluctuations in In content and the associated isoelectronic trap. However, this model only explained the low temperature PL spectra in terms of the spatial separation of

the carriers, and did not aim to provide insight into the microstructural nature of the "pseudo-donor" and "pseudo-acceptor" traps, i.e., how they are localised and on what length scale. Thus, although hole localisation on In-N-In chains may explain the origin of pseudo-acceptors, the nature of pseudo-donor-like electron localisation was not clear.

Another suggested cause of electron localisation on the nanometre scale is the presence of approximately monolayer (i.e. one atomic layer) fluctuations in well width (called well width fluctuations (WWFs)), which have been observed experimentally [99, 128]. Theoretically, WWFs have been shown to impact electron localisation in III-N QWs [103, 129, 130], and experimentally have been shown to impact carrier localisation in, for example, GaAs-based QWs [131]. However, other explanations have also been put forward, such as electrons becoming trapped on extended defects with energies near the band edges, but not recombining nonradiatively, or the formation of V-shaped pits around threading dislocations during growth. Both of these phenomenon could prevent electrons from reaching nonradiative recombination centres. For further discussion see Ref. [9].

In this section we have seen that the localisation of carriers due to alloy disorder can lead to many non-trivial results. However, the ABC model described in Sec. 1.3 usually neglects these effects. Recently, efforts have been made to gain insight into the impact of carrier localisation on the efficiency of III-N QWs, particularly InGaN QWs. For example, carrier localisation effects have been shown to theoretically increase the radiative and Auger recombination rates in those systems [29, 40]. However, ideally, a framework that can determine the radiative and Auger recombination rates to gain insight into the IQE would include a number of features. Such a framework would be fully 3D, in order to take growth direction and in-plane localisation into account. It would include the effects of local fluctuations in strain and polarisation field as well as being atomistic in nature to account for the localisation of holes on In-N-In chains. Finally, it would also take into account length scales large enough to capture the more extended nature of localised electrons. With an understanding of the impact of carrier localisation on the radiative and Auger rates in such a framework, we could gain insight into the IQE via the ABC model described above. Developing such a framework to investigate the impact of alloy disorder on the IQE poses a significant modelling challenge, as to calculate the recombination rates we must first determine the electronic structure of the system. Thus, in the next chapter we

discuss how to calculate the electronic structure of semiconductors and semiconductor heterostructures, while accounting for alloy disorder.

Chapter 2

Electronic structure theory

2.1 Introduction

The radiative and nonradiative properties of, for instance, the nitride QWs targeted in this work will depend on their underlying electronic structure. In general, the realistic description of the electronic structure of a material or nanostructure is a formidable task. Determining the electronic structure essentially amounts to solving the Schrödinger equation for the system of electrons including their interaction with each other and the lattice. Generally, there are around 10^{23} valence electrons involved in bonding in a cubic centimetre of a solid, presenting a significant, if not insurmountable, computational task [132].

However, methods to reduce the computational complexity of this problem while still capturing the essential physics have been developed. Approaches to determining the electronic structure are broadly divided into two categories, *ab initio* and semi-empirical methods. *Ab initio* (or first-principles) methods target solutions to the Schrödinger equation that, at least in principle, do not require the fitting of model parameters to experimental results. Semi-empirical models, in contrast, will require the fitting of input parameters to either experimental or first-principles results. In this chapter we will discuss state-of-the-art *ab initio* methods used in electronic structure calculations of III-N materials and to develop semi-empirical models. Subsequently, we will outline our tight-binding model in more detail. Before proceeding, however, we first revise some foundational concepts underlying the description of electronic states which will be useful in our subsequent discussions.

2.2 Basic considerations

To begin, we will look at the so-called reciprocal lattice and some preliminary approximations often applied when determining the electronic structures of solids. Next, we will introduce the idea of an energy band and Bloch's theorem, including some consequences of this theorem.

2.2.1 Reciprocal space

In Chapter 1 above we described the wurtzite crystal structure and some of the experimentally relevant directions and crystallographic planes, e.g., the c-plane, the a-plane and the m-plane. These planes are categorised by Miller-Bravais indices which are related to the reciprocal of the intersections of the plane with the Cartesian axes. Experimentally, information about the crystallographic planes can be extracted by diffraction measurements, and can be used to determine information about the underlying material properties, such as lattice constants [133]. Diffraction is related to the so-called "reciprocal" lattice, which in turn is related to the spatial frequency of points in the real space lattice.

Given an ideal real space lattice with primitive lattice vectors $\mathbf{a}_j$, we recall that any point in the lattice, $\mathbf{R}$, is described by

$$\mathbf{R} = n_1\mathbf{a}_1 + n_2\mathbf{a}_2 + n_3\mathbf{a}_3 \ ,$$

with $n_i \in \mathbb{Z}$. The associated reciprocal lattice is described by vectors $\mathbf{G}$ such that [48, 134]

$$e^{i\mathbf{G}\cdot\mathbf{R}} = 1 \ , \tag{2.1}$$

where $\mathbf{G} = m_1\mathbf{b}_1 + m_2\mathbf{b}_2 + m_3\mathbf{b}_3$ and $m_i \in \mathbb{Z}$. The condition given in Eq. (2.1) requires that $\mathbf{b}_i \cdot \mathbf{a}_j = 2\pi\delta_{ij}$, with $i, j \in \{1, 2, 3\}$ [48]. Thus, (with $i \neq j, k$) $\mathbf{b}_i$ is perpendicular to both $\mathbf{a}_j$ and $\mathbf{a}_k$, and we can write

$$\mathbf{b}_i = C(\mathbf{a}_j \times \mathbf{a}_k) \ ,$$

where C is some constant. Making use of the requirement that $\mathbf{a}_i \cdot \mathbf{b}_i = 2\pi$,

$$\mathbf{a}_i \cdot \mathbf{b}_i = \mathbf{a}_i \cdot (C(\mathbf{a}_j \times \mathbf{a}_k)) = 2\pi \ ,$$

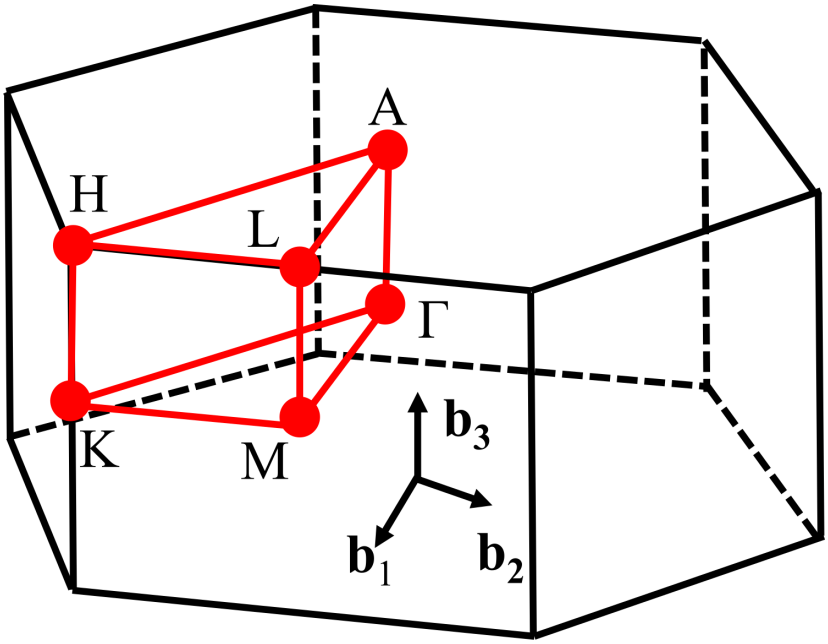


Figure 2.1: Schematic of the first Brillouin zone for a hexagonal lattice spanned by the reciprocal lattice vectors $\mathbf{b}_i$. High symmetry points, including the Γ-point at $\mathbf{k} = \mathbf{0}$ are indicated.

and so

$$C = \frac{2\pi}{\mathbf{a}_i \cdot (\mathbf{a}_j \times \mathbf{a}_k)} \ .$$

Hence, in 3D, the vectors $\mathbf{b}_i$ are given by [48, 134]

$$\mathbf{b}_i = 2\pi \frac{\mathbf{a}_j \times \mathbf{a}_k}{\mathbf{a}_i \cdot (\mathbf{a}_j \times \mathbf{a}_k)} \ .$$

The vectors $\mathbf{b}_i$ define the reciprocal lattice and span the reciprocal space. They can be thought of as a discrete 3D Fourier transform of the real space (sometimes called direct) lattice, defined by the vectors $\mathbf{a}_i$. An arbitrary vector in the reciprocal space is often represented by the vector $\mathbf{k}$.

In the real space lattice it is possible to define a primitive unit cell as the parallelepiped defined by the primitive lattice vectors, $\mathbf{a}_i$, which is the minimum repeatable volume that generates the lattice. This primitive unit cell is called the Wigner-Seitz cell. Similarly, in the reciprocal lattice one may define such a unit cell using the primitive reciprocal lattice vectors, $\mathbf{b}_i$. In the reciprocal lattice, this unit cell is called the first Brillouin zone (FBZ) and is depicted for a hexagonal real space lattice in Fig. 2.1 [48]. These ideas will be useful in the next section, as we return to the overall problem at hand, solving the Schrödinger equation.

2.2.2 Electronic band structures

As previously stated, in order to determine the electronic structure of a crystal, we must solve the Schrödinger equation to find the energy levels and wave functions of the electrons. To do so, the form of the Hamiltonian operator, $\hat{H}$ must be known. In principle, the full Hamiltonian for a system of electrons in a crystal lattice must take into account interactions between the electrons as well as interactions between electrons and ions of the lattice, and the interactions between electrons and ions of the lattice [135]:

$$\begin{aligned}\hat{H} = &\overbrace{-\frac{\hbar^2}{2m}\sum_i^n \nabla_i^2}^{\hat{T}_\mathrm{e}} \overbrace{-\frac{\hbar^2}{2M}\sum_\alpha^N \nabla_\alpha^2}^{\hat{T}_\mathrm{I}} \overbrace{-\frac{1}{4\pi\epsilon_0}\sum_i^n\sum_\alpha^N \frac{Ze^2}{|\mathbf{r}_i - \mathbf{R}_\alpha|}}^{\hat{V}_\mathrm{eI}} \\ &\underbrace{+\frac{1}{8\pi\epsilon_0}\sum_i^n\sum_{j\neq i}^n \frac{e^2}{|\mathbf{r}_i - \mathbf{r}_j|}}_{\hat{V}_\mathrm{ee}} \underbrace{+\frac{1}{8\pi\epsilon_0}\sum_\alpha^N\sum_{\beta\neq\alpha}^N \frac{(Ze)^2}{|\mathbf{R}_\alpha - \mathbf{R}_\beta|}}_{\hat{V}_\mathrm{II}} \ .\end{aligned} \tag{2.2}$$

For simplicity, we have assumed here that there is only one species of ion in the lattice, with proton number Z. Furthermore, we consider n electrons of mass m, at positions $\mathbf{r}_i$, and N ions of mass M at positions $\mathbf{R}_\alpha$. Electrons are indexed by Latin labels, and ions by Greek labels. Here we have neglected relativistic effects, e.g., spin-orbit coupling, which is of secondary importance in III-N semiconductors [132]. The Hamiltonian can thus be represented as

$$\hat{H} = \hat{T}_\mathrm{e} + \hat{T}_\mathrm{I} + \hat{V}_\mathrm{eI} + \hat{V}_\mathrm{ee} + \hat{V}_\mathrm{II} \ , \tag{2.3}$$

where $\hat{T}_\mathrm{e}$ is the kinetic energy operator for the electrons, $\hat{T}_\mathrm{I}$ is the kinetic energy operator for the ions, $\hat{V}_\mathrm{eI}$ is the potential operator for the attractive electron-ion interaction, $\hat{V}_\mathrm{ee}$ is the potential operator for the repulsive electron-electron interaction and $\hat{V}_\mathrm{II}$ is the potential operator for the repulsive ion-ion interaction.

Given that the mass of the ions is much larger than the mass of the electrons (i.e. $M \gg m$), we employ here the Born-Oppenheimer approximation to decouple the electronic system from the ionic part [136]. Thus, we neglect the $\hat{T}_\mathrm{I}$ term and recast the problem as that of a number of electrons moving in an effective potential due to the ions. To do so, we combine the $\hat{V}_\mathrm{eI}$ and $\hat{V}_\mathrm{II}$ terms into $\hat{V}_\mathrm{eff}$, leaving a separate interaction potential term that describes the interaction of the electrons with each other [135]. Thus, Eq. (2.3) is reduced

to [137]

$$\hat{H} = \hat{T}_{\text{e}} + \hat{V}_{\text{eff}} + \hat{V}_{\text{ee}} = \sum_{i}^{n} \left(-\frac{\hbar^2}{2m} \nabla_i^2 + V_{\text{eff}}\left(\mathbf{r}_i\right) \right) + \sum_{i}^{n} \sum_{j \neq i}^{n} V\left(\mathbf{r}_{ij}\right) \ . \tag{2.4}$$

For the purpose of discussion, for now we will neglect the Coulomb interaction between electrons and assume that the impact of these interactions is accounted for in the effective potential. In this simplified picture, the effective potential is static, and so we must solve the time independent Schrödinger equation,

$$\hat{H}\Psi_n = \text{E}_n \Psi_n \ , \tag{2.5}$$

to find the energy levels, E_n, and wave function, Ψ_n, of the system. When the interactions between electrons are neglected, the wave function for the system of electrons, Ψ_n, can be written as the product of the single particle wave functions, $\psi_{n,i}$, that individually solve Eq. (2.5). The energy of the system, E_n is then the sum of the single particle energies, $\text{E}_{n,i}$. Even in this simplified picture, solving the single particle Schrödinger equation over the length scale of the entire solid is a significant challenge. However, the effective potential above will have the periodicity of the crystal lattice, thus we may make use of Bloch's theorem [48, 138].

Bloch's theorem applies to perfectly crystalline materials in which the translational invariance of the potential is not violated. In such a material, for some arbitrary real space vector $\mathbf{r}$, and a lattice vector $\mathbf{R}$, defined above, we would have

$$V_{\text{eff}}\left(\mathbf{r} + \mathbf{R}\right) = V_{\text{eff}}\left(\mathbf{r}\right) \ .$$

This being the case, Bloch's theorem states that the single particle electronic wave functions, ψ_n, will be the product of a plane wave, $e^{i\mathbf{k}\cdot\mathbf{r}}$, with wave vector $\mathbf{k}$ and a function with the same periodicity as the lattice (called a Bloch factor), $u_{\mathbf{k}}(\mathbf{r})$, i.e.,

$$\psi_{n,\mathbf{k}}\left(\mathbf{r}\right) = e^{i\mathbf{k}\cdot\mathbf{r}} u_{n,\mathbf{k}}\left(\mathbf{r}\right) \ ,$$

where, for a given $\mathbf{k}$,

$$u_{n,\mathbf{k}}\left(\mathbf{r} + \mathbf{R}\right) = u_{n,\mathbf{k}}\left(\mathbf{r}\right) \ .$$

Thus

$$\psi_{n,\mathbf{k}}\left(\mathbf{r} + \mathbf{R}\right) = e^{i\mathbf{k}\cdot\mathbf{R}} \psi_{n,\mathbf{k}}\left(\mathbf{r}\right) \ ,$$

i.e., the electronic wave function is periodic with the periodicity of the lattice,

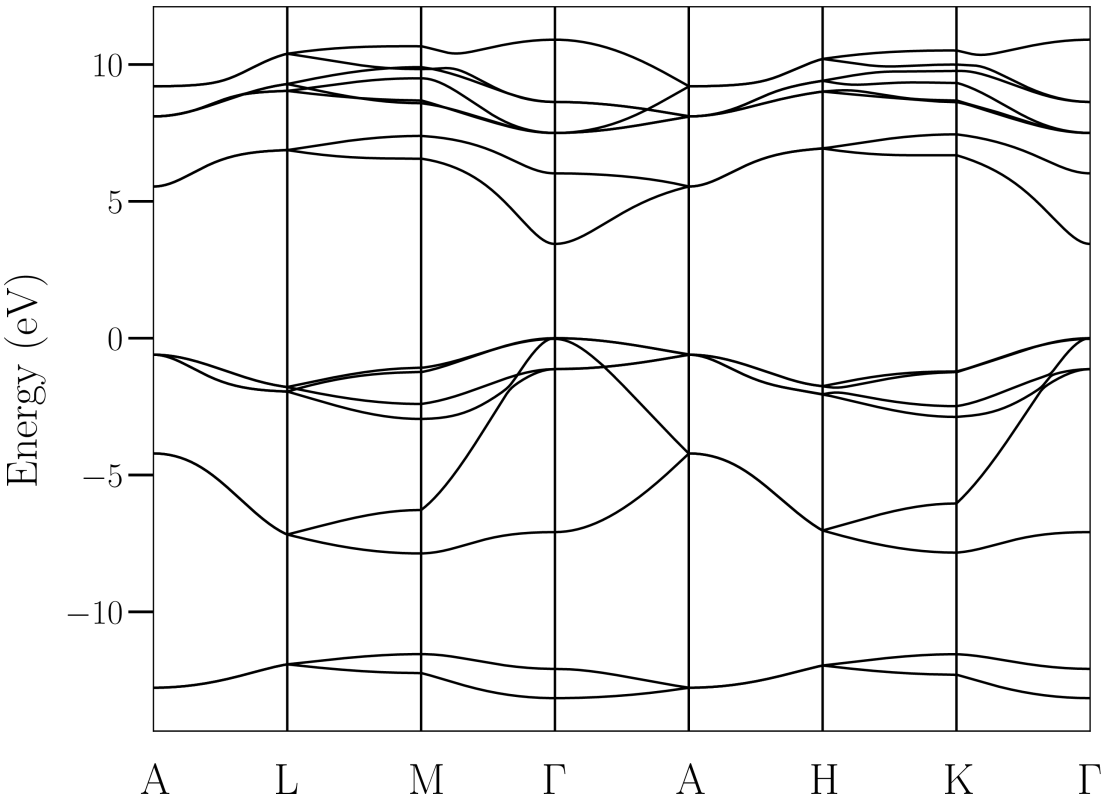


Figure 2.2: Band structure of wurtzite GaN determined in a tight-binding model. Tight-binding parameters from Ref. [82] have been used.

up to a phase factor of $e^{i\mathbf{k}\cdot\mathbf{R}}$, and, as a result, the charge density, $|\psi_{n,\mathbf{k}}|^2$, will be the same at $\mathbf{r}$ and $\mathbf{r}+\mathbf{R}$. A wave function that fulfills Bloch's theorem, i.e., has the form of a plane wave times a Bloch factor, is called a Bloch wave function. Thus, if we know the nature of the (Bloch) wave function within a Wigner-Seitz cell, we could extend that knowledge to encompass the whole lattice, while taking the plane wave phase factor into account. From Bloch's theorem, a wave vector $\mathbf{k}$ can be associated with each energy state, E_n. So, for a given value of $\mathbf{k}$, we will find a (discrete) set of allowed energies, E_n by solving the Schrödinger equation (Eq. (2.5)) assuming a Bloch wave function.

Furthermore, due to the periodicity of the lattice, it can be shown that the wave vectors, $\mathbf{k}$, are not uniquely determined. To illustrate this, we take the approach used in Ref. [37] and consider a 1D periodic lattice with a unit cell of length L, thus

$$\psi_{n,k}(x) = e^{ikx}u_{n,k}(x) \ ,$$

and $u_{n,k}(x) = u_{n,k}(x+L)$. Multiplying by a plane wave with the periodicity of the lattice, $e^{i2\pi mx/L}$, where m is any integer, and its complex conjugate, we

have

$$\begin{aligned}\psi_{n,k}(x) &= e^{ikx}e^{i\frac{2\pi m}{L}x}e^{-i\frac{2\pi m}{L}x}u_{n,k}(x) \\ &= e^{i(k+\frac{2\pi m}{L})x}\left(e^{-i\frac{2\pi m}{L}x}u_{n,k}(x)\right) \ .\end{aligned}$$

The term $2\pi m/L$ can be identified as a 1D reciprocal lattice vector, denoted G_m, as it satisfies Eq. (2.1). Thus, the term $\exp(-iG_m x)u_k(x)$ also has the periodicity of the lattice and so the properties of $\psi_{n,k}$ are equivalent at k and $k+G_m$ (up to a phase factor): e.g., for the energy, $\mathrm{E}_n(k)$, of the state ψ_n at a given point k in reciprocal space, we have that $\mathrm{E}_n(k+G_m) = \mathrm{E}(k)$. This allows us to restrict our analysis to the interval $-\frac{\pi}{L} < k < \frac{\pi}{L}$, which corresponds to the FBZ in this 1D example. This is the so-called "reduced zone scheme" where any value of k outside the FBZ is translated back to the FBZ by suitable choice of G_m. The variation of E_n with k gives rise to so-called energy "bands" for a given value of n. A plot of all the energy bands (i.e. for all values of n) gives rise to the "band structure" of a material. However, visualising 3D reciprocal space is generally more difficult than in the 1D example above. Thus, we select certain "high symmetry" points in the FBZ to gain insight into the 3D band structure. For example, the point $\mathbf{k} = \mathbf{0}$ at the centre of the FBZ is a high symmetry point often referred to as the Γ-point. Other so-called high symmetry points in the first Brillouin zone include A, L, M, H and K (see, for instance, Ref. [74], and Fig. 2.1 above). An example of a band structure is shown in Fig. 2.2 for GaN. Moving along the x-axis of Fig. 2.2 corresponds to moving along a straight line in reciprocal space between high symmetry points.

Above, we briefly discussed the independent particle model, in which the interaction between electrons is neglected and the solution wave function is a combination of the single particle (i.e. independent particle) wave functions. We now turn to discuss more advanced models that aim to include the electron-electron interaction.

2.3 *Ab initio* methods

In the single particle picture described above we noted that the overall solution wave function of Eq. (2.5), Ψ_n, would be the product of the single particle wave functions, $\psi_{n,i}$. However, due to the Fermionic nature of electrons, Ψ_n must be anti-symmetric, which can be achieved by constructing a Slater determinant from the single particle wave functions. For a system of N

electrons at positions $\mathbf{r}_\alpha$, with $\alpha \in \{1, \ldots, N\}$ [137]:

$$\Psi_n(\mathbf{r}_1, \mathbf{r}_2, \ldots, \mathbf{r}_N) = \frac{1}{\sqrt{N!}} \det \begin{pmatrix} \psi_{n,1}(\mathbf{r}_1) & \psi_{n,2}(\mathbf{r}_1) & \cdots & \psi_{n,N}(\mathbf{r}_1) \\ \psi_{n,1}(\mathbf{r}_2) & \psi_{n,2}(\mathbf{r}_2) & \cdots & \psi_{n,N}(\mathbf{r}_2) \\ \vdots & \cdots & \ddots & \vdots \\ \psi_{n,1}(\mathbf{r}_N) & \psi_{n,2}(\mathbf{r}_N) & \cdots & \psi_{n,N}(\mathbf{r}_N) \end{pmatrix} . \quad (2.6)$$

However, the true many-body wave function is a linear combination of Slater determinants. As such, we must account for the quantum mechanical nature of the wave function including exchange and correlation energies and effects. Generally, the accurate calculation of solutions to the Schrödinger equation in the presence of interacting electrons is a significant challenge. Even so, the groundbreaking work of Hohenberg and Kohn [139], and the subsequent work of Kohn and Sham [140], paved the way for density functional theory, and frameworks based on this approach that aim to treat both exchange and correlation effects accurately. This is the subject of our next section.

2.3.1 Density functional theory

Density functional theory (DFT) has found widespread use in electronic structure calculations and has been applied to a wide variety of materials, including III-N materials [40, 141, 142, 143]. Indeed, it is DFT that underlies the current state-of-the-art approach to determining the electronic structure of the optoelectronically relevant III-N semiconductors, the so-called Heyd-Scuseria-Ernzerhof (HSE) hybrid functional DFT [82, 144]. However, in order to discuss the strengths and weaknesses of this approach we must briefly discuss the underlying ideas of DFT and the HSE hybrid functional. To do so, we follow the approach taken in Ref. [37].

The foundation of DFT is the proof by Hohenberg and Kohn [139] that the ground state energy of a many particle system is uniquely determined by a functional of the ground state electron density. The primary benefit of this approach is that it avoids the need to determine the total wave function described above in Eq. (2.6), Ψ_n. From Eq. (2.6) we can see that Ψ_n depends on the three spatial coordinates of every electron, and as mentioned, there are around 10^{23} valence electrons involved in bonding in every cubic centimetre of a solid. Thus, the total wave function of such a system would depend on around 3×10^{23} variable spatial coordinates. Instead, the ground state electron density, $\rho(\mathbf{r})$, depends only on three spatial variables. Proof of the theorem of

Hohenberg and Kohn can be found in the original paper in Ref. [139] and is also discussed in Refs. [37] and [137]. Although Hohenberg and Kohn's theorem provided a general framework for the determination of the ground state electron density, ρ_{GS}, and energy, E_{GS}, in principle, one still must determine the functional form of the Hamiltonian. For instance, how the kinetic energy, T, depends on the electron density, ρ, in general.

An important approach developed to overcome this was the method of Kohn and Sham [140]. In Kohn and Sham's method, the interacting many particle system is mapped to an effective single particle system, where the kinetic energy contribution is given by the kinetic energy of the non-interacting single particle system, T_0, with an effective potential, V_{eff}, where part of V_{eff} takes into account exchange and correlation effects. The energy functional, $\text{E}[\rho]$, of the system can then be decomposed as follows [137];

$$\begin{aligned}\text{E}[\rho] &= T_0[\rho] + V_{\text{eff}}[\rho] \ , \\ &= T_0[\rho] + \int d\mathbf{r}\rho(\mathbf{r}) \left[V_{\text{ext}}(\mathbf{r}) + U(\mathbf{r})\right] + \text{E}_{\text{xc}}[\rho] \ , \end{aligned} \tag{2.7}$$

where $T_0[\rho]$ is the kinetic energy of the non-interacting system with density ρ, V_{ext} is the external potential in which the particles move, $U(\mathbf{r})$ is the Hartree contribution to the interaction, which would be the Coulomb potential for electrons;

$$U(\mathbf{r}) = \frac{e^2}{2} \int d\mathbf{r} \int d\mathbf{r}' \frac{\rho(\mathbf{r})\rho(\mathbf{r}')}{|\mathbf{r} - \mathbf{r}'|} \ ,$$

and finally, the term $\text{E}_{\text{xc}}[\rho]$ is the so-called exchange-correlation functional. All of the terms in Eq. (2.7) except E_{xc} can be treated exactly, i.e., the form of their functionals can be determined. Furthermore, even though the kinetic energy of the non-interacting system will not generally be equal to the kinetic energy of the interacting system, it is assumed that corrections to the kinetic energy due to the interaction will be accounted for in the, as yet undetermined, exchange-correlation functional.

One of the first approximations explored for E_{xc} was the local density approximation (LDA), in which an inhomogeneous electron density is approximated locally by a homogeneous electron gas with a given density [140, 145]. LDA DFT has been shown to work remarkably well when applied to some materials, while systematically failing for others [37, 146, 147]. One of the most well known issues with LDA is its underestimation of the band gap of many semiconductors and insulators, the

so-called band gap problem [146].

Beyond LDA, the generalised gradient approximation (GGA) was developed, in which the exchange-correlation functional includes terms that depend on the gradient of the density [148, 149]. However, even in GGA approaches, the band gap problem persisted. To overcome this, the idea to combine Hartree-Fock theory and LDA/GGA functional-based approaches was introduced by Becke *et al.* [37, 150]. In Hartree-Fock theory, exchange effects can be taken into account exactly, thus Becke *et al.* introduced the idea of "hybrid functionals" which contain contributions from the Hartree-Fock exchange functional and an LDA/GGA exchange-correlation functional.

Many different approaches to approximate the exchange-correlation functional are available in the literature [37]. As mentioned at the beiginning of this section, an approach that has attracted a lot of attention recently is due to Heyd *et al.*, who introduced the Heyd-Scuseria-Ernzerhof (HSE) screened hybrid functional, which is a combination of the Hartree-Fock exchange functional and a so-called PBE0 functional, with a linear mixing parameter a [144, 151]. One of the primary benefits of the HSE hybrid functional is that it makes use of the screening of the long range part of the Coulomb potential to significantly reduce computational cost [152].

The HSE hybrid functional has been applied to a wide range of material systems with great success [153, 154, 155, 156], including III-N semiconductors [53, 54, 82, 157]. However, the introduction of the mixing parameter, a, represents a step away from the *first principles* origins of DFT and can introduce ambiguity in certain situations. For instance, the a parameter that describes certain defect geometries of a system might differ from the a that describes the band gap accurately [158, 159]. Furthermore, and of particular relevance to this work, is the ambiguity in choosing a parameters for alloys of, for instance, III-N semiconductors. While the a parameters of the constituent binary III-N materials may be well determined by fitting, there is no rigorous prescription for assigning an a parameter to an alloy of these materials, other than semi-empirical fitting [54].

A further limitation of DFT methods within the Kohn-Sham framework is that the computational complexity of the problem scales with the cube of the number of atoms considered [160]. Thus, even though the HSE functional represents a significant improvement in terms of computational cost relative to, for instance PBE0 hybrid functional methods [152], typical HSE

simulations are generally on the order of 10s to, at most, 100s of atoms [54, 158, 161]. Although implementations of linear-scaling DFT are currently being developed, so far they have only been applied to a small subset of material science problems [162, 163, 164]. A very recently developed state-of-the-art linear scaling DFT software, the CONQUEST code [164], may provide a promising route to realising DFT-based simulations of, for instance, mesoscopic nanostructures. However, any linear-scaling DFT approach would require significant research efforts to be applied to and optimised for, e.g., III-N-based systems. Further work would also be required to accurately describe a semiconductor alloy in such a framework.

As we have discussed above in Sec. 1.4, the need to include many 1000s of atoms in models of III-N heterostructures arises from the length scales over which electrons and holes localise. Typical localisation lengths for holes in, for instance, InGaN QW systems, are on the order of 1 nm [129], and so simulation supercells must have larger dimensions to capture these effects. Generally, it is important to balance accuracy with computational cost, and computationally less intense semi-empirical methods have been developed that accurately reproduce important features of bulk band structures. Semi-empirical approaches can be designed to reproduce experimental or DFT results by fitting model input parameters to data, allowing the semi-empirical model to be extended to larger systems. These methods are the topic of the next section.

2.4 Semi-empirical methods

Semi-empirical methods have been widely used in electronic structure calculations of solids generally [39] and due to their lower computational cost (compared to *ab initio* methods) have found widespread use in the analysis of many optoelectronically relevant materials, nanostructures and devices [37, 39, 45]. Broadly, these methods can be divided into two categories, continuum-based and atomistic. Continuum-based approaches essentially assume a uniform repeated unit cell describes a material, while atomistic approaches include internal degrees of freedom, i.e., parameters that may vary within unit cells. In this section we will discuss the ideas underlying a class of continuum-based models, so-called $\mathbf{k} \cdot \mathbf{p}$ theories, widely used in the analysis of not only conventional III-V semiconductors, but also III-Ns, despite most of these continuum-based models not taking carrier localisation effects

into account, a key component in modelling III-Ns. We will then discuss recent efforts to include carrier localisation in these models, as well as the limitations of these approaches. Finally, we will turn to the atomistic tight-binding approach upon which the work here is based.

2.4.1 Effective mass approximation and $\mathbf{k}\cdot\mathbf{p}$ theories

In our discussion of *ab initio* methods above, we saw that, for instance, DFT approaches can be used to determine the band structure. We also saw that for a given energy band, $\mathrm{E}(\mathbf{k})$, we can restrict our analysis to the first Brillouin zone (FBZ). DFT approaches allow the determination of $\mathrm{E}(\mathbf{k})$ throughout the entire FBZ. However, certain properties of a system may be strongly dependent on a specific region of the FBZ, for example the optical properties of GaAs systems are determined by the behaviour of $\mathrm{E}(\mathbf{k})$ around $\mathbf{k}=\mathbf{0}$ as it is a direct band gap semiconductor [37]. In principle, the behaviour of any given energy band at a given $\mathbf{k}$-point will depend on all the other bands, however, the influence of bands that are further away (in energy) will be negligible. In a first step, we explicitly analyse only one band, and encompass modifications to this band due to the coupling between it and the other bands via an effective mass approximation (EMA). In such an approach, the energy dispersion relation, $\mathrm{E}(\mathbf{k})$, around $\mathbf{k}=\mathbf{0}$ is approximated to be parabolic [37];

$$\mathrm{E}(\mathbf{k}) = \frac{\hbar^2 k^2}{2m^*} \ ,$$

where $k=|\mathbf{k}|$, $\hbar$ is the reduced Planck constant and m^* is the so-called "effective" mass of the carrier. The effective mass is implicitly modified by the other bands and can be determined from, for example, experimental measurements or DFT band structures [134].

Single band EMAs are often applied to bands around $\mathbf{k}=\mathbf{0}$, the Γ-point, both for valence and conduction bands when dealing with direct gap III-V materials and heterostructures. Figure 2.3 shows an illustrative band structure of GaN near the Γ-point. Compared to the top of the valence band, the bottom of the conduction band is energetically isolated, and so a single band EMA may be a suitable description. However, the more complicated structure of the top of the valence band, consisting of a number of valence "sub-bands" energetically close together, requires ideally an approach that takes into account more bands. Thus, to improve the accuracy of the EMA we can take more bands into

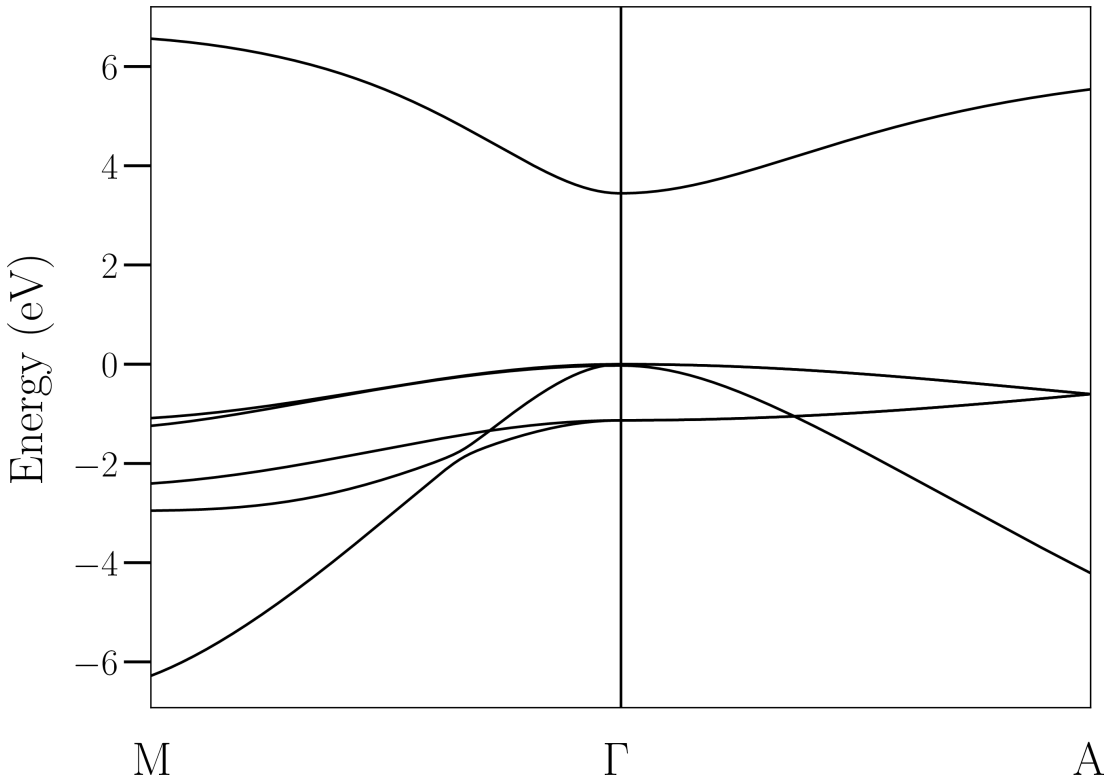


Figure 2.3: Band structure of wurtzite GaN determined in a tight-binding model around the Γ-point. Tight-binding parameters from Ref. [82] have been used. The figure highlights the more complicated valence band structure when compared to the conduction band.

account and include the coupling between these bands explicitly. Doing so will also provide a better description of energetically higher and lower lying conduction and valence bands, respectively, which are important for processes such as Auger recombination, in contrast to radiative recombination, where the structure of the band edges (i.e. near the band gap) is more important [37]. To do so, we begin by considering the single particle Hamiltonian of an electron in a periodic solid;

$$\hat{H} = -\frac{\hbar^2}{2m}\nabla^2 + V(\mathbf{r}) \ , \tag{2.8}$$

where $V(\mathbf{r}) = V(\mathbf{r} + \mathbf{R})$ is the periodic potential arising from the ions of the lattice. We will seek to construct the Hamiltonian in a basis that allows us to account for couplings between bands. To do so, we follow the approach laid out in Ref. [37].

The basic assumption underlying this multi-band EMA is that we already have knowledge of the energy levels, $\mathrm{E}_n(\mathbf{k})$, and periodic Bloch factors, $u_{n,\mathbf{k}}(\mathbf{r})$, at

some $\mathbf{k}$-point, which we denote by $\mathbf{k}_0$. By Bloch's theorem (Sec. 2.2), the electronic wave functions, $\Psi_{n,\mathbf{k}}(\mathbf{r})$, can be expressed as a plane wave times this periodic function, $u_{n,\mathbf{k}}(\mathbf{r})$, such that $\Psi_{n,\mathbf{k}}(\mathbf{r}) = e^{i\mathbf{k}\cdot\mathbf{r}}u_{n,\mathbf{k}}(\mathbf{r})$. Thus, the Schrödinger equation at $\mathbf{k}_0$ is

$$\hat{H}\Psi_{n,\mathbf{k}_0} = \hat{H}\left(e^{i\mathbf{k}_0\cdot\mathbf{r}}u_{n,\mathbf{k}_0}(\mathbf{r})\right) = \mathrm{E}_n(\mathbf{k}_0)\left(e^{i\mathbf{k}_0\cdot\mathbf{r}}u_{n,\mathbf{k}_0}(\mathbf{r})\right) \ . \tag{2.9}$$

We now seek to find $\mathrm{E}_n(\mathbf{k})$ for some $\mathbf{k}$-point close to $\mathbf{k}_0$, at which point the Schrödinger equation is

$$\hat{H}\Psi_{n,\mathbf{k}} = \hat{H}\left(e^{i\mathbf{k}\cdot\mathbf{r}}u_{n,\mathbf{k}}(\mathbf{r})\right) = \mathrm{E}_n(\mathbf{k})\left(e^{i\mathbf{k}\cdot\mathbf{r}}u_{n,\mathbf{k}}(\mathbf{r})\right) \ . \tag{2.10}$$

We introduce a dependence on $\mathbf{k}-\mathbf{k}_0$ by rewriting $e^{i\mathbf{k}\cdot\mathbf{r}} = e^{i(\mathbf{k}-\mathbf{k}_0+\mathbf{k}_0)\cdot\mathbf{r}}$ and rearranging;

$$\hat{H}e^{i(\mathbf{k}-\mathbf{k}_0)\cdot\mathbf{r}}\left(e^{i\mathbf{k}_0\cdot\mathbf{r}}u_{n,\mathbf{k}}(\mathbf{r})\right) = \mathrm{E}_n(\mathbf{k})e^{i(\mathbf{k}-\mathbf{k}_0)\cdot\mathbf{r}}\left(e^{i\mathbf{k}_0\cdot\mathbf{r}}u_{n,\mathbf{k}}(\mathbf{r})\right) \ . \tag{2.11}$$

We now multiply both sides of Eq. (2.11) by $e^{-i(\mathbf{k}-\mathbf{k}_0)\cdot\mathbf{r}}$;

$$\left[e^{-i(\mathbf{k}-\mathbf{k}_0)\cdot\mathbf{r}}\hat{H}e^{i(\mathbf{k}-\mathbf{k}_0)\cdot\mathbf{r}}\right]\left(e^{i\mathbf{k}_0\cdot\mathbf{r}}u_{n,\mathbf{k}}(\mathbf{r})\right) = \left[e^{-i(\mathbf{k}-\mathbf{k}_0)\cdot\mathbf{r}}\mathrm{E}_n(\mathbf{k})e^{i(\mathbf{k}-\mathbf{k}_0)\cdot\mathbf{r}}\right]\left(e^{i\mathbf{k}_0\cdot\mathbf{r}}u_{n,\mathbf{k}}(\mathbf{r})\right) \ .$$

The resulting modified Schrödinger equation includes a Hamiltonian that depends on $\mathbf{q} = \mathbf{k}-\mathbf{k}_0$. We denote this new Hamiltonian by $\hat{H}_\mathbf{q}$, such that

$$\hat{H}_\mathbf{q} = e^{-i\mathbf{q}\cdot\mathbf{r}}\hat{H}e^{i\mathbf{q}\cdot\mathbf{r}} \ .$$

This $\mathbf{q}$-dependent Hamiltonian acts on Bloch wave functions, $\Phi_{n,\mathbf{k}}(\mathbf{r})$, where

$$\Phi_{n,\mathbf{k}}(\mathbf{r}) = e^{i\mathbf{k}_0\cdot\mathbf{r}}u_{n,\mathbf{k}}(\mathbf{r}) \ .$$

With some manipulation to expand the $\nabla^2(\exp(i\mathbf{q}\cdot\mathbf{r})\Phi_{n,\mathbf{k}}(\mathbf{r}))$ term we can

look at how $\hat{H}_{\mathbf{q}}$ acts on $\Phi_{n,\mathbf{k}}(\mathbf{r})$. It can be shown that

$$\begin{aligned}
\hat{H}_{\mathbf{q}}\Phi_{n,\mathbf{k}}(\mathbf{r}) &= \left[e^{-i\mathbf{q}\cdot\mathbf{r}}\left(-\frac{\hbar^2}{2m}\nabla^2 + V(\mathbf{r})\right)e^{i\mathbf{q}\cdot\mathbf{r}}\right]\Phi_{n,\mathbf{k}}(\mathbf{r}) \ , \\
&= \left[-\frac{\hbar^2}{2m}\nabla^2 + V\left(\mathbf{r}\right) + \frac{\hbar^2}{m}\mathbf{q}\cdot\frac{1}{i}\nabla + \frac{\hbar^2 q^2}{2m}\right]\Phi_{n,\mathbf{k}}(\mathbf{r}) \ , \\
&= \left[\hat{H} + \frac{\hbar^2}{m}\mathbf{q}\cdot\frac{1}{i}\nabla + \frac{\hbar^2 q^2}{2m}\right]\Phi_{n,\mathbf{k}}(\mathbf{r}) \ , \\
&= \left[\hat{H} + \hat{H}'\right]\Phi_{n,\mathbf{k}}(\mathbf{r}) \ ,
\end{aligned}$$

where $q = |\mathbf{q}|$. Using Eq. (2.8) to identify $\hat{H}$, the above can be written as $\hat{H}$ plus a correction, $\hat{H}'$, that is given by

$$\hat{H}' = \frac{\hbar^2}{m}\mathbf{q}\cdot\frac{1}{i}\nabla + \frac{\hbar^2 q^2}{2m} = \frac{\hbar}{m}\mathbf{q}\cdot\mathbf{p} + \frac{\hbar^2 q^2}{2m} \ , \tag{2.12}$$

where we have used the definition of the momentum operator $\mathbf{p} = -i\hbar\nabla$ to recast $\hat{H}'$ in terms of $\mathbf{q}$ and $\mathbf{p}$. As mentioned above, the optical properties of the direct band gap semiconductors studied here are determined by the behaviour of the band structure around the Γ-point, thus, this point is often of most interest [37]. When $\mathbf{k}_0 = \mathbf{0}$, $\mathbf{q} = \mathbf{k}$, hence the name of this class of theories derives from the resulting $\mathbf{k}\cdot\mathbf{p}$ term in Eq. (2.12). However, we note that this method can be also be applied to other choices of $\mathbf{k}_0$.

Having identified the correction to $\hat{H}$ when studying the band structure at $\mathbf{k}$ with $\mathbf{k} \neq \mathbf{k}_0$, we can treat these extra terms as perturbations. To do so, we apply second-order perturbation theory to derive an expression for the variation of $\mathrm{E}_n(\mathbf{k})$ near $\mathbf{k}_0 = \mathbf{0}$, i.e., near the Γ-point [132]. As an illustration, we consider a non-degenerate band, where, for the n^{th} such band, we have

$$\mathrm{E}_n(\mathbf{k}) = \mathrm{E}_n(\mathbf{0}) + \frac{\hbar}{m}\mathbf{k}\cdot\mathbf{p}_{nn} + \frac{\hbar^2 k^2}{2m} + \frac{\hbar^2}{m^2}\sum_{n'\neq n}\frac{|\mathbf{k}\cdot\mathbf{p}_{nn'}|^2}{\mathrm{E}_n(\mathbf{0}) - \mathrm{E}_{n'}(\mathbf{0})} \ . \tag{2.13}$$

where

$$\mathbf{p}_{nn'} = \langle u_{n,\mathbf{0}}|\,\mathbf{p}\,|u_{n',\mathbf{0}}\rangle \ ,$$

and $\mathbf{p}$ is the momentum operator as before. The momentum matrix elements, $\mathbf{p}_{nn'}$, contribute corrections to the energy of a given state near Γ due to the presence of other energy states. It can be shown, due to symmetry, that in diamond crystal structures $\mathbf{p}_{nn} = 0$ [37], and in III-N systems this term is generally small relative to the quadratic term in Eq. (2.13) [37, 165]. It is also

possible to expand the wave function $\Phi_{n,\mathbf{k}}(\mathbf{r})$ near Γ in terms of the known wave functions, $\Psi_{n,\mathbf{k}_0}(\mathbf{r})$, at Γ via [134];

$$\Phi_{n,\mathbf{k}}(\mathbf{r}) = \Psi_{n,\mathbf{k}_0}(\mathbf{r}) + \frac{\hbar}{m}\sum_{n'\neq n}\frac{\mathbf{k}\cdot\mathbf{p}_{nn'}}{\mathrm{E}_n(\mathbf{0}) - \mathrm{E}_{n'}(\mathbf{0})}\Psi_{n',\mathbf{k}_0}(\mathbf{r}) \ .$$

In practice, the sum over n' in Eq. (2.13) will be dominated by contributions from bands close in energy to the target band, limiting the number of bands we need to consider explicitly. Löwdin provided a method to categorise bands into "A" bands, which will be included explicitly, and "B" bands, the impact of which will be included implicitly via the effective mass [166]. Thus, Eq. (2.13) becomes

$$\begin{aligned}\mathrm{E}_n(\mathbf{k}) =& \mathrm{E}_n(\mathbf{0}) + \frac{\hbar^2k^2}{2m} \\ &+ \frac{\hbar^2}{m^2}\sum_{n'\in A\neq n}\frac{|\mathbf{k}\cdot\mathbf{p}_{nn'}|^2}{\mathrm{E}_n(\mathbf{0}) - \mathrm{E}_{n'}(\mathbf{0})} + \frac{\hbar^2}{m^2}\sum_{n'\in B}\frac{|\mathbf{k}\cdot\mathbf{p}_{nn'}|^2}{\mathrm{E}_n(\mathbf{0}) - \mathrm{E}_{n'}(\mathbf{0})} \ . \end{aligned} \tag{2.14}$$

In general, Eq. (2.14) can be written as [134]

$$\mathrm{E}_n(\mathbf{k}) = \mathrm{E}_n(\mathbf{0}) + \underbrace{\frac{\hbar^2}{m^2}\sum_{n'\in A\neq n}\frac{|\mathbf{k}\cdot\mathbf{p}_{nn'}|^2}{\mathrm{E}_n(\mathbf{0}) - \mathrm{E}_{n'}(\mathbf{0})}}_{\text{Explicit A Bands}} + \underbrace{\sum_{i\in\{1,2,3\}}\frac{\hbar^2k_i^2}{2}\left(\frac{1}{m_i^*}\right)}_{\text{Implicit B Bands}} ,$$

where the sum over i is over the three directions of reciprocal space, k_i is the magnitude of $\mathbf{k}$ in the i-direction and m_i^* is the effective mass in that direction. The effective mass in direction i, which is modified by the presence of the B bands, is given by

$$\frac{1}{m_i^*} = \frac{1}{m} + \frac{2}{m^2}\sum_{n'\in B}\frac{|\hat{\mathbf{k}}_i\cdot\mathbf{p}_{nn'}|^2}{\mathrm{E}_n(\mathbf{0}) - \mathrm{E}_{n'}(\mathbf{0})} \ ,$$

where $\hat{\mathbf{k}}_i$ is a unit vector in the i-direction of reciprocal space.

The theories described above can also be extended to degenerate bands, as would be required, for instance, for the topmost valence bands in the band structure in Fig. 2.3. This can be achieved within the framework of degenerate perturbation theory [39]. Multi-band approaches have also been developed that take into account spin-orbit coupling, such as the models of Luttinger and Kohn [167], Kane [134] and Pidgeon and Brown [168]; for III-Ns, it turns out that this effect is generally of secondary importance [132]. Multi-band $\mathbf{k}\cdot\mathbf{p}$

theories of increasing levels of complexity have been developed, generally named after how many bands are treated explicitly [37].

However, when considering semiconductor alloys, the above analysis should, in principle, break down due to the presence of alloy disorder. Despite this, it has been found that for many conventional III-V semiconductor alloys (e.g. AlGaAs) the alloy disorder represents a weak perturbation to the system and interpolating material parameters can give a reasonable description of the electronic structure [38]. Such an approximation is another example of a virtual crystal approximation (VCA), as mentioned in Sec. 1.4 to determine, for instance, the lattice parameters of an InGaN alloy via a linear interpolation scheme. Conceptually, the problem of solving the Schrödinger equation in a disordered, aperiodic potential, is converted to a picture in which the electrons move in a fictitious ideal "virtual" crystal. The atoms of this crystal then have the interpolated properties of the alloy constituents, and the model above is applied to an "effective" periodic unit cell. VCAs form the basis of many $\mathbf{k}\cdot\mathbf{p}$ descriptions of semiconductor alloys underlying bulk materials and/or heterostructures.

Multi-band $\mathbf{k}\cdot\mathbf{p}$ approaches have been applied to the analysis of many nanostructures of realistic sizes, beyond the reach of standard DFT [37, 38, 39, 132]. Using VCAs, 1D descriptions of QWs can be targeted as the confining potential is still periodic in the growth plane. In this case, if the growth plane is coplanar with the x-y plane, then k_x and k_y can be used as "good" quantum numbers and we need only to solve a particle in a box problem along the growth direction. However, as we discussed in Sec. 1.4, in III-N alloys, alloy disorder leads to a breakdown of the VCA description due to variations in the electronic structure even within a unit cell. As a result, k_x and k_y are no longer good quantum numbers and standard continuum-based approaches like those discussed above may not provide a good description of III-N alloys [45]. Thus, a number of modified continuum-based approaches have been developed.

2.4.2 Modified continuum-based approaches

To develop modified continuum-based models the confining potential is described in a fully 3D picture. To obtain the confining potential one often starts from a 3D "compositional" map of, e.g., cation species in the alloy [18, 41, 129, 169, 170, 171]. In this section, as an example, we will

consider the case of InGaN alloys and QWs. Having determined information about the In and Ga atom distributions from, for example, experimental data (i.e. atom clustering or random distribution), a digital alloy is generated with either In or Ga atoms at a given position. However, that resolution may be too fine for a continuum-based model. Thus, a map is generated on a larger length scale that gives the average In/Ga concentration in a given region. Often a Gaussian smoothing procedure is used to determine the local In or Ga content.

In order to determine the confining potential, the position dependence of the local energy band edges are inferred from a VCA-like description. At every point in the simulated material, the conduction and valence band edge energies are determined from the variation of the band gap with In content given by Végard's law (see Sec. 1.4):

$$\mathrm{E_g}(\mathrm{In}_x\mathrm{Ga}_{1-x}\mathrm{N}) = x\mathrm{E}_g(\mathrm{InN}) + (1-x)\mathrm{E_g}(\mathrm{GaN}) + bx(1-x)\ , \tag{2.15}$$

where x is the In composition at a given point and b is the quadratic bowing parameter. Equation (2.15) is widely used [36] and can be refined based on the work in Ref. [82]. Fluctuations in strain and built-in field can also be accounted for based on the local alloy content (see, for example, Ref. [170]). Similar VCA-like interpolation schemes, if known, can be used for all material parameters (such as relative permittivity or effective mass [170]). The 3D potential map is then used as input for solving the Schrödinger equation. Most often, modified continuum-based models use EMAs. However, even when working in a single band EMA, when targeting finer and finer resolutions of the effective confining potential map, as well as when modelling larger regions of the structure (for instance in device simulations [172]), the computational expense can be significant. Much of the computational expense stems from solving the eigenvalue problem associated with the Schrödinger equation. Recently, a numerical approach to avoid explicitly solving the Schrödinger equation for random energy landscapes has been developed, the so-called localisation landscape theory.

In general, localisation landscape theory (LLT) is a method that allows the estimation of a local ground state wave function in a disordered potential energy landscape without solving the Schrödinger equation. Instead, in LLT, an upper bound for the amplitude of the ground state wave function is determined from the solution to a system of linear equations. For more details

on LLT, and a derivation of the so-called landscape equation,

$$\hat{H}\,|u\rangle = \mathbb{1}\,, \tag{2.16}$$

see Ref. [173]. The mathematical object $|u\rangle$ can be used to approximate the ground state wave function and by taking the inverse of $\langle r|u\rangle = u(r)$, an effective confining potential can be found that describes the energy landscape [174]. It is possible to construct the higher lying, excited states using $|u\rangle$ as well [174].

So far, LLT has been applied to a number of topics using a single band EMA, i.e., by using a single band effective mass Hamiltonian, $\hat{H}$, in Eq. (2.16). Very recently, the method has been established for single band tight-binding Hamiltonians, with some theoretical results being reported [175, 176]. The numerical efficiency of the method is a clear advantage when determining properties of disordered systems that require larger simulation cells, such as the determination of the density of states or absorption edges [170, 177]. On top of this, the effective confining potential, $1/u(r)$, can be used as input to larger scale transport calculations [178, 179], thus, device simulations.

As already indicated above, so far LLT has only been developed for single band models and it is not clear how to extend this scheme to multi-band models. For InGaN systems, since the valence band structure is similar between InN and GaN systems (i.e. the highest valence bands in both InN and GaN are mostly p_x/p_y-like in orbital character [180]), a single band approach may be a reasonable approximation to describe localised states in a disordered energy landscape. However, for AlGaN structures, the valence band ordering is different (as the highest valence band in AlN is mostly p_z-like in character [181]) and changes with Al content. Thus, the single band EMA may present a significant shortcoming and fail to describe important physics that is also relevant for device applications, such as the polarisation characteristics of emitted light [57].

Furthermore, some processes, such as Auger recombination, may require a description of the electronic structure of the full first Brillouin zone, beyond the reach of a single band framework. Thus, modified continuum-based approaches have been developed in which a multi-band $\mathbf{k}\cdot\mathbf{p}$ theory is used in conjunction with the extracted 3D confining potential map described above [18, 41, 129, 169, 171]. However, due to the underlying eigenvalue

problem, solving the Schrödinger equation with a multi-band EMA (with the 3D potential map as input) can also be numerically expensive. Furthermore, for both LLT and multi-band approaches, a Gaussian smoothing of the compositional map is used [41, 129, 170]. This smoothing procedure introduces another degree of freedom, which is related to the softening/interpolation scheme, and may "wash out" carrier localisation effects by averaging out large variations in, for instance, confining potential.

Overall, in this section we have seen that there are a number of modified continuum-based approaches that can be applied to determine the electronic structure of semiconductors. However, there are trade-offs that must be made between, for instance, single band versus multi-band descriptions or simulation resolution versus numerical expense. All these modified continuum-based approaches have in common that they cannot resolve atomistic features and can even be computationally expensive when trying to use a fine numerical resolution. A model that bypasses this shortcoming is the tight-binding approach, which allows for an atomistic resolution as well as single band or multi-band descriptions. In the next section we discuss tight-binding models in general and the model underpinning this work.

2.4.3 Tight-binding

In the tight-binding (TB) approach, we assume that the electrons in a system are tightly bound, or strongly localised, to the ions in the lattice. The wave functions of the extended bulk, or heterostructure, carrier states are then constructed as linear combinations of these strongly localised atomic-like orbitals [182]. Tight-binding models of varying levels of sophistication have been developed and can be categorised by a number of parameters. For instance, in this work we consider a TB model based on four atomic-like orbitals: s, p_x, p_y and p_z [183]. Such a TB model is said to have an sp^3 basis but examples of models using, for instance, an $sp^3d^5s^*$ basis can be found [47, 184, 185].

Given the strongly localised nature of the atomic-like orbitals, it is expected that the interaction between orbitals on nearby atoms decays rapidly, and so TB models with differing "cutoff distances" have been used, referred to as nearest neighbour, second nearest neighbour, etc. [186, 187]. These two assumptions, that a small number of atomic-like orbitals can describe much of the band structure, and that the overlap of atomic-like orbitals decreases

rapidly with increasing distance between atomic sites, are the main assumptions of the TB method [75]. In this work we use a nearest neighbour TB model. Although spin-orbit coupling effects can be taken into account in the TB approach (see, e.g., Ref. [75]), as we have mentioned before, in III-N materials these effects are generally of secondary importance [132]. We begin by discussing the fundamental ideas underlying the TB approach before turning to methods used to include strain and polarisation effects with an atomistic resolution.

2.4.3.1 Basic considerations

To discuss the TB method we will first construct the Hamiltonian for the system. To do so we follow the approach of Ref. [75]. For illustration, we will consider the case of a ideal bulk crystal so that we may apply Bloch's theorem, and subsequently will discuss the modification of the model for alloys. We begin by considering the strongly localised basis states, $|\mathbf{R}_n, \alpha, \nu\rangle$, describing the atomic-like orbital of orbital character ν, with $\nu \in \{s, p_x, p_y, p_z\}$, in the unit cell at position $\mathbf{R}_n$, in which there may be anions and cations of differing species labeled by α, and n runs over the unit cells of the lattice. Assuming, in a first step, an isolated atom located at spatial position $\mathbf{R}_l$, the Schrödinger equation reads;

$$\hat{H}_{\text{at}} |\mathbf{R}_l, \alpha, \nu\rangle = \mathrm{E}_{\text{at}}^{\alpha,\nu} |\mathbf{R}_l, \alpha, \nu\rangle \ ,$$

where the atomic Hamiltonian is

$$\hat{H}_{\text{at}} = \frac{\hat{\mathbf{p}}^2}{2m} + V_{\text{at}}(\mathbf{R}_l, \alpha) \ .$$

Here, $V_{\text{at}}(\mathbf{R}_l, \alpha)$ is the atomic potential of the atom α at $\mathbf{R}_l$. Due to the presence of the other atoms in the lattice, the electronic structure of such an atom will be modified, with the associated single particle Hamiltonian;

$$\hat{H}_{\text{SP}} = \hat{H}_{\text{at}}(\mathbf{R}_l, \alpha) + \hat{V}_{\text{lattice}}(\mathbf{R}_l, \alpha) \ , \tag{2.17}$$

where

$$\hat{V}_{\text{lattice}}(\mathbf{R}_l, \alpha) = \sum_{m \neq l} \sum_{\alpha'} V_{\text{at}}(\mathbf{R}_m, \alpha')$$

is the lattice periodic potential due to the other atoms in the lattice. For a single particle wave function characterised by wave vector $\mathbf{k}$, $|\mathbf{k}\rangle$, we are

required to solve

$$\hat{H}_{\text{SP}} \left|\mathbf{k}\right\rangle = \text{E}(\mathbf{k}) \left|\mathbf{k}\right\rangle \ . \tag{2.18}$$

The bulk single particle wave functions can then be represented as linear combinations of Bloch-type wave functions constructed from the atomic orbitals:

$$\begin{aligned} \left|\mathbf{k}\right\rangle &= \sum_{\alpha,\nu} c_{\alpha,\nu}(\mathbf{k}) \left(\sqrt{\frac{V_0}{V}} \sum_n e^{i\mathbf{k}\cdot(\mathbf{R}_n+\boldsymbol{\Delta}_\alpha)} \left|\mathbf{R}_n,\alpha,\nu\right\rangle \right) \ , \\ &= \sum_{\alpha,\nu} c_{\alpha,\nu}(\mathbf{k}) \left|\mathbf{k},\alpha,\nu\right\rangle \ , \end{aligned} \tag{2.19}$$

where $c_{\alpha,\nu}(\mathbf{k})$ are the expansion coefficients, V_0 is the volume of a unit cell, V is the volume of the full system, n runs over all unit cells as before and the position of the atom α within unit cell n is given by Δ_α. It can be shown that this ansatz for $\left|\mathbf{k}\right\rangle$ satisfies Bloch's theorem [75], thus we restrict our analysis to $\mathbf{k}$ being in the first Brillouin zone. Our next step will be to determine the expansion coefficients. To do so, we substitute our ansatz for $\left|\mathbf{k}\right\rangle$ given in Eq. (2.19) into Eq. (2.18) and multiply on the left by the bra vector $\left\langle\mathbf{k},\alpha',\nu'\right|$. After some manipulation we are left with the following matrix equation:

$$\sum_{\alpha,\nu} H^{\text{SP}}_{\alpha',\nu';\alpha,\nu}(\mathbf{k}) c_{\alpha,\nu}(\mathbf{k}) = \text{E}(\mathbf{k}) \sum_{\alpha,\nu} S_{\alpha',\nu';\alpha,\nu}(\mathbf{k}) c_{\alpha,\nu}(\mathbf{k}) \ , \tag{2.20}$$

where the Hamiltonian matrix elements, $H^{\text{SP}}_{\alpha',\nu';\alpha,\nu}(\mathbf{k})$, and overlap matrix elements, $S_{\alpha',\nu';\alpha,\nu}(\mathbf{k})$, are given by

$$H^{\text{SP}}_{\alpha',\nu';\alpha,\nu}(\mathbf{k}) = \frac{V_0}{V} \sum_{m,n} e^{i\mathbf{k}\cdot(\mathbf{R}_m+\Delta_{\alpha'}-\mathbf{R}_n-\Delta_\alpha)} \left\langle\mathbf{R}_m,\alpha',\nu'\right| \hat{H}_{\text{SP}} \left|\mathbf{R}_n,\alpha,\nu\right\rangle \ ,$$

and

$$S_{\alpha',\nu';\alpha,\nu}(\mathbf{k}) = \frac{V_0}{V} \sum_{m,n} e^{i\mathbf{k}\cdot(\mathbf{R}_m+\Delta_{\alpha'}-\mathbf{R}_n-\Delta_\alpha)} \left\langle\mathbf{R}_m,\alpha',\nu'|\mathbf{R}_n,\alpha,\nu\right\rangle \ .$$

The atomic-like orbitals are not generally mutually orthogonal to each other when calculating the overlap of wave functions localised on different atoms in the lattice. Thus, the condition that

$$\left\langle\mathbf{R}_m,\alpha',\nu'|\mathbf{R}_n,\alpha,\nu\right\rangle = \delta_{n,m}\delta_{\alpha',\alpha}\delta_{\nu',\nu} \ ,$$

for nearest neighbour sites will not necessarily be fulfilled. However, the orthogonalisation procedure of Löwdin permits the transformation of the TB

basis into an orthogonal basis while preserving the localised nature of the basis orbitals and their symmetry [166].

Proceeding now under the assumption that we have used a Löwdin transformation to work with an orthogonal basis, the elements of the overlap matrix, S, become

$$S_{\alpha',\nu';\alpha,\nu} = \delta_{\mathbf{R}_m,\mathbf{R}_n}\delta_{\alpha',\alpha}\delta_{\nu',\nu} \ ,$$

and overall Eq. (2.20) reduces to

$$\sum_{\alpha,\nu} H^{\text{SP}}_{\alpha',\nu';\alpha,\nu}(\mathbf{k})c_{\alpha,\nu}(\mathbf{k}) = \text{E}(\mathbf{k})c_{\alpha',\nu'}(\mathbf{k}) \ . \tag{2.21}$$

In order to discuss some of the features of the solutions to Eq. (2.21), we consider a simplified situation in which there is only one atomic species and one atomic-like orbital in the basis. Thus, the sum over α and ν is eliminated in our discussion here:

$$H^{\text{SP}}_{\alpha,\nu;\alpha,\nu}(\mathbf{k}) = \langle \mathbf{k},\alpha,\nu|\, \hat{H}_{\text{SP}}\, |\mathbf{k},\alpha,\nu\rangle = \text{E}(\mathbf{k}) \ .$$

And,

$$\begin{aligned}\langle \mathbf{k},\alpha,\nu|\, \hat{H}_{\text{SP}}\, |\mathbf{k},\alpha,\nu\rangle &= \frac{V_0}{V}\sum_{m,n} e^{i\mathbf{k}\cdot(\mathbf{R}_m-\mathbf{R}_n)} \langle \mathbf{R}_m,\alpha,\nu|\, \hat{H}_{\text{SP}}\, |\mathbf{R}_n,\alpha,\nu\rangle \ , \\ &= \frac{V_0}{V}\sum_{m,n} e^{i\mathbf{k}\cdot(\mathbf{R}_m-\mathbf{R}_n)} I_{mn} \ . \end{aligned} \tag{2.22}$$

Due to the localised nature of the basis states, the I_{mn} terms in Eq. (2.22) become exponentially small for large values of $|\mathbf{R}_m - \mathbf{R}_n|$. Referring back to our definition for $\hat{H}_{\text{SP}}$ in Eq. (2.17), and considering now a specific atomic site, m, we can approximate the integrals, I_{mn} by

$$\begin{aligned} I_{mn} &= \delta_{m,n}\left[\langle \mathbf{R}_m,\alpha,\nu|\, \hat{H}_{\text{at}}\, |\mathbf{R}_n,\alpha,\nu\rangle + \sum_{l\neq n}\langle \mathbf{R}_m,\alpha,\nu|\, V_{\text{at}}(\mathbf{R}_l,\alpha)\, |\mathbf{R}_n,\alpha,\nu\rangle\right] \\ &+ \delta_{m,n\pm1}\left[\sum_l \langle \mathbf{R}_m,\alpha,\nu|\, V_{\text{at}}(\mathbf{R}_l,\alpha)\, |\mathbf{R}_n,\alpha,\nu\rangle\right] \\ &+ \delta_{m,n\pm2}\left[\sum_l \langle \mathbf{R}_m,\alpha,\nu|\, V_{\text{at}}(\mathbf{R}_l,\alpha)\, |\mathbf{R}_n,\alpha,\nu\rangle\right] + \ldots \\ &= \delta_{m,n}\widetilde{\text{E}} + \delta_{m,n\pm1}\lambda + \ldots \ . \end{aligned} \tag{2.23}$$

In our nearest neighbour model we truncate the expression after the $\delta_{m,n\pm1}$

term. The term $\widetilde{\mathrm{E}}$ is called the on-site energy, and can be interpreted as the atomic energy modified by the presence of the other atoms in the lattice. The λ term involves integrals of orbitals located at different atomic sites and is called a hopping integral/matrix element, as it gives the probability amplitude of an electron moving from one site to the other [75].

The contributions to the sums in Eq. (2.23) involve so-called "two centre" and "three centre" integrals depending on $\mathbf{R}_m$, $\mathbf{R}_n$ and $\mathbf{R}_l$. A two centre integral involves $\mathbf{R}_m = \mathbf{R}_l \neq \mathbf{R}_n$. A three centre integral involves $\mathbf{R}_m \neq \mathbf{R}_l \neq \mathbf{R}_n$. The two centre approximation of Slater and Koster proposes to discard three centre integrals as they are relatively smaller than the two centre integrals [75]. Slater and Koster also evaluated expressions for the hopping matrix elements depending on the orbital and bond type, while taking into account the directional cosines between the atomic sites under consideration [182].

The remaining question is now how to determine the quantities $\widetilde{\mathrm{E}}$ and λ, which we call the TB matrix elements. Generally, there are two approaches to determining the TB matrix elements in Eq. (2.23). One approach is to assume an explicit form for the basis states and calculate the matrix elements, for instance using *ab initio* methods. This leads to density functional tight-binding (DFTB) approaches [75]. Alternatively, the TB matrix elements can be treated as free parameters and fitted to band structure data, either experimental or determined via *ab initio* methods. The latter approach is often referred to as empirical or semi-empirical TB. In this work we use such a semi-empirical TB method that has been fitted to HSE hybrid functional DFT band structures of bulk InN, GaN and AlN and has also been benchmarked against experimental data for alloyed systems and heterostructures [82, 130]. The HSE functional HSE06 was utilised for the fitting with an exact exchange parameter $\alpha = 0.25$ and screening parameter $\mu = 0.2$. The cutoff energy for plane waves was 600 eV and a $6 \times 6 \times 4$ Γ-centred Monkhorst $\vec{k}$-point mesh was used. Further details can be found in Ref. [82].

Throughout this chapter we have stressed the need for an atomistic resolution when modelling an alloy, and above we have discussed the application of a TB model to determine the band structures of III-N bulk materials. However, extending the model to wurtzite III-N alloys is reasonably intuitive. For cation sites (e.g. In, Ga and Al) the nearest neighbour environment always consists of four N anions, in the absence of defects. Thus, in principle (i.e. in the absence of strain effects), assigning a value to the on-site matrix element for cation

sites is straightforward, and the bulk value would be appropriate. The InN/GaN band offset can be taken into account by shifting the InN on-site matrix element by the valence band offset, $\Delta \mathrm{E_{VB}} = 0.62$ eV, as determined via HSE DFT calculations [54]. For the anion sites, however, the nearest neighbour environment can have varying numbers of, e.g., In and Ga atoms. Thus, we must take into account the difference in the on-site matrix element for N in InN compared to GaN [82]. A common approach is to take a weighted average of the bulk values, weighted in the ratio of nearest neighbour atomic species [188, 189, 190].

To determine the hopping matrix elements, in the absence of strain effects, the relevant bulk value would be appropriate. However, strain effects will modify the hopping matrix elements due to variations in bond lengths and bond angles. Furthermore, strain effects will also modify the on-site energy due to variations in the local potential due to the surrounding lattice. In the next section we first discuss how we will include these strain effects in the TB model described above, before turning to look at how we determine the strain state of the system. Lastly, we will see how we factor the impact of the built-in polarisation field into our TB model.

2.4.3.2 Including strain effects

In principle, incorporating strain effects in a TB model would require some knowledge of how both the on-site and hopping matrix elements change with variations of the nearest neighbour bond lengths and bond angles. TB models have been developed with this approach but require the fitting of a large number of parameters [191, 192]. However, it has been shown, at least for an sp^3 basis, that strain can be included as an on-site correction to the TB Hamiltonian such that [191, 193]

$$\hat{H} = \hat{H}_0 + \hat{H}_{\text{strain}} \ .$$

$\hat{H}_0$ is the Hamiltonian of the unstrained system and $\hat{H}_{\text{strain}}$ is a site diagonal Pikus-Bir Hamiltonian for the atomic site i such that [82, 194, 195]

$$\hat{H}^i_{\text{strain}} = \begin{pmatrix} S_s & 0 & 0 & 0 \\ 0 & S_{xx} & S_{xy} & S_{xz} \\ 0 & S_{xy} & S_{yy} & S_{yz} \\ 0 & S_{xz} & S_{yz} & S_{zz} \end{pmatrix} \ . \tag{2.24}$$

In Eq. (2.24),

$$
\begin{aligned}
S_s &= a_{ct}(\varepsilon_{11}+\varepsilon_{22}) + a_{cp}\varepsilon_{33} \ , \\
S_{xx} &= (D_2+D_4)(\varepsilon_{11}+\varepsilon_{22}) + D_5(\varepsilon_{11}-\varepsilon_{22}) + (D_1+D_3)\varepsilon_{33} \ , \\
S_{yy} &= (D_2+D_4)(\varepsilon_{11}+\varepsilon_{22}) - D_5(\varepsilon_{11}-\varepsilon_{22}) + (D_2+D_3)\varepsilon_{33} \ , \\
S_{zz} &= D_2(\varepsilon_{11}+\varepsilon_{22}) + D_1\varepsilon_{33} \ , \\
S_{xy} &= 2D_5\varepsilon_{12} \ , \\
S_{xz} &= \sqrt{2}D_6\varepsilon_{13} \ , \\
S_{yz} &= \sqrt{2}D_6\varepsilon_{23} \ ,
\end{aligned}
$$

where the D_i terms are the valence band deformation potentials, extracted from HSE DFT [196] and a_{cp} and a_{ct} are the conduction band deformation potentials, related to the band gap deformation potentials, a_1 and a_2, given in Ref. [20], by $a_1 = a_{cp} - D_1$ and $a_2 = a_{ct} - D_2$. The term S_s would give, for example, the change in energy of the conduction band edge state with strain. As above, for anion sites, a weighted average in the nearest neighbour atomic species ratio is used. Using this approach, the deformation potentials for the highest valence band and lowest conduction band states are included directly from the HSE DFT calculations, avoiding further fitting of parameters [82].

We note that the deformation potentials are fitted in the vicinity of the Γ-point [196], and so may not accurately reproduce the variation of the band structure with strain away from Γ. However, alloy disorder breaks the translational symmetry of the lattice, meaning we can no longer label quantum states by $\mathbf{k}$, and it is assumed in our analysis below that $\mathbf{k} = \mathbf{0}$ anyway. Moreover, even at Γ, the energy shift of higher/lower lying states may not be correctly described by these band edge deformation potentials. Regardless, this approach is used in, for instance, 8-band $\mathbf{k}\cdot\mathbf{p}$ models [194] in the literature and, furthermore, although knowledge of the higher lying states is required to calculate Auger rates, overall, they are of secondary important.

To implement this approach we require some information about the local strain field, which will determine the on-site correction. As discussed above in Sec. 1.4, strain arises in a material when there is a deformation of the crystal. From an atomistic perspective, local strain fluctuations are caused by the displacement of atoms within a given unit cell as well as overall deformations of the unit cells in the crystal. Thus, we must determine how the atoms in the lattice will be displaced in order to minimise the elastic energy of the system.

To evaluate the elastic energy of the system we require some knowledge of the interactions between atoms. A number of methods have been developed to model the interatomic interactions [197, 198, 199, 200]. Here we use the approach developed by Martin [201], which is an example of a valence force field (VFF) model and is adapted from the work in Ref. [200]. Further details are given in Ref. [202]. In this VFF model, a specific form is chosen for the interatomic interaction potential that takes into account changes in energy due to changes in bond geometries (discussed in detail below). Overall, when assuming this form for the interatomic potential, the elastic/potential energy at a given atomic site, V_i, is given by

$$\begin{aligned} V_i = & \frac{1}{2}\sum_{j\neq i} \overbrace{\frac{1}{2}k_r \Delta r_{ij}^2}^{\text{bond stretching}} \\ & + \sum_{j\neq i}\sum_{k\neq i, k>j} \overbrace{\left\{\frac{1}{2}k_\theta^i r_{ij}^0 r_{ik}^0 \Delta\theta_{ijk}^2\right.}^{\text{bond bending}} + \overbrace{k_{r\theta}^i \Delta\theta_{ijk}\left(r_{ij}^0\Delta r_{ij} + r_{ik}^0 \Delta r_{ik}\right)}^{\text{bond-angle}} + \overbrace{\left. k_{rr}^i \Delta r_{ij}\Delta r_{ik}\right\}}^{\text{bond-bond}} \\ & + \sum_{j'\neq i} \underbrace{\frac{e^2}{4\pi\epsilon_0\epsilon_r}\frac{Z_i^* Z_{j'}^*}{r_{ij'}}}_{\text{Attractive Coulomb}} - \frac{1}{2}\sum_{j\neq i} \underbrace{\frac{1}{4}\alpha_M \frac{e^2}{4\pi\epsilon_0\epsilon_r}\frac{Z_i^* Z_j^*}{r_{ij}^2}\Delta r_{ij}}_{\text{Repulsive Coulomb screening}} \ . \end{aligned} \tag{2.25}$$

In this expression k_r, k_θ^i, $k_{r\theta}^i$ and k_{rr}^i are the force constants related to changes in bond length (bond stretching term), changes in bond angle (bond bending term), the coupling between changes in bond length and changes in bond angle (bond-angle term) and the coupling between changes in bond lengths (of different bonds, bond-bond term), respectively. In the unstrained bulk system, the bond length between atomic site i and j is given by r_{ij}^0, while the angle between the bonds connecting atomic site i to atomic sites j and k is given by θ_{ijk}^0. The bond lengths and bond angles in the strained system are given by r_{ij} and θ_{ijk}, respectively, with the associated variations $\Delta r_{ij} = r_{ij} - r_{ij}^0$ and $\Delta\theta_{ijk} = \theta_{ijk} - \theta_{ijk}^0$ (see Fig. 2.4 below). The elementary charge is denoted by e, the permittivity of vacuum is ϵ_0 and the relative permittivity is ϵ_r, Z_i^* is the effective charge for atom i, and finally, α_M is the Madelung constant. We will discuss each individually below.

Figure 2.4 shows schematics of the origin of the bond stretching, bond bending, bond-angle and bond-bond terms. The bond stretching term in Eq. (2.25), due to the situation depicted in Fig. 2.4 a), is reasonably straightforward, and tracks the change in energy due to changes in bond

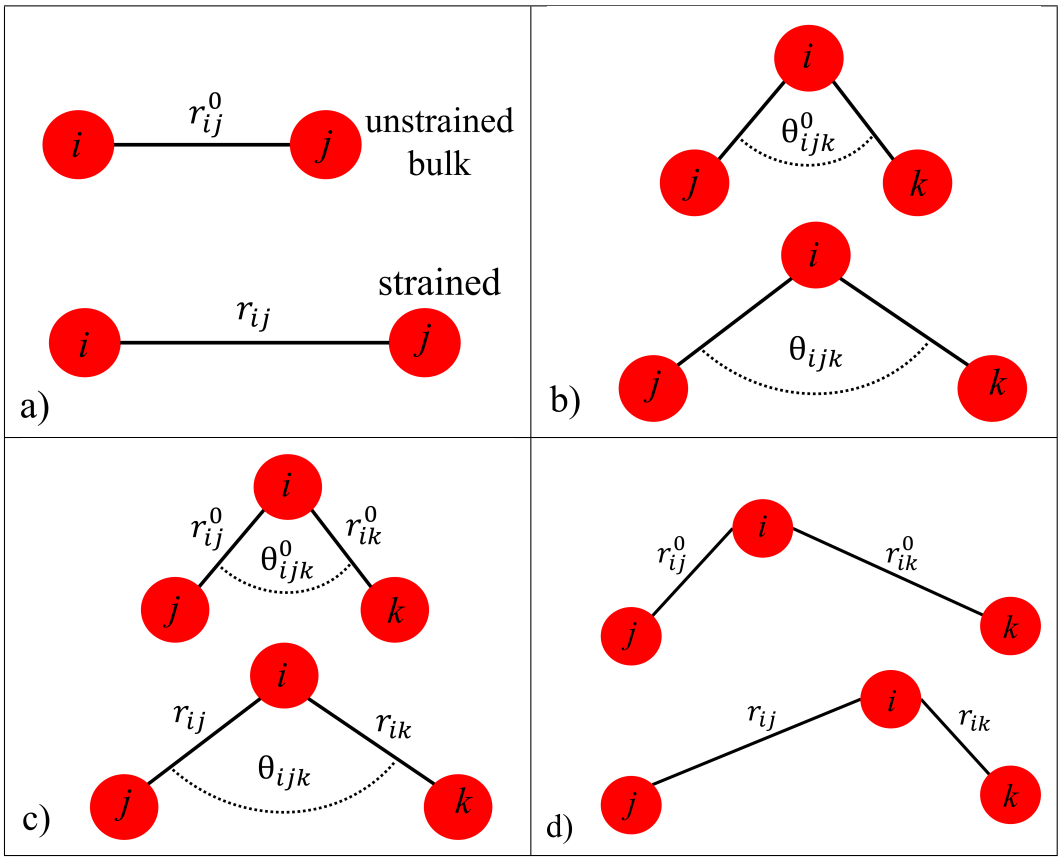


Figure 2.4: Schematics of the origins of the a) bond stretching, b) bond bending, c) bond-angle and d) bond-bond terms in Eq. (2.25). In all four diagrams, the top configuration represents the unstrained, ideal bulk situation, while the bottom is an example of a modification to bond length or bond angle that may occur in an alloy situation, wherein the system will be strained. Atomic sites are labeled by i, j and k. Equilibrium (i.e. unstrained bulk) bond lengths and bond angles are denoted by r^0_{ij} and θ^0_{ijk}, respectively. Alloy (strained) bond lengths and bond angles are denoted by r_{ij} and θ_{ijk}, respectively.

lengths. The bond bending term, seen in Fig. 2.4 b), accounts for changes in energy due to changes in the angle between bonds. In Fig. 2.4 c) we see that changes in bond length may induce changes in bond angle, thus the bond-angle term takes these contributions into account. Lastly, Fig. 2.4 d) depicts a situation in which the change in length of one bond induces a change in length of a different bond, which is included via the bond-bond term in Eq. (2.25). In each of the situations depicted in Fig. 2.4, only one possible deformation is shown in the strained case as an example. For instance in Fig. 2.4 a), $r_{ij} > r^0_{ij}$, but depending on the local environment, it could also be the case that $r_{ij} < r^0_{ij}$ in the strained system.

Each sum in Eq. (2.25), except the sums involving Coulomb terms, runs over

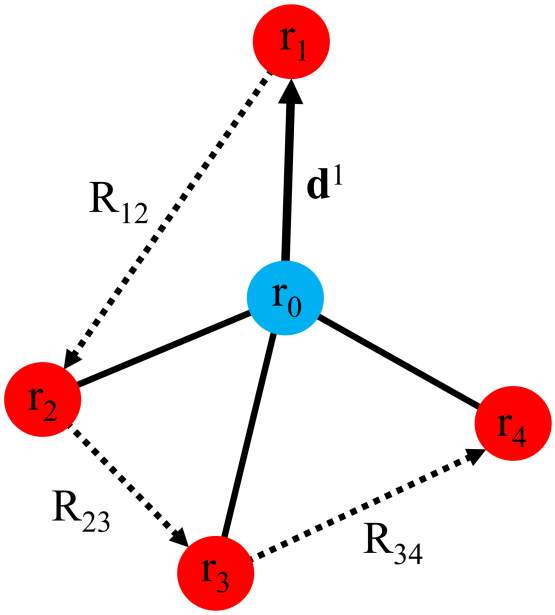


Figure 2.5: Local tetrahedron of the cation (blue filled circle) atomic site located at position $\mathbf{r}_0$ formed by nearest neighbours located at vectors $\mathbf{d}^\alpha$ from atom 0. Only the vector to atom 1, $\mathbf{d}^1$, is shown. Bonds are depicted by solid lines. $\mathbf{d}^1$ is colinear with the bond between atom 0 and atom 1. The edges of the local tetrahedron, $\mathbf{R}_{ij}$, are depicted by dashed arrows.

the four nearest neighbour bonds and six nearest neighbour angles in a local tetrahedron, in the case of the wurtzite structures considered here, illustrated in Fig. 2.5. In the attractive Coulomb term, the sum over j runs over all atoms in the crystal, thus taking into account the potential due to the rest of the lattice. The repulsive Coulomb screening term in Eq. (2.25) is included to screen the Coulomb interaction in the nearest neighbour tetrahedron, a step which is required to preserve the stability of the crystal [201]. The force constants and effective charges are fitted to HSE DFT results to accurately reproduce elastic constants and internal strain in bulk InN, GaN and AlN. The model also reproduces the non-ideal c/a ratio of wurtzite nitrides, as well as the internal parameter u. For more details see Refs. [89] and [203]. The model has been implemented in the molecular dynamics software package LAMMPS, in which the potential energy of the structure is minimised in order to determine the relaxed atomic positions [204]. In the implementation of an alloy in this framework, when a mix of, for instance, InN and GaN bonds are involved, weighted averages of the bulk material force constants are taken, otherwise the bulk parameters are used.

Finally, with the relaxed atomic positions determined, a local strain tensor can be constructed using the method in Ref. [205], see also Ref. [82]. The local

strain tensor at $\mathbf{r}$, $\varepsilon_{ij}(\mathbf{r})$, is given by

$$\begin{pmatrix} \varepsilon_{xx} & \varepsilon_{yx} & \varepsilon_{zx} \\ \varepsilon_{xy} & \varepsilon_{yy} & \varepsilon_{zy} \\ \varepsilon_{xz} & \varepsilon_{yz} & \varepsilon_{zz} \end{pmatrix} = \begin{pmatrix} R^0_{12,x} & R^0_{23,x} & R^0_{34,x} \\ R^0_{12,y} & R^0_{23,y} & R^0_{34,y} \\ R^0_{12,z} & R^0_{23,z} & R^0_{34,z} \end{pmatrix}^{-1} \begin{pmatrix} R_{12,x} & R_{23,x} & R_{34,x} \\ R_{12,y} & R_{23,y} & R_{34,y} \\ R_{12,z} & R_{23,z} & R_{34,z} \end{pmatrix} - \mathbb{1} \ , \quad (2.26)$$

where, for example, $\mathbf{R}_{12} = (R_{12,x}, R_{12,y}, R_{12,z})^T$ is the edge of the local tetrahedron between atoms 1 and 2 in Fig. 2.5. With the local strain tensor determined, we can include the effect of strain on the TB Hamiltonian determined above via Eq. (2.24). However, as discussed above in Sec. 1.4, strain effects will also lead to piezoelectric polarisation effects, and we seek a method to treat local fluctuations in piezoelectric polarisation that arise from local fluctuations in strain. We now turn to discuss the method developed to achieve this.

2.4.3.3 Including polarisation field effects

As discussed above in Sec. 1.4, strain in wurtzite III-N QWs lead to piezoelectric polarisation effects. Indeed, in an InGaN alloy the difference in lattice constants between InN and GaN is $\sim 10\%$, thus we expect relatively large local fluctuations may occur depending on the local atomic environment. With the model that can describe local fluctuations in strain established above, we are in a position to determine the associated local fluctuations in piezoelectric polarisation via the approach detailed in Ref. [82]. The central result of that work is that the i^{th} component of the total polarisation at an atomic site can be separated into a macroscopic and local contribution, given by, for the atomic site labeled 0;

$$P_i = \underbrace{\sum_{j=1}^{6} e^{(0)}_{ij} \varepsilon_j}_{\text{macroscopic}} + \underbrace{P^{\text{SP}}_i - \frac{e}{V_0} \frac{Z^0_i}{N^0_{\text{coor}}} \left[\mu_i - \sum_{j=1}^{3} \left(\delta_{ij} + \varepsilon_{ij} \right) \mu_{j,0} \right]}_{\text{local}} \ . \quad (2.27)$$

In this expression $e^{(0)}_{ij}$ are the piezoelectric coefficients determined by a "clamped-ion" calculation in which the internal degrees of freedom are not allowed to relax [85]. The macroscopic strain is denoted by ε_j in Voigt notation. The i^{th} component of the spontaneous polarisation is denoted by P^{SP}_i. The volume of the local tetrahedron is V_0, Z^0_i is the Born effective charge of atom 0, N^0_{coor} is the number of nearest neighbours of atom 0. The i^{th}

component of the bond asymmetry parameter, μ_i, is given by

$$\mu_i = \sum_{\alpha=1}^{N^0_{\text{coor}}} d_i^\alpha \ ,$$

where

$$d_i^\alpha = \sum_{j=1}^{3} \left(\delta_{ij} + \varepsilon_{ij}\right) d_{j,0}^\alpha + t_i^\alpha - t_i^0 \ ,$$

and $d_{j,0}^\alpha$ is the j^{th} component of the vector from the atom under consideration, atom 0, to each of the nearest neighbours for the unstrained system (see Fig. 2.5). The i^{th} component of the internal strain vector for atom α is t_i^α, hence t_i^0 corresponds to atom 0. Summing these vectors over all the nearest neighbours gives a measure of the bond asymmetry, $\boldsymbol{\mu}$, from which the piezoelectricity in strained systems arises. Determining this vector for an unstrained binary wurtzite system, $\boldsymbol{\mu}_0$, we would see that only the z component is nonzero, while for an unstrained zinc blende binary structure, every component is zero [206]. The components of $\boldsymbol{\mu}_0$ contribute to the local part of Eq. (2.27) via $\mu_{j,0}$.

A number of approximations have been employed in the derivation of this equation in Ref. [82]. These include 1) truncating the description of the piezoelectric response to strain to first order in both the macroscopic and internal strain, 2) assuming the spontaneous polarisation is constant throughout the crystal for binaries, 3) that the off-diagonal components of the Born effective charge tensor are zero, 4) using a spherical approximation for the Born effective charge of the nearest neighbours of the atom under consideration and 5) neglecting the strain dependence of the Born effective charge. The impact of these approximations on the results is discussed at length in Ref. [82].

Having determined the polarisation vector, we must now determine the associated potential, as described above in Sec. 1.4. Previously, we used Poisson's equation (Eq. (1.6)) to determine the potential in a continuum-based approach. In the atomistic approach here, however, the relaxed atomic positions make an irregular grid, presenting a further technical challenge. Instead, a point-dipole method is used, in which the potential at each atomic site is determined as the sum of all the dipoles in the lattice [82].

Generally, polarisation is defined to be dipole moment per unit of volume, and so here, the P_i in Eq. (2.27) can be considered a density of dipole moments. A

natural discretisation of the strained, irregular grid determined by the relaxed atomic positions is the irregular tetrahedron formed by the nearest neighbours of a given atomic site. This volume, determined by the atomic positions $\mathbf{r}_j$, $j \in \{1,2,3,4\}$ as in Fig. 2.5, can be determined to be

$$V_{1234} = \frac{1}{6}|(\mathbf{r}_1 - \mathbf{r}_4) \cdot [(\mathbf{r}_2 - \mathbf{r}_4) \times (\mathbf{r}_3 - \mathbf{r}_4)]| \ .$$

Labeling the grid points by their positions $\mathbf{R}_i$ (and ensuring that the volume of the full simulation cell is considered [82]), the dipole moment, $\mathbf{p}_i$, in the corresponding volume, V_i, is given by

$$\mathbf{p}_i = \mathbf{P}_i V_i \ .$$

For instance, the point dipole at $\mathbf{R}_i$ will generate an $\mathbf{r}$-dependent potential, $\phi_i(\mathbf{r})$, given by the multipole expansion [83];

$$\phi_i(\mathbf{r}) = \frac{1}{4\pi\epsilon_0\epsilon_r}\frac{\mathbf{p}_i \cdot (\mathbf{r} - \mathbf{R}_i)}{|\mathbf{r} - \mathbf{R}_i|^3} \ .$$

Thus, the total potential at a given atomic site will be the sum of all the contributions at that point. For example, the polarisation potential, φ_{pol}, at the atomic site at position $\mathbf{r}_i$, will be given by

$$\varphi_{\text{pol}}(\mathbf{r}_i) = \sum_{j \neq i} \phi_j(\mathbf{r}_i) \ . \tag{2.28}$$

To include the polarisation in the calculation of the electronic structure in our TB framework, we use a site-diagonal correction, similar to the approach for strain corrections described above. For the atomic site at $\mathbf{r}_i$, the correction to the Hamiltonian is

$$\hat{H}_{\text{pol}}(\mathbf{r}_i) = \begin{pmatrix} \varphi_{\text{pol}}(\mathbf{r}_i) & 0 & 0 & 0 \\ 0 & \varphi_{\text{pol}}(\mathbf{r}_i) & 0 & 0 \\ 0 & 0 & \varphi_{\text{pol}}(\mathbf{r}_i) & 0 \\ 0 & 0 & 0 & \varphi_{\text{pol}}(\mathbf{r}_i) \end{pmatrix} \ .$$

Finally, the full Hamiltonian is

$$\hat{H} = \hat{H}_{\text{SP}} + \hat{H}_{\text{strain}} - q\hat{H}_{\text{pol}} \ .$$

In summary, the following is an overview of the method used to set up the TB Hamiltonian for a strained, alloy disordered III-N alloy or heterostructure:

1. TB parameters are determined by fitting to HSE-DFT band structures (DFT implemented in VASP, see Ref. [82] for further details).
2. Large scale disorderd supercells set up with random seeding of In and Ga atoms in accordance with experimental data and usual practice in semi-empirical calculations (implemented in custom code).
3. Equilibrium atomic positions are determined (via atomistic VFF) by minimising the elastic energy for each supercell generated in Step 2 above. The VFF model is implemented in the numerically efficient and massively parallelised software package LAMMPS [204].
4. The local strain tensor of the relaxed supercell is determined on the basis of Eq. (2.26) (implemented in custom code).
5. The built-in polarisation field is determined via the procedure outlined in Sec. 2.4.3 (implemented in custom code).
6. TB Hamiltonian is constructed including strain and polarisation fields as outlined above (implemented in custom code).
7. Diagonalising this TB Hamiltonian returns the energy eigenvalues and eigenstates of the disordered system (a Jacobi-Davidson method, JDQR, is used to calculate a selected number of eigenstates and eigenvalues of large sparse matrices in a numerically efficient manner [207]).

The electronic structure model established allows us to determine the energies and wave functions that are required to calculate the radiative and Auger recombination rates. Gaining insight into these rates will ultimately enable us to target questions about the IQE and the influence of carrier localisation. We proceed in the next chapter to describe a framework for achieving this, as well as discussing the screening of the polarisation field as carrier density increases.

Chapter 3

Calculating radiative and Auger recombination rates in a tight-binding framework

In the preceeding chapter we established that determining the electronic structure to an atomistic resolution while including strain, polarisation and carrier localisation effects is crucial for the analysis of c-plane III-N-based QWs. We now proceed within the TB framework detailed above, seeking a way to determine the radiative and Auger recombination rates entering the ABC model discussed above in Sec. 1.3. Doing so will allow us to gain insight into the competition between these processes, and subsequently their impact on the IQE. The framework described below can be applied generally, but we will highlight where the approach is specific to III-N systems or the TB model employed here. We will first discuss the determination of the rate of radiative recombination, before turning to the rate of Auger recombination, and finally, modifications to the framework to take into account carrier density dependent built-in field screening effects in III-N QWs.

3.1 Calculation of the radiative recombination rate

To gain insight into the IQE, as determined in the ABC model, we must determine the coefficient of spontaneous radiative recombination, B. The B coefficient is related to the rate of spontaneous radiative recombination per

unit volume per time, r_{sp} via $B = r_{\text{sp}}/(np)$, where n is the electron and p is the hole carrier density. We begin by deriving an expression for the total spontaneous radiative recombination rate in the active layer, R_{sp}. We mainly follow Ref. [208], but have modified the approach to connect it to our TB framework. To begin, we consider the transition rate between two discrete energy levels, E_i for an electron state in the conduction band and E_f for a hole state in the valence band.

We apply Fermi's Golden Rule to derive an expression for the transition probability per unit time (rate), $W_{i\to f}$, between such states [38, 208, 209]:

$$W_{i\to f} = \frac{2\pi}{\hbar} |\langle i| \hat{H} |f\rangle|^2 \rho(\text{E}) \delta(\hbar\omega - \text{E}_i - \text{E}_f) \ , \tag{3.1}$$

where $\rho(\text{E})$ is the density of photon states of energy $\text{E} = \hbar\omega$ per unit volume per unit energy, the δ-function ensures that the emitted photon obeys energy conservation and the modulus square of the interaction matrix element, $|\langle i| \hat{H} |f\rangle|^2 = |H_{if}|^2$, is given by

$$|H_{if}|^2 = \frac{e^2}{m^2} \frac{2\hbar}{\epsilon_0 n_r^2 \omega} \frac{1}{4} |\langle i| \mathbf{a} \cdot \mathbf{p} |f\rangle|^2 \ . \tag{3.2}$$

In Eq. (3.2), e is the electron charge, m is the electron mass, ϵ_0 is the vacuum permittivity, n_r is the refractive index of the material, ω is the frequency of the photon, $\mathbf{a}$ is a unit vector defining the light polarisation, $\mathbf{p}$ is a vector of the momentum operator for each direction, $\mathbf{k}$ is the photon wave vector, $\mathbf{r}$ is a position vector and we have made use of the dipole approximation [208]. The dipole approximation assumes that the extent of the carrier wave function is much smaller than the wavelength of emitted light, thus $\mathbf{k} \cdot \mathbf{r} \ll 1$ and so $e^{i\mathbf{k}\cdot\mathbf{r}} \approx 1$. It is a commonly used approximation given the wavelength of UV (100 – 280 nm) and visible (280 – 700 nm) light in comparison to the extent of carriers ($\sim$ 1 nm). The quantity $\rho(\text{E})$ is derived in detail in Ref. [208] and in general obtained by counting the number of emitted photon modes per volume per unit energy:

$$\rho(\text{E}) = \frac{n_r^3 \omega^2}{\pi^2 c^3 \hbar} \ , \tag{3.3}$$

where c is the speed of light in vacuum. The expression in Ref. [208] is given in terms of the speed of light in a medium, v_l, which is related to c and n_r by $v_l = c/n_r$. Lastly, we have included a factor of two to account for left and right

circular polarised light. Thus, overall the expression in Eq. (3.1) becomes

$$W_{i\to f} = \frac{4e^2 n_r \omega}{\epsilon_0 \hbar m^2 c^3} \frac{1}{4\pi} |\langle i| \mathbf{a}\cdot\mathbf{p} |f\rangle|^2 \delta(\hbar\omega - \mathrm{E}_i - \mathrm{E}_f) \ . \tag{3.4}$$

So far we have only considered linearly polarised light propagating in one direction. To take into account all possible polarisations over propagation directions, we average Eq. (3.4) over a sphere. Calculating the average over solid angles of $|\mathbf{a}\cdot\mathbf{p}_{if}|^2$ we find

$$\langle |\mathbf{a}\cdot\mathbf{p}_{if}|^2 \rangle_{\mathrm{av}} = \frac{4\pi}{3} |p_{if}|^2 \ , \tag{3.5}$$

where p_{if} are the so-called momentum matrix elements;

$$|p_{if}|^2 = (\langle i| \hat{p}_x |f\rangle)^2 + (\langle i| \hat{p}_y |f\rangle)^2 + (\langle i| \hat{p}_z |f\rangle)^2 \ .$$

Finally, using Eq. (3.5) in Eq. (3.4) we find that

$$W_{i\to f} = \frac{4e^2 n_r \omega}{\epsilon_0 \hbar m^2 c^3} \frac{|p_{if}|^2}{3} \delta(\hbar\omega - \mathrm{E}_i - \mathrm{E}_f) \ . \tag{3.6}$$

Following Ref. [208], to determine the total spontaneous radiative recombination rate we must sum over all possible energies of emitted photons. Thus we take the integral of Eq. (3.6) over all possible values of $\hbar\omega$:

$$\begin{aligned} W_{i\to j} &= \int_0^\infty d(\hbar\omega) \frac{4e^2 n_r \omega}{\epsilon_0 \hbar m^2 c^3} \frac{|p_{if}|^2}{3} \delta(\hbar\omega - \mathrm{E}_i - \mathrm{E}_f) \ , \\ &= \frac{1}{2} \int_{-\infty}^\infty d(\hbar\omega) \frac{4e^2 n_r \omega}{\epsilon_0 \hbar m^2 c^3} \frac{|p_{if}|^2}{3} \delta(\hbar\omega - \mathrm{E}_i - \mathrm{E}_f) \ , \\ &= \frac{2}{3} \frac{n_r e^2}{m^2 c^3 \epsilon_0} \frac{(\mathrm{E}_i - \mathrm{E}_j)}{\hbar^2} |p_{ij}|^2 \ . \end{aligned} \tag{3.7}$$

Determining the momentum matrix elements requires knowledge of the wave functions of states $|i\rangle$ and $|f\rangle$. In our case we will use the TB wave functions and employ the method developed in Ref. [183]. To do so we recast the momentum matrix elements as dipole matrix elements, $d_{ij} = \langle i| \mathbf{a}\cdot\hat{\mathbf{r}} |j\rangle$, where $\mathbf{a}$ is the light polarisation vector as before and $\hat{\mathbf{r}}$ is a vector of the position operators. To do so, as an illustration we first look component-wise at the commutator of the Hamiltonian, $\hat{H}_0$, of an electron in a periodic potential, V,

and the position operator for the x-direction. It can be shown that in general

$$\left[\hat{H}_0, \hat{x}\right] = \left[\frac{\hat{\mathbf{p}}\cdot\hat{\mathbf{p}}}{2m} + V, \hat{x}\right] = -\frac{i\hbar}{m}\hat{p}_x \ ,$$

given that $[\hat{A}\hat{B}, \hat{C}] = \hat{A}[\hat{B}, \hat{C}] + [\hat{A}, \hat{C}]\hat{B}$ and $[\hat{p}_x, \hat{x}] = -i\hbar$. Applying this result to our system above, described by the Hamiltonian $\hat{H}$, we can find that

$$-i\frac{\hbar}{m}\left\langle i\right|\hat{p}_x\left|j\right\rangle = \left\langle i\right|\left[\hat{H}, \hat{x}\right]\left|j\right\rangle = \left(\mathrm{E}_i - \mathrm{E}_j\right)\left\langle i\right|\hat{x}\left|j\right\rangle \ ,$$

where $|i\rangle$ and $|j\rangle$ are eigenstates of $\hat{H}$. Thus,

$$\left\langle i\right|\hat{p}_x\left|j\right\rangle = \frac{\left(\mathrm{E}_i - \mathrm{E}_j\right)}{-i\hbar}m\left\langle i\right|\hat{x}\left|j\right\rangle \ .$$

Similar expressions hold for $\hat{y}$ and $\hat{z}$ and so overall we have that

$$|p_{ij}|^2 = \frac{\left(\mathrm{E}_i - \mathrm{E}_j\right)^2}{\hbar^2}m^2|d_{ij}|^2 \ . \tag{3.8}$$

Substituting Eq. (3.8) back into Eq. (3.7) we find that the transition rate between states i and j is

$$W_{i\to j} = \frac{2}{3}\frac{n_r e^2}{c^3\epsilon_0}\frac{\left(\mathrm{E}_i - \mathrm{E}_j\right)^3}{\hbar^4}|d_{ij}|^2 \ .$$

To account for the temperature and carrier density dependence of the involved transition rates, the above expression is weighted by the factor $P_{ij}(n,p,T) = f_i^e(n,T)f_j^h(p,T)$, where f_i^e and f_j^h are Fermi factors that account for the occupation of states as temperature and carrier density vary. These factors are determined via Fermi-Dirac statistics [132]:

$$\begin{aligned} f_i^e(n,T) &= f^e(\mathrm{E}_i, n, T) = \frac{1}{1+\exp[(\mathrm{E}_i - \mathrm{E}_{fn}(n))/k_BT]} \ , \\ f_j^h(p,T) &= f^h(\mathrm{E}_j, p, T) = \frac{1}{1+\exp[(\mathrm{E}_{fp}(p) - \mathrm{E}_j)/k_BT]} \ . \end{aligned} \tag{3.9}$$

The quasi-Fermi levels, $\mathrm{E}_{fn}(n)$ and $\mathrm{E}_{fp}(p)$ for electrons and holes, respectively, depend on the electron, n, and hole, p, carrier densities, while k_B is the Boltzmann constant and T is the system temperature. To determine the quasi-Fermi levels the electron and hole carrier densities are used in conjunction with the volume of the active region to find the number of carriers

available to undergo recombination, N for electrons (or P for holes). Then, the expression

$$g(\mathrm{E}_{fn}) = \int f^e(\mathrm{E}, \mathrm{E}_{fn}) d\mathrm{E} - N$$

is minimised to determine E_{fn} for electrons and similarly for holes by replacing E_{fn} by E_{fp} and N by P. Thus, each f^α in Eq. (3.9) is a function of carrier density, n (or p), and temperature, T. In what follows we assume that the material is electrically neutral (i.e. that $n = p$) as is commonly done in other works [40, 210, 211].

Lastly, we sum over the available conduction and valence band states, taking into account the two possible spin states of the electrons, to find the total spontaneous radiative recombination rate:

$$R_{\mathrm{sp}} = 2\frac{2}{3}\frac{e^2}{\epsilon_0 c^3 \hbar^4} \sum_{i,j} P_{ij}(n,T) n_r(\lambda_{ij}) (\Delta \mathrm{E}_{ij})^3 |d_{ij}|^2 \ , \tag{3.10}$$

where $\Delta \mathrm{E}_{ij} = \mathrm{E}_i - \mathrm{E}_j$ and we have included the wavelength dependence of the refractive index, $n_r(\lambda_{ij})$, with $\lambda_{ij} = hc/\Delta \mathrm{E}_{ij}$. The wavelength/emission energy dependence of the refractive index is evaluated using a Sellmeier type description [212];

$$n_r(\lambda_{ij}) = \sqrt{A + \frac{B\lambda_{ij}^2}{(\lambda_{ij}^2 - C^2)}} \ ,$$

where the Sellmeier coefficients, A, B, and C, are material dependent. In the study of InGaN/GaN QWs below, we have used the Sellmeier coefficients of the GaN barriers, as has been done previously for InGaN/GaN systems in Ref. [212]. For GaN the values of these coefficients are $A = 5.15$, $B = 0.35$ and $C = 339.8$ nm [213]. For the study of AlGaN/AlN QWs we have used values for AlN reported in Ref. [213]: $A = 1.00$, $B = 3.12$ and $C = 138.0$ nm.

Once R_{sp} has been determined, the rate of spontaneous emission per unit volume ($r_{\mathrm{sp}}^{\mathrm{3D}}$) or unit (in-plane) area ($r_{\mathrm{sp}}^{\mathrm{2D}}$) of the well can be calculated via $r_{\mathrm{sp}}^{\mathrm{3D}} = R_{\mathrm{sp}}/V_{QW}$ or $r_{\mathrm{sp}}^{\mathrm{2D}} = R_{\mathrm{sp}}/A_{QW}$. In order to compare our results with reported experimental data we calculate both the sheet (2D) radiative recombination coefficient, $B_{\mathrm{2D}} = r_{\mathrm{sp}}^{\mathrm{2D}}/np$ where n and p are the sheet carrier densities for electrons (n) and holes (p) in units of cm^{-2}, and the volume (3D) radiative recombination coefficient, $B_{\mathrm{3D}} = r_{\mathrm{sp}}^{\mathrm{3D}}/np$ where n and p are the volume carrier densities for electrons and holes in units of cm^{-3}. A widely made assumption in the literature when modelling the recombination coefficients is that of charge neutrality in the well, i.e., that

$n = p$ [40, 210, 211]. We note that full LED structures in general employ multi-quantum well (MQW) systems which may lead to the situation of inhomogeneous current spreading between the wells under *electrical injection*, i.e., $n \neq p$. However, resonant optical excitation of (In,Ga)N QWs is often applied to gain insight into the fundamental properties of recombination processes. In such experiments the wavelength of the excitation light pulse is tuned to the band gap of a well so that carriers are directly excited within the well and not the barrier material. Under these conditions the assumption that $n = p$ is expected to be valid and provides an ideal set up to compare theory and experiment [66, 68].

As previously mentioned, the TB energies and wave functions determined in Sec. 2.4.3 are used to calculate the dipole matrix elements, or, in general, interaction matrix elements. In empirical atomistic models such as the TB framework employed here, the alloy "properties" (e.g. gradient in composition, random vs. clustered alloys, "bleeding" of atoms into the barrier material) are input to the calculation of the electronic structure. Thus, in general one requires some information about the alloy distribution which is usually based on experimental data. In line with experimental atom probe tomography (APT) data, the cation species in InGaN and AlGaN QWs are randomly distributed [26, 96, 214]. This approach is used elsewhere in the literature in empirical atomistic studies of random alloys [121, 122, 123, 124], and also in modified continuum-based approaches [41].

Building on such an assumption, our previous theoretical studies provided good agreement with experimental and other literature theoretical data on, for instance, low temperature FWHM values of InGaN QWs over a wide composition range [23]. Given that a large FWHM value at low temperatures in directly connected to fluctuations in the band gap of the well (thus, is affected by local alloy configurations), it is important to capture configurations that result in, for instance, strong carrier localisation effects and thus low band gap values. As such, one may find "extreme" alloy configurations that significantly deviate from, for example, special quasi-random structures often considered in DFT calculations [125]. The significance of these "extreme", or potentially, "outlier", configurations can be judged in several ways; (i) by analysing their total energy (e.g. are these configurations more unlikely than others), (ii) by their statistical significance, e.g. how often these configurations are found when studying a large number of random alloy configurations and (iii) by comparison with experimental studies. To give an example for (iii), if

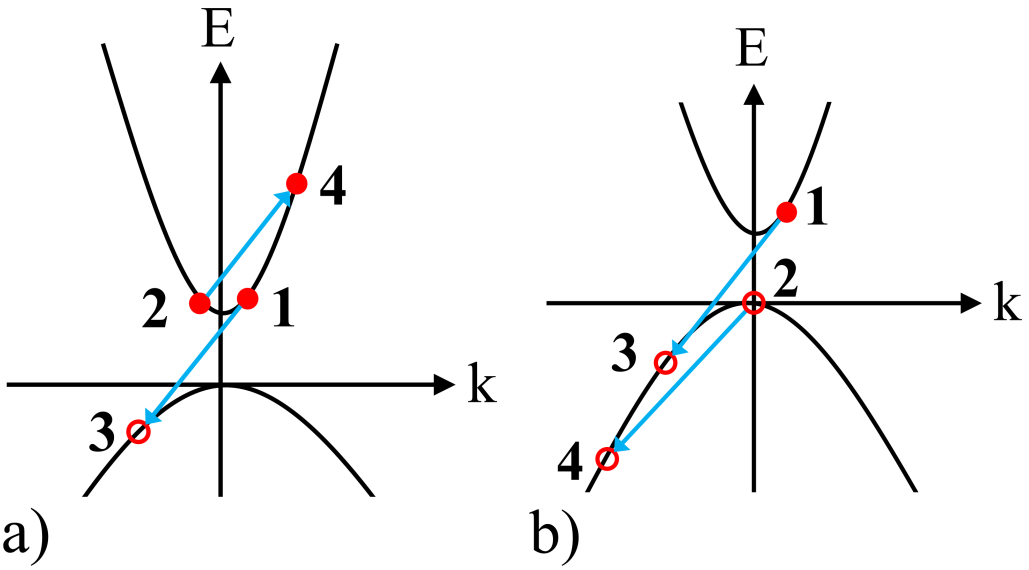


Figure 3.1: a) Schematic representation of the direct electron-electron-hole (eeh) Auger recombination process between electron states **1** and **2**, and hole state **3**. State **4** is an unoccupied electron state that the electron in state **2** is scattered into. b) Schematic representation of the direct hole-hole-electron (hhe) Auger recombination process between electron state **1** and hole states **2** and **3**. State **4** is an unoccupied hole state that the hole in state **2** is scattered into.

an "extreme" configuration leads to, for instance, faster radiative recombination in comparison to other configurations, then such a configuration can be expected to dominate the recombination processes, as it out performs the other processes and can provide a characteristic feature in, e.g., time resolved PL studies. Thus, even when one can study only a limited number of configurations, comparison with experimental data can shed light onto the importance of the different configurations randomly generated in the theoretical model. Therefore, we follow here the widely used assumption from the literature and investigate the impact of the alloy microstructure on the results by carrying out the calculations described above for a number of alloy configurations. For each configuration, the targeted carrier density and temperature are used to determine the quasi-Fermi level, as described above. Subsequently, the B coefficient is averaged over the number of investigated configurations.

3.2 Calculation of Auger recombination rate

As described above in Sec. 1.3, and illustrated schematically in Fig. 3.1, Auger recombination is a three particle process. Several Auger processes exist, including direct and indirect (phonon-assisted) [40], as well as trap/defect-assisted Auger recombination [63, 215]. We focus here on direct Auger recombination in the presence of alloy disorder (so-called alloy-enhanced direct Auger). It has been found theoretically that alloy disorder can increase the rate of direct Auger recombination in bulk InGaN, which is essentially negligible in the absence of alloy disorder [40]. The alloy-enhanced Auger recombination rate was also found to be larger in bulk InGaN compared to the phonon-assisted Auger rate in the band gap range of 1.9 – 3.0 eV, thus we expect that alloy-enhanced Auger recombination plays an important role in InGaN QWs too. For the study of AlGaN QWs with band gaps outside this range below, a similar analysis of the competition between alloy-enhanced direct Auger and indirect Auger recombination in bulk AlGaN or AlGaN QWs has not been reported. However, given the observation of carrier localisation effects in AlGaN QWs (see Sec. 1.4), we expect that the alloy-enhanced Auger process may also play an important role. Trap-assisted Auger recombination has recently been explored as an explanation for the large overall (i.e. sum of direct, indirect, alloy-enhanced, trap-assisted contributions) Auger rates observed experimentally but the nature and origin of the "trap" states has yet to be determined [63, 215]. Taking all of this together, we focus in the following on alloy-enhanced Auger, and other processes may be targeted in future studies.

As an illustration, in the follow analysis we focus on the eeh Auger process, noting that similar arguments hold for the hhe Auger process. In eeh Auger recombination an electron and hole pair recombine and interact with another electron, but rather than emitting a photon another electron is scattered into an energetically higher lying excited state. In order to calculate the rate of Auger recombination, we consider the interaction of the electrons via the Coulomb force to be a perturbation to the system. Building on Fermi's Golden Rule, introduced above, the transition rate between initial state i and final state j is determined. We mainly follow the approach of Ref. [40] but highlight changes due to the presence of alloy disorder.

Overall, the Auger recombination rate is given by

$$R = 2\frac{2\pi}{\hbar}\sum_{\mathbf{1234}} P(n,T)\left|M_{\mathbf{1234}}\right|^2 \delta\left(\mathrm{E_1}+\mathrm{E_2}-\mathrm{E_3}-\mathrm{E_4}\right) \ , \tag{3.11}$$

where the factor of 2 accounts for spin. In a semiconductor material where translational invariance is preserved, the bold indices denote both band index and $\mathbf{k}$-point. Given that random alloy fluctuations lead to strong carrier localization effects in InGaN/GaN QW systems [129, 203, 216], and similar effects have been observed in AlGaN/AlN QWs [217, 218], the alloy microstructure breaks the translational symmetry of the system so that the wave vector $\mathbf{k}$ is no longer a "good" quantum number. The δ-function assures energy conservation. The pre-factor

$$P(n,T) = f^e_{\mathbf{1}}(n,T) f^e_{\mathbf{2}}(n,T) f^h_{\mathbf{3}}(p,T) f^e_{\mathbf{4}}(n,T) \ ,$$

accounts for state occupations, and ensures that transitions only occur between occupied and empty states; f denotes the occupation number according to Fermi-Dirac statistics, as described above. The Coulomb interaction between carriers in different states, $\psi_{\mathbf{m}}$, is described by the matrix elements $M_{\mathbf{1234}}$ such that

$$\left|M_{\mathbf{1234}}\right|^2 = \left|M^d_{\mathbf{1234}} - M^x_{\mathbf{1234}}\right|^2 + \left|M^d_{\mathbf{1234}}\right|^2 + \left|M^x_{\mathbf{1234}}\right|^2 \ ,$$

where $M^d_{\mathbf{1234}}$ ($M^x_{\mathbf{1234}}$) are the direct (exchange) screened Coulomb matrix elements:

$$\begin{aligned} M^d_{\mathbf{1234}} &= \langle \psi_{\mathbf{1}}\psi_{\mathbf{2}} \left| W \right| \psi_{\mathbf{3}}\psi_{\mathbf{4}} \rangle \ , \\ M^x_{\mathbf{1234}} &= \langle \psi_{\mathbf{1}}\psi_{\mathbf{2}} \left| W \right| \psi_{\mathbf{4}}\psi_{\mathbf{3}} \rangle \ . \end{aligned}$$

The direct, screened Coulomb interaction (noting that similar arguments hold for the exchange term) may thus be written as:

$$M^d_{\mathbf{1234}} = \int\int d^3r d^3r' \psi^*_{\mathbf{1}}(\mathbf{r})\psi^*_{\mathbf{2}}(\mathbf{r}')\psi_{\mathbf{3}}(\mathbf{r}')\psi_{\mathbf{4}}(\mathbf{r}) \frac{e^2}{4\pi\epsilon_0\epsilon_\infty}\frac{e^{-\alpha|\mathbf{r}-\mathbf{r}'|}}{|\mathbf{r}-\mathbf{r}'|} \ . \tag{3.12}$$

The wave functions, $\psi_{\mathbf{m}}$, required for evaluating the above matrix elements are obtained from our TB model. Furthermore, when evaluating $M^\lambda_{\mathbf{1234}}$, with $\lambda = d$ or $\lambda = x$ for direct or exchange matrix elements respectively, we assume a position independent, and constant, background dielectric function [134]. For

the study of InGaN/GaN QWs below, we take the GaN barrier value, $\epsilon_\infty(\text{GaN}) = 5.5$, as has been done in Ref. [40]. This approximation is often applied in Auger matrix element calculations [219, 220]. In the study of 50% Al AlGaN/AlN QWs we use a 50/50 ratio of AlN and GaN of $\epsilon_\infty(\text{Al}_{0.5}\text{Ga}_{0.5}\text{N}) = 5.0$, based on a dielectric constant of $\epsilon_\infty(\text{AlN}) = 4.64$ for AlN. This value for AlN is determined from the average of the values reported in Ref. [221] for two theoretical investigations ($\epsilon_\infty^{\text{theo, a}}(\text{AlN}) = 4.61$; $\epsilon_\infty^{\text{theo, b}}(\text{AlN}) = 4.62$) and an experimental investigation ($\epsilon_\infty^{\text{exp}}(\text{AlN}) = 4.68$).

In Ref. [40], the inverse screening length α in Eq. (3.12) is determined separately for electrons (α_e), and holes (α_h), by using the Debye-Hückel equation:

$$\alpha_e = \sqrt{\frac{4\pi n e^2}{\epsilon_0 \epsilon_\infty k_B T}} \ ,$$
$$\alpha_h = \sqrt{\frac{4\pi p e^2}{\epsilon_0 \epsilon_\infty k_B T}} \ ,$$

where k_B is the Boltzmann constant, T is the temperature, ϵ_0 is the vacuum permittivity, n (p) is the electron (hole) carrier density and e is the elementary charge. The total inverse free-carrier screening length is then given by $\alpha^2 = \alpha_e^2 + \alpha_h^2$, which is used in Eq. (3.12).

To calculate $M^\alpha_{\mathbf{1234}}$, we largely follow the procedure detailed in Ref. [183] to obtain Coulomb matrix elements from TB wave functions. The TB wave functions may be written as:

$$\psi_{\mathbf{m}}(\mathbf{r}) = \sum_{\mathbf{R},\sigma} c^{\mathbf{m}}_{\mathbf{R},\sigma} \phi_{\mathbf{R},\sigma}(\mathbf{r}) \tag{3.13}$$

where $\phi_{\mathbf{R},\sigma}(\mathbf{r})$ are the localised, atomic-like orbitals, $\sigma = \{s, p_x, p_y, p_z\}$, located at a lattice site, $\mathbf{R}$, and $c^{\mathbf{m}}_{\mathbf{R},\sigma}$ are the expansion coefficients of the orbital σ at site $\mathbf{R}$. Equipped with this information, the matrix elements are evaluated as

$$M^d_{\mathbf{1234}} \ = \ \sum_{\mathbf{R},\mathbf{R}'} \sum_{\alpha,\beta} c^{\mathbf{1}*}_{\mathbf{R},\alpha} c^{\mathbf{2}*}_{\mathbf{R}',\beta} c^{\mathbf{3}}_{\mathbf{R}',\beta} c^{\mathbf{4}}_{\mathbf{R},\alpha} W(\mathbf{R} - \mathbf{R}') \ ,$$

with

$$W(\mathbf{R} - \mathbf{R}') = \frac{e^2}{4\pi\epsilon_0\epsilon_\infty} \frac{e^{-\alpha|\mathbf{R}-\mathbf{R}'|}}{|\mathbf{R} - \mathbf{R}'|} \ , \ \text{for} \quad \mathbf{R} \neq \mathbf{R}'$$

and

$$W(\mathbf{0}) = \frac{1}{v_{\text{tet}}^2} \int_{\text{tet}} \frac{e^2}{4\pi\epsilon_0} \frac{1}{|\mathbf{r} - \mathbf{r}'|} \approx W_0 \,, \text{ when } \mathbf{R} = \mathbf{R}' \,.$$

The on-site energy, W_0, can be calculated quasi-analytically, as described in Ref. [183], and in more detail in Appendix A, by integrating over a sphere of volume equal to that of the local tetrahedron formed by the nearest neighbors of an atom in a wurtzite unit cell. This approximation is widely used in determining the Coulomb matrix elements from TB wave functions [183, 222, 223, 224], building on the finding that in general the dominant contributions to the Coulomb matrix elements stem from the long-ranged part; therefore, the localised orbitals, $\phi_{\mathbf{R},\sigma}(\mathbf{r})$, underlying the TB model can be treated, in a first approximation, as point charges, and thus the explicit structure of the localised orbitals is of secondary importance [183, 222, 225, 226]. The impact of the on-site Coulomb energy, W_0, on the Auger rate is also discussed in more detail in Appendix A.

Finally, and following previous work on calculating the Auger rate in III-N materials [41, 227], the fourth state (**4**) in Eq. (3.11), into which the carriers can scatter, is always considered to be unoccupied. In addition to the pre-evaluated large number of electron and hole states (≥ 100 for each carrier type) calculated for the results presented below, we have also performed further calculations to investigate the impact of this energetically higher/lower lying (fourth) state on the results. Firstly, our calculations revealed a continuum of states (energy separation ≤ 0.5 meV) in the range of the magnitude of the band gap above (below) the conduction (valence) "band" edge. Testing Auger rates with different "final" fourth states from this continuum revealed that the specific choice of the fourth state was of secondary importance to the results when compared to the spread in values introduced by alloy fluctuations. Thus, a pre-calculated continuum state is used for each alloy composition investigated (10%, 15% and 25% for the study of InGaN QWs and 50% for the study of AlGaN QWs). Additionally, despite the existence of such a continuum of states, the energy conservation requirement in the Auger rate calculation, given by the δ-function in Eq. (3.11), is never exactly numerically satisfied. Therefore, the δ-function was replaced by a Gaussian function and the impact of the broadening parameter on the results was tested. These investigations showed that a broadening parameter of 1 meV is sufficient to achieve converged results, i.e., choosing a

smaller value did not change the results.

Equipped with this information, we obtain the Auger coefficients from the Auger rate, R, using $C = R/(Vn^3)$ (see Sec. 1.3). This is repeated for the two possible Auger recombination processes, eeh and hhe, also discussed above. Here, V is the volume of the well, and n is the carrier density. As was assumed for the determination of the radiative recombination rate, for all Auger recombination calculations we let $n = p$, i.e., we assume that the structure is electrically neutral, as is done in other works [40, 210, 211]. Unlike in the case of the radiative recombination rate above, we do not calculate sheet (2D) Auger recombination rates but only the volume (3D) Auger recombination rate, as this is the quantity most often reported in the experimental literature [69, 59, 170]. The total Auger rate is then calculated as $C_{\text{tot}} = C_{eeh} + C_{hhe}$.

As we have seen in our discussion of the calculation of the radiative and Auger recombination rates above, we expect that both rates will depend on temperature and carrier density. However, as we have discussed above in Sec. 1.4, as carrier density is increased in III-N heterostructures, the polarisation field will be screened, and as a result the electronic structure may also change. In the next section we will discuss this effect and a method we have developed to take this change into account.

3.3 Polarisation field screening

As we have previously discussed, c-plane III-N heterostructures exhibit strong built-in polarisation fields. These fields lead to the spatial separation of charge carriers on opposite QW interfaces, which is part of the so-called quantum confined Stark effect (QCSE) (see for example Fig. 1.8 in Sec. 1.4). However, the separation of electron and hole charge densities leads to an electric field pointing in the direction opposite to the built-in polarisation field. The potential arising from this "new" field counteracts the polarisation field, diminishing it, thus the introduction of charge carriers to the system "screens" the polarisation field. The screening of the polarisation field will depend on the charge (i.e. carrier) density, and can change the electronic structure of the QW significantly (e.g. reducing the spatial separation of carriers/QCSE).

For *low* carrier densities in III-N QWs, the TB model outlined above is sufficient to determine the electronic structure, as the impact of screening is

essentially negligible. As a result, it is possible to use the obtained single particle TB states and energies to calculate, e.g., radiative recombination rates [4], excitonic effects [228], or Auger recombination rates at low carrier densities [3]. However, at *higher* carrier densities this is no longer the case as the electrostatic built-in field will be noticeably screened. Theoretical and experimental works investigating InGaN/GaN QWs indicate that, for those systems, the screening effect becomes important at carrier densities on the order of $n = 1 \times 10^{19}$ cm^{-3} and above [229, 230, 231]. Similarly, it has been suggested in theoretical studies of AlGaN QW systems that screening effects become relevant above $n = 1 \times 10^{19}$ cm^{-3} [232]. Thus, a self-consistent approach is required to account for the screening of the built-in field and the change in the electronic structure.

However, as established above, to capture carrier localisation effects in III-N QWs, very large simulation supercells and an atomistic resolution are required, as provided by the TB model employed here. In general it is numerically extremely demanding to carry out such a self-consistent Schrödinger-Poisson calculation, but especially so in a TB framework, since it has to be performed for each carrier density and for a large number of electronic states when targeting, for instance, an investigation of Auger recombination rates in large supercells. To keep the information about alloy-induced carrier localization effects, but at the same time take built-in field screening effects into account, we proceed as follows.

We start from a one dimensional Schrödinger equation describing a wurtzite III-N QW grown along the c-axis:

$$\left[-\frac{\hbar^2}{2m_b}\frac{\partial^2}{\partial z^2} + U^b(z)\right]\psi(z) = \mathrm{E}_b\psi(z) \ , \tag{3.14}$$

where the confining potential $U^b(z)$ for electrons, $b = e$, or holes, $b = h$, is given by [233]

$$U^b(z) = U_0^b(z) + U_p^b(z) + U_{\mathrm{scr}}^b(z) \ . \tag{3.15}$$

The different contributions to $U^b(z)$ are the bare (band offset) confining potential, $U_0^b(z)$, the intrinsic (spontaneous and piezoelectric related) electrostatic potential, $U_p^b(z)$, and the screening potential $U_{\mathrm{scr}}^b(z)$, respectively. Here, $U_{\mathrm{scr}}^b(z)$ arises from the spatial separation of electron and hole wave functions in the well due to the presence of the intrinsic built-in field.

Following Haug and Koch [134], the screening potential is calculated via:

$$U_{\text{scr}}^{e,h}(z) = \pm\frac{e^2 n_{\text{sys}}}{2\epsilon_0\epsilon_r}\int dz' \left[|\psi^e(z)|^2 - |\psi^h(z)|^2\right]|z - z'|\,. \tag{3.16}$$

Eqs. (3.14) - (3.16) are evaluated self-consistently for a given carrier density, n_{sys}, within the well. We use band offsets, average strain fields, spontaneous and piezoelectric coefficients as well as effective masses from our TB model as input for Eqs. (3.14) - (3.16) for the studied c-plane III-N QW systems. Solving these equations self-consistently allows us to determine $U_{\text{scr}}^{e,h}(z)$ for a given carrier density, n_{sys}. As a result, one can determine by how much the intrinsic electrostatic built-in field is reduced at a given n_{sys}. This information is then fed back into the TB model by adjusting/scaling the built-in potential across the well and diagonalising the Hamiltonian for each carrier density n_{sys}. In doing so, we obtain, for a given n_{sys}, the (screened) TB wave functions and energies for the studied supercell, while still including local alloy contributions. The obtained wave functions and energies then form the input for the radiative and Auger recombination rate calculations detailed above.

We note that a similar screening approach has been used by Auf der Maur *et al.* [29], to study the impact of alloy fluctuations on the radiative recombination rate in c-plane InGaN/GaN QWs. Although we will return to the discussion of the impact of polarisation field screening on the electronic structure below, for InGaN and AlGaN QW systems we find that (i) we obtain an onset of the built-in potential screening at carrier densities similar to experimental and theoretical studies [229, 232] and (ii) the expected behavior of the electron and hole wave function separation is observed (i.e. that the separation decreases) with increasing carrier density. Thus, we expect that the above detailed approach is sufficient to capture the main effects of the built-in field screening on the results. Future studies can target a self-consistent 3D approach. Having established the theoretical framework used to determine the electronic structure in c-plane III-N QWs, along with the radiative and Auger recombination rates, we now present results for, in a first step, InGaN/GaN QWs, before turning to AlGaN/AlN QWs.

Chapter 4

Temperature dependent recombination in InGaN QWs

4.1 Introduction

In the preceding chapters we have discussed the ingredients of our theoretical framework that can be used to calculate the radiative and Auger recombination rates in c-plane III-N QWs. This framework accounts for effects unique to III-N systems, such as the strong built-in polarisation field, and accurately includes carrier localisation effects. With this framework established we seek to gain insight into the experimentally observed thermal droop in InGaN/GaN QWs [31]. To do so we need to understand the temperature dependence of the recombination processes, thus, our primary aim in this chapter is to investigate the temperature dependence of the radiative and Auger recombination rates in such systems. This will allow us to discuss the competition between these rates, and the impact that Auger recombination may have on the IQE of InGaN/GaN QWs, which are at the heart of modern short wavelength visible LEDs. Before doing so, in a first step, we will discuss the specifics of the QW model systems studied here. In a second step, and before looking at radiative and Auger recombination, we will investigate the impact of alloy disorder on the electronic and optical properties in general. Here we will look, for instance, at the density of states (DOS) and Stokes shift. Finally, we will turn to the temperature dependence of the radiative and Auger recombination rates.

4.1.1 QW model systems

In this and the following chapter discussing InGaN/GaN QW systems, we have targeted structures similar to those grown, and analysed experimentally, in Refs. [23] and [99]. Details of the model systems and experimental information can be found in Ref. [23], and here we only summarise the main points. The results for electronic and optical properties obtained from our TB model discussed above and in detail in Ref. [23] are in good agreement with low temperature experimental data, such as the photoluminescence (PL) peak positions and full width at half maximum (FWHM) values, on c-plane InGaN/GaN QWs with In contents ranging from 5% up to 25% [23]. All calculations have been carried out on simulation cells with a size of $(10 \times 9 \times 10)$ nm^3, with periodic boundary conditions; the system corresponds to $32 \times 32 \times 20$ wurtzite unit cells. For all of these studies the assumption of a random alloy has been made, in agreement with general atom probe tomography results on c-plane InGaN/GaN QWs [234], and as discussed above in more detail in Chapter 1. For the study of DOS, absorption, Stokes shift and radiative recombination rate, we have generated 125 microscopic In alloy distributions, in order to investigate the impact of alloy microstructure on the results.

Subsequently, in the study of Auger recombination, due to computational expense we have carried out the analysis for 10 microscopic configurations. In our model we also allow for the "bleeding" of In atoms into the GaN barrier. However, we restrict this penetration of In atoms into the barrier material to a disc-like region with a height of 2 monolayers (ML), and a width of approximately 5 nm, following the experimental and theoretical work of Refs. [103], [129], and [203]. Given that we assume a random alloy distribution of the In atoms in the QW region, the actual "shape" of the structural inhomogeneities (well width fluctuations) vary between different microscopic alloy configurations. For the following study of temperature dependent radiative and Auger recombination rates, along with absorption coefficients, DOS and Stokes shift, we have calculated 100 electron and 100 hole states closest to the respective band edges (i.e. the energetically lowest lying states). We note that the temperature dependence in the calculations arises from the population of states via Fermi-Dirac statistics described above in Sec. 3.1; the TB parameters are kept at their values determined by fitting to DFT band structures which are effectively calculated at zero temperature.

Future studies could also target temperature dependent TB parameters. In the calculation of Auger coefficients, a further temperature dependence is introduced via the temperature and carrier density dependent screening length described as above in Sec. 3.2.

As discussed in the preceding chapter, in general, the introduction of charge carriers into the QW will tend to screen the polarisation field, however in the following we have targeted a relatively low carrier density in line with the experimental study in Ref. [34], which has also been investigated theoretically in Ref. [46]. Our calculations have been carried out at a fixed carrier density of $n_{3D} = 3.8 \times 10^{18}$ cm^{-3} (corresponding to a sheet carrier density of $n_{2D} = 1.2 \times 10^{12}$ cm^{-2}). For this relatively low carrier density we have performed initial, self-consistent, one-dimensional Schrödinger-Poisson calculations which show that the screening of the built-in field (i.e. its reduction) is of secondary importance. This approximation is supported by the experimental and theoretical works of Refs. [229], [231], and [230]. Furthermore, we have tested several configurations with such a reduced (i.e. screened) field and found that the screening of the intrinsic (spontaneous and piezoelectric) built-in field only affected the ground and excited electron and hole states by less than 24 meV (most often by only $\approx$ 3 – 5 meV).

However, the screening of the built-in field may affect states near the band edges (e.g. localised hole states) differently to energetically higher lying states, which may exhibit a more delocalised character (see Ref. [130] for more details on the distribution of localised, "semi-localised" and delocalised states). To analyse this situation in more detail, while taking into account the numerical expense of these calculations, we have evaluated the Auger coefficient at a temperature of 300 K for one configuration with and without the built-in field screening. In such a higher temperature calculation not only energetically lower lying states but also excited states will become relevant, which provides insight into the impact of the screening on the energetically higher lying states (both valence and conduction states). This study revealed that the results differed by less than 8%. Overall, this difference is regarded as not only smaller than the uncertainties in some of the material parameters entering the calculations (e.g. the dielectric constants), but also smaller than variations introduced by the alloy microstructure. Furthermore, the calculations by David *et al.* [235, 236] show that the Coulomb enhancement of the radiative recombination rate is of secondary importance for a carrier density of $n_{3D} = 3 \times 10^{18}$ cm^{-3}. Thus, we directly use the TB wave functions

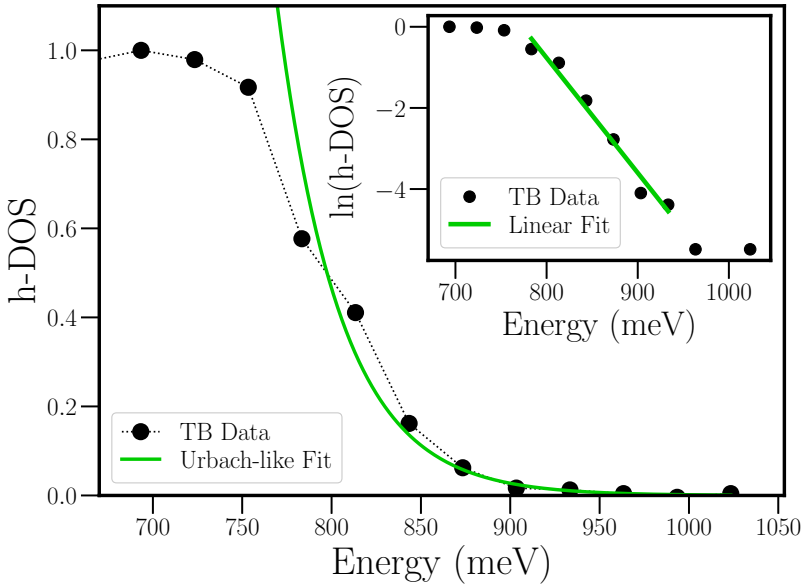


Figure 4.1: Hole density of states (h-DOS) for an $In_{0.25}Ga_{0.75}N$/GaN well. Black circles: tight-binding data; green solid line: fit to the data based on an Urbach-type model (see main text for details). Inset: natural logarithm of the data from the main figure, indicating the region used for the fitting of the Urbach-type model. Zero of energy is the unstrained GaN valence band edge.

(without Coulomb enhancement or built-in field screening effects) when calculating the C and B coefficients.

4.2 Results

Before discussing the temperature dependence of the radiative and Auger recombination rates in InGaN/GaN QWs, we first discuss the impact of carrier localisation on general features which allows us to connect our theory results to experimentally measurable quantities in these systems. In particular, we look at the density of hole states (h-DOS), as this provides insight into the energy range over which localisation effects are important. In a second step we discuss the broadening of the absorption edge, also due to the presence of localised states, and the Stokes shift, which is the difference in PL peak energy and absorption edge energy.

4.2.1 Impact of localisation on optical properties

In Sec. 1.4 we discussed that the presence of localised states in a QW system introduces an exponential tail to the ideally "step-function"-like DOS (in a

homogeneous QW, see Fig. 1.10). With this in mind, we now turn to the results from our theoretical framework that accounts for carrier localisation. Figure 4.1 shows, as an example, the calculated h-DOS for an InGaN/GaN QW with 25% In. To calculate the h-DOS, hole state energies from all 125 configurations are collected and sorted, before being counted into energy "bins" to find $N(E)$ where N is the number of hole states in the energy bin from E to $E + \Delta E$, where ΔE is the size of the bin. For the 5% and 10% In systems, a bin size of $\Delta E = 20$ meV is used, while for 15% and 25% In, the bin size is $\Delta E = 30$ meV. Lastly, we calculate dN/dE to find the DOS. The TB data is denoted by the solid black circles and indicates the departure from an ideally "step-function"-like DOS of a homogeneous QW; the presence of tail states is observed for energies larger than approximately 750 meV. In all calculations, the zero of energy is the valence band edge of unstrained GaN. Random alloy fluctuations and the resulting fluctuations in strain and (macroscopic and local) built-in potentials lead to the situation that the valence "band" edge varies with position across the QW structure; the h-DOS then includes a contribution from all these factors. For our analysis primarily the evolution of the h-DOS (shape of the curve) with energy is important. An Urbach-like exponential decay of the h-DOS of the form

$$\text{h-DOS}(E) = A \exp\left(\frac{E_0 - E}{E_{\text{tail}}}\right) , \tag{4.1}$$

which is assumed in many studies [237], is confirmed through the plot of the natural logarithm of the data, as shown in the inset of Fig. 4.1. In Eq. (4.1), A, E_{tail} and E_0 are free fitting parameters. The TB data is again given by solid black circles and the green solid line is a fit to the region in which the natural logarithm of the TB data changes linearly with energy (above 750 meV). From the slope of the solid green line we extract the characteristic tail energy, E_{tail}, from

$$\ln\left(\text{h-DOS}(E)\right) = \left(\frac{1}{E_{\text{tail}}}\right)(E_0 - E) + \ln\left(A\right) \ .$$

Using this information, the solid green line in the main part of Fig. 4.1 yields a very good description of the h-DOS calculated from our atomistic model. The same analysis has been carried out for all considered In contents (5%, 10%, 15%, 25% In) and provides an equally good description (not shown).

Figure 4.2 displays the extracted tail state energies, E_{tail}, as a function of the In content, x, and reveals an increase in E_{tail} with increasing x. For the 25% In

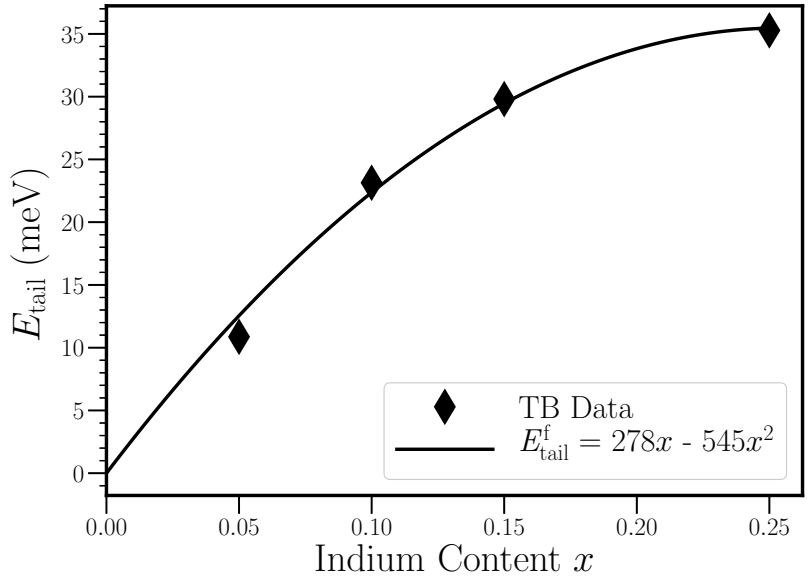


Figure 4.2: Tail state energies, E_{tail}, as a function of the In content, x, in $\text{In}_x\text{Ga}_{1-x}\text{N}$/GaN quantum wells. The black diamonds are the tight-binding data and the black solid line gives a fit, $E^{\text{f}}_{\text{tail}} = ax - bx^2$, with the coefficients a and b given in figure.

case, E_{tail} reaches a value of over 30 meV. However, even for the low 5% In content well, a tail state energy of around 10 meV is found. We also note that the rate of increase in E_{tail} in the 5% to 15% In content range is larger than that in the 15% to 25% In content range, despite the In content difference being equal (Δx = 0.1). In order to estimate tail state energies for other In contents we use $E^{\text{f}}_{\text{tail}}(x) = ax - bx^2$ to fit the TB results (solid black line), which gives a good description of the data.

While this analysis provides insight into the broadening of the h-DOS, it cannot be directly measured or validated against experimental data. However, the presence of tail states in the DOS leads to a broadening of the absorption spectrum, which is widely observed in experiment, and characterised by the so-called Urbach energy (which is distinct from the tail energy E_{tail} above) [105, 170, 238]. Thus, building on our calculations of the DOS, we evaluate the absorption spectra of our InGaN/GaN QWs via $\alpha'(h\nu) \propto \sum_{i,j} |d^{e,h}_{ij}|^2 \Theta\left(h\nu - E_{e,i} - E_{h,j}\right)$ [103], where $E_{e,i}$ ($E_{h,j}$) is the electron (hole) eigenenergy of state i (j) and $d^{e,h}_{ij} = e\langle\psi^e_i|\mathbf{a}\cdot\mathbf{r}|\psi^h_j\rangle$ are the dipole matrix elements; e is the elementary charge, $\mathbf{r}$ is the position operator, and $\mathbf{a} = 1/\sqrt{3}(1,1,1)$ is the light polarisation vector. As discussed in Sec. 3.1, the dipole matrix elements have been directly calculated employing the TB wave

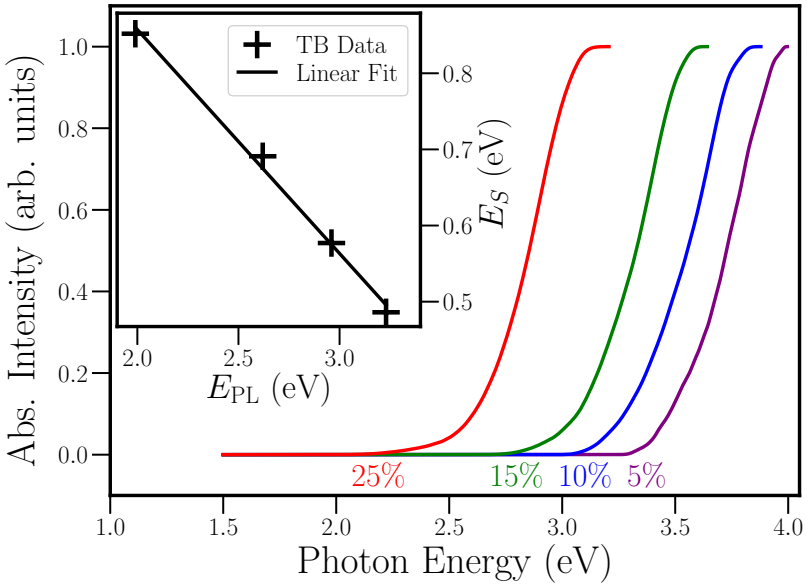


Figure 4.3: Calculated absorption spectra for $In_xGa_{1-x}N$/GaN quantum wells with 5% (violet line), 10% (blue line), 15% (green line) and 25% (red line) In content. Inset: Stokes-shift energies, E_S, as a function of the PL peak energies, E_{PL}.

functions [183]. The absorption spectrum, $\alpha'(h\nu)$, is evaluated for each of the 125 different microscopic configurations per In content (5%, 10%, 15%, 25%) using 100 electron and 100 hole TB states.

Figure 4.3 displays the final spectra, which are obtained by averaging over the 125 configurations per In content x. These spectra reflect the experimentally well known broadening, which is often described by a sigmoidal function [105, 238]:

$$\alpha'(h\nu) = \frac{\alpha_0}{1 + \exp\left(\frac{h\nu - E_{\mathrm{a}}}{E_{\mathrm{u}}}\right)} \,. \tag{4.2}$$

In Eq. (4.2), E_{u} is the characteristic, or Urbach, tail energy, and E_{a} is the absorption edge energy. Using the above expression to fit the TB data displayed in Fig. 4.3 enables the extraction of E_{u} and E_{a} as functions of the In content, x. The obtained E_{u} and E_{a} values are summarised in Table 4.1. E_{u} values on the order of 90 - 100 meV are found, which do not show much variation as In content, x, increases. The extracted absorption edge energies, E_a, decrease with increasing x, given that InN has a lower band gap than GaN. Equipped with this information and having previously calculated (low T) PL peak energies, E_{PL} [23], which are summarised in Table 4.1, we can calculate the Stokes shift, E_S, as a function of In content, x, via $E_S(x) = E_{\mathrm{a}}(x) - E_{\mathrm{PL}}(x)$ [103]; these results are presented in Table 4.1. In the

Table 4.1: Absorption edge energy (E_{a}), low temperature photoluminescence peak energy (E_{PL}), Urbach tail energy (E_{u}), and Stokes shift (E_S) for $In_xGa_{1-x}N$/GaN QWs with varying In contents extracted from a sigmoidal model. E_{PL} have been taken from Ref. [23].

In content	E_a (eV)	E_{u} (meV)	E_{PL} (eV)	E_S (meV)
5 %	3.72	95.5	3.23	490
10 %	3.54	103.6	2.96	580
15 %	3.31	98.3	2.62	690
25 %	2.84	94.2	1.99	850

experimental study of Ref. [105], a Stokes shift energy of E_S = 830 meV is reported for a well with a PL peak energy of E_{PL} = 1.96 eV. The $In_{0.25}Ga_{0.75}N$ QW studied here has a PL peak energy of E_{PL} = 1.99 eV and a Stokes shift of E_S = 850 meV, thus, is in good agreement with the experiment [105]. The experimentally observed linear increase of E_S with decreasing E_{PL} is reflected in our data (cf. inset of Fig. 4.3).

4.2.2 Radiative recombination

Having discussed the h-DOS, absorption spectra, and Stokes shifts of InGaN/GaN QWs for a wide In content range, and thus emission wavelength range, we now turn to the discussion of the temperature dependence of the radiative recombination rate. Figure 4.4 displays our calculated B_{2D}(T) for QW systems with 10%, 15%, and 25% In, averaged over 125 microscopic configurations, along with the experimental data from Ref. [34]. Several factors are important to note when looking at the experimental data in comparison to our theoretical results. Firstly, it should be noted that in the experimental study of Ref. [34], B_{2D} values are extracted by fitting A, B and C coefficients simultaneously. Thus, different combinations of A and C values may affect the extracted B_{2D} values. On the theoretical side we have not targeted the specific QW structures analysed in Ref. [34] in terms of In content or well width. Therefore, a one-to-one comparison is not possible and not targeted. However, in general the comparison between our theoretical results and the experimental data from Ref. [34] provides a good initial reference frame to investigate *trends* in the evolution of B_{2D} with increasing temperature T.

Overall, we find the expected trend that for a given temperature, B_{2D} decreases with increasing In content, x. This stems from two factors. Firstly, as our assumed QW model systems were targeting the InGaN QW systems

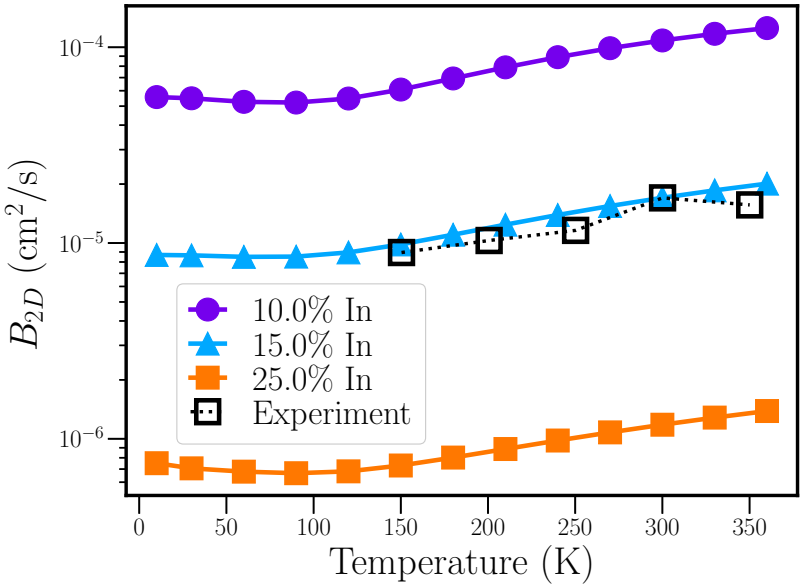


Figure 4.4: Radiative recombination rate B_{2D} in $In_xGa_{1-x}N$/GaN wells as a function of temperature and alloy composition at a carrier density $n = p = 1.2 \times 10^{12}$ cm^{-2}. 10% In (purple filled circles), 15% In (blue filled triangles), 25% In (orange filled squares), and experimental data from Ref. [34] (black open squares). The data are averaged over 125 microscopic configurations.

studied in Refs. [23] and [99], the well width increases slightly with increasing x. Secondly, a higher In content leads to a stronger piezoelectric field, since this quantity is strain dependent, as discussed in Sec. 1.4. The combination of these two factors leads to a stronger quantum confined Stark effect, and thus a stronger spatial separation of electron and hole wave functions, which reduces the spontaneous emission rate and thus B_{2D}.

Furthermore, Fig. 4.4 shows that for all three In contents, B_{2D} (slightly) increases with increasing T. The extremely good agreement between theory and experiment should be regarded as a coincidence, following our discussion of, for instance, the structural properties above. Nevertheless, given that independent of the In content considered in the calculations the same trend is reflected, our theoretical model captures the main effects observed in the experiment. This result is achieved *without* assuming In atom clustering in the QW and so is in contrast to Ref. [46], where In atom clustering is *essential* to model an increasing B_{2D} with increasing T; in the random alloy case, the data in Ref. [46] shows a *decrease* in B with increasing T. Our presented results are fully consistent with the experimental observation of a random In atom distribution in InGaN/GaN QWs while still predicting the experimentally observed trend of increasing B_{2D} with T.

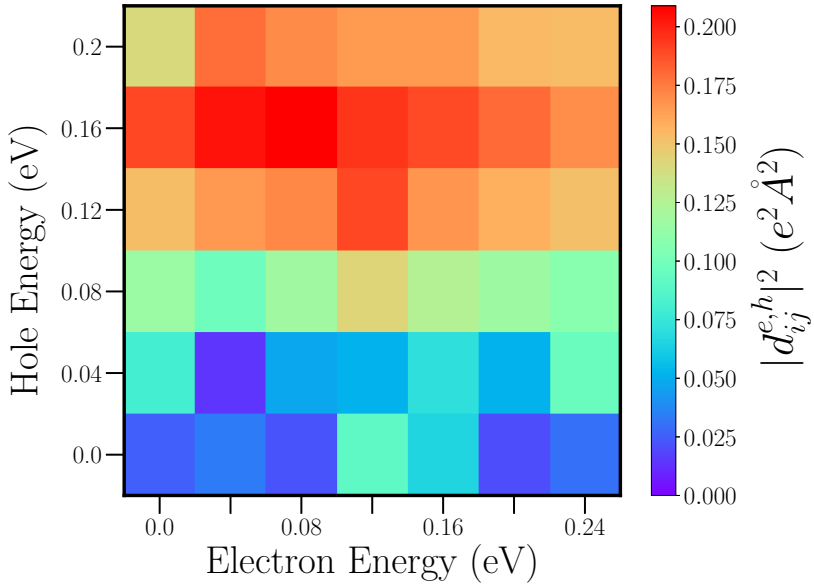


Figure 4.5: Energy resolved dipole matrix elements, $|d_{ij}^{e,h}|^2$, for an $In_{0.1}Ga_{0.9}N$/GaN well. Energies are given with respect to the "band" edges. More details are given in the main text.

The cause of the above discussed trend in B_{2D} with T can be traced back to the changes in the magnitude of the dipole matrix elements between electron and hole states when populating energy levels further away from the "band" edges. Figure 4.5 displays $|d_{ij}^{e,h}|^2$ as a function of electron and hole state energies relative to the conduction and valence "band" edges; the In content in the well is 10%. The results from the 125 different configurations are collated and grouped into energy bins of width 40 meV and averaged over the number of elements in each bin. The bottom left corner of Fig. 4.5 corresponds to dipole matrix elements between states near the "band" edges, that are strongly localised states and which contribute mainly at low temperatures and carrier densities. Energetically higher lying states, exhibiting larger dipole matrix elements, are populated as T increases thus resulting in the observed increase of B_{2D} with T in Fig. 4.4.

The above analysis shows that the unusual temperature dependence of B_{2D} stems from carrier localisation, and thus indicates that an accurate description of these effects is key. The description of alloy fluctuations and connected carrier localisation effects may noticeably vary between different models, even within the same theoretical framework. In TB models, one factor is for instance how local built-in potential fluctuations are treated. TB models which include or exclude local field fluctuations may predict different carrier

localisation characteristics; these differences will be further compounded by differences in TB parameters [23]. Similar but also different aspects come into play in modified continuum-based models, in which, for example, the local In content is obtained by an averaging procedure [41]. This leads to a coarser spatial resolution in comparison to an atomistic model and may lead to different spatial localisation characteristics and deviations in energies of the electron and hole states when compared to an atomistic model.

We also note that, for instance, the observed slight increase in B_{2D} with temperature may be dependent on the carrier density. With increasing carrier density the localised states may then be occupied so that the B_{2D} could become temperature independent. Furthermore, given that in the experiment B_{2D} is extracted by fitting A and C coefficients simultaneously, further investigations of, for instance, how C changes with temperature and carrier density are important. To answer this question from a theory perspective we discuss in the next section the temperature dependence of the C coefficient. Equipped with information on the temperature dependence of B and C we then target the competition between these processes to gain insight into the thermal droop.

4.2.3 Auger recombination

As discussed above in Sec. 3.2, the theoretical framework above allows us to investigate the *alloy-enhanced* electron-electron-hole, C_{eeh}, and hole-hole-electron, C_{hhe}, Auger coefficients; the total Auger coefficient, C_{tot}, is then obtained via $C_{\text{tot}} = C_{eeh} + C_{hhe}$. Phonon-assisted Auger processes are not considered since the DFT calculations in Ref. [40] show that (i) Auger processes can be significantly enhanced by alloy fluctuations and that (ii) in the band gap range of approximately 1.9 - 3.0 eV, which corresponds to the ground state transition energies of the QW structures studied here, contributions from phonon-assisted Auger processes are smaller compared to the alloy-enhanced scattering effects. Thus, it can be expected that alloy-enhanced Auger recombination is the dominant contribution in the InGaN-based QWs investigated here. As mentioned above, due to the large computational expense in calculating Auger coefficients (compared to, for instance, radiative recombination coefficients), we target now 10 randomly selected microscopic alloy configurations, in contrast to the 125 investigated for the calculation of the B coefficient above.

As already mentioned above, we are interested in the temperature dependent

competition between the radiative and Auger recombination processes, thus we consider a relatively low carrier density of $n_{3D} = 3.8 \times 10^{18}$ cm^{-3}. As such it is justified to take the TB wave functions directly as input for the Auger recombination rate calculation framework detailed in Chapter 3. However, we note that while the wave functions are directly taken from the TB model, a carrier density dependent Debye screening length for the Coulomb interaction between the carriers has been taken into account (see Eq. (3.12) in Sec. 3.2 above). Moreover, previous studies indicate that a carrier density of $n_{3D} = 3.8 \times 10^{18}$ cm^{-3} is not large enough to saturate the localised hole states in InGaN-based QWs with 10%, 15%, and 25% In [239]; electrons are far less strongly affected by alloy fluctuations and exhibit a more delocalised wave function character [130]. Therefore, one can still expect that carrier localisation effects will impact the Auger recombination processes in the systems studied here.

Equipped with all this information, Figs. 4.6 a) and 4.6 b) display the evolution of the alloy-enhanced C_{eeh} and C_{hhe} Auger coefficients, respectively, as a function of temperature, T, for the different In contents considered; as already highlighted above, the carrier density is fixed at $n_{3D} = 3.8 \times 10^{18}$ cm^{-3}. The data are averaged over the 10 different microscopic configurations per In content; error bars indicate the *maximum/minimum* value of C_α ($\alpha = \{eeh, hhe\}$) at a given T. The reason for using the min/max values is to highlight that the magnitude of the predicted coefficients may strongly depend on the alloy microstructure. Therefore, using just a single alloy configuration to evaluate Auger coefficients may over- or underestimate these coefficients. Overall, we observe that the C_{eeh} coefficients increase with increasing T, Fig. 4.6 a), while the C_{hhe} coefficients show a weak T dependence or (slight) decrease, Fig. 4.6 b). Furthermore, Figs. 4.6 a) and b) reveal that, independent of temperature and In content, C_{hhe} is greater than C_{eeh} (note the different scales in Figs. 4.6 a) and b)).

To gain further insight into the relative contributions from C_{eeh} and C_{hhe} to C_{tot}, a detailed break-down is presented in Fig. 4.6 c). As already discussed above, in general, the contribution from C_{eeh} to C_{tot} is smaller relative to the contribution from C_{hhe}. For all considered In contents, C_{hhe} makes up $\gtrapprox 99\%$ of C_{tot}, independent of T. This finding is consistent with previous *theoretical* studies [40, 41]. There are very few *experimental* studies that aim to determine the relative contributions from C_{eeh} and C_{hhe} to C_{tot} however the studies of Ref. [67] and [240] suggest that C_{eeh} should be larger than C_{hhe} by a factor of

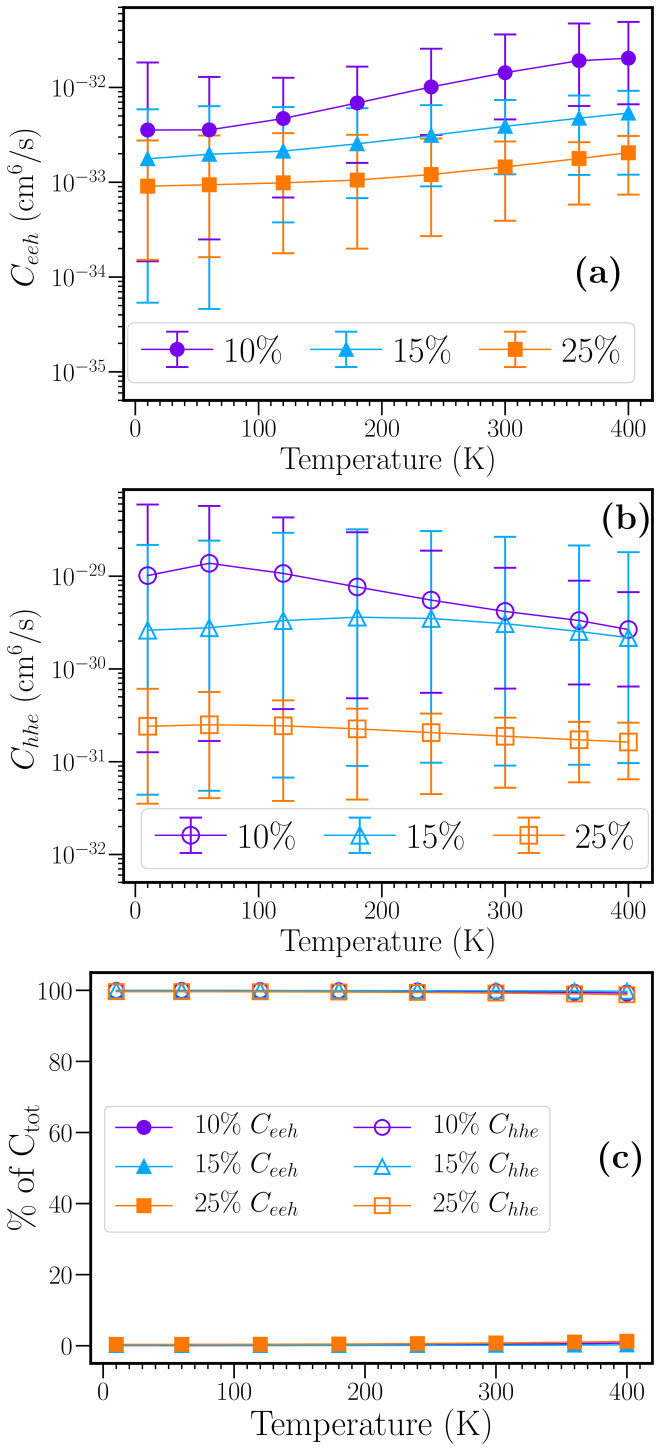


Figure 4.6: a) Electron-electron-hole, C_{eeh}, and b) hole-hole-electron, C_{hhe}, Auger coefficients as a function of temperature for c-plane InGaN/GaN quantum wells with different In contents (10%, 15% and 25%). The data, averaged over 10 microscopic alloy configurations, are given by the filled symbols; error bars indicate maximum and minimum values of C_{eeh} at a given temperature. The carrier density is fixed at $n_{3D} = 3.8 \times 10^{18}$ cm^{-3}. c) Percentage break-down of the contribution from C_{eeh} and C_{hhe} to the total Auger coefficient, C_{tot}.

1 – 12. However, the approach used in both experimental studies does not take into account the carrier density dependence of the Auger coefficients.

Having discussed the relative contributions from C_{eeh} and C_{hhe} to the total Auger coefficient, C_{tot}, in the next step we focus on the interplay of the alloy microstructure, temperature and In content. Starting with C_{hhe}, Fig. 4.6 b) shows that the Auger coefficient decreases with increasing In content as one may expect due to the increasing (piezoelectric) built-in field. A stronger built-in field will result in stronger spatial separation of the electron and hole wave functions, which thus will affect the Coulomb matrix elements determining the Auger rate. We note, however, that there is a large "spread" in the Auger coefficients due to the alloy microstructure; we will come back to this aspect below. Turning to C_{eeh}, Fig. 4.6 a), we find a similar trend: with increasing In content C_{eeh} decreases, also due to the increasing built-in field.

We now turn to the impact of the alloy disorder and temperature on the results. The error bars in Figs. 4.6 a) and b) give insight into the importance of the alloy microstructure for the Auger coefficients. We observe that with increasing T the "spread" in both C_{eeh} and C_{hhe} coefficients, in general, decreases. We attribute this to the effect that at low temperatures only states near the conduction and valence "band" edges are populated by the carriers. These are strongly localised states [130] and the wave function overlap between them may strongly depend on the alloy microstructure. As the temperature is increased, the carriers start to populate states where the corresponding wave functions are more delocalised compared to the "band" edge states. This has three consequences: (i) in general, the wave function overlap between electron and hole wave functions along the growth direction is (slightly) increased, (ii) in contrast, potential contributions from locally strongly overlapping hole wave functions due to carrier localisation effects are reduced and (iii) for these more delocalised states the alloy fluctuations present a weaker perturbation and the wave function overlap is less dependent on the alloy disorder. A similar effect is seen for the B coefficient above and illustrated by the dipole matrix elements shown in Fig. 4.5. As shown in Figs. 4.6 a) and b), consequences (i) and (ii) lead to opposite effects, with C_{eeh} slightly increasing with increasing temperature while C_{hhe} (slightly) decreases with increasing temperature. Furthermore, consequence (iii) results in the situation that the importance of the alloy microstructure is reduced with increasing temperature and thus the "spread" in both the C_{eeh} and C_{hhe} coefficients decreases.

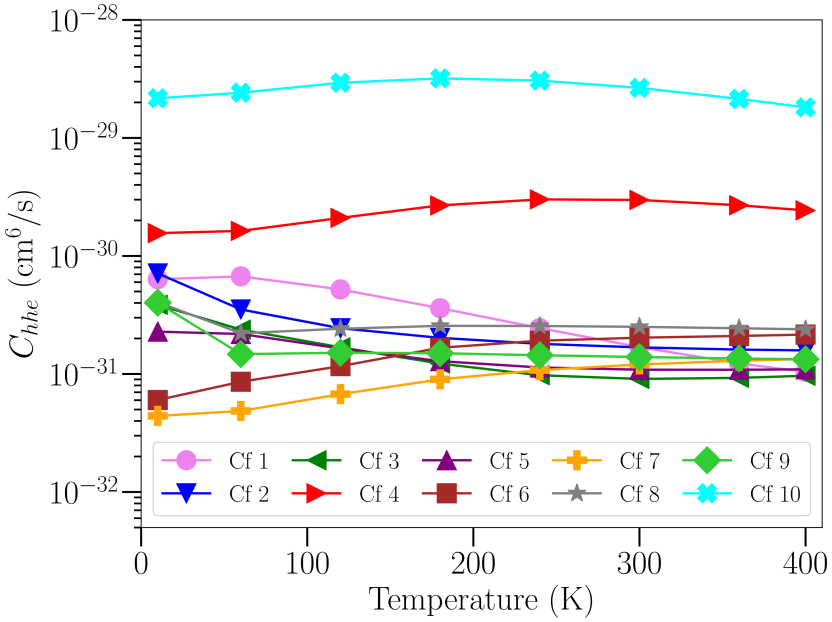


Figure 4.7: Hole-hole-electron Auger coefficient, C_{hhe}, as a function of temperature for 10 different microscopic alloy configurations of an $In_{0.15}Ga_{0.85}N$/GaN quantum well at a fixed, low carrier density of $n = 3.8 \times 10^{18}$ cm^{-3}.

However, for the 15% In QWs we find that even at higher temperatures there is still a noticeable spread in the Auger coefficient values. As previously shown, for instance in Ref. [130], the interplay of the built-in field, structural inhomogeneities and the alloy microstructure can affect the wave function localisation. When breaking the 15% In QW average C_{hhe} coefficient down into the contributions from individual configurations, we find 8 configurations which exhibit very similar C_{hhe} values while two configurations result in much higher values. Figure 4.7 summarises data on C_{hhe} as a function of temperature for the QW system with 15% In studied here.

To gain further insight into how the Auger coefficient value, C_{hhe}, is related to the electronic structure, Fig. 4.8 shows the C_{hhe} coefficients for the different alloy configurations with respect to their valence "band" edge, i.e., the lowest hole ground state ("GS", filled symbols) and first excited hole state ("1st", open symbols) energy at 10 K. As one can see from this plot, the two configurations (Cfs. 4 and 10) with the highest Auger coefficient values have the highest valence "band" edge (lowest hole ground state) energy. Such a high valence band energy value is indicative of strong carrier (hole) localisation effects [130]. We also find that the next valence states (first excited hole state), for both Cfs. 4 and 10, have energies larger than the valence "band" edge energy of most of the remaining 8 configurations. This indicates that not

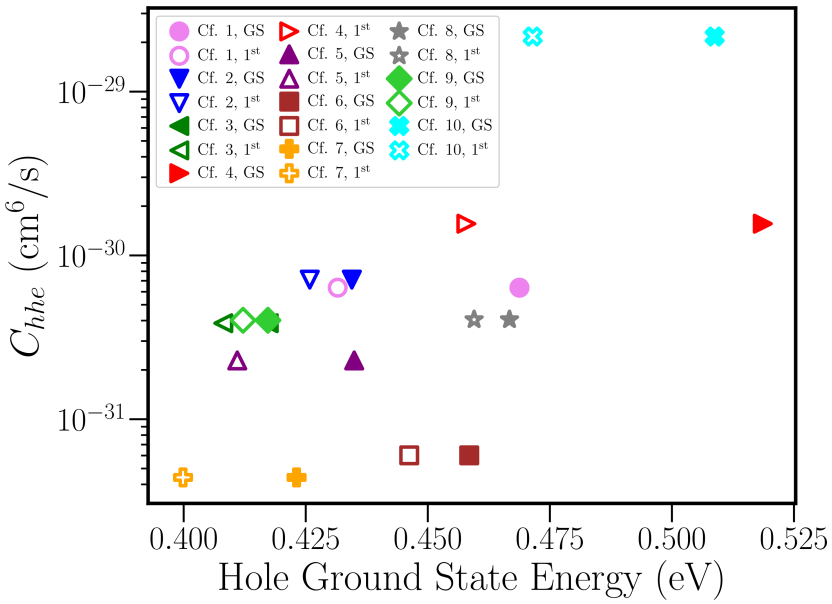


Figure 4.8: Auger coefficient, C_{hhe}, as a function of the valence "band" edge energy (hole ground state energy, GS, filled symbols) and the first excited state (1st, open symbols) for the 10 different alloy configurations of the 15% In quantum well system.

only the hole ground state/valence "band" edge state but also excited states exhibit strong localisation effects. So, even at elevated temperatures, contributions from strongly localised states to the Auger coefficients can arise. Given the elevated nature of the Auger coefficients associated with Configs. 4 and 10, along with the fact that the hole ground state and first excited hole state sit energetically above the effective valence "band" edge of most of the other 8 configurations, these strongly localised (hole) states may be connected to recent literature discussions of trap-assisted Auger recombination (TAAR) processes [215, 241].

TAAR processes require trap-like (localised) states that sit in the band gap similar to a defect state [63]. However, the nature of the trap-like states underlying TAAR is not yet clear. A number of possible defect/impurity states exist in InGaN systems such as nitrogen interstitials, unintentionally incorporated Ca or Mg dopants [242, 243, 244]. Although defect states have been suggested as significant contributors to TAAR [63], the strongly localised states found here also sit in the band gap and are linked to elevated Auger coefficients, thus they may also play a role in TAAR. We stress that 10 configurations are, of course, not sufficient to evaluate the statistical significance of the above observed "extreme" configurations. However, if such configurations played an important role in InGaN QWs, experimental studies

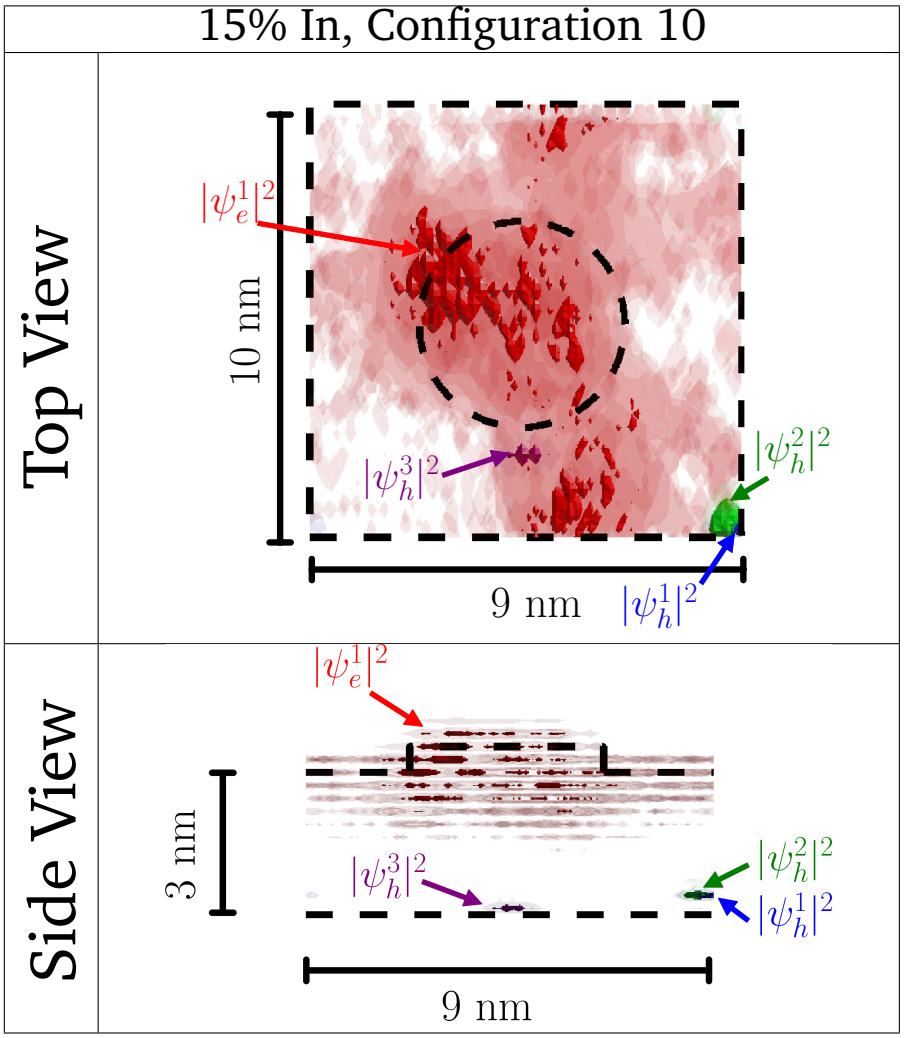


Figure 4.9: Isosurface plots of the charge densities of the electron ground state ($|\psi_e^1|^2$, red), hole ground state ($|\psi_h^1|^2$, blue), first ($|\psi_h^2|^2$, green) and second excited hole state ($|\psi_h^3|^2$, purple) for microscopic Configuration 10 of a 3 nm wide c-plane $In_{0.15}Ga_{0.85}N$/GaN QW. The light (dark) isosurfaces correspond to 10% (40%) of the respective maximum charge density. The top view is along the growth direction, while the side view is along an axis perpendicular to the growth direction.

should give indications about their importance: given the large Auger coefficient these configurations should dominate the nonradiative recombination rates. A comparison with experimental studies could therefore provide insight into this question, which we target in Sec. 5.2.

Nevertheless, to shed light onto the electronic structure of the outlier/extreme configurations, Fig. 4.9 shows isosurface plots of the charge densities of the electron ground state ($|\psi_e^1|^2$, red), hole ground state ($|\psi_h^1|^2$, blue), first ($|\psi_h^2|^2$, green) and second excited hole states ($|\psi_h^3|^2$, purple) for Cf. 10, as an example.

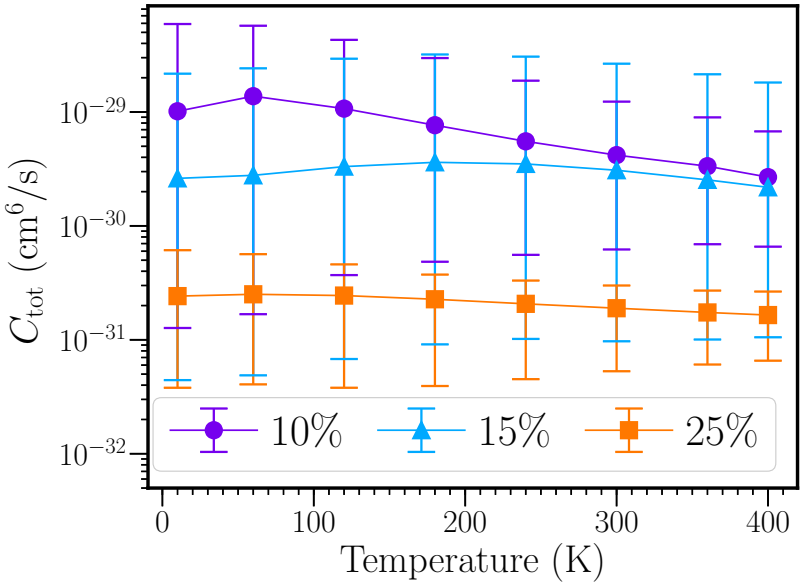


Figure 4.10: Total Auger coefficient, C_{tot}, as a function of the temperature, T, for c-plane InGaN/GaN quantum wells with different In contents (10%, 15% and 25%). The data, averaged over 10 microscopic configurations, are given by the filled symbols; error bars indicate maximum and minimum values of C_{tot} at a given temperature, across the 10 configurations. The calculations have been carried out at a fixed carrier density of $n_{3D} = 3.8 \times 10^{18}$ cm^{-3}.

The charge densities of these different states show that indeed all states are localised by the random alloy fluctuations. A further important observation is that the hole ground and first excited state localise in the same spatial position. Therefore, this particular configuration behaves almost like a quantum dot with two bound energy levels. We note as well that the presence of local quantum dots inside InGaN QWs was put forward to explain experimental observations, e.g., the S-shaped temperature dependence of the PL peak energy, which requires localised states [245]. This co-localisation leads to an enhanced hole-hole wave function overlap entering the calculation of the hhe Auger coefficient even at elevated temperatures where excited states are being populated. Such a situation may thus arise naturally in a random alloy context, or may even depend on the growth conditions in experiments. This co-localisation of the ground and first excited hole states is not found in the 8 non-“extreme” configurations, while for Config. 4 these states are located in close proximity to each other. Hence, the much larger magnitude of the Auger coefficients in Configs. 4 and 10 are driven by the co-localisation of these states.

Having discussed the temperature dependence of, and the impact of the alloy

microstructure on, C_{eeh} and C_{hhe} in detail, we now turn to analysing the *total* Auger coefficient, $C_{\text{tot}} = C_{eeh} + C_{hhe}$. Figure 4.10 displays C_{tot} as a function of temperature for the three different In contents considered. In general, C_{tot} reflects the features of C_{hhe} in that (i) C_{tot} decreases with increasing In content, independent of the temperature, (ii) the impact of the alloy microstructure and thus the spread in the C_{tot} values, in general decreases with increasing T and that (iii) the Auger coefficient shows a weak T dependence, or a (slight) decrease with increasing T.

As already highlighted in the Sec. 2.4, there have been multiple theoretical studies focusing on Auger coefficients in InGaN/GaN QWs. While these studies come in different flavours (e.g. effective-mass models plus scaling of the bulk Auger coefficients, 8-band $\mathbf{k}\cdot\mathbf{p}$ models, full-zone $\mathbf{k}\cdot\mathbf{p}$ models) they basically all rely on continuum-based electronic structure models. Thus, most of these models neglect alloy fluctuations. Looking at the results from some of these theoretical models/approaches; Bertazzi *et al.* [44] find an upper bound estimate for the Auger coefficient in an $In_{0.25}Ga_{0.75}N$/GaN QW of $C_{\text{tot}} \approx 5 \times 10^{-31}$ cm^6 s^{-1} using a full-zone $\mathbf{k}\cdot\mathbf{p}$ model. While this number is similar to our calculated values, the approach in Ref. [44] neglects not only polarisation fields but carrier localisation effects too. The polarisation fields may reduce the Auger coefficients, while alloy fluctuations should increase the Auger coefficients, since k-selection rules are removed. This was already highlighted by Jones *et al.* [41] where, by using a 3D effective mass model in conjunction with scaled bulk Auger coefficients, they showed that including alloy fluctuations led to an enhancement of the Auger coefficients compared to systems in which alloy fluctuations are neglected in the simulations. For a c-plane $In_{0.25}Ga_{0.75}N$/GaN QW, Jones *et al.* report total Auger coefficients of $C_{\text{tot}} \approx 7 \times 10^{-33}$ cm^6 s^{-1}, at 300 K and a carrier density of $n_{3D} = 1 \times 10^{19}$ cm^{-3}, when alloy fluctuations are taken into account. This value is smaller than the value reported here, but as we have recently shown, effective mass models can significantly underestimate carrier localisation effects. Thus, if alloy fluctuations lead to an increase in the Auger coefficient, stronger carrier localisation may increase the values reported by Jones *et al.* significantly.

A direct comparison of our calculated Auger coefficients with experiment, in terms of the In content evolution is difficult since, for instance, in Refs. [34] and [246] only emission wavelengths, or classifications such as “green” or “blue” emitting wells, are reported and these different wavelength regimes may be realised by different alloy and well width combinations. However, to

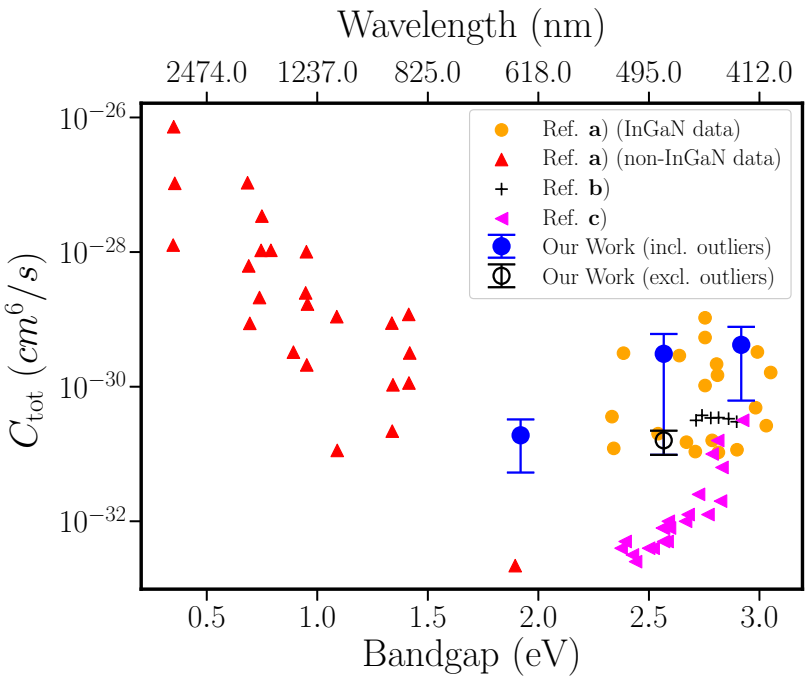


Figure 4.11: Comparison of calculated and measured Auger coefficients (C_{tot}) as a function of (effective) band gap and emission wavelength. Data from several literature sources are included. Ref. **a** = Ref. [59], Ref. **b** = Ref. [69], Ref. **c** = Ref. [211].

gain some first insights into how our calculated values compare with literature data, Fig. 4.11 compares our calculated total Auger coefficients at a temperature of 300 K with literature data, both from experiment and theory, as a function of the (effective) band gap/emission wavelength. To make this comparison we have used the expression from Ref. [114],

$$E_g(T) = E_g(0) - \frac{\alpha T^2}{\beta + T} - \frac{\sigma^2}{k_B T^2} \ ,$$

to obtain the (effective) band gap for our QW structures at 300 K. The low temperature band gap, $E_g(0)$, is found by calculating the TB single-particle electron-hole ground state transition energy averaged over the 10 microscopic configurations considered. The values used for α, β and σ are taken from Ref. [23]. As already seen in other work [59], Fig. 4.11 indicates the unconventional plateau/increase of C_{tot} with increasing (effective) band gap in the InGaN systems, when compared to the sharp decline in C_{tot} for other material systems with increasing band gap; furthermore, our calculated values are within the large spread of literature values.

The above analysis cannot give insight into the statistical significance of the

extreme configurations, therefore it is important to study, in general, how the results may change if such extreme/outlier configurations are present in an alloy. When including all 10 microscopic configurations in the averaging procedure (blue filled circle), our calculations indicate that the Auger coefficient increases with increasing band gap. Although the magnitudes are different, a similar dependence of the Auger coefficient on the (effective) band gap value is observed in the experimental studies from Ref. [211]. On the other hand, when excluding the two "outlier" configurations in the 15% In results (averaging over 8 alloy configurations), we find that the Auger coefficient is, in terms of magnitude, very similar to the 25% In case. As a consequence, our calculated Auger coefficients only vary weakly in the energy range of ≈ 1.9 eV (≈ 644 nm at 25% In) to ≈ 2.6 eV (≈ 482 nm at 15% In); a similar behaviour was found in the experimental studies of, for instance, Schiavon *et al.* [246]. However, we find that when going to larger effective band gaps (i.e. ≈ 2.9 eV/424 nm at 10% In) the Auger coefficient increases, while in Ref. [246] the coefficient is largely constant/may only be slightly increasing beyond 2.6 eV. Overall, our analysis highlights that the alloy microstructure (for instance "trap states") can play an important role in the magnitude of the Auger coefficient and thus further studies are required to gain insight into this question. Continuing our analysis of the temperature dependence of the recombination rates and to provide further insight into the thermal droop phenomenon in InGaN-based QW systems, we briefly recap the previously studied temperature dependence of the radiative recombination (expressed by the B coefficient) at high temperatures, alongside the nonradiative Auger recombination rate; special emphasis will be placed on the competition between these two rates to gain insight into the thermal droop.

4.2.4 Competition between radiative and Auger recombination

The calculation of B is discussed in more detail above, and in Ref. [4]. We highlight two important aspects here. Firstly, the strong decrease in B with increasing In content can be attributed to the increase in the strain-dependent piezoelectric polarisation field. Secondly, at low temperatures only states near the band edge are populated. These states are strongly localised, especially in the case of the holes [130]. With increasing temperature, excited states may be populated, which results in an increase in the overlap of the electron and

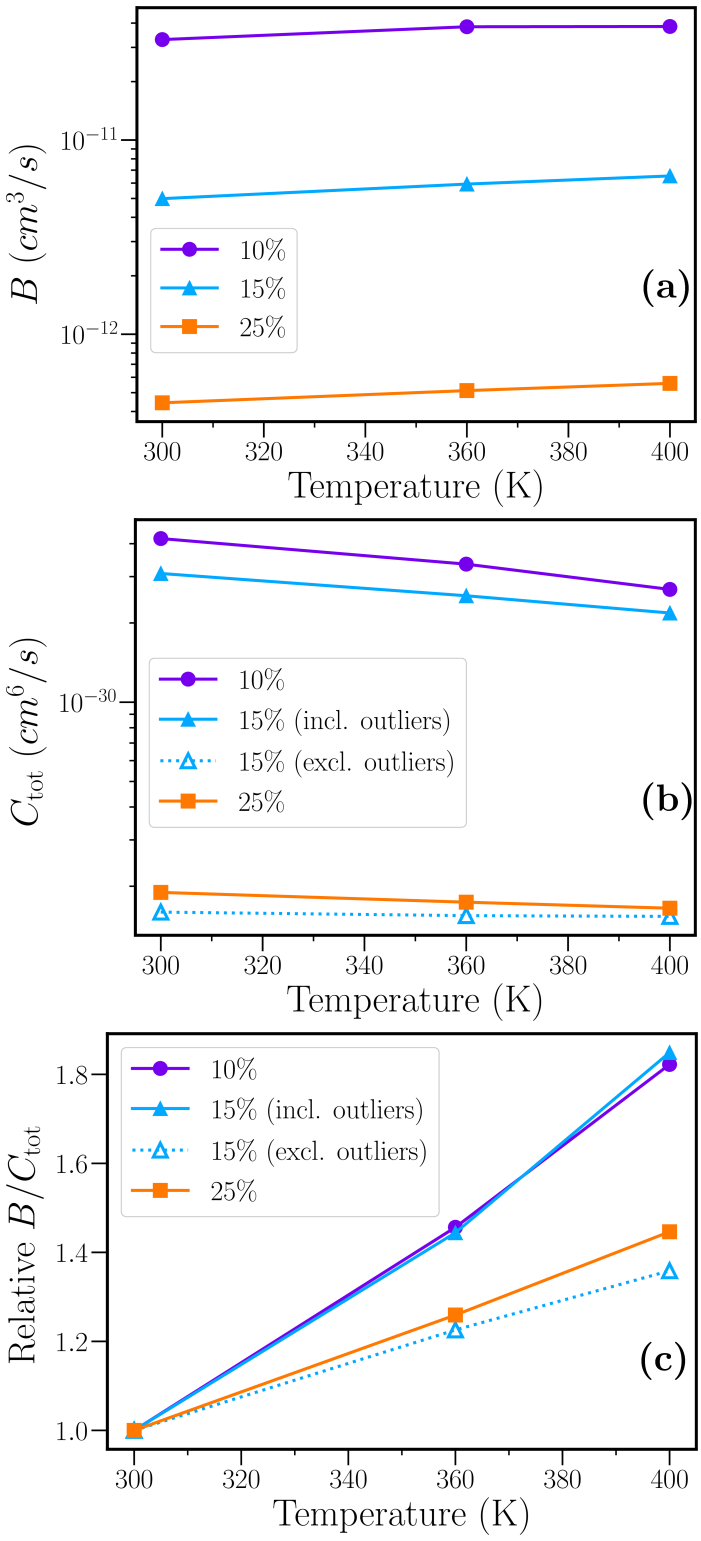


Figure 4.12: a) Radiative coefficient, B, b) total nonradiative Auger coefficient, C_{tot} and c) ratio of these coefficients, B/C_{tot}, as a function of temperature (above 300 K) for 10%, 15% and 25% indium in the well, averaged over 125 configurations. The carrier density is fixed at $n_{3D} = 3.8 \times 10^{18}$ cm^{-3}. The B/C_{tot} ratio is normalised to its value at 300 K.

hole wave functions. This, in turn, can lead to the unusual behaviour that the B coefficient increases with increasing temperature, T; as discussed above and observed in the experimental studies by Nippert *et al.* [34]. Figures 4.12 a), b) and c) display B, C_{tot} and the B/C_{tot} ratio as a function of the temperature (above 300 K) for the three different In contents considered, respectively; the B/C_{tot} ratio has been *normalised* to the respective values at 300 K. We stress that the carrier density is fixed and that we present the *relative* change in B/C_{tot} to gain insight into the *temperature-dependent* competition between radiative and Auger recombination. As a result, Fig. 4.12 c) will be identical when plotting the *relative* change of, for instance, $B/(C_{\text{tot}}n_{3D})$. The data show that B increases slightly (Fig. 4.12 a)) while C_{tot} varies weakly with T in the 25% In case, or decreases with increasing temperature in the 10% and 15% In cases (Fig. 4.12 b)), when including outliers.

Looking at the B/C_{tot} ratio in Fig. 4.12 c), we always find values > 1, noting again that this value is relative to the value at 300 K, which would indicate that the "efficiency" of the systems should increase with increasing temperature, even though, overall, the absolute magnitude of the B/C_{tot} ratio is decreasing as In content increases (further discussion below). We note that the smaller rate of increase of the B/C_{tot} ratio for the 25% case is primarily explained by the weaker T dependence of the 25% total Auger rate, in contrast to the decreasing rates for 10% and 15% In, at least when taking all alloy configurations for the 15% In case into account. Excluding the two extreme configurations of the 15% In case from the calculations, the situation slightly changes: while the B/C_{tot} ratio is still larger than 1, the weaker T dependence of C_{tot} in the 15% In case leads to a B/C_{tot} ratio similar to the 25% In system.

Overall, given our finding of an increase of B/C_{tot} with temperature above 300 K, one could expect that the likelihood of a photon being produced during a recombination event would increase relative to the likelihood of the carrier undergoing a nonradiative Auger process. Thus, our results indicate that the alloy-enhanced Auger processes studied here should not lead to a deterioration of device efficiency as temperature increases. Therefore, we conclude that the experimentally observed thermal droop [31] is not caused by alloy-enhanced Auger recombination, and other, for instance, defect-assisted nonradiative recombination processes are more likely to be its origin.

Having analysed the impact of temperature on the radiative recombination rate, as well as its impact on the nonradiative Auger recombination rate, and

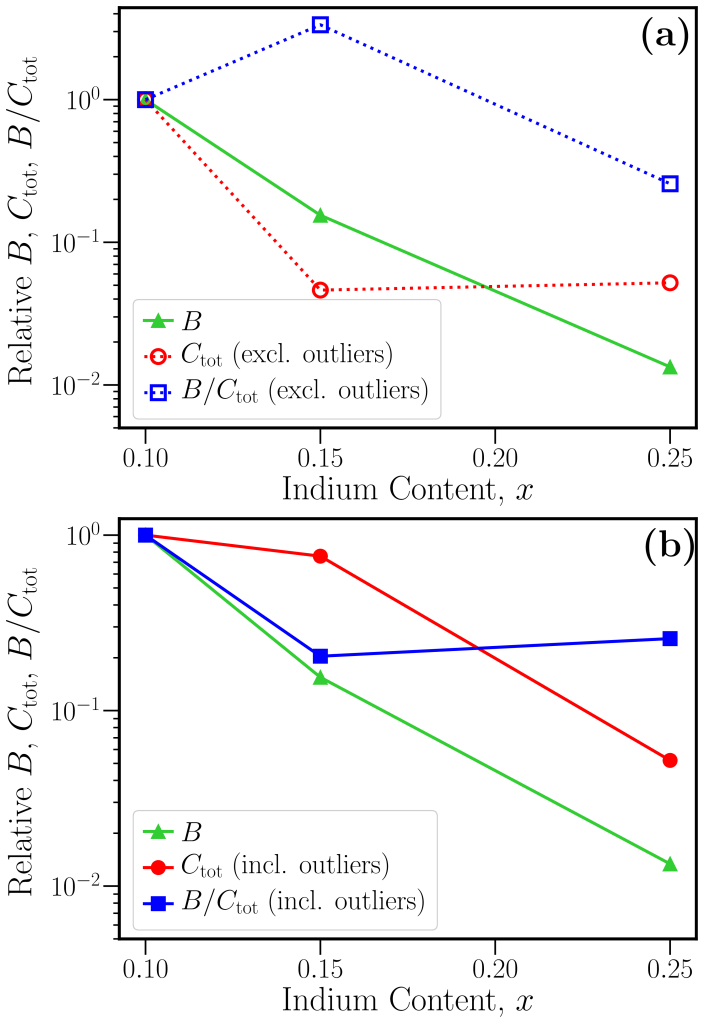


Figure 4.13: Radiative coefficient, B, nonradiative Auger coefficient, C_{tot}, and ratio of these coefficients, B/C_{tot}, as a function of the In content, x, when a) *excluding* and b) *including* outlier configurations. The data are shown relative to their respective values at 10% In. All data are given at a temperature of 300 K and a fixed carrier density of $n_{3D} = 3.8 \times 10^{18}$ cm^{-3}.

the competition between the two rates, we now briefly turn to investigate the impact of In content on the recombination rates and their competition. We note again that with increasing In content the strain-dependent piezoelectric field increases, which in turn leads to a spatial separation of electron and hole wave functions and will thus modify the electronic structure of the wells.

Figures 4.13 a) and b) show the change of B, C_{tot} and B/C_{tot} with increasing In content at a fixed temperature of 300 K and fixed carrier density; the data are shown *relative* to the 10% In system; for the 15% In QW system we present the results when *excluding*, Fig. 4.13 a), and *including*, Fig. 4.13 b), the two "outlier" alloy configurations. Looking at the results when excluding the

outliers first, Fig. 4.13 a), we find that when going from 10% to 15% In content, C_{tot} drops faster than B, resulting in an increase of the B/C_{tot} ratio. When increasing the In content further to 25%, we find that B continues to drop quickly while C_{tot} shows only a weak In content dependence, slightly increasing by approximately 10%. As a consequence, the B/C_{tot} ratio drops, but this drop can be attributed to the reduction of B when increasing the In content from 15% to 25%, and is not due to a significant increase in C_{tot}.

Turning to our results when including the outliers in the 15% In system, Fig. 4.13 b), we find that when increasing the In content from 10% to 15%, the B coefficient decreases more quickly than the nonradiative Auger coefficient, C_{tot}. However, when increasing the In content from 15% to 25%, B and C_{tot} decrease at a similar rate. Between 15% and 25% In, the B/C_{tot} ratio in Fig. 4.13 b) is approximately flat, or increases slightly, but is essentially independent of composition.

Overall, both investigations indicate that the so-called "green gap" [23], i.e., the reduction of IQE in InGaN-based light emitters operating in the green to yellow spectral range, and thus at higher In contents (i.e. $> 15\%$), may not be caused by *alloy-enhanced* Auger recombination effects, since Figures 4.13 a) and b) both indicate that it is the reduction of B and not an increase in C that determines the composition dependence of B/C_{tot}. In other words, the alloy-enhanced Auger recombination may not present an intrinsic roadblock to achieving efficient recombination in the green to yellow range. Thus, in addition to the reduction of the radiative recombination rate when increasing the In content, other factors, such as an increasing defect density and the connected nonradiative recombination processes (e.g. *trap-assisted* Auger recombination [215] or Shockley-Read-Hall recombination [247]) in higher In content samples are more likely to be responsible for the green gap problem. This suggests that by reducing defect densities and thus the connected nonradiative recombination in high In content systems, there may be a way forward to close the green gap. David *et al.* [215] comes to a similar conclusion and suggests that reducing the (point) defect density could close the green gap.

4.3 Conclusion

In this chapter we targeted an investigation of thermal droop in c-plane InGaN/GaN QWs. To do so, we disentangled the effects of changing temperature and carrier density by carrying out the analysis at a fixed, low carrier density of $n = 3.8 \times 10^{18}$ cm^{-3}. We determined the temperature dependence of the radiative and Auger recombination rates for three different In contents in the well; 10%, 15% and 25%. We found that the radiative rate increases with increasing temperature, in line with experimental studies. This unconventional behaviour stands in contrast to the expected decrease of radiative rate with increasing temperature predicted from a fundamental physics perspective. We found total radiative recombination coefficients of $B \approx 3 \times 10^{-11}$ cm^3/s (10% In), $B \approx 5 \times 10^{-12}$ cm^3/s (15% In) and $B \approx 4.5 \times 10^{-13}$ cm^3/s (25% In) at a temperature of 300 K and the carrier density above. These values are averaged over 125 microscopic alloy configurations, used to investigate the impact of the alloy microstructure on the results. We found that at low temperatures, when mainly the strongly localised band edge states are populated, the alloy microstructure has a strong impact on the radiative rate, evidenced by the large variations in B coefficient. As temperature increases, the spread in values decreases, due to the population of excited, less localised or even extended states that are less perturbed by the alloy disordered confining potential.

Turning to the Auger recombination rates, in order to calculate the total Auger rate we first determined the rates of electron-electron-hole (eeh) and hole-hole-electron (hhe) Auger recombination. The calculations revealed that the eeh Auger rate shows a weak temperature dependence, or increases slightly, with increasing temperature. In comparison, the hhe Auger rate shows a weak temperature dependence, or a slight decrease, with increasing temperature. Our studies revealed that the relative contributions from eeh and hhe Auger rates to the total rate do not change with In content. The hhe Auger recombination process is the dominant contributor, even with increasing In content, and temperature. We found total Auger coefficients of $C_{\text{tot}} \approx 4 \times 10^{-30}$ cm^6/s (10% In), $C_{\text{tot}} \approx 2 \times 10^{-30}$ cm^6/s (15% In) and $C_{\text{tot}} \approx 2 \times 10^{-31}$ cm^6/s (25% In) at a temperature of 300 K when averaged over the 10 microscopic alloy configurations investigated. The analysis was restricted to 10 configurations due to the computational expense of Auger rate calculations.

With the temperature dependence of the radiative and Auger rates determined,

we were in a position to discuss the thermal droop. Our investigations showed that at temperatures greater than 300 K the radiative recombination rate slightly increases while the total Auger recombination rate (slightly) decreases. As mentioned above, this finding would indicate a positive impact of increasing temperature on device efficiency when only considering the Auger process as the main nonradiative recombination process. However, this stands in contrast to experimental studies which show that the device efficiency decreases with increasing temperature above 300 K. Therefore, we conclude that the alloy-enhanced Auger recombination process is not responsible for the thermal droop observed in c-plane InGaN/GaN quantum wells and other factors, such as carrier transport, defects, and defect-assisted Auger recombination, are more likely to explain the experimentally observed droop effect. Having determined the radiative and Auger rates for three different In contents, we also briefly commented on the decrease of efficiency observed in InGaN QW-based emitters when targeting longer wavelength emission (corresponding to higher In contents): the so-called "green gap".

We found that, when increasing the In content in the well, the radiative recombination rate drops. However, the analysis of the composition dependence of the Auger rate was complicated by the presence of "outlier" configurations with elevated Auger rates. Our subsequent analysis of these configurations, particularly our comparison to experimental data which is presented in detail in the following chapter, strongly suggested that the situation found in these outliers is not representative of InGaN/GaN QWs. Thus, when excluding them from the analysis we found that the Auger rate initially drops from 10% to 15% In in the well, but is composition independent when going to 25% In. Thus, it is the reduction of the radiative recombination rate and not an increase in the Auger rate that determines the composition dependence of the competition between these processes. As a result, we expect that the reduction of IQE in InGaN-based light emitters operating in the green to yellow spectral range, and thus at higher In contents (i.e. $> 15\%$), may not be caused by *alloy-enhanced* Auger recombination effects. In other words, the alloy-enhanced Auger recombination may not present an intrinsic roadblock to achieving efficient recombination in the green to yellow range. Thus, in addition to the reduction of the radiative recombination rate when increasing the In content, other factors, such as an increasing defect density and the connected nonradiative recombination processes (e.g. *trap-assisted* Auger recombination or SRH recombination) in higher In content samples are

more likely to be responsible for the green gap problem. This suggests that by reducing defect densities and thus the connected nonradiative recombination in high In content systems, there may be a way forward to close the green gap. Having discussed the thermal droop and green gap in InGaN-based QWs, we now turn to an analysis of the carrier density dependent droop.

Chapter 5

Carrier density dependent recombination in InGaN QWs

The phenomenon of carrier density dependent droop is a significant roadblock to the optimisation of InGaN/GaN QW-based LEDs [9]. To gain insight into the carrier density dependence of the IQE, as discussed above, we now investigate the radiative and Auger recombination rates as a function of carrier density, and the impact that the screening of the built-in polarisation field has on the electronic structure. The chapter is organised as follows. First we will detail the ingredients of the calculations, before turning to the impact of the polarisation field screening. Then, we will turn to the carrier density dependence of the Auger recombination coefficient, before finally comparing the Auger and radiative recombination rates with experimental IQE data.

5.1 Introduction

In the previous chapter we studied InGaN/GaN QWs with In contents of 10%, 15% and 25%. Here, we now focus on the 15% In case (which has a well width of 3 nm) as this composition and well width are often found in experimental realisations of InGaN/GaN QWs [211, 248] and moreover, have been targeted for analysis by colleagues at the Universities of Manchester and Cambridge, which will allow us to compare theory and experiment [2]. More details, e.g., about the simulation cell, can be found above in Chapter 4 and in Ref. [3].

The theoretical framework and QW model systems are essentially the same as above in Chapter 4, however now we calculate 150 electron and hole state (in

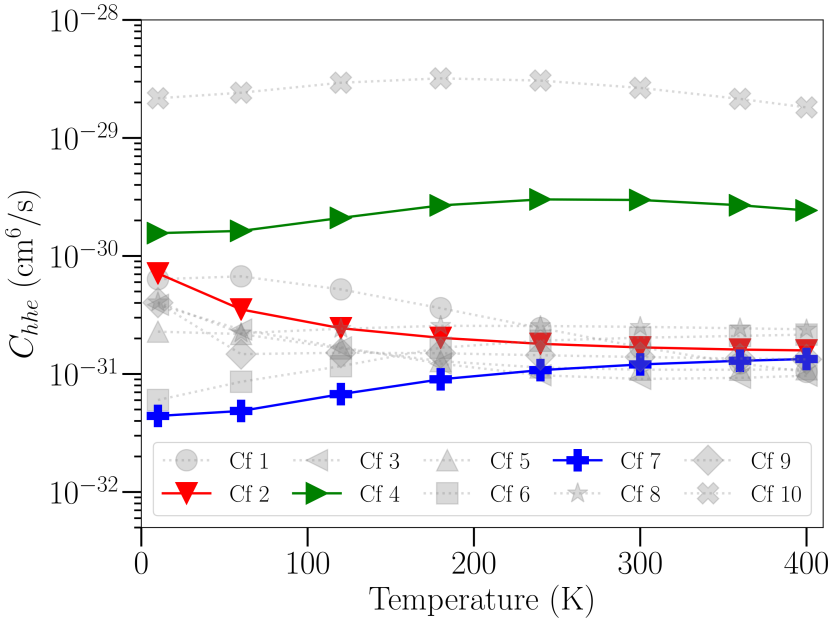


Figure 5.1: Hole-hole-electron Auger coefficient, C_{hhe}, as a function of temperature for 10 different microscopic alloy configurations of an $In_{0.15}Ga_{0.85}N$/GaN quantum well at a fixed, low carrier density of $n = 3.8 \times 10^{18}$ cm^{-3} [3].

contrast to 100 above) to account for the occupation of states at very high carrier densities and a temperature of 300 K. We note that in LED devices, which are electrically driven, the operating temperatures can exceed 300 K. However, in the theory experiment comparison discussed below, we deal with an optically pumped QW system. In the experimental studies conducted by our colleagues at the University of Manchester, the temperature of the QW sample was held constant at 300 K. Therefore, we assume for our calculations a temperature of 300 K. Furthermore, as discussed above in Chapter 3, with the introduction of charge carriers into the well, the built-in polarisation field will be screened. Thus, the calculation of 150 electron and hole states must be carried out for each carrier density, while taking the built-in field screening effect into account as outlined in Sec. 3.3.

The computational expense of Auger rate calculations, given the large number of states and Coulomb matrix elements involved at high carrier densities ($\geq 1 \times 10^{19}$ cm^{-3}), is immense. Thus, we have selected three configurations from the previously studied 10, namely configurations (Cfs.) 2, 4 and 7 (also highlighted in Fig. 5.1). We have selected these configurations since Cfs. 2 and 7 give a very similar Auger coefficient at higher temperatures, similar to 8 of the 10 previously investigated systems. On the other hand, at lower temperatures, the behaviour of Cf. 2 (C_{hhe} decreases with increasing T) and

Cf. 7 (C_{hhe} increases with increasing T) are opposites. Finally, we have selected Cf. 4 to study the carrier density dependence of one of the configurations with a significantly larger Auger coefficient, which may be connected to defect-related/trap-assisted Auger processes discussed previously and in the literature [63, 215]. As mentioned previously, a number of possible defect/impurity states exist in InGaN systems such as nitrogen interstitials and unintentionally incorporated Ca or Mg dopants [242, 243, 244]. A configuration with such a high Auger coefficient may dominate the recombination process in InGaN QWs. However, as we will discuss in more detail below, comparing the results on the carrier density dependence of C with experimental data gives very little indication that this is the case, and suggests that Cfs. 2 and 7 describe the most commonly found situation in InGaN QWs [2]. However, it is still important to investigate how the Auger rate of such an "extreme" configuration changes with carrier density. Overall, the three selected configurations furnish a good overview of how the Auger coefficient can change with carrier density in $In_{0.15}Ga_{0.85}N$/GaN QW systems.

5.2 Results

Before turning to the carrier density dependence of the Auger coefficients, and subsequently the competition between the radiative and Auger recombination rates as carrier density increases, we first analyse how the screening of the built-in field affects the electronic structure of the QW.

5.2.1 Impact of polarisation field screening on electronic structure

Figure 5.2 depicts the ground-state electron (red) and hole (blue) charge densities for Cf. 2 for varying carrier densities (increasing from left to right). We have selected Cf. 2 here since (i) at low temperatures its Auger coefficient C_{hhe} is very similar to Cf. 4, which gives a significantly larger Auger coefficient over the full temperature range, and (ii) C_{hhe} decreases with increasing temperature for Cf. 2, thus also providing insight into the importance of excited states (further discussion below). Looking first at the "Top View" (first row, view along c-axis), for lower carrier densities the electron charge density (indicated in red in Fig. 5.2) is mainly localised by the well width fluctuation (WWF) and with increasing carrier density starts to "delocalise" in the c-plane.

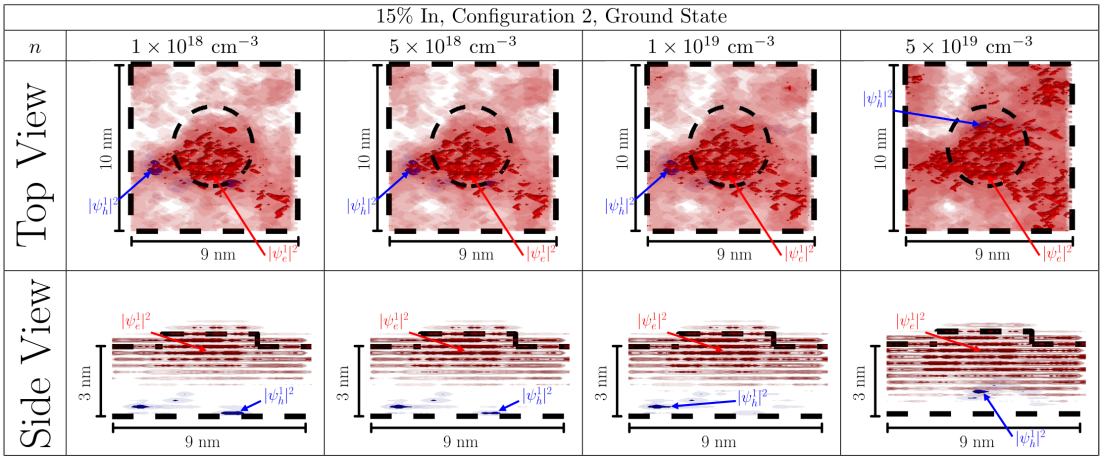


Figure 5.2: Isosurface plots of the ground state electron (red) and hole (blue) charge densities for Configuration 2 with a built-in field determined for varying carrier densities in an $In_{0.15}Ga_{0.85}N$/GaN quantum well. The light (dark) isosurfaces correspond to 10% (40%) of the maximum value of the respective charge density. In the "Top View", the black dashed square indicate the limits of the simulation cell and the dimensions of a well width fluctuation (black dashed circle) considered. In the "Side View", the black dashed lines give an indication of the quantum well interfaces.

However, the alloy microstructure is of secondary importance when compared to holes (charge densities indicated in blue in Fig. 5.2). Here, the hole charge density is strongly localised, and remains so even at higher carrier densities.

However, looking at the "Side View" (second row), while still being strongly localised by the alloy fluctuations, the hole ground state localisation region changes (when comparing charge densities for built-in fields determined at carrier densities of 1×10^{18} cm^{-3} and 5×10^{19} cm^{-3}). We attribute this to the following. At low carrier densities, the electrostatic built-in field forces both electron and hole wave functions to be localised at the lower (holes) and upper (electrons) QW barrier interfaces. Thus, only the alloy microstructure at and near these interfaces plays a role for alloy-induced carrier localisation effects. However, when the built-in field is reduced by screening effects, local potential "pockets" away from the interfaces now also play a role for carrier localisation effects. This is an important observation as it means that screening of the built-in field not only changes the electron and hole wave function overlap (both in-plane and out-of plane), but it can be accompanied by significant changes in the electronic structure of the well in general.

Moreover, Fig. 5.2 also reveals the expected effect that the built-in polarisation

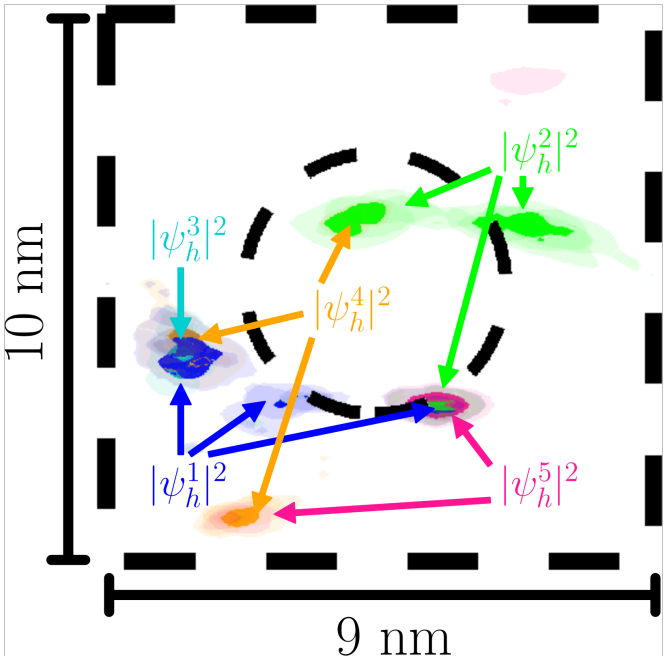


Figure 5.3: Isosurface plots of the five energetically lowest hole charge densities, $|\psi_h^{1,2,3,4,5}|^2$, for Configuration 2 of an $In_{0.15}Ga_{0.85}N$/GaN quantum well; the built-in potential has been determined for a carrier density of $n = 5 \times 10^{18}$ cm^{-3}. The light (dark) isosurfaces correspond to 10% (40%) of the maximum value of the respective charge density.

field spatially separates the electron and hole wave functions at lower carrier densities along the c-axis. With increasing carrier density the built-in field is screened so that the spatial separation between electron and hole wave functions, along the growth direction, is reduced. As a result, the electron and hole wave function overlap is increased. Overall, and based on the method described above, we find that the screening of the built-in field becomes noticeable (i.e. reduction of the electrostatic built-in field by, for example, more than 10%) for carrier densities exceeding $n = 5 \times 10^{18}$ cm^{-3}; this finding is in line with recent literature data [229, 231].

However, with increasing carrier density and/or temperature, not only ground states, but also excited states are important for Auger recombination, especially for holes where one is left with strong alloy-induced carrier localisation effects. Figure 5.3 displays the first five hole states for Cf. 2, with the built-in field determined for a carrier density of $n = 5 \times 10^{18}$ cm^{-3}. Several features of these states are important. Firstly, Fig. 5.3 clearly shows that not only the ground state exhibits strong localisation effects, but also the first few excited states. Secondly, one can see that while the ground state, ψ_h^1, and the first excited state, ψ_h^2, are localised by alloy fluctuations, they localise in

different spatial in-plane regions. This result is not captured by a calculation where these localisation features are neglected, e.g., a standard one-dimensional continuum-based description (e.g. a virtual crystal approximation (VCA)) of InGaN/GaN QWs, which is often used in literature to evaluate Auger recombination [43, 249, 250]. Thus, Coulomb matrix elements involving wave functions localised in different in-plane regions are strongly reduced in magnitude compared to a VCA description of the same system. However, Fig. 5.3 also reveals that the second excited state, ψ_h^3, is strongly localised and localises in the same spatial position as the ground state, ψ_h^1; this situation could for instance be approximated or described by a "local" quantum dot with a ground and an excited state. This also indicates that Coulomb matrix elements involving these states may be strongly enhanced compared to a VCA description. The situation is further modified and complicated by the spatial separation of the third and fourth excited hole states, which have multiple localisation centers, sometimes spatially overlapping with other hole states, and sometimes not.

Overall, the results presented above indicate that while the wave function overlap *along* the c-axis increases with increasing carrier density, the wave function overlap between hole states *within* the c-plane may strongly depend on the alloy microstructure. This should at least be the case for lower temperatures and lower carrier densities since here mainly the localised hole states near the "band" edge are important. As a consequence, and even though with increasing carrier density more states are involved in the Auger rate, Eq. (3.11), their contribution may be small due to the spatial in-plane separation of the (hole) states. Furthermore, it is important to note that to evaluate the Auger *coefficient*, the rate is divided by the carrier density cubed. Thus, at lower temperatures, the Auger coefficient may increase or decrease with increasing carrier density, depending on whether n^3 or the number and magnitude of the involved states/Coulomb matrix elements dominate the Auger rate, Eq. (3.11). Finally, the evolution of the Auger coefficient may be further impacted by the fact that the electronic structure changes with increasing carrier density as seen above in Fig. 5.2, where, for instance, the hole ground state at lower carrier densities is different from the hole ground state in the high carrier density regime and the same may be the case for some excited states.

In general, at higher temperatures and/or higher carrier densities, where the localised states are saturated, and one is approaching the situation that the

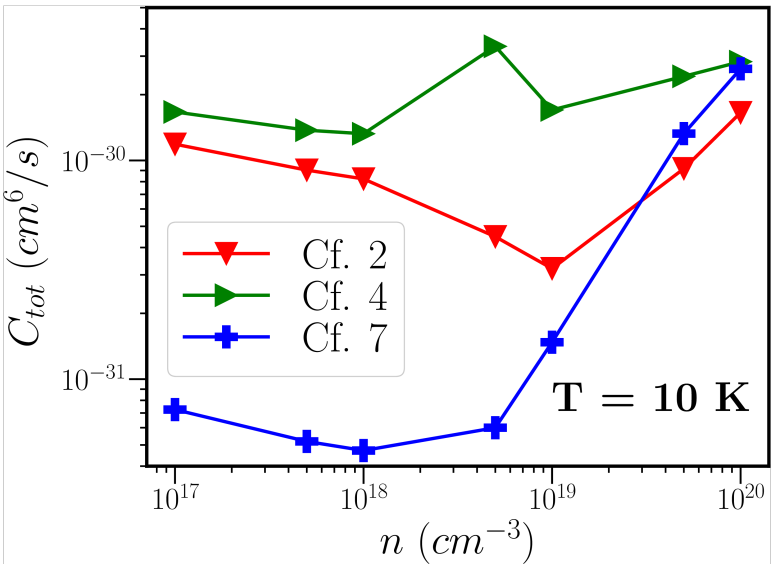


Figure 5.4: Total Auger coefficient, C_{tot}, as a function of carrier density, n, at a temperature of T = 10 K for three different microscopic alloy configurations (Cfs.) for a c-plane $In_{0.15}Ga_{0.85}N$/GaN quantum well with a well width of 3 nm.

wave functions for electrons and holes are more delocalised, the alloy microstructure is expected to be less important. Thus, more macroscopic effects, e.g., the spatial separation of electrons and holes along the c-axis, become important.

Equipped with this insight and taking these considerations as a whole into account, we present now in a first step the calculated total Auger coefficient, C_{tot}, as a function of the carrier density, n. We start our analysis with low temperature (T = 10 K) results, before turning to room temperature data (T = 300 K). Finally, we investigate in more detail the contribution from electron-electron-hole (C_{eeh}) and hole-hole-electron (C_{hhe}) processes to the total Auger coefficient, $C_{\text{tot}} = C_{eeh} + C_{hhe}$.

5.2.2 Auger recombination

Figure 5.4 displays the total Auger coefficient, C_{tot}, for a temperature of T = 10 K as a function of carrier density, n; the data are shown for the three microscopic alloy configurations considered in this study (see discussion above). This figure reveals that for carrier densities below $n = 1 \times 10^{19}$ cm^{-3}, the alloy microstructure significantly impacts not only the magnitude of C_{tot}, but also how C_{tot} evolves with increasing carrier density n. At low carrier densities, the behaviour seen already in Fig. 5.1, is here also visible, namely a large spread in the values of C_{tot}. As carrier density in the well increases up to

$n = 1 \times 10^{19}$ cm^{-3}, the configurations show different behaviours. In the case of Cf. 7, C_{tot} decreases up to $n = 1 \times 10^{18}$ cm^{-3} before starting to increase. Although at low carrier densities Cfs. 2 and 4 exhibit Auger coefficients of similar magnitudes, their carrier density dependence is quite different: C_{tot} for Cf. 2 decreases when the carrier density increases up to $n = 1 \times 10^{19}$ cm^{-3}; C_{tot} for Cf. 4 has an almost constant (slight decrease) behaviour up to a carrier density of $n = 1 \times 10^{18}$ cm^{-3} and a "kink" in the evolution of C_{tot} at $n = 5 \times 10^{18}$ cm^{-3}. Overall, and as discussed above, several factors play an important role (e.g. number of states involved, wave function localisation effects and associated magnitudes of the Coulomb matrix elements, potential changes in the electronic structure, scaling by $1/n^3$) in determining how the Auger coefficient evolves with increasing carrier density, which makes it difficult to deconvolute the impact of these different factors.

However, Fig. 5.4 also shows that for carrier densities $\geq 1 \times 10^{19}$ cm^{-3}, and independent of the configuration, the Auger coefficients, C_{tot}, start to increase with increasing carrier density. Moreover, at the highest carrier density considered here, we find that all three alloy configurations give, to a first approximation, very similar Auger coefficients. Overall, we attribute this to the following two effects. Firstly, with increasing carrier density the electrostatic built-in field is significantly screened (at a carrier density of $n = 5 \times 10^{19}$ cm^{-3} the built-in field is reduced by a factor of around 2 when compared to a situation that neglects any screening), which increases the electron and hole wave function overlap, as indicated in Fig. 5.2. As a consequence, one may expect the increase observed in C_{tot}. Furthermore, with increasing carrier density the localised states become saturated and for all configurations more delocalised electron and hole states become populated and thus start to contribute. These more delocalised states are less impacted by the alloy microstructure and thus less prone to in-plane carrier separation. All in all, with increasing carrier density the Auger coefficient increases, and differences between the three different alloy configurations are "smeared" out, resulting in the observed very similar results for the Auger coefficient at higher carrier densities.

Based on these considerations, one may also expect that at elevated temperatures, for which the carriers are distributed over a larger range of (localised hole) states than at lower temperatures, variations in Auger coefficient for each configuration become less pronounced. This is reflected in Fig. 5.5, which depicts C_{tot} as a function of the carrier density at a temperature

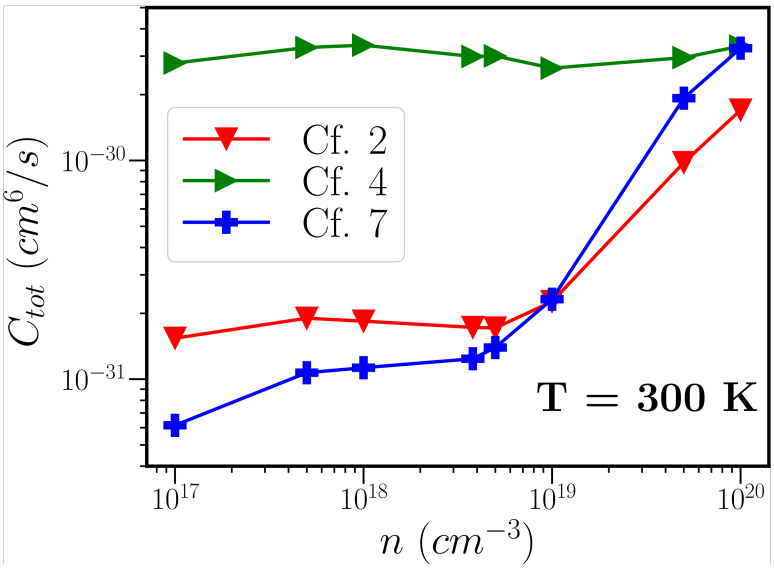


Figure 5.5: Total Auger recombination coefficient, C_{tot}, as a function of carrier density, n, at a temperature of T = 300 K for three different microscopic alloy configurations (Cfs.) for a c-plane $In_{0.15}Ga_{0.85}N$/GaN quantum well with a well width of 3 nm.

of T = 300 K. For carrier densities $\leq 1 \times 10^{18}$ cm^{-3} all configurations show, in general, a (slight) increase with increasing carrier density. Turning to the magnitude of the Auger coefficient in the lower carrier density regime of $n \leq 1 \times 10^{18}$ cm^{-3}, we find that Cfs. 4 and 7 are only slightly affected by increasing the temperature from T = 10 K (see Fig. 5.4) to T = 300 K when compared to Cf. 2. For Cf. 2 we observe a noticeable decrease in the magnitude of C_{tot} when increasing the temperature from T = 10 K (see Fig. 5.4) to T = 300 K. This reflects the results already seen above in Chapter 4 and summarised in Figs. 4.7 and 5.1.

In the carrier density range of $n = 1 \times 10^{18}$ cm^{-3} to $n = 5 \times 10^{18}$ cm^{-3}, the Auger coefficient C_{tot} exhibits only a slight carrier density dependence. Turning to the results when increasing the carrier density beyond $n = 5 \times 10^{18}$ cm^{-3}, we observe that for all configurations studied, C_{tot} starts to increase. Moreover, and similar to the low temperature results, Cfs. 4 and 7 give very similar Auger coefficients at the high carrier density of $n = 1 \times 10^{20}$ cm^{-3}, and Cf. 2 is of the same order of magnitude. Overall, we attribute this to similar effects discussed above. Firstly, at these higher carrier densities the localised states are, to a large extent, saturated. Thus, with increasing carrier density more delocalised states, which are less sensitive to the alloy microstructure, contribute to the Auger rate. Secondly, at high carrier densities the intrinsic built-in field is reduced, and in conjunction with the population of the more

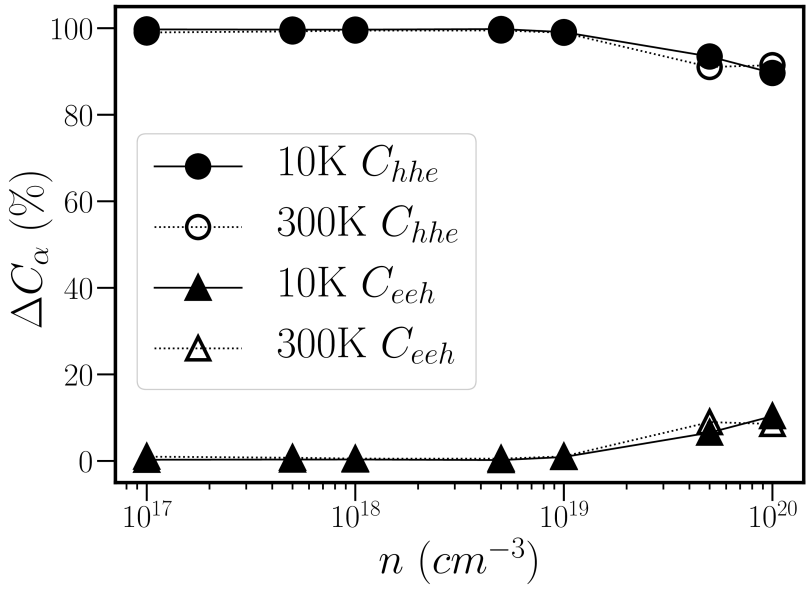


Figure 5.6: Percentage contribution to the total Auger coefficient, $\Delta C_\alpha = (C_\alpha/C_{\text{tot}})$, from the electron-electron-hole ($\alpha = eeh$, represented by triangles) and hole-hole-electron ($\alpha = hhe$, represented by circles) coefficients as a function of carrier density, n, at T = 10 K (filled symbols, solid line) and T = 300 K (open symbols, dashed line) for a c-plane $In_{0.15}Ga_{0.85}N$/GaN quantum well with a well width of 3 nm. The data are averaged over three microscopic configurations.

delocalised states, the electron and hole wave function overlap along the growth direction is increased, which results in larger Coulomb matrix elements and consequently an increase in the Auger rate and thus the coefficient C_{tot}.

So far we have only discussed the *total* Auger coefficient, $C_{\text{tot}} = C_{eeh} + C_{hhe}$, but not the individual contributions from the electron-electron-hole, C_{eeh}, and hole-hole-electron, C_{hhe}, processes. As discussed above in Chapter 4 (see also Ref. [3]), at lower carrier densities, the C_{hhe} part dominates the magnitude of the total Auger coefficient, C_{tot}, and C_{eeh} is of secondary importance. This is consistent with the DFT studies in Ref. [40] on InGaN *bulk* systems and also theoretical work on c-plane InGaN QWs using a modified continuum-based model and analytic considerations [41, 211]. However, experimental investigations by Nirschl *et al.* [67] on InGaN QWs, concluded that the eeh Auger rate is equal to, or larger than, the hhe rate. The work by David *et al.* [211] discusses in general that screening the built-in field increases the relative importance of the C_{eeh} contribution. Jones *et al.* [41], using a modified continuum-based model to describe the Auger recombination, conclude when studying *non-polar* InGaN QWs, which do not exhibit any

macroscopic polarisation field [228], that indeed screening of the polarisation field may lead to the situation found in the experiments.

Thus, to gain insight into this question, Fig. 5.6 presents the (percentage) contribution from the electron-electron-hole, $\Delta C_{eeh}(n) = (C_{eeh}(n)/C_{\text{tot}}(n))$, and hole-hole-electron, $\Delta C_{hhe}(n) = (C_{hhe}(n)/C_{\text{tot}}(n))$, processes to the total Auger coefficient, C_{tot}, as a function of the carrier density, n. The data are shown for low (T = 10 K) and room temperatures (T = 300 K). At low carrier densities ($n \leq 5 \times 10^{18}$ cm^{-3}) and independent of the temperature, Fig. 5.6 reveals that C_{hhe} dominates the total rate, being over 95% of C_{tot}. This finding is consistent with our previous results [3] and literature theoretical data [41, 211] on c-plane InGaN/GaN QWs. In the higher carrier density regime, i.e., when increasing the carrier density beyond $n = 5 \times 10^{18}$ cm^{-3}, C_{eeh} increases slightly, relative to the contribution from C_{hhe}; the general trend is thus consistent with expectations in, for example, Ref. [211].

At high carrier densities, C_{hhe} still contributes $\geq 90\%$ of C_{tot} which stands in contrast to the experimental results of Nirschl *et al.* [67], and the calculations by Jones *et al.* [41] for non-polar InGaN QWs. We note that the electronic structure of a non-polar QW system is different to that of a c-plane well [228]. Thus, Auger rates may behave differently in a non-polar well when compared to c-plane systems with partially screened built-in fields. Further studies comparing atomistic and modified continuum-based models are required to shed light on the importance of electron-electron-hole Auger processes in polar c-plane and non-polar InGaN QWs.

Having calculated the carrier density dependence of the Auger coefficient, the competition with the radiative recombination process as a function of carrier density is essential for understanding the “droop” phenomenon. Thus, in our next step, we focus on the carrier density dependence of the competition between the radiative and Auger recombination rates and how our theoretical data compares to experimental data obtained by collaborators at the University of Manchester on samples grown at the University of Cambridge.

5.2.3 Competition between radiative and Auger recombination - theory experiment comparison

With the theoretical data on the carrier density dependence of the radiative and Auger rates determined, we now seek further insight into the role of

carrier localisation in causing droop. Furthermore, given the recent literature discussions of defect-assisted Auger recombination, we aim to disentangle the importance of the extrinsic, defect-related process from the intrinsic, alloy-enhanced Auger process. To do so, we have carried out a comparison between theoretical and experimentally determined efficiency droop data in collaboration with colleagues at the University of Manchester, using InGaN/GaN MQW samples grown at the University of Cambridge.

To investigate the impact of defect-assisted Auger processes the samples were designed to have the same density of extended defects but different densities of point defects. Full details of the comparison and sample growth can be found in Ref. [2]. Here, the main features are summarised. The samples contain five approximately 3 nm wide InGaN QWs embedded in approximately 7 nm wide GaN barriers. The In content in the wells was determined to be 17% $\pm$ 2%. Thus, the well width and In content are in line with those targeted in our theoretical framework. The samples emit in the green spectral range. The density of point defects is controlled by varying the growth temperature, which has been shown to inversely correlate with the density of point defects, i.e., higher growth temperatures lead to lower point defect densities [251]. The samples are labelled by the growth temperature T_G in degrees Celsius. In order of increasing expected point defect density the samples studied are labelled 716, 706 and 698.

The samples are simplified structures compared to those employed in actual LEDs, for instance lacking an AlGaN electron blocking layer. However, they consist of 5-period multi-QW structures, in contrast to the single QW structure investigated theoretically. The purpose of this design is so that PL measurements can be taken of carriers excited in the QW regions alone, so-called resonant PL since the excitation energy is below the band gap energy of the GaN barrier. The use of resonant PL is employed to isolate the recombination processes occurring in the QW regions, thus disentangling the IQE from external effects such as transport losses or inhomogeneous carrier distribution across multi-QW structures, and is a technique that has been employed previously [66, 68].

As discussed above in Chapter 4, it was found that at 300 K and a carrier density of $n = 3.8 \times 10^{18}$ cm^{-3}, for a 15% In QW, eight of the 10 investigated configurations showed similar values for C_{tot}, while two were classified as outliers. So far in this chapter we have analysed three configurations, two

"standard" configurations, Cfs. 2 and 7, and one "outlier", Cf. 4. The analysis below was carried out including and excluding this outlier, allowing us to identify the potential impact of a much larger Auger rate stemming from the "outlier" configuration. Several things are important to note here: given the numerical expense of the calculations, the statistical importance of the outlier configuration cannot be quantified based on the theoretical calculations alone. However, such an extreme/outlier configuration should dominate the nonradiative recombination process in the QW system studied experimentally, given that the outlier configuration exhibits a much larger Auger coefficient. Bearing in mind that there is no fitting involved in our theory experiment comparison, one should see clear indications of such an increased nonradiative process, meaning that the Auger coefficients of the "standard"/non-outlier configurations would not explain the experimental data. Furthermore, the spot size of the optical beam is much larger than the simulation cell. Therefore, it will sample a large number of "local" alloy configurations simultaneously. Again, if such an outlier configuration would be realised, it should dominate the recombination process, as it could act as a "sink" for carriers due to the much larger associated Auger rate in a specific spatial region. Finally, to further shed light onto the question of the presence of configurations classified as "outliers" in the theoretical model, the measurements have been repeated for different spots on the sample; this accounts for possible experimental bias in which a region on the sample exhibiting a non-extreme Auger rate could be selected for analysis by luck.

Building on this, our theory experiment comparison gives very little evidence for the presence of the configurations regarded as outliers in the theoretical model, and the experimental data is best described by the "standard" configurations. We note that all this does not rule out entirely the presence of these extreme configurations as it may depend on growth conditions and In content. Indeed, other recent experimental studies suggest that defect-related/trap-assisted Auger recombination only accounts for a small fraction of the total nonradiative recombination rates [252]. Finally, as already discussed above, we cannot classify the statistical significance of the outlier configurations. Based on the 10 configurations studied initially we find 2 outliers out of 10, i.e., 20%. However, if we would repeat the calculations for a much larger number of configurations, we may still find these configurations but at a much lower percentage and may indeed also theoretically confirm that these extreme configurations are unlikely to appear in a random alloy. In

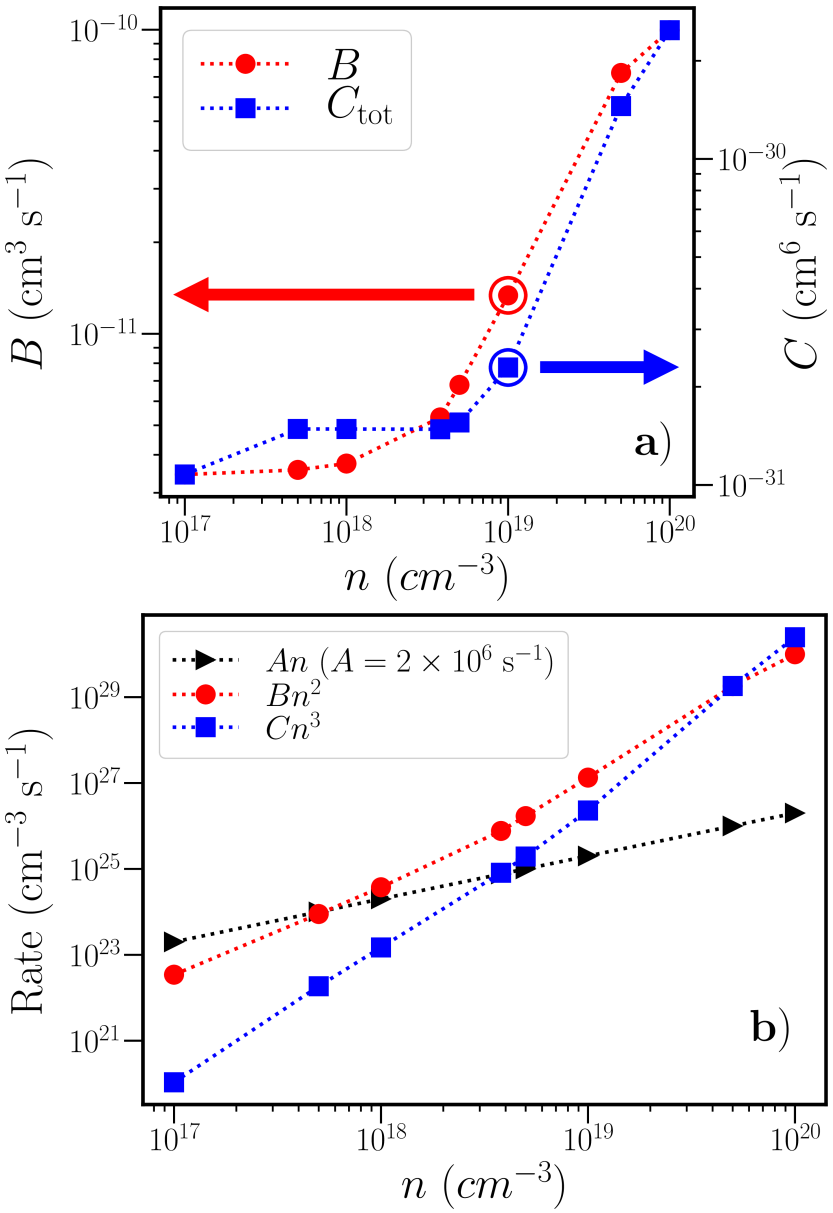


Figure 5.7: a) *Theoretical* radiative and Auger recombination coefficients as a function of carrier density and b) *theoretical* radiative, Auger and SRH recombination rates (per volume) as a function of carrier density. For both a) and b) the radiative and Auger recombination data are averaged over Cfs. 2 and 7 for an InGaN/GaN QW with 15% In at T = 300 K. The value of SRH coefficient, $A = 2 \times 10^6\ \text{s}^{-1}$, has been estimated experimentally (see text for details) and lies within the range of values reported in the literature.

summary, our combined theory experiment comparison indicates that the Auger rate is best described by the "standard" configurations and that the outlier configurations are statistically less likely, even though their existence in an alloy cannot be fully ruled out.

Before turning to discuss our theory experiment comparison in more detail, in

our theoretical framework we have determined the B and C coefficients, so we begin by presenting the theoretical B and C coefficients (the calculation of which is described above in Chapter 3) as functions of carrier density at T = 300 K in Fig. 5.7 a). Both B and C have been averaged over Cfs. 2 and 7. As mentioned above in Sec. 1.3, in the simplest formulation of the ABC model, the A, B and C coefficients are carrier density independent. Here, we see a significant deviation from this assumption for the B and C coefficients, particularly as carrier density increases above approximately $n = 1 \times 10^{18}$ cm^{-3}. This strong dependence of the coefficients on carrier density is largely driven by the built-in polarisation field screening we previously discussed in Sec. 3.3. Above approximately $n = 5 \times 10^{18}$ cm^{-3} the reduction of the c-direction separation of the electron and hole wave functions due to screening effects enhances the wave function overlap, leading to an increase in not only the Auger coefficient, but also the the radiative coefficient. Thus, we expect that both the radiative and the Auger recombination rate will increase as carrier density increases. While we may expect an increase in efficiency when the radiative rate increases due to the screening of the polarisation field, this will be counteracted by an increase in the Auger rate as well.

In order to compare our theoretical results with experimentally determined IQE data, within the ABC model, we require some knowledge of the Shockley-Read-Hall (SRH) A coefficient. We have not calculated this parameter but typical values are reported in the range of $A = 1 \times 10^5$ – 1×10^7 s^{-1} [246, 253, 254]. Thus, in Fig. 5.7 b), using a typical value of SRH coefficient, $A = 2 \times 10^6$ s^{-1}, the radiative and Auger recombination rates are presented alongside an illustrative SRH recombination rate. Figure 5.7 b) shows that as the carrier density increases above $n = 1 \times 10^{18}$ cm^{-3} the radiative recombination rate overtakes the SRH recombination rate, while as the carrier density increases past $n = 5 \times 10^{19}$ cm^{-3} the Auger recombination rate exceeds the radiative recombination rate. As a consequence we would expect a reduction in efficiency in this high carrier density regime.

Figure. 5.7 b) also shows that in the high carrier density regime (above approximately $n = 1 \times 10^{19}$ cm^{-3}) the SRH recombination rate is already approximately an order of magnitude smaller than both the Auger and radiative recombination rate, and becomes negligible at higher carrier densities. Thus, we expect that the behaviour of the IQE will be dominated by the radiative and Auger recombination rates at high carrier density. The A value used here is often reported in literature and used in theoretical analyses,

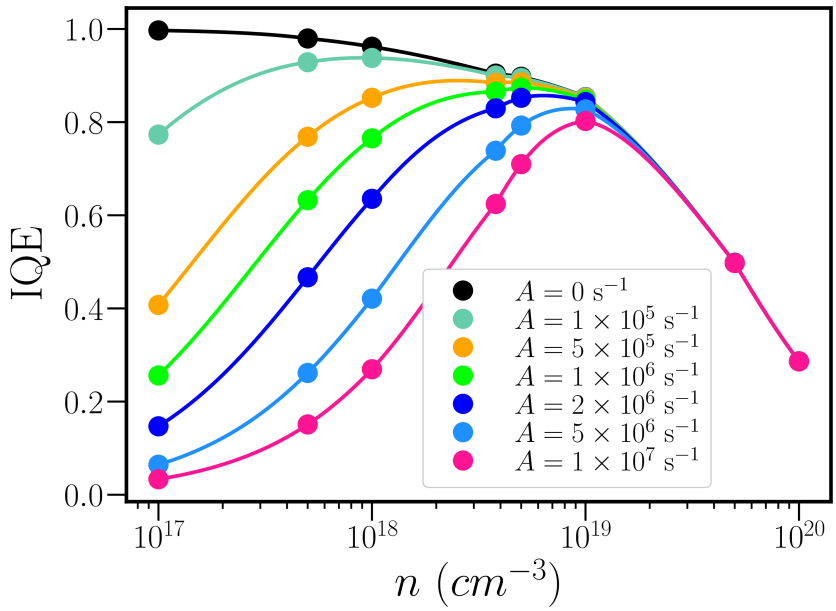


Figure 5.8: Theoretically determined IQE as a function of carrier density, n, for varying values of SRH coefficient, A.

as mentioned above, thus, it is not, for instance, an extreme value.

Although we now expect that at high carrier densities the IQE is determined by B and C, the value of A may impact the IQE behaviour in the "intermediate" carrier density range (i.e. $n = 1 \times 10^{18}$ – 1×10^{19} cm^{-3}), thus, for instance, changing the onset of the droop regime. To investigate this, Fig. 5.8 shows the IQE as a function of carrier density using our calculated B and C coefficients and a range of A coefficients. Figure 5.8 demonstrates that the impact of A becomes significant below $n = 1 \times 10^{19}$ cm^{-3}, and further shows the robustness of the high carrier density behaviour of the IQE against varying values of A. Further details on the determination of the A coefficient from experimental data is given in Ref. [2]. Lastly, Fig. 5.8 also demonstrates that already the B and C coefficients calculated in our TB framework predict droop, without considering any defect related Auger processes; a threshold for droop onset between approximately $n = 5 \times 10^{18}$ cm^{-3} and $n = 1 \times 10^{19}$ cm^{-3} is found in our calculations.

Of course, it is possible to fit the IQE curve with A, B and C as free, adjustable parameters, thus extracting a single, carrier density *independent* value for each coefficient that can describe the IQE curve. However, it has been found that when such a fitting procedure is carried out on a specific experimental sample, the same parameter set may not describe different samples [65]. This approach also neglects the fundamental underlying physics of III-N

heterostructures, particularly the screening of the built-in field, which also depends on the carrier density. We have also investigated the impact of using constant (i.e. carrier density independent) values for B and C that are evaluated at a fixed carrier density from our model. As an example, using the values of B and C determined at $n = 5 \times 10^{18}$ cm^{-3} shifts the droop onset threshold carrier density from approximately $n = 7.5 \times 10^{18}$ cm^3 to approximately $n = 2 \times 10^{18}$ cm^{-3}, and moreover, reduces the slope of the theoretical IQE in the high carrier density regime by approximately 13%. Thus, the carrier density dependence of the B and C coefficients is an important component in understanding droop and the role that Auger recombination plays for this effect.

To be able to compare theory with experiment, a key ingredient is knowledge of the carrier density in the QW. In our theoretical framework the free carrier density is input to the model, which is fixed to the required value. Experimentally, determining the carrier density in the QW is more challenging [65, 229, 255]. The PL measurements are taken in a pulsed excitation regime. In this framework a 150 fs pulse of light illuminates the sample and the PL measurement is taken over the course of many of these pulse cycles. The reported measure of PL intensity is then the intensity of emitted light integrated over a single pulse. A pulse cycle begins when the sample is illuminated by light, causing excitation. The initial carrier density, n_0, can be determined from the absorbed energy density of the pulse as the excitation occurs on a much faster timescale than recombination, i.e., the initial carrier density is not affected by recombination dynamics. The carriers then recombine, which leads to a reduction of the carrier density accompanied by a reduction of the PL intensity.

It is common for the integrated PL intensities to be divided by the initial carrier density, essentially giving a carrier density-averaged PL intensity. As a result, reported IQE(n) values are averaged over n. However, to reliably compare the *fixed* carrier density in the theoretical approach to the variable carrier density in the experimental situation, the IQE at a fixed n must be determined. R. Barrett and D. Binks at the University of Manchester developed an approach to determine IQE(n_0) [2, 256]. A brief description of the idea underlying the experimental approach is given below. Starting from the ABC

model, the carrier density decay is governed by

$$\frac{dn}{dt} = -\left(An(t) + B(n(t))[n(t)]^2 + C(n(t))[n(t)]^3\right) \ . \tag{5.1}$$

One can assume that the photon emission rate per volume, $\phi(t)$, is essentially the rate of spontaneous radiative recombination,

$$\phi(t) = Bn^2 = B(n(t))[n(t)]^2 \ . \tag{5.2}$$

Building on this, we can find an expression for the emitted photon density, Φ, as it is proportional to the integral of $\phi(t)$ over a pulse. Thus,

$$\begin{aligned}
\Phi &= \int_0^\infty \phi(t)dt \ , \\
&= \int_0^\infty B(n(t))[n(t)]^2 dt \ , \\
&= \int_{n_0}^0 B(n)n^2 \left(-\frac{dn}{An + B(n)n^2 + C(n)n^3}\right) \ , \\
&= \int_0^{n_0} \left(\frac{B(n)n^2}{An + B(n)n^2 + C(n)n^3}\right) dn \ , \\
&= \int_0^{n_0} \text{IQE}(n)dn \ ,
\end{aligned} \tag{5.3}$$

where we have used Eq. (5.1) to carry out the change of variable. Finally, by taking

$$\frac{d\Phi}{dn_0} = \text{IQE}(n_0) \ , \tag{5.4}$$

the IQE at n_0 can be determined given experimental data describing Φ.

Having done so, Fig. 5.9 a) shows the experimental IQE(n_0) in filled symbols calculated using Eq. (5.4) and the theoretically determined IQE(n_0) calculated using the definition of IQE (see Eq. (5.3)) and our calculated $B(n)$ and $C(n)$ values determined above, along with a value of $A = 2 \times 10^6$ s^{-1} for the SRH coefficient, as discussed above. Due to the process of numerical differentiation when applying Eq. (5.4) to the experimental data, there is additional scatter introduced to the data. To combat this, a Savitsky-Golay filter has been used to smooth the data [257]. Overall, Fig. 5.9 a) shows a close agreement between theory and experiment in the high carrier density regime, along with the very similar behaviours of the IQE at high carrier densities between different samples, i.e., different defect densities. We will return to discuss the similarity of the behaviour of the IQE in the high carrier density regime below.

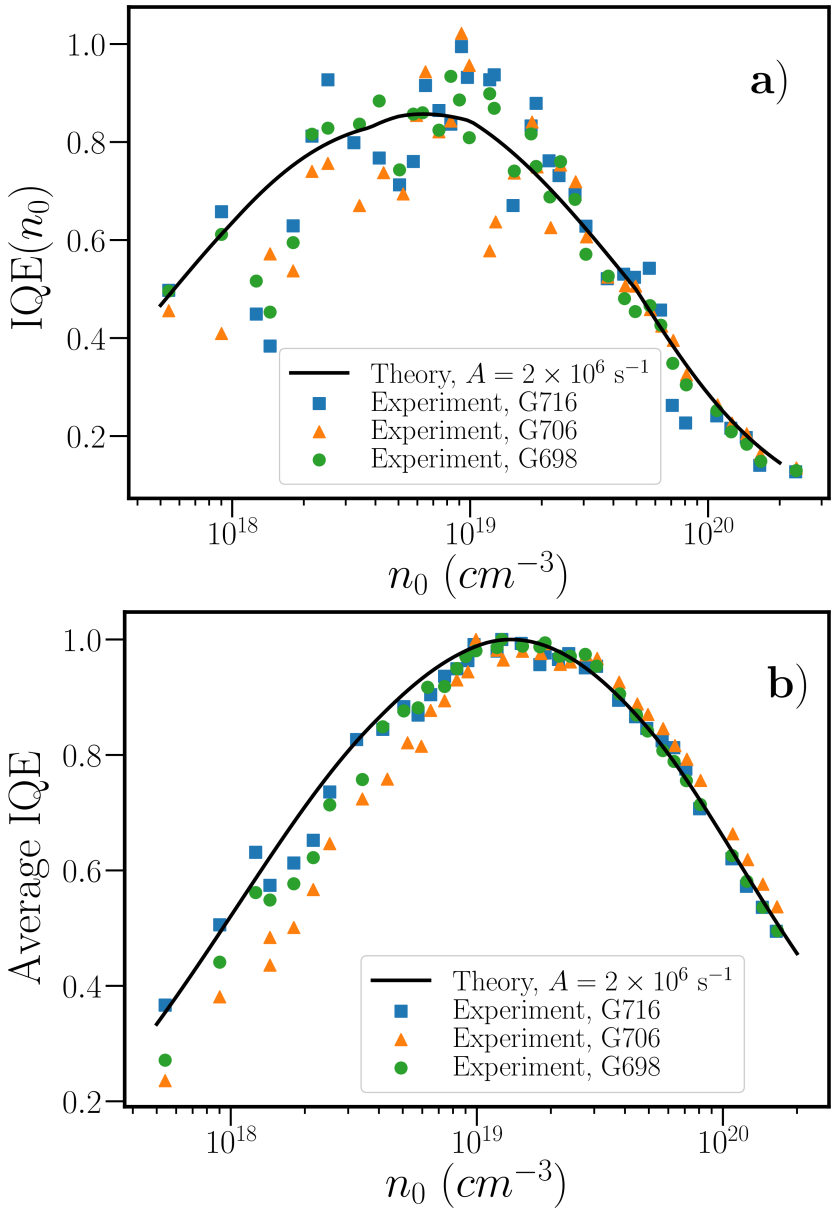


Figure 5.9: a) Experimental IQE(n_0) for all three samples (filled symbols) with the theoretically determined IQE(n_0) (black line) using a value of $A = 2 \times 10^6$ s^{-1} for the SRH coefficient. b) Experimental IQE averaged over a pulse for all three samples (filled symbols) along with the theoretically determined IQE averaged over a pulse (black line). For more details see main text. The calculations use a value of $A = 2 \times 10^6$ s^{-1} for the SRH coefficient.

Figure 5.9 a) shows the IQE at the beginning of a pulse. However, it is also possible to evaluate the average IQE over the course of a pulse. To do so experimentally, the integrated intensity is divided by the initial carrier density, as mentioned above. Theoretically, the average IQE can be determined from Eq. (5.3) and dividing by n_0. This can then be compared to the reported average experimental PL integrated intensity. Doing so yields the data

presented in Fig. 5.9 b) and shows again that the theoretically determined B and C coefficients, in conjunction with the experimentally verified A values, reproduce the experimental data closely in the high carrier density regime. It is important that the B and C parameters used here stem from the independent calculations carried out above, and are not free fitting parameters.

Overall, our analysis highlights that the carrier density dependence of the recombination coefficients is key, and experimental studies should not assume carrier density independent coefficients. This comparison also suggests that carrier localisation and polarisation field screening effects play an important role in causing droop in InGaN-based LEDs, primarily due to the impact of these factors on Auger recombination. This is further suggested when we recall that the experimental samples were grown so as to have differing point defect densities. In the high carrier density regime in Figs. 5.9 a) and b), there is no significant variation in the experimental data between the three samples. This data is also consistent with theoretical data that does not include defect-assisted processes. Thus, all this highlights that, at least for the samples studied here, defect-assisted Auger processes are likely to be of secondary importance in the droop carrier density regime.

5.3 Conclusion

In this chapter we presented an atomistic theoretical analysis of nonradiative Auger recombination processes in c-plane InGaN/GaN QWs as a function of carrier density. The model included the screening of the electrostatic built-in field with increasing carrier density. The investigation in Chapter 4 showed that at low temperatures and carrier densities, the Auger coefficients are strongly impacted by the alloy microstructure. However, as temperature and carrier density are increased and the localised states are saturated, the different microscopic alloy configurations exhibit very similar Auger coefficients. Moreover, we found that the contribution from the electron-electron-hole Auger process is of secondary importance when compared to the hole-hole-electron process, and its relative importance increases only slightly with increasing carrier density. We found Auger coefficients that vary from $C_{\text{tot}} \approx 1 \times 10^{-31}$ cm^6/s at a carrier density of $n = 1 \times 10^{17}$ cm^{-3} to $C_{\text{tot}} \approx 2 \times 10^{-30}$ cm^6/s at $n = 1 \times 10^{20}$ cm^{-3}. Thus, based on the work of Meneghini *et al.* this is already indicative that our calculated Auger coefficient values should lead to a significant droop.

Equipped with the theoretical data on the radiative and Auger recombination coefficients as functions of carrier density, we targeted a comparison to experimental data. Using samples provided by colleagues in the University of Cambridge, optical studies were carried out in the University of Manchester. Manchester established a novel method to carefully determine the carrier density in InGaN QWs when using pulsed excitation schemes. As literature data recently indicated the presence of defect-assisted Auger recombination processes in InGaN-based devices, special attention was paid to the impact of point defect density and carrier localisation effects on the droop carrier density regime behaviour of the IQE.

To do so, three different samples where grown at different growth temperatures to modify the density of point defects in the well. Using these samples, the experimental data revealed that independent of sample (i) droop onset occurs at similar carrier densities in the well and (ii) the high carrier density regime evolution of the integrated PL intensity was basically identical. All this indicated that trap-assisted (defect related) Auger recombination seems to be of secondary importance for the studied samples.

Furthermore, when using our calculated carrier density dependent radiative and Auger recombination coefficients, excellent agreement was found between theory and experiment for not only the onset of droop, but also the evolution of the IQE in the high carrier density regime. Although we found that the carrier density dependent droop may be driven by Auger recombination intrinsic to the active region, the analysis also found a peak IQE of 70%, relatively high for a green emitting QW. Thus, our study suggested that factors external to the QW, such as injection efficiency or carrier distribution homogeneity (to avoid regions of locally high carrier density), should be targeted for improving the efficiency of longer wavelength visible III-N emitters. Having established the theoretical framework to investigate the recombination rates in visible InGaN-based emitters, we now turn to UV emitting AlGaN-based QWs.

Chapter 6

Temperature dependent radiative and Auger recombination in AlGaN/AlN QWs

6.1 Introduction

As discussed above in the Prologue, III-N semiconductors can, in principle, be used to create efficient light emitters operating from the deep UV spectral range all the way to the red emission wavelength window. The material of choice is InGaN for visible emitters and AlGaN alloys for UV emitters. However, in comparison to InGaN systems, AlGaN QWs have received far less attention, particularly in terms of understanding the fundamental properties of AlGaN-based emitters. AlGaN-based QWs have recently attracted significant research attention for use in UV LEDs, including potentially into the deep UV range ($\lambda < 280$ nm) [22]. Over the last few years, spurred by a renewed interest in developing fast, efficient and safe methods of anti-microbial sterilisation due to the COVID-19 pandemic [258] interest in these systems has grown rapidly.

The UV spectral range is generally divided into three sub-ranges, UVA (400 nm to 315 nm), UVB (315 nm to 280 nm) and UVC (also called the deep UV range, < 280 nm). All three UV regimes have numerous applications. For instance, UVA has applications in the curing of polymers, resins and inks, while UVB is used in phototherapies for the treatment of various skin diseases, as well as to generate extra nutrients in vegetables when used in plant growth lighting.

Relevant to COVID-19, it has been found that UV light with wavelengths near 265 nm is the most effective for anti-microbial sterilisation, and, in general, UVC emitters in the wavelength range of 250 nm to 280 nm have been targeted for use in large-scale water, sewage and other sterilisation treatment applications. An overview of these applications can be found in Ref. [22].

Overall, UV LEDs could form the basis for robust, long-lived and wavelength tunable light-emitting devices for use in a wide range of applications. They may provide a route to UV light emission that is more efficient and much more environmentally friendly than conventional UV emission technologies (e.g. those that incorporate mercury [22]). Although SQW and MQW AlGaN-based UV LED systems have been realised in research settings, they generally suffer from very low wall plug efficiencies (WPEs), especially when compared to high quality commercial InGaN-based devices. This disparity in efficiency may stem from a number of sources, for instance due to large defect densities when growing on sapphire substrates or issues with *p*-type doping [22]. A comprehensive discussion of the current state-of-the-art, along with details of the technical challenges facing UV LEDs, can be found in Ref. [259], and we will briefly mention some examples of these challenges now.

For example, the WPEs of AlGaN-based UVB and UVC LEDs currently lag behind UVA devices, and so industrial scale production of AlGaN QW-based UVB and UVC LEDs has not become widespread, although several companies have started to commercialise UV LED devices (particularly in the UVA range) [22]. UVB and UVC LEDs may suffer from poorer light extraction efficiencies in comparison to UVA LEDs due to the higher Al compositions required to access smaller wavelengths, along with the differences in electronic structure between AlN and GaN mentioned above and discussed in, for instance, Ref. [57]. These shorter wavelength emitters also currently suffer from high threading dislocation densities, which contribute to stronger nonradiative recombination [22]. Understanding the fundamental properties of these emitters is crucial to overcoming these efficiency bottlenecks.

Although there have been studies investigating the fundamental material properties and electronic structures of bulk AlN and AlGaN [260, 261, 262, 263], relatively few studies target an understanding of the electronic and optical properties of AlGaN QWs, despite their potential for use in energy efficient and environmentally friendly UV LEDs [259]. For instance, even though AlGaN QW systems also exhibit both

thermal [32, 264, 265] and carrier density dependent droop [35, 266, 267, 268, 269], the fundamental origin of either form of droop in AlGaN QWs is still unclear. Furthermore, knowledge of the processes contributing to InGaN QW efficiency droops cannot be directly applied due to the fundamental differences of AlN compared to InN and GaN alloys, for example differences in structural or polarisation properties, or the more complicated orbital character of the valence band edge in AlN. In this chapter, we seek further insights into the electronic structure of AlGaN QWs, the effect of carrier localisation in these systems and the resulting impact on the radiative and Auger recombination rates. Before proceeding, we briefly discuss some recent relevant literature results on AlGaN QWs.

Generally, most experimental studies reporting data on optical properties in AlGaN-based QWs do not go beyond the ABC model of recombination described above [35, 264, 267, 268, 270]. Other approaches use continuum-based models, such as Ref. [271], that do not take alloy fluctuations into account. In InGaN QW systems the effect of carrier localisation is reflected in, for instance, the "S"-shaped dependence of the PL peak on temperature, and also in the broadening of low temperature PL peaks (see above in Sec. 1.4). Both of these features have also been observed in AlGaN-based QWs, indicating that AlGaN systems also experience carrier localisation effects [217, 218]. As we have seen above in Chapters 4 and 5, in the case of InGaN-based systems, carrier localisation effects can have a major impact on not only the electronic structure, but also the recombination processes and efficiency of these systems. Thus, an understanding of the impact of carrier localisation on the underlying electronic structure of AlGaN QWs is required before we can target optical properties. As we have discussed throughout this thesis, the accurate description of carrier localisation effects in III-N QWs requires, ideally, an atomistic resolution.

Recently, the work of Ref. [57] has targeted this gap in understanding by employing a similar theoretical framework to that described above for InGaN QWs; i.e., an sp^3 empirical tight-binding model in conjunction with a valence force field model, as well as a local strain and polarisation theory. In that work, AlGaN QWs of varying Al contents embedded in pure AlN barriers were investigated. With the assumption of random alloy fluctuations in the well region, a number of microscopic configurations were investigated and the carrier ground and excited states determined for each.

They found a broadening of the fundamental transition energy of the wells due to the impact of the alloy microstructure, and that although there is variation in both the electron and hole ground state energies, the impact is larger for the holes. Analysis of the charge densities of the ground states showed the impact of random alloy fluctuations on the carrier wave functions, including the very strong hole localisation. Notably, at higher Al contents, $\geq$ 50%, the ground state electron wave function was also affected by the alloy microstructure in some configurations, however this effect was less pronounced for excited electron states. This stands in contrast to typical InGaN QWs (i.e. with In contents from 10% to 20%), in which the impact of the alloy fluctuations is generally small for all electron states, although, as the authors point out, a direct comparison between the systems is not possible due to the differences in low band gap material content and the experimentally challenging nature of growing a high quality InGaN QW with an In content $\geq$ 50%.

Thus, the work in Ref. [57] shows that alloy fluctuations lead to carrier localisation effects in AlGaN QWs, and can affect the electronic structure. Based on our experience with InGaN QWs in Chapters 4 and 5 we expect that the recombination processes in AlGaN QWs will also be impacted by carrier localisation. With regard to carrier density dependent droop in InGaN QWs, our results in Chapter 5, consistent with the literature, show that the Auger recombination process (or a related process) is one of the most important factors. Despite the studies mentioned earlier in this section reporting carrier density dependent (and thermal) droop in AlGaN QWs, the importance of Auger recombination in causing these efficiency droops has not been studied in detail.

In order to shed light onto these questions about the links between both types of droop and the recombination processes, the corresponding recombination coefficients must be determined. As we have previously discussed, the *experimental* determination of recombination coefficients is, in general, non-trivial and requires fitting to experimental data that can give rise to much uncertainty. The few studies targeting an analysis of Auger recombination report significant Auger coefficients in AlGaN QWs of $C_{\text{tot}} \sim 1 - 4 \times 10^{-30}$ cm^6/s [35, 267, 268]. However, issues with the use of the temperature dependent PL approach used to determine the efficiency droop have also been raised by Nippert *et al.* [35]. This approach may introduce errors as low temperature efficiency is assumed to be perfect.

In their study of 1.5 nm wide, c-plane $Al_{0.45}Ga_{0.55}N$ QWs in pure AlN barriers, Nippert *et al.* reported that the process governing efficiency droop is indeed an internal loss mechanism (i.e. is not related to carrier injection or light extraction) [35]. Furthermore, their results indicated that this internal loss mechanism is, in fact, Auger recombination. With careful experimental analysis they extracted a value for the Auger coefficient of $C = 3.4 \times 10^{-30}$ cm^6/s. They also determined a value for the radiative coefficient of $B = 2.4 \times 10^{-11}$ cm^3/s. Other experimental reports investigating recombination rates targeted wider wells ($\sim$ 2.4 nm) compared to Nippert *et al.* above, such as in Ref. [268]. However, in that study, the Al contents of both the well and barriers differ to the studies above, having 57% Al in the well region and 81% Al in the barrier. Furthermore, although Ref. [268] reports radiative ($B = 2.13 \times 10^{-11}$ cm^3/s) and Auger ($C = 2.88 \times 10^{-30}$ cm^6/s) coefficients, the assumption of carrier density independent coefficients is made in order to fit the coefficients to experimental IQE data.

Another experimental work highlighting the impact of carrier localisation effects investigated a range of QW widths between 1.5 nm and 3 nm, with similar Al content in the well ($\sim$ 50%) and pure AlN barriers [97]. They found that well width strongly impacts the strength of carrier localisation due to the strength of the built-in polarisation field. However, that study did not report radiative or Auger recombination rates. We will return to the discussion of experimental results for B and C, as well as the impact of carrier localisation, below. However, we note that generally experimental studies reporting recombination rates continue to work in the ABC model [35, 264, 267, 268, 270] and thus we will also continue in that framework.

Before discussing the impact of carrier localisation on the electronic structure of the AlGaN QWs studied here, and subsequently the temperature dependence of the radiative and Auger recombination rates, we briefly discuss the theoretical framework for the study and the QW model systems targeted.

6.1.1 Theoretical framework and quantum well model systems

As mentioned above, when investigating carrier localisation effects in III-N QWs, ideally an atomistic resolution is required. We note that an approach using a modified continuum-based model can be found in Ref. [42], in which

the authors take localisation of the hole wave function into account as an input parameter to the model, while assuming that the electron wave functions are completely delocalised. As we have discussed above, the work of Finn *et al.* in Ref. [57] suggests that, to an extent, electron wave functions may also be impacted by alloy fluctuations. We have seen in previous chapters, and it is also discussed in the literature [272], that continuum-based approaches may underestimate the impact of carrier localisation. Thus, we approach the problem with the atomistic sp^3 empirical tight-binding (TB) model described above in Chapter 2. The model was modified for the analysis of AlGaN/AlN QWs and wave functions and energies were determined by R. Finn in the Photonics Theory Group at the Tyndall National Institute. We now aim to use these existing wave functions and energies as input to the framework for determining the recombination rates described above in Chapter 3.

Before proceeding, we briefly recap the ingredients to the model used and established by R. Finn to determine the wave functions and energies. In line with experimental studies on the structural properties of AlGaN QWs, a random alloy distribution of Al and Ga atoms in the well was assumed [214]. The wave functions and energies for 150 electron and 150 hole states for 20 alloy configurations (i.e. microscopic distributions) were calculated. The simulation supercells had dimensions of $(10 \times 9 \times 10)$ nm^3 (containing approximately 82,000 atoms). Due to the computational load of Auger recombination rate calculations, in this study we focus on the QW structures investigated by Finn *et al.* in Ref. [57] that are similar in composition to those in the experimental work of Frankerl *et al.* [97] and Nippert *et al.* [35]. Here, the active region consists of a single approximately 2.85 nm wide $Al_{0.5}Ga_{0.5}N$ QW embedded in pure AlN. This Al content is similar to the 45% Al QW investigated by Frankerl *et al.* and Nippert *et al.*. However, the wells investigated here are (slightly) wider, compared to the 2.5 nm wells in Ref. [97] and the 1.5 nm wells investigated in Ref. [35]. We will discuss below how the obtained results may be affected by the well width.

Using the TB wave functions and energies as input, we employ the same framework detailed in Chapter 3 for the determination of the B and C coefficients in InGaN systems, with modifications for AlGaN. We continue to use a Sellmeier-type description of the wavelength dependent refractive index, $n(\lambda)$, but using the coefficients for AlN of $A = 1.00$, $B = 3.12$ and $C = 138.0$ nm given in Ref. [213]. Previously, for InGaN/GaN QW systems we used the high frequency dielectric constant of the barrier (GaN) material ($\epsilon_\infty(\text{GaN}) = 5.5$),

as this approach was employed in other studies of InGaN/GaN systems [40]. In this study, we assume a 50/50 ratio of AlN and GaN such that $\epsilon_\infty(\mathrm{Al_{0.5}Ga_{0.5}N}) = 5.0$, based on a dielectric constant for AlN of $\epsilon_\infty(\mathrm{AlN}) = 4.64$. This value for AlN is determined from the average of the values reported in Ref. [221] for two theoretical investigations ($\epsilon_\infty^{\text{theo, a}}(\mathrm{AlN}) = 4.61$; $\epsilon_\infty^{\text{theo, b}}(\mathrm{AlN}) = 4.62$) and an experimental investigation ($\epsilon_\infty^{\text{exp}}(\mathrm{AlN}) = 4.68$).

We have also adapted the 1D self-consistent Schrödinger-Poisson framework for determining the screening of the built-in polarisation field when charge carriers are introduced into the well. In InGaN QWs we saw above that the screening of the built-in field can have a significant impact on the electronic structure above a carrier density of approximately $n = 1 \times 10^{19}$ cm^{-3} [1]. To adapt the model for AlGaN QWs we have used parameters for spontaneous and piezoelectric polarisation for AlGaN linearly interpolated from AlN and GaN parameters available in Ref. [82] for the determination of the polarisation field. We have used band offsets available in Ref. [263] and average strain fields extracted from our TB model. Having adapted the framework, we determined that at the low carrier density investigated here, $n = 2.5 \times 10^{18}$ cm^{-3}, there is no significant screening of the built-in field. This carrier density has been chosen as it is in the range widely investigated and reported as typical for AlGaN QWs [35, 265, 267, 270, 271].

We note that in InGaN QWs it has been suggested that at carrier densities below approximately $n = 1 \times 10^{18}$ cm^{-3} Coulomb enhancement of the radiative recombination coefficient may be observed [235]. Carrying this assumption over to the AlGaN systems here, we expect that Coulomb effects are of secondary importance at the carrier density we investigate. However, future studies may target this question explicitly for AlGaN QW systems. Having now discussed the QW structures and theoretical framework used to determine the electronic structure, along with how AlGaN specific aspects are included in the calculation of the radiative and Auger coefficients in AlGaN/AlN QWs, we are in a position to analyse and investigate the impact of carrier localisation on the results.

6.2 Results

We begin by first looking at the electronic structure of c-plane $\mathrm{Al_{0.5}Ga_{0.5}N}$/AlN QWs, before turning to the radiative and Auger coefficients, and the

competition between the radiative and Auger coefficients as a function of temperature.

6.2.1 Electronic structure

The electronic structure can strongly affect the recombination rates, where the recombination rates are determined as above in Chapter 3, particularly via the wave function overlap. By looking at the charge densities of the electronic states we can gain some first insights into the impact of carrier localisation on the electronic structure and thus on the recombination rates. In the following we will discuss the electronic structure and point out some expected consequences for the radiative and Auger recombination rates along the way.

When considering the Auger recombination rates, the estimation is complicated by the need to factor in the electron-electron wave function overlap and the hole-hole wave function overlap for the eeh and hhe Auger recombination processes, respectively. As discussed above, for the configurations investigated here, *excited electron* states tend to not be greatly perturbed by the alloy disorder and are generally delocalised over the growth plane. Thus (and as we will see below), variations in both radiative and Auger recombination rates between microscopic configurations are primarily driven by variations in hole localisation characteristics (i.e. how strongly localised the hole states are, where they are localised in relation to the electron or other hole states, hole state energies, etc.). On top of this, given our observations of hole localisation being linked to enhancement of the hhe Auger process, as well as the observation of a much larger hhe Auger rate in comparison to the eeh rate in InGaN/GaN QWs above in Chapter 5, in the analysis that follows, we focus mainly on the nature of hole states, and only briefly discuss the electron ground state.

Figure 6.1 shows isosurface plots of the ground state electron (red) and hole (blue) charge densities, along with the first (green) and second (purple) excited hole states for a sample of three microscopic alloy configurations from the 20 investigated. Figure 6.1 shows both a “Side View”, in which we can see the c-direction separation of the electron and hole states due to the built-in field, and also a “Top View,” in which the varying in-plane separation of both carriers can be observed. The dark isosurfaces represent 40% of the maximum value of the charge density, and the light isosurfaces represent 10%.

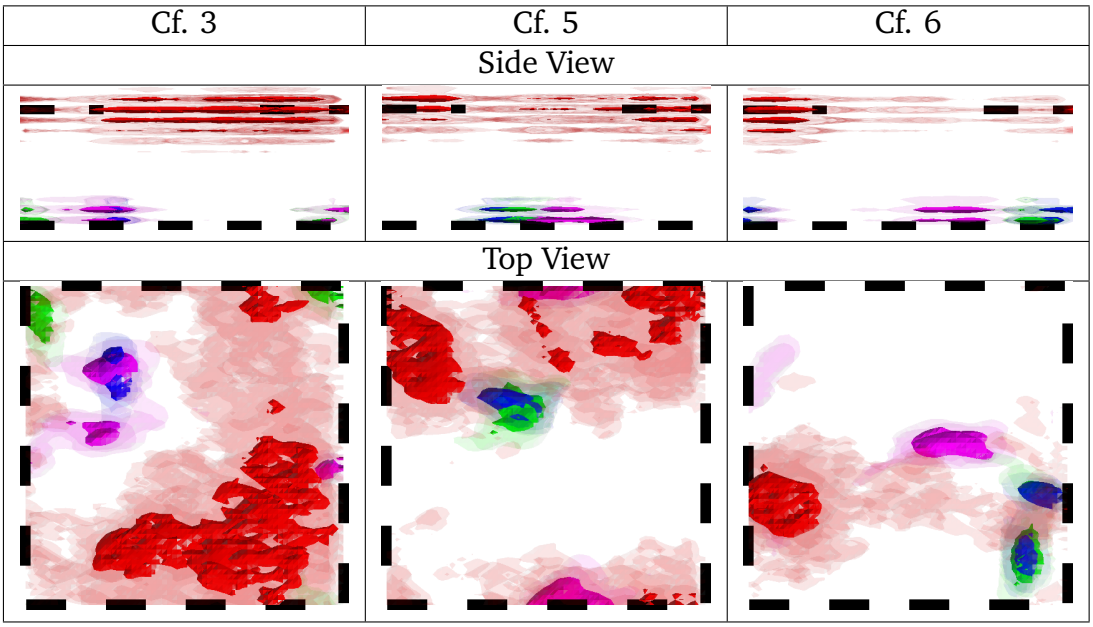


Figure 6.1: Isosurface plots of the charge densities of the electron ground state (red), hole ground state (blue), first excited hole state (green) and second excited hole state (purple) for three configurations (Cfs. 3, 5 and 6) of a 2.85 nm wide c-plane $Al_{0.5}Ga_{0.5}N$/AlN QW. The light (dark) isosurfaces correspond to 10% (40%) of the respective maximum charge density.

Starting with some common features of the configurations (Cfs.), in the "Top View" we can see that all three Cfs. exhibit strong hole localisation, not only of the ground state (blue) but also the first two excited states (green and purple). Also, in all three Cfs., the electron ground state (red) is less perturbed by the alloy fluctuations compared to the hole states. However, this effect is less pronounced for Cf. 6, for example, compared to Cf. 3, i.e., the electron ground state in Cf. 6 appears to be more strongly localised than in Cf. 3.

Continuing to look at the Top View, although there is strong hole localisation exhibited by all three Cfs., in Cfs. 5 and 6 the hole ground state and first excited state are spatially co-localised, in contrast to Cf. 3. In Cf. 3 however, the second excited hole state is co-localised with the hole ground state, while these hole states are spatially separated in Cfs. 5 and 6. The Top View of the charge density visualisations is also indicative of the spatial separation of the electron and hole ground states, although the spatial relationship between these states varies significantly between configurations. Before moving on, we note that in Cfs. 3 and 5 the hole ground state has one localisation centre. In Cf. 6 the hole ground state appears to have two localisation centres in the bottom right of the Top View figure, both spatially separated from the electron ground state. However, in the bottom left of the Cf. 6 Side View figure, we can

see that part of the hole ground state is localised under the electron ground state, and so is not visible in the Top View. This spatial co-localisation of the electron and hole ground states may have a significant impact on the wave function overlaps.

Overall, it is clear that the alloy microstructure will strongly impact the hole states. Furthermore, we have seen that the alloy microstructure can also impact the electron ground state, and thus the spatial relationship between the electron ground state and valence "band" edge hole states. Although it is possible to pick out some general features of the wave function localisation from the plots in Fig. 6.1, we now seek to quantify and gain further insight into the wave function overlap via calculating and analysing the dipole matrix elements between states.

The dipole matrix element (DME) between an electron and a hole state is proportional to the wave function overlap between those states and is an essential ingredient in the calculation of the radiative recombination rate (see Sec. 3.1). The DMEs between the electron ground state and the 10 energetically lowest hole states for Cfs. 3, 5 and 6 are presented as a function of the hole state number, j, in Fig. 6.2. The first three DMEs shown in Fig. 6.2, for instance, are related to the overlaps between the electron ground state ($i = 0$) and the first three hole states (ground, $j = 0$; first excited $j = 1$; second excited, $j = 2$) displayed above in Fig. 6.1.

Beginning with the DMEs between the electron and hole ground states, the effect of spatial co-localisation/separation becomes clear. For example, above we noted that for Cf. 6 although the two main localisation centres of the hole ground state were spatially separated from the electron ground state, the third localisation centre was actually co-localised with the electron ground state. In Fig. 6.2 we see a large DME for the hole ground state ($j = 0$) in Cf. 6 in comparison to the hole ground state DMEs for Cfs. 3 and 5. In stark contrast, for Cf. 3 we noted that the electron and hole ground states were spatially separated, which is reflected in the much smaller ground state DME for Cf. 3 compared to Cfs. 5 and 6. Cf. 5 then lies somewhere in the middle. From this analysis we may expect that, at least at low temperatures (T $\approx$ 10 K), when mainly the ground states are populated, the radiative recombination rate for Cf. 6 will be larger than Cf. 5, and the rate for Cf. 5 will be larger than for Cf. 3.

As temperature is increased above 10 K, excited states will be populated and

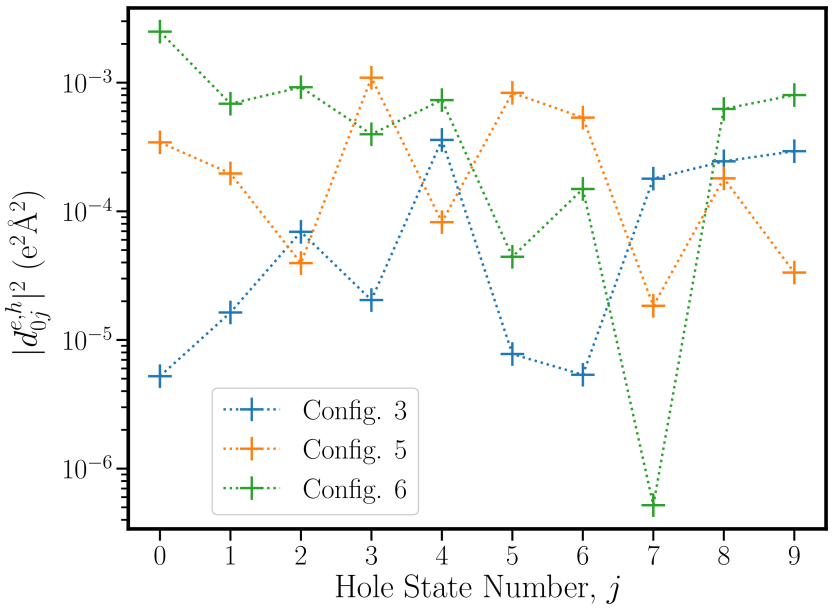


Figure 6.2: Dipole matrix elements, $|d_{ij}^{e,h}|^2$, (see Sec. 3.1) between electron ground state and varying hole states (j) for three configurations (Cfs. 3, 5 and 6) of a 2.85 nm wide c-plane $Al_{0.5}Ga_{0.5}N$/AlN QW.

thus will contribute to the radiative recombination rate. Looking at the DMEs between the electron ground state and excited hole states ($j > 0$), Fig. 6.2 shows that the alloy microstructure impacts the DMEs involving excited hole states, as well as the hole ground state. Looking at Cf. 6, there is an overall decreasing trend of DME with increasing hole state number, at least until the 7$^{\text{th}}$ excited hole state. For hole states energetically higher than the 7$^{\text{th}}$ excited state the DMEs begin to increase again but excited electron states will also begin to contribute and the situation becomes more complicated due to the Fermi-Dirac statistical weightings. Thus, the related B coefficient may exhibit very difference trends for different alloy configurations. A similar argument may hold for Cf. 3, leading to a contrasting trend where the radiative recombination rate will increase in the low temperature range due to the increasing trend of DME with increasing hole state number seen in Fig. 6.2. For Cf. 3, for hole states with $j > 2$, the trend of DME with hole state number is less clear than in the Cf. 6 case. However, again, at temperatures high enough for these states to be significantly populated the Fermi-Dirac weighting and contributions from excited electron states complicate the analysis. For Cf. 5, in the low temperature range we may expect a decrease of radiative recombination rate with temperature, due to the decreasing trend of DME with increasing hole state number up to $j = 2$.

So far we have only discussed our expectations for the impact of the alloy

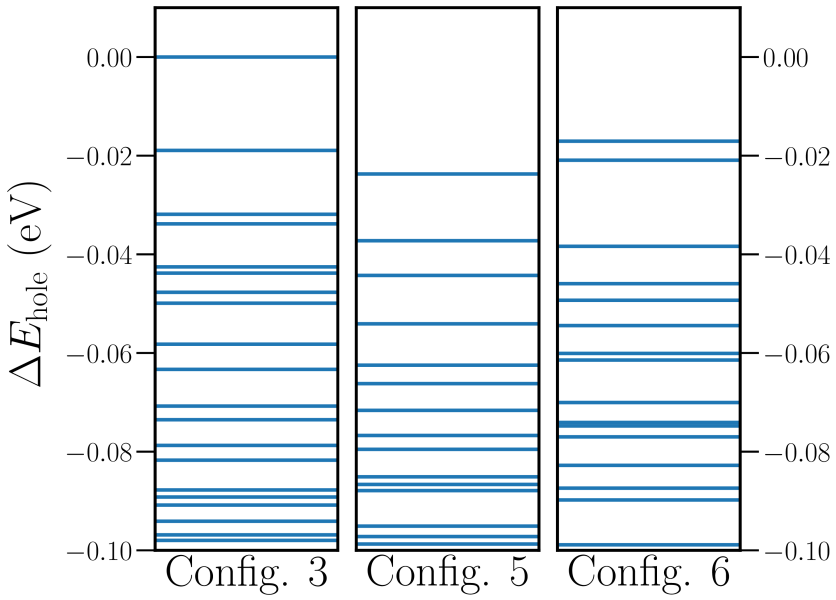


Figure 6.3: Energy difference, ΔE_{hole}, between the hole ground state and excited hole states for Cfs. 3, 5 and 6 for a 2.85 nm wide c-plane $Al_{0.5}Ga_{0.5}N$/AlN QW. The data are normalised to the energy of the hole ground state of Cf. 3. States within 100 meV of the Cf. 3 hole ground state energy are shown. Horizontal blue lines represent the energy differences between hole states and the Cf. 3 hole ground state.

microstructure on the radiative recombination rate, based on the impact of alloy fluctuations on the DMEs. As mentioned above, extending this analysis to Auger recombination is complicated by the contributions from electron-electron (for eeh Auger) and hole-hole (for hhe Auger) wave function overlaps. On top of the added complexity due to the introduction of electron-electron and hole-hole overlaps, the temperature dependence of not only the eeh and hhe Auger rates, but also the radiative rate, will be affected by the energetic distribution of states. The population of higher lying states is described by Fermi-Dirac statistics and will depend on this energetic spacing (see Sec. 3.1). Before discussing our results for the radiative and Auger recombination rates directly, we briefly look at the energy level spacing of the hole states of the three configurations above, to gain some insight into how the carrier localisation effects impact the energetic separation of states. We note that the conduction states are generally distributed in a similar manner when comparing different configurations and behave as might be expected from a VCA description. This is shown in more detail by Finn *et al.* [57].

Figure 6.3 shows a representation of the difference in energy between the hole ground state and excited hole states for Cfs. 3, 5 and 6. The data are

normalised to the Cf. 3 hole ground state, and states within 100 meV of this reference level are shown. We see that there is a significantly different valence "band" structure between configurations. This is particularly clear for Cf. 6, in which the first excited hole state is very closely spaced in energy to the hole ground state ($\Delta E = 4$ meV), in stark contrast to Cf. 3 ($\Delta E = 19$ meV) and Cf. 5 ($\Delta E = 13$ meV). Such a close energy spacing results in the first excited state being significantly populated even at T = 10 K. Thus, we might expect the radiative and Auger recombination rates to be enhanced in Cf. 6. For the radiative rate, even at T = 10 K there will be a contribution from not only the hole ground state, but also the first excited hole state, in contrast to Cfs. 3 and 5. For the hhe Auger rate, the contribution from the first excited hole state may bring a further enhancement effect due to the strong co-localisation of the hole ground state and first excited hole state seen in Fig. 6.1, via the hole-hole overlap entering the hhe Auger rate calculation.

The energy level spacings of Cfs. 3 and 5 differ from Cf. 6 but also from each other. In Cf. 3, as mentioned, the first excited hole state is approximately 20 meV below the hole ground state, but subsequent pairs of hole states are closely spaced. For example, the second and third excited holes states ($\Delta E = 2$ meV), the fourth and fifth excited hole states ($\Delta E = 1$ meV) and the sixth and seventh excited hole states ($\Delta E = 2$ meV) are closely spaced. Although, the spacing between the last two pairs (fourth/fifth and sixth/seventh) is only 4 meV so this may be closer to a group of four states. Regardless, in contrast, the energy spacing in Cf. 5 is more uniform down to states approximately 90 meV below the reference level.

With this contrast in mind, we might expect that as temperature increases, in Cf. 3 the states in pairs will be populated in quick succession, and so we might expect a stronger increase in the radiative and Auger rates compared to Cf. 5. This may be compounded by the generally increasing trend of DME with hole state number seen above in Fig. 6.2. In Cf. 5 the situation is less clear although our expectation above, i.e., that there is an initial decrease in the radiative recombination rate (based on the DMEs in Fig. 6.2) as temperature increases, may still be reasonable. Subsequently, as temperature continues to increase, higher lying, delocalised hole states (with larger overlaps with the electron states compared to the strongly localised hole states of Cf. 5) will start to contribute, potentially leading to an increase in the radiative recombination rate with increasing temperature for Cf. 5. Overall though, it is difficult to predict how the system will behave with increasing temperature. The impact

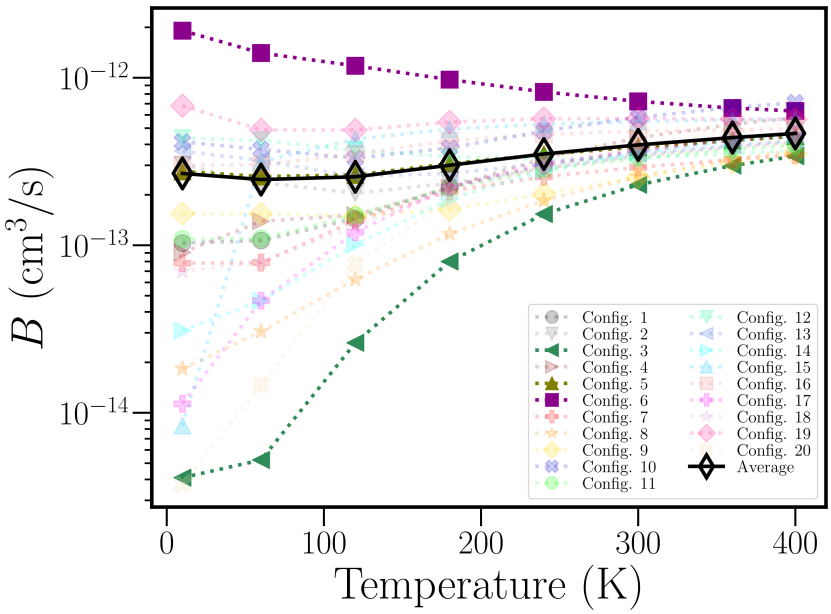


Figure 6.4: Radiative recombination coefficient, B, as a function of temperature for 20 microscopic configurations of a 2.85 nm wide c-plane $Al_{0.5}Ga_{0.5}N$/AlN QW. The average value of the coefficients (Average) taken over the 20 configurations is also presented. The carrier density is $n = 2.5 \times 10^{18}$ cm^{-3}. Configurations used in Auger recombination study (Cfs. 3, 5, and 6) are highlighted, see main text for details.

of the spatial co-localisation or separation of states introduces significant complexity when considering the population of excited states.

Overall, we have seen that alloy fluctuations can strongly impact the energetic distribution, as well as the spatial distribution of states (e.g. hole states can co-localise, electron and hole states are spatially separated along the growth direction but can co-localise in the growth plane, etc.), and thus, the wave function overlap. We also discussed the impact that we expect from these features (i.e. the spatial and energetic distributions of states and the wave function overlaps of states) on the radiative and Auger recombination processes. With these effects in mind, we now turn to look at the coefficient of radiative recombination, B, as a function of temperature. Subsequently we will discuss the results for the Auger recombination coefficients, C_{eeh} and C_{hhe}, as a function of temperature, as well as the total Auger coefficient, C_{tot}, and lastly the competition between B and C_{tot}.

6.2.2 Radiative recombination

We begin our discussion of the radiative recombination rate by presenting the B coefficient as a function of temperature for a 2.85 nm wide $Al_{0.5}Ga_{0.5}N$/AlN

QW in Fig. 6.4. We note a large variation in magnitude in the value of B at low temperatures (T = 10 K). We attribute these variations to differences in the alloy microstructure between configurations. At low temperatures mainly the "band" edge states are populated, which we saw above, for three example configurations in Fig. 6.1, are significantly impacted by the alloy fluctuations. Returning to Fig. 6.4, we see that the variation in B between configurations at a given temperature decreases as temperature increases. This is due to the population of higher lying, less localised states. These excited states, due to their extended nature, are not as strongly affected by the underlying variations in alloy disorder potential. This effect is also seen for B as a function of temperature in InGaN/GaN QWs above (see Sec. 4.2).

In terms of the evolution of B with temperature, we see that on average, B increases slightly with increasing temperature. The magnitude of the increase is similar to that observed in InGaN QWs (see Fig. 4.4 in Sec. 4.2), and stands in contrast to the usually expected decrease in B with increasing temperature observed for other, more conventional III-V semiconductor QW structures (see discussion in Sec. 4.2). We note that only one configuration shows the opposite trend, Cf. 6, with B decreasing as temperature increases across the whole temperature range studied.

For 50% of the configurations, B increases with increasing temperature across the whole studied temperature range. For the other 50%, there is an initial decrease of B with increasing temperature between 10 K and approximately 60/120 K, before B begins to increase with increasing temperature for higher temperatures. Generally, we also attribute this behaviour to the population of higher lying, less localised states as temperature increases. We will discuss the differing behaviour of Cf. 6 below. We will also analyse the behaviours of Cfs. 3 and 5, as these three configurations (Cfs. 3, 5 and 6) represent the wide range of possible situations seen for B as a function of temperature in Fig. 6.4. Configuration 6 is strictly decreasing with increasing temperature, Cf. 3 is strictly increasing and Cf. 5 initially decreases before starting to increase subsequently.

For the majority of configurations, as temperature increases excited hole states that are less localised will be populated with two resulting effects. Firstly, there will be more states contributing to the radiative recombination rate. Secondly, these less localised states (including less localised hole states) may have larger wave function overlaps with the extended electron states (see the

DMEs in Fig. 6.2). Thus, the evolution of the B coefficient indicates that these effects start to dominate for temperatures greater than approximately 120 K.

However, as mentioned, Cf. 6 does not follow this generally increasing trend and the behaviours of B for Cfs. 3 and 5 are also different from Cf. 6, and each other. So, we now examine the dependence of the B coefficient on temperature for each of these configurations. For Cf. 6, we noted above that we expected an overall larger B coefficient at low temperature (T = 10 K) compared to Cfs. 3 and 5 due to the spatial co-localisation of the electron ground state and part of the hole ground state (see Fig. 6.1). On top of this, we noted that the first excited hole state is also strongly localised and energetically close to the hole ground state, and so will contribute to B even at T = 10 K, which further contributes to enhancing it compared to the other configurations. This effect explains why the 10 K B coefficient for Cf. 6 is much larger than Cfs. 3 and 5 in Fig. 6.4. However, as temperature increases we would (as is the case for the other configurations) expect that the higher lying states, being less localised, contribute larger DMEs, on average, and thus B should increase.

To understand the behaviour of Cf. 6 we consider again the idea that the excited, extended states are less perturbed by the alloy microstructure. So, we expect that the DMEs of the excited states of Cf. 6 may be, on average, similar to the DMEs of the excited states of Cfs. 3 and 5. Indeed, for Cf. 6 the large electron hole ground state DME is larger than the average value of the DMEs between the electron ground state and all of the hole states of Cf. 6. Thus, as temperature increases, the higher lying states are given larger weightings by the Fermi-Dirac statistics at the cost of reducing the contributions from the strongly localised states. As a consequence, the importance of the strongly localised states for the overall B coefficient is diminished and Cfs. 3, 5 and 6 all give similar values in the high temperature range. For Cf. 6 this effect manifests as a decrease in B as temperature increases. For Cfs. 3 and 5 the opposite is true and the electron hole ground state DME is smaller than the respective averages of the DMEs between the electron ground state and the hole states. Thus, overall, as temperature increases, DMEs for excited states contribute more. These contributions are larger compared to the band edge state DMEs, and they now contribute more, leading to an increase in B.

Turning to look at the low temperature ($\lessapprox$ 180 K) behaviours of B for Cfs. 3 and 5 we see different evolutions with increasing temperature. For Cf. 3, from

T = 10 K to T = 60 K, there is a slight increase in B, before a much stronger increase up to T = 180 K. For Cf. 5, in contrast, B decreases from T = 10 K to T = 60 K, before a much slower increase up to T = 180 K. We attribute this difference to effects described above, i.e., that the first few DMEs in Fig. 6.2 are increasing for Cf. 3 and decreasing for Cf. 5, and due to the structure of the valence "band" in Fig. 6.3. For Cf. 3, pairs of states will begin to contribute as temperature increases, whereas the more uniform energetic distribution of states in Cf. 5 means only single states may contribute. Thus, we expect that the less strong increase of B with temperature above T = 60 K (for Cf. 5 compared to Cf. 3) is due to the valence "band' structure.

We turn now to the overall magnitude of the B coefficient and how it compares to experimental results. Overall, factors such as Al content, carrier density and well width will significantly affect the built-in potential and thus the electronic and optical properties of AlGaN QWs. For instance, experimentally, Frankerl *et al.* investigated a range of well widths (from 1.5 nm to 3.0 nm) with similar structural characteristics to the QWs studied here ($\sim$ 45% Al content, AlN barriers) and found that efficiency decreases, which could be linked to a decrease in the B coefficient [97]. From our discussion of the built-in field in InGaN/GaN QWs above, we expect that a stronger built-in field will lead to a smaller B coefficient, and that a wider well will also lead to a smaller B coefficient due to the larger potential drop between the QW interfaces and resulting increase in carrier separation along the growth direction. For AlGaN/AlN QWs, theoretically, Rudinsky *et al.* confirmed this in their investigation of 1.5 nm and 2.5 nm wells, both with 45% Al in the well and pure AlN barriers [42]. Thus, a one-to-one comparison between our theoretical results and literature data for QWs with different structural parameters (such as Al content and well width) will be complicated by the impact of the built-in field. Bearing this in mind, we discuss now general trends.

Nippert *et al.* report values of $B = 2 \times 10^{-11}$ cm^3/s for a 1.5 nm wide $Al_{0.45}Ga_{0.55}N$/AlN QW at room temperature (T $\approx$ 300 K) and a carrier density of $n = 1.8 \times 10^{18}$ cm^{-3} [35]. However, uncertainties in determining the B coefficient experimentally are mentioned in that work, such that the values may be as low as $B = 6 \times 10^{-12}$ cm^3/s. Given the wider, 2.85 nm, well investigated here compared to the experimental work of Nippert *et al.*, we expect that our values for B should be lower than those reported in Ref. [35]. From our calculations we determined an average value for B of $B \approx 4 \times 10^{-13}$

cm^3/s at a temperature of T = 300 K and a carrier density of $n = 2.5 \times 10^{18}$ cm^{-3} for the $Al_{0.5}Ga_{0.5}N$/AlN QWs studied here. Again, although differences in carrier density and Al content will also impact any comparison, this value for B is consistent with the expected trend due to the significant difference in well width between theory and experiment.

Comparing our results now to the theoretical work of Rudinsky *et al.* [42], they report values of B for a 1.5 nm well, structurally similar to that investigated by Nippert *et al.*, on the order of $B \sim 1 \times 10^{-11}$ cm^3/s. Thus, our results are still consistent with the expected larger B coefficients for narrower wells. However, when investigating a 2.5 nm well, they find $B \sim 5 \times 10^{-12}$ cm^3/s, approximately an order of magnitude larger than the B value determined here. It is important to note that the model employed in Ref. [42] takes the strength of hole localisation as input to an essentially continuum-based model, and electrons are assumed to be entirely delocalised. On top of this, the model requires assumptions about the dependence of the h-DOS on energy, as detailed in Ref. [273], and essentially averages the localisation radius of the ensemble of localised hole states. Thus, the strength of hole localisation may be underestimated.

Lastly, it is now interesting to compare, but also highlight differences, to InGaN QW systems in terms of the obtained B coefficients. Just as in the case of InGaN/GaN QWs, the interplay of carrier localisation and its impact on the electronic structure can be complex. We find here B coefficients smaller than those calculated for InGaN QWs above, although a direct comparison with the systems studied above in Chapters 4 and 5 is difficult to make. This is in part due to the fundamental differences in the AlGaN and InGaN systems but also due to differences in well width and composition. Even with the same well width and equivalent "low band gap" material composition, there will still be significant differences in the magnitude of the built-in polarisation field between an AlGaN QW and an InGaN QW due to differences in spontaneous and piezoelectric polarisation (see discussion in Sec. 1.4).

Notwithstanding these differences, we expect that the smaller B coefficient in the AlGaN QWs studied here may be due to an overall stronger built-in polarisation field. To gain some insight into this, we have estimated the magnitude of the built-in polarisation field in a 1D VCA-like description by following the process in Ref. [21]. We find that, to a first approximation, the built-in polarisation field in the $Al_{0.5}Ga_{0.5}N$/AlN QWs studied here is

approximately twice as strong as in the $In_{0.15}Ga_{0.85}N$/GaN QWs studied in Chapters 4 and 5. Using the 1D VCA-like model in Ref. [21], and described above, we find that for a 2.85 nm wide $Al_{0.5}Ga_{0.5}N$/AlN QW the potential drop across the well is $\varphi = 1.46$ V, compared to a 3 nm $In_{0.15}Ga_{0.85}N$/GaN QW which exhibits a potential drop of $\varphi = 0.55$ V. In this 1D, VCA approach we take a linear interpolation of the material parameters in the well, and so the large differences in potential drop stem primarily from the much larger difference in low band gap material composition between the well and barriers in the AlGaN system compared to the InGaN system, as opposed to arising from differences in, for example, the magnitude of the spontaneous polarisation in GaN versus InN or AlN. In the presence of a stronger built-in polarisation field, carriers will be more strongly localised at opposite interfaces of the well, as well as more strongly localised within local potential "pockets", leading to lower wave electron hole wave function overlaps and thus a lower radiative recombination rate.

We now have a general understanding of the temperature dependence of the radiative recombination rate. To study the thermal droop in AlGaN QWs we need also to determine the temperature dependence of the Auger recombination rates. This is the topic of the next section.

6.2.3 Auger recombination

Given the large computational expense of Auger rate calculations, we seek a way to restrict the analysis to a subset of configurations. As discussed above, Cfs. 3, 5 and 6 are representative of the different impacts that the alloy microstructure can have on the evolution of B with temperature. Thus, we focus now on these configurations. As well as representing the different trends of B with temperature, these three configurations also represent the highest, lowest and average value of B at each temperature data point. We begin our discussion of the Auger recombination rate in 2.85 nm wide c-plane $Al_{0.5}Ga_{0.5}N$/AlN QWs by discussing the breakdown of the total Auger rate into contributions from the two Auger processes considered here, electron-electron-hole (eeh) and hole-hole-electron (hhe) Auger recombination. Figures 6.5 a) and b) show the hhe, C_{hhe}, and eeh, C_{eeh}, Auger coefficients, respectively, for the three configurations along with the average value of the coefficients (Average) taken over the configurations considered, for the QW systems described above as functions of temperature at a carrier

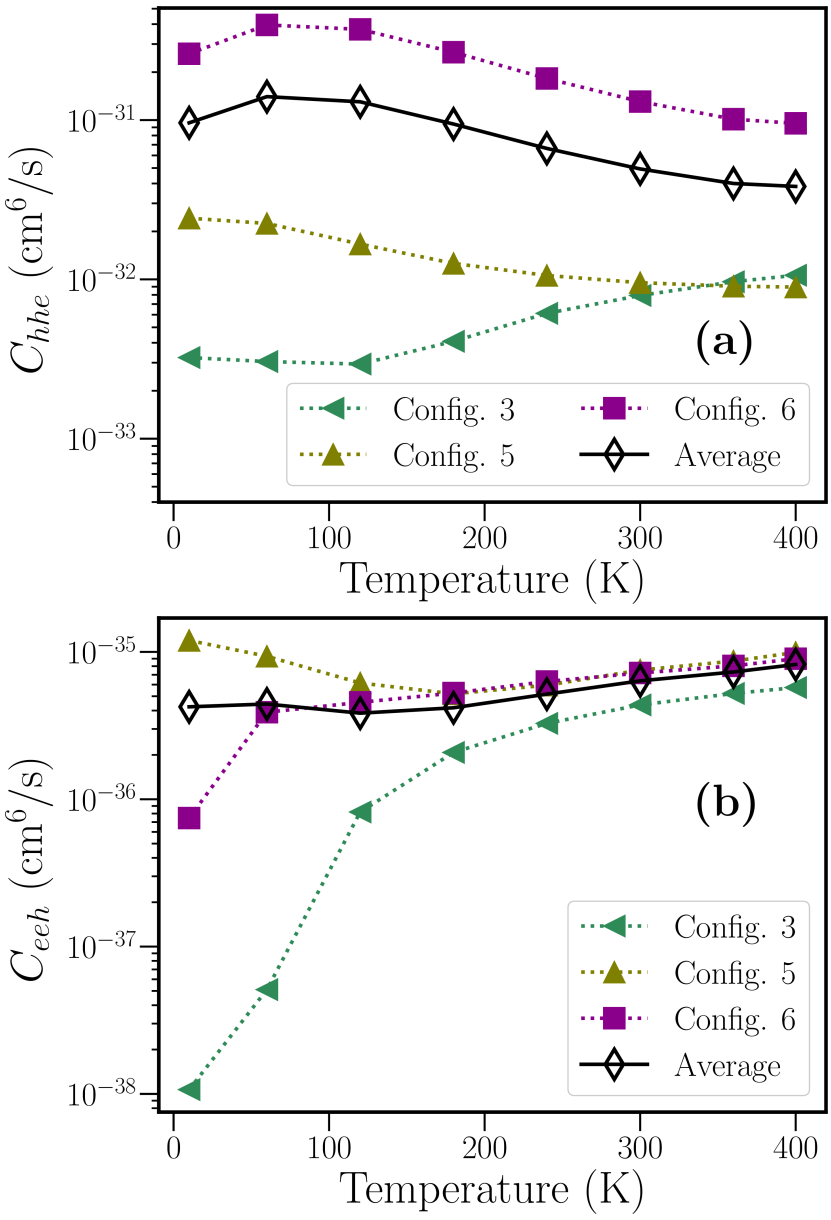


Figure 6.5: a) Hole-hole-electron (hhe) Auger recombination coefficient, C_{hhe}, and b) electron-electron-hole (eeh) Auger recombination coefficient, C_{eeh}, as a function of temperature for Cfs. 3, 5 and 6 of a 2.85 nm wide c-plane $Al_{0.5}Ga_{0.5}N$/AlN QW, along with the average value for the coefficients (Average) taken over the three configurations considered. The carrier density is $n = 2.5 \times 10^{18}$ cm^{-3}.

density of $n = 2.5 \times 10^{18}$ cm^{-3}. Before discussing the breakdown we note some general features.

Recalling that the total Auger recombination coefficient, C_{tot}, is related to the eeh and hhe coefficients via $C_{\text{tot}} = C_{eeh} + C_{hhe}$, we first note that Figs. 6.5 a) and b) show that $C_{hhe} \gg C_{eeh}$. Looking at the average of the configurations, at

T = 300 K we find values of $C_{hhe} = 5 \times 10^{-32}$ cm^6/s. But for C_{eeh}, at T = 300 K a value of $C_{eeh} = 6 \times 10^{-36}$ cm^6/s is found on average. Being 4 orders of magnitude larger than C_{eeh}, C_{hhe} makes up well over 99% of C_{tot}. This is a similar result to the InGaN QWs studied above, where we found that C_{eeh} is smaller than C_{hhe} by approximately the same factor ($\approx$ 4 orders of magnitude) across the same temperature range and at a similar carrier density. There has not yet been a study that estimates the relative magnitudes of C_{eeh} and C_{hhe} in AlGaN QWs. Thus, in the following, we will primarily focus on C_{hhe}, as this will determine the behaviour of C_{tot}.

We note that a common approach to estimating the Auger coefficients is via the triple wave function overlap [41]. For instance the hhe Auger coefficient may be estimated via

$$C_{hhe} \sim \int \psi^e \psi^h \psi^h \ . \tag{6.1}$$

Thus, as mentioned previously, we must now also account for the wave function overlap of hole states. With this in mind, we turn to Fig. 6.5 a) and C_{hhe} as a function of temperature for Cfs. 3, 5 and 6. At low temperature (T = 10 K), the relative differences in magnitude of C_{hhe} between the three configurations follows from our analysis above of the impact of alloy fluctuations on the electronic structure. At T = 10 K, C_{hhe} for Cf. 6 may be larger than for Cfs. 3 and 5 due primarily to the very close energetic separation between the hole ground state and first excited state. Not only will this extra excited hole state now contribute even at T = 10 K, but due to the spatial co-localisation of the hole ground state and the first excited hole state, the $\psi^h \psi^h$ overlap in Eq. (6.1) will be further enhanced, in contrast to Cfs. 3 and 5, wherein there will not even be a contribution from the first excited hole state at T = 10 K. For Cfs. 3 and 5, the relative magnitudes of C_{hhe} may be driven by the electron hole wave function overlaps for the band edge states.

In terms of the temperature dependence of C_{hhe} for the three configurations, we see different behaviours for each. Overall, as temperature increases, C_{hhe} for Cf. 3 increases, in contrast to Cfs. 5 and 6 which see a decrease of C_{hhe} with increasing temperature. The low temperature (T < 180 K) behaviour of C_{hhe} is also different between Cfs. 5 and 6, even though overall C_{hhe} decreases in the temperature range studied for those two configurations. In Cf. 5, C_{hhe} decreases over the whole low temperature range, whereas C_{hhe} for Cf. 6 initially increases with increasing temperature from T = 10 K to T = 60 K, before decreasing for all subsequent higher temperatures.

Turning first to Cf. 3, as temperature increases, the first excited hole state will be populated. However, looking at the Top View of the charge densities in Fig. 6.1 suggests that the first excited hole state of Cf. 3 is spatially separated from the hole ground state, leading to a small hole-hole wave function overlap between these states. Thus, in contrast to the radiative recombination rate for Cf. 3 above, in which there was a strong increase of B as temperature increased from T = 60 K to T = 180 K, for C_{hhe} there is not an increase until much higher temperatures. As temperature initially increases above T = 10 K, for C_{hhe} there is a competition between the larger electron hole wave function overlaps (see Fig. 6.2) that begin to contribute, and the smaller wave function overlap between the hole ground state and first excited state due to the spatial separation of these states, which is not a factor in the calculation of the radiative coefficient. Subsequently, as the second excited hole state begins to contribute at higher temperatures, the value of C_{hhe} begins to increase due to the spatial co-localisation of this state with the hole ground state.

For Cf. 5, C_{hhe} decreases as temperature increases across the whole temperature range. At least in the low temperature range (T < 180 K), when mainly "band" edge states are populated, we might expect this given the spatial separation of the second excited hole state charge density from the ground and first excited hole states in Fig. 6.1. Furthermore, the DMEs between some of the higher lying excited hole states with the electron ground state are smaller than the DME between the electron ground state and the hole ground state, as per Fig. 6.2. Thus, the decrease of C_{hhe} between T = 10 K and T = 180 K may stem primarily from the population of higher lying, spatially separated hole states, via the smaller hole-hole overlap entering Eq. (6.1) and also the smaller electron hole overlaps. As temperature increases beyond T = 180 K we might expect an increase of C_{hhe} due to the population of higher lying, delocalised states which have, on average, larger overlaps compared to the "band" edge states. However, the large number of states populated above T = 240 K makes an explicit analysis difficult, so instead we note that the C_{hhe} coefficient for Cf. 5 appears to start to plateau above T = 240 K, potentially due to the increasing contributions from these higher lying states and the lower "weight" of the band edge states.

Turning lastly to Cf. 6, as temperature is initially increased from 10 K to 60 K we see an increase in C_{hhe}, likely related to the strong hole-hole wave function overlap between the hole ground state and the first excited hole state. Subsequently, as temperature increases further and the second excited hole

state is populated, we might expect this decrease due to the spatial separation of this state from both the hole ground state and first excited state. Interestingly, even at elevated temperatures (T $\gtrapprox$ 240 K), when we would expect the C_{hhe} coefficient to reflect the more homogenised nature of the excited, extended states by converging to a value similar to the Cf. 3 and 5 values, as the radiative recombination rate does above, we see instead that C_{hhe} for Cf. 6 remains elevated across the whole investigated temperature range.

A similar behaviour was observed in our investigation of the temperature dependence of C_{hhe} in $In_{0.15}Ga_{0.85}N$/GaN QWs, discussed above in Chapter 4. In that context we found two configurations exhibited significantly larger C_{hhe} values compared to the majority of the investigated configurations. This phenomenon was linked to very strongly localised hole states, both ground and first excited. Both of these states sat energetically far above the valence "band" edge, compared to the valence "band" edge states of all the other configurations studied. Effectively, these states were energetically in the band gap and we suggested that they may be related to so-called trap-like states. Returning to the AlGaN case here, in contrast, these hole states lie (energetically) *within* the broadened valence "band" edge (see Fig. 6.3), and so we do not associate them with trap-like states. Rather, it is the co-localisation of the hole states, coupled with their small energetic separation, that drives the elevated Auger rate. Furthermore, C_{hhe} for Cf. 6 is elevated over the whole temperature range, showing that even at higher temperatures when excited, extended states are populated, the underlying contributions from strongly localised states are still significant, and can vary between configurations.

As mentioned, C_{eeh}, presented in Fig. 6.5 b), is approximately four orders of magnitude smaller than C_{hhe} and thus is of secondary importance. We note that the alloy microstructure can be seen to play a role in C_{eeh} at low temperatures, but this effect diminishes at higher temperatures likely due to the contribution of higher lying, extended states that are less perturbed by the alloy microstructure. Overall though, the behaviour of C_{eeh} is of secondary importance for the discussion of the total Auger rate. Thus, we only discuss C_{hhe} in detail and now move on to the temperature dependence of the total Auger coefficient, C_{tot}.

Figure 6.6 shows the total Auger recombination coefficient for the three

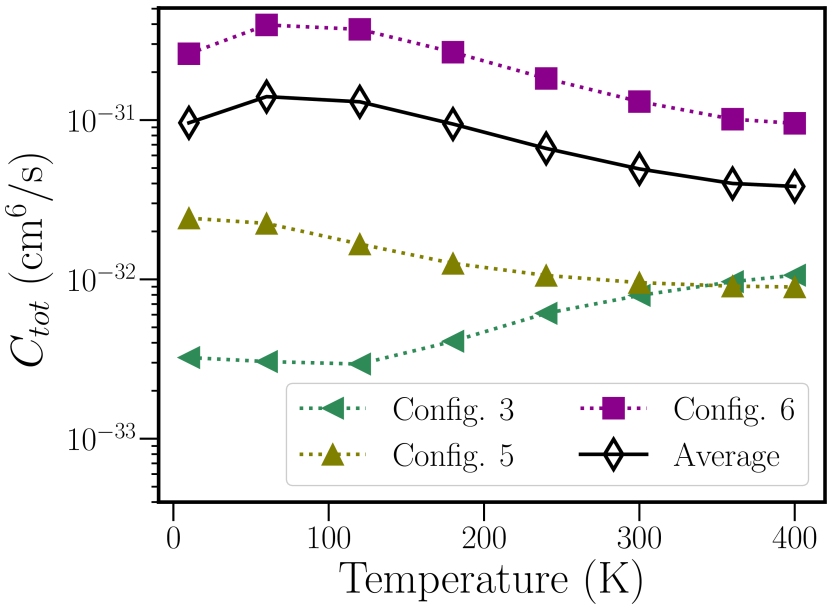


Figure 6.6: Total Auger recombination coefficient, C_{tot}, as a function of temperature for Cfs. 3, 5 and 6 of a 2.85 nm wide c-plane $Al_{0.5}Ga_{0.5}N$/AlN QW, along with the average of the configurations (Average). The carrier density is $n = 2.5 \times 10^{18}$ cm^{-3}.

configurations investigated, along with the average of the configurations. At 300 K, the average value is $C_{\text{tot}} = 5 \times 10^{-32}$ cm^6/s. As the total rate is dominated by hhe Auger process, the evolution of C_{tot} with increasing temperature is essentially the same as for C_{hhe}. Nippert *et al.* [35] report a value of $C_{\text{tot}} = 3.4 \times 10^{-30}$ cm^6/s, approximately two orders of magnitude greater than the values determined here, but for narrower wells of well width 1.5 nm. Rudinsky *et al.* [42], using their modified continuum-based model that includes hole localisation, also significantly underestimate the total Auger coefficient (finding values of C_{tot} in range of $C_{\text{tot}} = 7 \times 10^{-32} - 4 \times 10^{-31}$ cm^6/s) in comparison to the experimental values of Nippert *et al.* (see Fig. 3 (b) in Ref. [42]). However, when targeting wider QWs similar to our study (with a well width of 2.5 nm, 45% Al in the well and AlN barriers) they find total Auger coefficients in the range of $C_{\text{tot}} = 5 \times 10^{-32} - 2 \times 10^{-31}$ cm^6/s at carrier densities between $n = 1 \times 10^{18} - 1 \times 10^{19}$ cm^{-3}. Thus, the trend of wider wells leading to smaller recombination coefficients is seen theoretically, and when accounting for difference in well width it seems reasonable to suggest that the theoretical models are in relative agreement. When comparing to the experimental results, however, a number of other factors may impact the values, which we will now discuss.

Rudinsky *et al.* suggest that the inclusion of an AlN cap in the experimental

setup of Nippert *et al.* may alter the band structure of all of the MQWs in the structures, leading to non-uniform carrier distributions across the wells. Furthermore, as we have discussed above, determining the carrier density in III-N QW systems can be challenging. The carrier density in Ref. [35] was determined by fitting the SRH A and Auger C coefficients to carrier density dependent IQE data, while assuming that A and C are carrier density *independent*. As we have seen above for InGaN QWs, this may not be the case for C (or B), which will impact the determined carrier density and also the value of B extracted (which depends on C in the fitting). We note also that in the experimental data, defect-assisted Auger processes may be an important factor which we do not account for here. Lastly, due to the computational expense of Auger rate calculations we focused here on only three configurations. Future studies may target a larger number of configurations to gain a better understanding of the range of expected Auger coefficients, as well as investigating the impact of defect-assisted processes. With our knowledge of the temperature dependence of the radiative and Auger recombination rates, we are now in a position to discuss the impact of Auger recombination on the thermal droop in AlGaN QWs.

6.2.4 Competition between radiative and Auger recombination

Experimentally, it has been found that in UV LEDs, as temperature increases, especially above 300 K, IQE decreases. This can be seen, for instance, in Refs. [32] and [264]. Figure 6.7 shows the ratio of the B and C_{tot} coefficients as a function of temperature in the range in which thermal droop has been observed experimentally [32]. The data are normalised to the value of the ratio at 300 K. We note as well that as we are varying temperature at a fixed carrier density a plot of B/C_{tot} will be equivalent to a plot of $B/(C_{\text{tot}}n)$, i.e., any factor of n will only scale the results.

We see that, on average, B/C_{tot} is increasing relative to its value at 300 K. Thus, we could expect the likelihood of a recombination event to result in the emission of a photon to increase relative to the likelihood of a recombination event resulting in a "hot" Auger carrier as temperature increases. This would indicate that device performance improves, in a first approximation. However, this stands in contrast to the decrease in device performance observed experimentally, thus, our results suggest that the here considered Auger

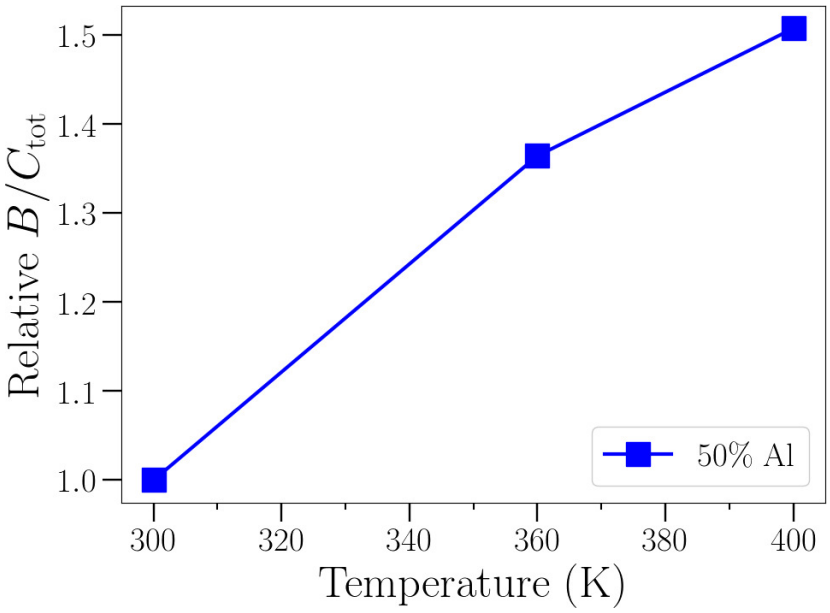


Figure 6.7: Ratio of B and C_{tot}, B/C_{tot}, as a function of temperature for a 2.85 nm wide c-plane $Al_{0.5}Ga_{0.5}N$/AlN QW. The data are normalised to the ratio at 300 K. The carrier density is fixed at $n = 2.5 \times 10^{18}$ cm^{-3}.

recombination process is probably not directly responsible for thermal droop in AlGaN/AlN QWs, as is suggested in the experimental studies above [264]. It is suggested in Refs. [32] and [264] that a different nonradiative process external to the active region is the underlying cause of thermal droop in AlGaN QWs.

However, we note that the large band gap of AlGaN QWs may result in the generation of very high energy Auger carriers, so-called "hot" Auger carriers. Interactions between these high energy carriers and the crystal structure may produce defects [274, 275], having a knock-on effect on the SRH-related A coefficient and potentially other processes such as defect-assisted Auger recombination or carrier injection. Furthermore, both Refs. [32] and [264] suggest that thermal droop is linked to recombination processes occurring outside of the active region. Thus, the generation of hot Auger carriers, which may undergo thermionic escape and reach regions of the LED structure outside of the active region, may still have an effect on the thermal droop. Further studies of the impact of such hot Auger carriers on device performance are thus required.

In this chapter we have discussed *thermal* droop in AlGaN-based QWs. However, *carrier density dependent* droop (as was discussed above for InGaN QWs) has also been observed in AlGaN QW-based systems [35]. Although we

have not yet carried out a study on the evolution of the radiative or Auger recombination rates with carrier density, we briefly note that for InGaN QWs, values of C_{tot} above approximately 1×10^{-31} cm^6/s are considered generally to be large enough to impact the carrier density dependent efficiency droop, due to the cubic dependence of the Auger rate on carrier density. However, the droop phenomena also depends on the carrier density dependence of the B coefficient. So, given that we find smaller values for B here than in the InGaN systems studied above, the threshold of $C_{\text{tot}} = 1 \times 10^{-31}$ cm^6/s may be an overestimation for AlGaN QWs. Thus, the values of C_{tot} determined here could be large enough to contribute to droop.

Furthermore, as we have seen in the case of InGaN QWs, screening of the built-in polarisation field as carrier density increases can lead to a significant enhancement of both the radiative and Auger recombination rates. Thus, the Auger coefficients determined here may represent a lower bound for c-plane $Al_{0.5}Ga_{0.5}N$/AlN QWs, and will increase with increasing carrier density. We note that it is commonly assumed that similar values of A can be found in AlGaN/AlN QWs as can be found in InGaN QWs (see, for instance, Refs. [35], [267] and [268]). This assumption for A, coupled with the smaller B and C_{tot} values determined in this work for AlGaN systems compared to InGaN systems, would suggest that at least in the ABC model, AlGaN QWs should enter the droop regime at higher carrier densities. Lastly, variations in carrier density through, for instance, an AlGaN MQW structure may lead to regions in which the carrier density is larger and so Auger recombination may be enhanced, negatively impacting device performance. Overall though, further studies targeting an analysis of carrier density dependent droop in AlGaN QWs are required.

6.3 Conclusion

In this chapter we applied our atomistic TB model to the investigation of the impact of random alloy fluctuations on the electronic structure, radiative and Auger recombination coefficients and the competition between these recombination processes as a function of temperature in 2.85 nm c-plane $Al_{0.5}Ga_{0.5}N$/AlN QWs. We found that alloy disorder leads to strong carrier localisation of not only the hole ground state, but also excited hole states. Electron states may also be impacted by carrier localisation, but to a lesser extent than holes.

Turning to the radiative recombination coefficient, B, we found that overall, at a carrier density of $n = 2.5 \times 10^{18}$ cm^{-3}, the B coefficient slightly increases with increasing temperature. The calculations showed that the alloy microstructure plays a crucial role at low temperatures as mainly the strongly localised "band" edge states are occupied. As temperature increases and higher lying, extended states are populated, the spread in B values is strongly reduced, as the details of the alloy microstructure impact the extended states less than the strongly localised states.

We found an average value of $B \approx 4 \times 10^{-13}$ cm^3/s at T = 300 K and $n = 2.5 \times 10^{18}$ cm^{-3}. Experimental studies reporting values of B are sparse. Data on B for structurally similar QWs (i.e. AlN barriers, similar Al contents in the well) is only available for much smaller well widths. That study yields a higher value for B in comparison to our data. However, this is expected as well width is a major factor that can impact the magnitude of B due to the separation of electron and hole states along the growth direction associated with the built-in polarisation field. Thus, we expect that narrower wells will have larger B coefficients. Future studies can now target an investigation of the dependence of B on well width.

Having discussed the radiative recombination rate via the B coefficient, we then turned to the temperature dependence of the Auger recombination processes. We calculated both the eeh and hhe Auger rates as a function of temperature. We found that both processes are strongly impacted by the alloy microstructure and the localisation of holes. Overall, the hhe Auger coefficient, C_{hhe}, was found to be greater than the eeh Auger coefficient, C_{eeh}, by four orders of magnitude. Thus, the total Auger rate is dominated by the hhe Auger rate. The total Auger coefficient at a carrier density of $n = 2.5 \times 10^{18}$ cm^{-3} and a temperature of T = 300 K was found to be, averaged over three microscopic configurations, $C_{\text{tot}} = 5 \times 10^{-32}$ cm^6/s. As in the case of the B coefficient above, one of the few experimental investigations of C_{tot} was carried out for AlGaN QW systems with smaller well widths. In a narrower well, we also expect that the reduction in the spatial separation of the electron and hole states along the growth direction will lead to an overall increase in the Auger rate. We found here Auger coefficients smaller than the experimental values, in line with this expected trend. However, we noted the significant experimental uncertainties in determining the radiative and Auger recombination coefficients more generally. We also found that strongly localised hole states can lead to significantly enhanced Auger rates. Further

studies of the impact of carrier localisation on the recombination processes in AlGaN-based QWs are required to shed light on the role of alloy-enhanced Auger in contrast to, for instance, defect-assisted Auger.

Having determined the temperature evolution of the radiative and nonradiative Auger recombination rates, we investigated the competition between these two processes via the B/C ratio. In principle, we expect that an increase of the B/C_{tot} ratio could correspond to an improvement in device performance. Experimentally it is found that device performance deteriorates as temperature is increased, including into the device operating temperature range of T > 300 K. If Auger recombination was a driving cause of thermal droop we would thus expect a decrease of B/C_{tot}. We found that the B/C_{tot} ratio increases with increasing temperature at high temperatures (T > 300 K). Thus, our findings stand in contrast to experimental reports, indicating to us that the here considered Auger recombination process is not directly causing thermal droop. However, we note that Auger recombination could have an indirect impact on device performance due to the generation of high energy Auger carriers which may cause defects in the material, thus increasing nonradiative recombination pathways and hampering efficiency.

Chapter 7

Concluding Remarks

To conclude, we first present a summary of the motivation of and results obtained in this thesis. Subsequently, we will discuss some open questions and potential next steps to gain even further insight into the efficiency of III-N-based QW emitters.

7.1 Summary

Most modern blue-violet short wavelength visible LEDs incorporate InGaN/GaN QWs, while AlGaN-based QWs have recently attracted significant attention for efficient UV LEDs. While these devices are highly efficient in the short wavelength visible regime, they suffer significant reductions in efficiency at other wavelengths. Moreover, even efficient III-N QW-based devices suffer from efficiency "droop" effects: deteriorations of efficiency as drive current density is increased, or when the temperature of the device rises. These drops in efficiency are known as current and thermal droop, respectively. Input from theory is important for understanding the fundamental origins of droop, as well as to guide device design to improve efficiency where possible. However, theoretical results for other semiconductor systems (such as those based on II-VI and other III-V materials) cannot be carried over to III-N systems due to significant differences in the fundamental material properties. In this thesis we sought fundamental understanding of the efficiency bottlenecks affecting III-N QW-based LEDs while accounting particularly for alloy fluctuations, an effect widely neglected in previous theoretical studies in literature.

One proposed origin of current density dependent droop in c-plane

InGaN/GaN QWs and connected devices is Auger recombination, a nonradiative process in which an electron recombines with a hole, but instead of a photon being emitted (as in radiative recombination), another carrier is excited, for instance higher into the conduction band. If the rate of Auger recombination grows faster than the rate of radiative recombination as current density increases, overall there will be a negative impact on device performance. The nature of the Auger process underlying droop is still under debate, and a number of recombination mechanisms have been suggested, including a defect-assisted process as well as alloy disorder enhanced Auger recombination. However, the interplay of Auger recombination and alloy disorder in III-N *QW* systems is widely unexplored. Both recent experimental and theoretical studies show that alloy disorder causes carrier localisation in III-N semiconductor alloys, which can significantly alter the electronic and optical properties of III-N heterostructures. Although experimental data indicates the importance of such effects, only very recently have they been accounted for in theoretical studies, as they present a significant modelling challenge. Thus, the aim of this thesis was to address this challenge using an atomistic model.

Our theoretical framework is based on a nearest neighbour sp^3 tight-binding model, which takes input from a valence force field model to determine the equilibrium lattice positions of the alloy disordered QW structures studied. On top of this, local variations in strain and polarisation fields are accounted for in the framework, along with polarisation field screening effects. The tight-binding energies and wave functions were then used to calculate the radiative and Auger recombination rates.

We first targeted an investigation of thermal droop in c-plane InGaN/GaN QWs. To do so, we disentangled the effects of changing temperature and carrier density by carrying out the analysis at a fixed, low carrier density of $n = 3.8 \times 10^{18}$ cm^{-3}. We determined the temperature dependence of the radiative and Auger recombination rates for three different In contents in the well; 10%, 15% and 25%. We found that the radiative rate increases with increasing temperature, in line with experimental studies performed at a similar, fixed carrier density. This behaviour stands in contrast to the expected decrease of radiative rate with increasing temperature predicted from a fundamental physics perspective. We found total radiative recombination coefficients of $B \approx 3 \times 10^{-11}$ cm^3/s (10% In), $B \approx 5 \times 10^{-12}$ cm^3/s (15% In) and $B \approx 4.5 \times 10^{-13}$ cm^3/s (25% In) at a temperature of 300 K and the carrier

density above. We found that at low temperatures, when mainly the strongly localised band edge states are populated, the alloy microstructure has a strong impact on the radiative rate, evidenced by the large variations in B coefficient. As temperature increases, the spread in values decreases, due to the population of excited, less localised or even extended states that are less perturbed by the alloy disordered confining potential.

Turning to the temperature dependence of the Auger recombination rates, in order to calculate the total Auger rate we first determined the rates of electron-electron-hole (eeh) and hole-hole-electron (hhe) Auger recombination. The calculations revealed that the eeh Auger rate shows a weak temperature dependence, or increases slightly, with increasing temperature. The hhe Auger recombination is the dominant contribution, even with increasing In content, and this does not change with temperature. The hhe Auger rate shows a weak temperature dependence, or a slight decrease, with increasing temperature. Our studies revealed that the relative contributions from eeh and hhe Auger rates to the total rate do not change with In content. We found total Auger coefficients of $C_{\text{tot}} \approx 4 \times 10^{-30}$ cm^6/s (10% In), $C_{\text{tot}} \approx 2 \times 10^{-30}$ cm^6/s (15% In) and $C_{\text{tot}} \approx 2 \times 10^{-31}$ cm^6/s (25% In) at a temperature of 300 K when averaged over the 10 microscopic alloy configurations investigated.

With the temperature dependence of the radiative and Auger rates determined, we were in a position to discuss the thermal droop. Our investigations showed that at temperatures greater than 300 K the radiative recombination rate slightly increases while the total Auger recombination rate (slightly) decreases. This finding would indicate a positive impact of increasing temperature on device efficiency when only considering the Auger process as the main nonradiative recombination process. However, this stands in contrast to experimental studies which show that the device efficiency decreases with increasing temperature above 300 K. Therefore, we conclude that the alloy-enhanced Auger recombination process is not responsible for the thermal droop observed in c-plane InGaN/GaN quantum wells and other factors, such as carrier transport or defect related processes are more likely to explain the experimentally observed droop effect.

Having determined the radiative and Auger rates for three different In contents, we also briefly commented on the decrease of efficiency observed in InGaN QW-based emitters when targeting longer wavelength emission

(corresponding to higher In contents): the so-called "green gap". We found that, when increasing the In content in the well, the radiative recombination rate drops. However, the Auger rate initially drops as In content increases from 10% to 15% In in the well, but is composition independent when going to 25% In. Thus, it is the reduction of the radiative recombination rate and not an increase in the Auger rate that determines the composition dependence of the competition between these processes. As a result, we expect that the reduction of IQE in InGaN-based light emitters operating in the green to yellow spectral range, and thus at higher In contents (i.e. $> 15\%$), may not be caused by *alloy-enhanced* Auger recombination effects. This suggests that by reducing defect densities and thus the connected nonradiative recombination in high In content systems, there may be a way forward to close the green gap. Having discussed the thermal droop and green gap in InGaN-based QWs, we turned to an analysis of the carrier density dependent droop.

To investigate the carrier density dependent droop we targeted a $In_{0.15}Ga_{0.85}N$/GaN QW. To determine the radiative and Auger recombination rates as a function of carrier density, we needed to account for the screening of the electrostatic built-in field. This was achieved by self-consistently solving the Schrödinger-Poisson equations in a 1D, VCA-like model. We discussed the impact that the built-in field screening can have on the electronic structure of the QWs, seeing the decrease in the spatial separation of the electron and hole charge densities along the growth direction as carrier density was increased.

Turning to look at the carrier density dependence of the Auger recombination rates, we again found that the contribution from the eeh Auger process is of secondary importance when compared to the hhe process, and its relative importance increases only slightly with increasing carrier density. The model predicted total Auger coefficients that vary from $C_{\text{tot}} \approx 1 \times 10^{-31}$ cm^6/s at a carrier density of $n = 1 \times 10^{17}$ cm^{-3} to $C_{\text{tot}} \approx 2 \times 10^{-30}$ cm^6/s at $n = 1 \times 10^{20}$ cm^{-3}. Thus, based on literature expectations, this indicates that our calculated Auger coefficient values should lead to a significant efficiency droop. These carrier density dependent Auger coefficients, along with the previously determined radiative recombination coefficients, could be used as input to device simulation models in order to include atomistic carrier localisation effects in large scale simulations [276].

Equipped with the theoretical data on the radiative and Auger recombination coefficients as functions of carrier density, we targeted a comparison to

experimental data. Using samples provided by colleagues in the University of Cambridge, optical studies were carried out in the University of Manchester. Manchester established a novel method to carefully determine the carrier density in InGaN QWs when using pulsed excitation schemes. As literature data recently indicated the presence of defect-assisted Auger recombination processes in InGaN-based devices, special attention was paid to the impact of point defect density and carrier localisation effects on the droop carrier density regime behaviour of the IQE. To do so, three different samples where grown at different growth temperatures to modify the density of point defects in the well. Using these samples, the experimental data revealed that independent of sample (i) droop onset occurs at similar carrier densities in the well and (ii) the high carrier density regime evolution of the integrated PL intensity was basically identical. All this indicated that trap-assisted (defect related) Auger recombination seems to be of secondary importance for the studied samples.

Furthermore, when using our calculated carrier density dependent radiative and Auger recombination coefficients, excellent agreement was found between theory and experiment for not only the onset of droop, but also the evolution of the IQE in the high carrier density regime. Although we found that the carrier density dependent droop may be driven by Auger recombination intrinsic to the active region, the analysis also found a peak IQE of 70%, relatively high for a green emitting QW. Thus, our study suggested that factors external to the QW, such as injection efficiency or carrier distribution homogeneity (to avoid regions of locally high carrier density), should be targeted for improving the efficiency of longer wavelength visible III-N emitters. Having established the framework for visible InGaN-based emitters, we turned to UV emitting AlGaN-based QWs.

Before targeting an analysis of thermal droop in AlGaN-based QWs, we first discussed the impact of alloy disorder on the electronic structure of a c-plane 2.85 nm wide $Al_{0.5}Ga_{0.5}N$/AlN QWs. We found that alloy disorder leads to strong carrier localisation of not only the hole ground state, but also excited hole states. Electron states may also be impacted by carrier localisation, but to a lesser extent than holes. Turning to the temperature dependence of the radiative recombination, at a fixed carrier density of $n = 2.5 \times 10^{18}$ cm^{-3}, the radiative recombination coefficient, B, slightly increases with increasing temperature, similar to InGaN/GaN QWs. Also, the calculations showed that the alloy microstructure plays a crucial role at low temperatures as mainly the strongly localised band edge states are occupied. As temperature increases and

higher lying, extended states are populated, the spread in B values is strongly reduced, as the details of the alloy microstructure impact the extended states less than the strongly localised states. We found a value of $B \approx 4 \times 10^{-13}$ cm^3/s at T = 300 K and $n = 2.5 \times 10^{18}$ cm^{-3}. Experimental studies reporting values of B are sparse and data on B for structurally similar QWs (i.e. with AlN barriers and similar Al contents in the well) is only available for much smaller well widths. That study yielded a higher value for B in comparison to our data. However, this is expected as well width is a major factor that can impact the magnitude of B due to the separation of electron and hole wave functions along the growth direction due to the built-in polarisation field. Thus, we expect that narrower wells will have larger B coefficients. Future studies can now target an investigation of the dependence of B on well width.

Having discussed the radiative recombination rate via the B coefficient, we then turned to the temperature dependence of the Auger recombination processes. Calculating both the eeh and hhe Auger rates as a function of temperature revealed that both processes are strongly impacted by the alloy microstructure and the localisation of holes. Overall, the hhe Auger coefficient, C_{hhe}, was found to be greater than the eeh Auger coefficient, C_{eeh}, by four orders of magnitude. The total Auger coefficient at a carrier density of $n = 2.5 \times 10^{18}$ cm^{-3} and a temperature of T = 300 K was $C_{\text{tot}} = 5 \times 10^{-32}$ cm^6/s. Experimental studies are sparse, and have been carried out for wells with different structural properties. In comparison to those studies we found smaller Auger coefficients, which is expected as the difference in well width is expected to have a major impact on this quantity due to the presence of the built-in field. We also noted the significant experimental uncertainties in determining the radiative and Auger recombination coefficients more generally. Further studies of the impact of carrier localisation on the recombination processes in AlGaN-based QWs are required to shed light on the role of alloy-enhanced Auger in contrast to, for instance, defect-assisted Auger.

Having determined the temperature evolution of the radiative and Auger recombination rates, we investigated the competition between these two processes as temperature increases. As before, we expect that if the ratio of radiative recombination rate to Auger rate increases, this would indicate an overall improvement in device performance. Experimentally it is found that device performance deteriorates as temperature is increased above 300 K. Our results showed that the ratio of radiative to Auger recombination rate increases with increasing temperature in this range. Thus, our findings stand

in contrast to experimental reports, indicating that the here considered alloy-enhanced Auger recombination process is not directly causing thermal droop. However, we note that Auger recombination could have an indirect impact on device performance due to the generation of high energy Auger carriers which may cause defects in the material, thus increasing nonradiative recombination pathways and hampering efficiency.

Overall, the results presented in this thesis show that alloy disorder can have a strong impact on the electronic structure and recombination rates in III-N QWs and thus, the IQE. Although Auger recombination may not represent an intrinsic roadblock to overcoming the green gap or thermal droop in InGaN/GaN QWs, current dependent droop is likely an intrinsic feature of these heterostructures. Thus, designs that aim to reduce current density in the active region may be the best route forwards to mitigate current droop in InGaN-based devices. For AlGaN/AlN QW-based devices, many questions remain. Although our results suggest that Auger recombination again may not represent an intrinsic roadblock to overcoming thermal droop in AlGaN-based devices, we have seen that carrier localisation effects can strongly impact the electronic structure and Auger recombination rate, and may lead to Auger rates large enough to be significant for current droop as well. Thus, we expect that similar strategies employed in InGaN-based emitters to reduce current droop should also be considered for AlGaN-based systems.

7.2 Outlook

As mentioned above, many questions remain with regard to carrier localisation and recombination in AlGaN-based systems. The theoretical framework developed here could be used to investigate the impact of well width, as well as other factors such as Al content in the well. Such an investigation would enable a more direct comparison of expected radiative and Auger coefficients between theory and experiment, along with providing insight into the impact of the built-in field on these processes. It would also be possible to extend the framework to AlGaN/AlGaN QWs (which have also been targeted in experimental studies). In such systems there are open questions over the impact of alloy disorder in the *barriers*.

Our theory experiment comparison in Chapter 5 suggested that defect-assisted processes appear to be of secondary importance when describing the current

dependent droop behaviour at high carrier densities in InGaN QWs, despite recent suggestions that defect-assisted Auger processes are responsible. However, we also observed potential "trap"-like states in InGaN/GaN QWs that caused enhanced Auger rates. In light of the recent discussions of trap-assisted Auger recombination, an investigation of such states, for instance to determine the rate of their occurrence, may provide important insights into their importance, especially given that most analyses of trap-assisted Auger recombination focus on defect-assisted processes.

Carrying out a similar experimental comparison for AlGaN/AlN QWs could also provide further insight into the role of alloy-enhanced and defect-assisted Auger in AlGaN systems. To achieve this, the carrier density dependence of the radiative and Auger recombination rates in AlGaN systems would need to be determined, while taking the screening of the built-in field into account. For the InGaN QWs studied here, due to the computational demand of carrying out a fully self-consistent tight-binding Schrödinger-Poisson calculation, we employed a 1D VCA-like model to determine the screening of the built-in field. Based on our theory experiment comparison (and literature results) this approach seems sufficient for InGaN/GaN QWs and so we have used this model for AlGaN/AlN QWs too. However, validating this approximation and investigating the impact of screening effects in a tight-binding framework could provide further valuable insights into carrier localisation effects in AlGaN/AlN QWs.

For InGaN systems, recent experimental studies have targeted QWs with much larger well widths ($\approx$ 10 nm) than conventionally used ($\approx$ 3 nm) as a potential route to increasing efficiency. In those studies it is argued that populating the energetically lowest band edge states (that are strongly localised and spatially separated at opposite QW interfaces) may be enough to fully screen the built-in polarisation field even at relatively low carrier densities, thus, higher lying states may not be affected by the built-in field. However, our results show that although the radiative recombination rate is indeed increased when the polarisation field is screened, so too is the Auger rate. Thus, an investigation of the competition between the radiative and Auger rates in wider QWs may provide insight into the competition between these processes.

Another lingering question is the discrepancy between theoretical and experimental estimations of the relative contributions from the electron-electron-hole (eeh) and hole-hole-electron (hhe) Auger rates. Some

experimental studies have found that for InGaN/GaN QWs the eeh rate is larger than the hhe rate by a factor of 1 – 12, but here we find the eeh rate is approximately four orders of magnitude smaller than the hhe rate, in line with basically all other theoretical studies that comment on this aspect. When discussing this discrepancy above we noted that electron localisation could have an impact on the eeh rate, and more generally the nature and impact of electron localisation remains under debate, for instance, the role of gross well width fluctuations and other mesoscopic structural phenomena in electron localisation.

The TB framework developed here could be used to guide the development of future modified continuum-based approaches, for instance acting as a benchmark for localisation landscape theory (LLT) calculations. Currently, the main disadvantage of LLT is that it has only been established in a single band framework, whereas the description of some semiconductor materials (such as AlN) and phenomena (such as light polarisation character) require multi-band approaches. Ideally then a multi-band LLT would be developed, but it is not clear if this is possible. In the meantime, our TB framework remains a balanced compromise between a full description of the system and computational feasibility.

Overall, it is an important tool for investigating a range of phenomena in III-N QWs while accurately taking alloy disorder effects into account. Furthermore, the framework could be extended to novel III-N materials and nanostructures, such as those incorporating boron containing alloys. The introduction of B into III-N alloys is targeted to reduce the lattice mismatch in heterostructures and to control the valence band structure, for instance in AlGaN-based UV emitters. In and B are significantly different in size, so effects such as carrier localisation could also play an important role which would need to be considered in future studies. Indeed, recent *ab initio* theoretical studies of BGaN have shown that the presence of B clusters can lead to carrier localisation effects [277]. As we have seen throughout this thesis, carrier localisation effects can strongly impact the electronic and optical properties of nitride-based devices.

Chapter 8

Bibliography

References

[1] J. M. McMahon, E. Kioupakis, and S. Schulz, "Carrier density dependent Auger recombination in c-plane (In,Ga)N/GaN quantum wells: insights from atomistic calculations," *Journal of Physics D: Applied Physics*, vol. 57, no. 12, p. 125102, 2023.

[2] R. M. Barrett, J. M. McMahon, R. Ahumada-Lazo, J. A. Alanis, P. Parkinson, S. Schulz, M. J. Kappers, R. A. Oliver, and D. Binks, "Disentangling the Impact of Point Defect Density and Carrier Localization-Enhanced Auger Recombination on Efficiency Droop in (In,Ga)N/GaN Quantum Wells," *ACS Photonics*, vol. 10, no. 8, pp. 2632–2640, 2023.

[3] J. M. McMahon, E. Kioupakis, and S. Schulz, "Atomistic analysis of Auger recombination in c-plane (In,Ga)N/GaN quantum wells: Temperature dependent competition between radiative and non-radiative recombination," *Phys. Rev. B*, vol. 105, p. 195307, 2022.

[4] J. M. McMahon, D. S. P. Tanner, E. Kioupakis, and S. Schulz, "Atomistic analysis of radiative recombination rate, Stokes shift, and density of states in c-plane InGaN/GaN quantum wells," *Appl. Phys. Lett.*, vol. 116, p. 181104, 2020.

[5] D. S. P. Tanner, J. M. McMahon, and S. Schulz, "Interface Roughness, Carrier Localization, and Wave Function Overlap in c-Plane $(\mathrm{In},\mathrm{Ga})\mathrm{N}/\mathrm{GaN}$ Quantum Wells: Interplay of Well Width, Alloy Microstructure, Structural Inhomogeneities, and Coulomb Effects," *Phys. Rev. Appl.*, vol. 10, p. 034027, 2018.

[6] IEA, "World electricity generation mix by fuel, 1971-2019." `https://www.iea.org/data-and-statistics/charts/world-`

electricity-generation-mix-by-fuel-1971-2019, 2021. Accessed: 30/06/2023.

[7] C. Weisbuch, "Historical perspective on the physics of artificial lighting," *Comptes Rendus Physique*, vol. 19, no. 3, pp. 89–112, 2018. LEDs: The new revolution in lighting / Les LED : la nouvelle révolution de l'éclairage.

[8] C. J. Humphreys, "Solid-state lighting," *MRS Bulletin*, vol. 33, p. 459, 2008.

[9] C. Weisbuch, "Review—on the search for efficient solid state light emitters: Past, present, future," *ECS Journal of Solid State Science and Technology*, vol. 9, no. 1, p. 016022, 2019.

[10] IEA, "Global electricity consumption in lighting in the Net Zero Scenario, 2010-2030." https://www.iea.org/data-and-statistics/charts/global-electricity-consumption-in-lighting-in-the-net-zero-scenario-2010-2030, 2023. Accessed: 24/08/2023.

[11] T. Sano, T. Doi, S. A. Inada, T. Sugiyama, Y. Honda, H. Amano, and T. Yoshino, "High Internal Quantum Efficiency Blue-Green Light-Emitting Diode with Small Efficiency Droop Fabricated on Low Dislocation Density GaN Substrate," *Japanese Journal of Applied Physics*, vol. 52, no. 8S, p. 08JK09, 2013.

[12] "Life-Cycle Assessment of Energy and Environmental Impacts of LED Lighting Products Part I: Review of the Life-Cycle Energy Consumption of Incandescent, Compact Fluorescent, and LED Lamps," tech. rep., US Department of Energy, 2012. Available at: https://www1.eere.energy.gov/buildings/publications/pdfs/ssl/2012_LED_Lifecycle_Report.pdf.

[13] M. Scholand and H. E. Dillon, "Life-Cycle Assessment of Energy and Environmental Impacts of LED Lighting Products Part 2: LED Manufacturing and Performance," tech. rep., US Department of Energy, 2012. Available at: https://www.osti.gov/biblio/1044508.

[14] J. Thiesen, T. S. Christensen, T. G. Kristensen, R. D. Andersen, B. Brunoe, T. K. Gregersen, M. Thrane, and B. P. Weidema, "Rebound

effects of price differences," *Int. J. Life Cycle Assess*, vol. 13, no. 104-114, 2008.

[15] T.-Y. Tsai, K. S. Qwah, J.-P. Banon, M. Filoche, C. Weisbuch, Y.-R. Wu, and J. S. Speck, "Carrier localization in III-nitride versus conventional III-V semiconductors: A study on the effects of alloy disorder using landscape theory and the Schrödinger equation," *Phys. Rev. Appl.*, vol. 20, p. 044069, 2023.

[16] H. Amano, M. Kito, K. Hiramatsu, and I. Akasaki, "P-Type Conduction in Mg-Doped GaN Treated with Low-Energy Electron Beam Irradiation (LEEBI)," *Japanese Journal of Applied Physics*, vol. 28, no. 12A, p. L2112, 1989.

[17] S. Nakamura, T. Mukai, M. S. M. Senoh, and N. I. N. Iwasa, "Thermal Annealing Effects on P-Type Mg-Doped GaN Films," *Japanese Journal of Applied Physics*, vol. 31, no. 2B, p. L139, 1992.

[18] J. Wu, W. Walukiewicz, W. Shan, K. M. Yu, J. W. Ager, III, S. X. Li, E. E. Haller, H. Lu, and W. J. Schaff, "Temperature dependence of the fundamental band gap of InN," *Journal of Applied Physics*, vol. 94, no. 7, pp. 4457–4460, 2003.

[19] J. Y. Tsao, S. Chowdhury, M. A. Hollis, D. Jena, N. M. Johnson, K. A. Jones, R. J. Kaplar, S. Rajan, C. G. Van de Walle, E. Bellotti, C. L. Chua, R. Collazo, M. E. Coltrin, J. A. Cooper, K. R. Evans, S. Graham, T. A. Grotjohn, E. R. Heller, M. Higashiwaki, M. S. Islam, P. W. Juodawlkis, M. A. Khan, A. D. Koehler, J. H. Leach, U. K. Mishra, R. J. Nemanich, R. C. N. Pilawa-Podgurski, J. B. Shealy, Z. Sitar, M. J. Tadjer, A. F. Witulski, M. Wraback, and J. A. Simmons, "Ultrawide-Bandgap Semiconductors: Research Opportunities and Challenges," *Advanced Electronic Materials*, vol. 4, no. 1, p. 1600501, 2018.

[20] I. Vurgaftman and J. R. Meyer, "Band parameters for nitrogen-containing semiconductors," *Journal of Applied Physics*, vol. 94, no. 6, pp. 3675–3696, 2003.

[21] M. A. Caro, S. Schulz, S. B. Healy, and E. P. O'Reilly, "Built-in field control in alloyed c-plane III-N quantum dots and wells," *Journal of Applied Physics*, vol. 109, no. 8, p. 084110, 2011.

[22] H. Amano, R. Collazo, C. D. Santi, S. Einfeldt, M. Funato, J. Glaab, S. Hagedorn, A. Hirano, H. Hirayama, R. Ishii, Y. Kashima, Y. Kawakami, R. Kirste, M. Kneissl, R. Martin, F. Mehnke, M. Meneghini, A. Ougazzaden, P. J. Parbrook, S. Rajan, P. Reddy, F. Römer, J. Ruschel, B. Sarkar, F. Scholz, L. J. Schowalter, P. Shields, Z. Sitar, L. Sulmoni, T. Wang, T. Wernicke, M. Weyers, B. Witzigmann, Y.-R. Wu, T. Wunderer, and Y. Zhang, "The 2020 UV emitter roadmap," *Journal of Physics D: Applied Physics*, vol. 53, no. 50, p. 503001, 2020.

[23] D. S. P. Tanner, P. Dawson, M. J. Kappers, R. A. Oliver, and S. Schulz, "Polar (In,Ga)N/GaN quantum wells: Revisiting the impact of carrier localization on the green gap problem," *Phys. Rev. Appl.*, vol. 13, p. 044068, 2020.

[24] S. Morikawa, K. Ueno, A. Kobayashi, and H. Fujioka, "Pulsed Sputtering Preparation of InGaN Multi-Color Cascaded LED Stacks for Large-Area Monolithic Integration of RGB LED Pixels," *Crystals*, vol. 12, no. 4, 2022.

[25] Z. G, B. P, and R. S. T, "Update on the Status of LED-Lighting world market since 2018," no. KJ-NA-30500-EN-N (online), 2021. Accessed: 30/06/2023.

[26] R. A. Oliver, S. E. Bennett, T. Zhu, D. J. Beesley, M. J. Kappers, D. W. Saxey, A. Cerezo, and C. J. Humphreys, "Microstructural origins of localization in InGaN quantum wells," *J. Phys. D: Appl. Phys*, vol. 43, p. 345003, 2010.

[27] M. Usman, M. Munsif, U. Mushtaq, A.-R. Anwar, and N. Muhammad, "Green gap in GaN-based light-emitting diodes: in perspective," *Critical Reviews in Solid State and Materials Sciences*, vol. 46, no. 5, pp. 450–467, 2021.

[28] F. C.-P. Massabuau, M. J. Davies, F. Oehler, S. K. Pamenter, E. J. Thrush, M. J. Kappers, A. Kovács, T. Williams, M. A. Hopkins, C. J. Humphreys, P. Dawson, R. E. Dunin-Borkowski, J. Etheridge, D. W. E. Allsopp, and R. A. Oliver, "The impact of trench defects in InGaN/GaN light emitting diodes and implications for the "green gap" problem," *Applied Physics Letters*, vol. 105, no. 11, p. 112110, 2014.

[29] M. Auf der Maur, A. Pecchia, G. Penazzi, W. Rodrigues, and A. Di Carlo,

"Efficiency Drop in Green InGaN/GaN Light Emitting Diodes: The Role of Random Alloy Fluctuations," *Phys. Rev. Lett.*, vol. 116, p. 027401, 2016.

[30] C. De Santi, M. Meneghini, M. La Grassa, B. Galler, R. Zeisel, M. Goano, S. Dominici, M. Mandurrino, F. Bertazzi, D. Robidas, G. Meneghesso, and E. Zanoni, "Role of defects in the thermal droop of InGaN-based light emitting diodes," *Journal of Applied Physics*, vol. 119, no. 9, p. 094501, 2016.

[31] M. Meneghini, C. De Santi, A. Tibaldi, M. Vallone, F. Bertazzi, G. Meneghesso, E. Zanoni, and M. Goano, "Thermal droop in III-nitride based light-emitting diodes: Physical origin and perspectives," *J. Appl. Phys.*, vol. 127, p. 211102, 2020.

[32] C. D. Santi, M. Meneghini, D. Monti, J. Glaab, M. Guttmann, J. Rass, S. Einfeldt, F. Mehnke, J. Enslin, T. Wernicke, M. Kneissl, G. Meneghesso, and E. Zanoni, "Recombination mechanisms and thermal droop in AlGaN-based UV-B LEDs," *Photon. Res.*, vol. 5, no. 2, pp. A44–A51, 2017.

[33] J. Piprek, "Efficiency droop in nitride-based light-emitting diodes," *Phys. Status Solidi A*, vol. 207, p. 2217, 2010.

[34] F. Nippert, S. Y. Karpov, G. Callsen, B. Galler, T. Kure, C. Nenstiel, M. R. Wagner, M. Strassburg, H.-J. Lugauer, and A. Hoffmann, "Temperature-dependent recombination coefficients in InGaN light-emitting diodes: Hole localization, Auger processes, and the green gap," *Appl. Phys. Lett.*, vol. 109, no. 16, p. 161103, 2016.

[35] F. Nippert, M. Tollabi Mazraehno, M. J. Davies, M. P. Hoffmann, H.-J. Lugauer, T. Kure, M. Kneissl, A. Hoffmann, and M. R. Wagner, "Auger recombination in AlGaN quantum wells for UV light-emitting diodes," *Applied Physics Letters*, vol. 113, no. 7, 2018. 071107.

[36] C. Weisbuch, S. Nakamura, Y.-R. Wu, and J. S. Speck, "Disorder effects in nitride semiconductors: impact on fundamental and device properties," *Nanophotonics*, vol. 10, no. 1, pp. 3–21, 2020.

[37] S. Schulz and E. P. O'Reilly, "Electronic band structure," in *Handbook of optoelectronic device modeling & simulation* (J. Piprek, ed.), vol. 1, CRC Press Taylor & Francis Group, 2017.

[38] P. Harrison, *Quantum wells, wires and dots*. John C. Wiley & Sons, 2 ed., 2005.

[39] L. Barletti, G. Frosali, and O. Morandi, "Kinetic and hydrodynamic models for multi-band quantum transport in crystals," in *Multi-Band Effective Mass Approximations* (M. Ehrhardt and T. Koprucki, eds.), Springer International Publishing, 2014.

[40] E. Kioupakis, D. Steiauf, P. Rinke, K. T. Delaney, and C. G. Van de Walle, "First principles calculations of indirect Auger recombination in nitride semiconductors," *Phys. Rev. B*, vol. 92, p. 035207, 2015.

[41] C. M. Jones, C.-H. Teng, Q. Yan, P.-C. Ku, and E. Kioupakis, "Impact of carrier localization on recombination in InGaN quantum wells and the efficiency of nitride light-emitting diodes: Insights from theory and numerical simulations," *Appl. Phys. Lett.*, vol. 111, p. 113501, 2017.

[42] M. E. Rudinsky and S. Y. Karpov, "Radiative and Auger Recombination Constants and Internal Quantum Efficiency of (0001) AlGaN Deep-UV Light-Emitting Diode Structures," *physica status solidi (a)*, vol. 217, no. 14, p. 1900878, 2020.

[43] F. Bertazzi, M. Goano, and E. Bellotti, "A numerical study of Auger recombination in bulk InGaN," *Appl. Phys. Lett.*, vol. 97, p. 231118, 2010.

[44] F. Bertazzi, X. Zhou, M. Goano, G. Ghione, and E. Bellotti, "Auger recombination in InGaN/GaN quantum wells: A full-Brillouin-zone study," *Appl. Phys. Lett.*, vol. 103, p. 081106, 2013.

[45] M. Auf der Maur, "Multiscale approaches for the simulation of optoelectronic devices," *JOURNAL OF GREEN ENGINEERING*, vol. 5, no. 3-4, pp. 133–155, 2016.

[46] A. Di Vito, A. Pecchia, A. Di Carlo, and M. Auf der Maur, "Impact of compositional nonuniformity in (In,Ga)N-based light-emitting diodes," *Phys. Rev. Applied*, vol. 12, p. 014055, 2019.

[47] A. Di Vito, A. Pecchia, A. Di Carlo, and M. Auf der Maur, "Simulating random alloy effects in III-nitride light emitting diodes," *Journal of Applied Physics*, vol. 128, no. 4, p. 041102, 2020.

[48] C. Kittel, *Introduction to solid state physics*, ch. Crystal structure, p. 23. John Wiley & Sons, Inc, 1971.

[49] S. M. Sze and M. K. Lee, *Semiconductor Devices*. John Wiley & Sons, Inc., 3 ed., 2012.

[50] S. Nakamura, "Nobel Lecture: Background story of the invention of efficient blue InGaN light emitting diodes," *Rev. Mod. Phys.*, vol. 87, pp. 1139–1151, 2015.

[51] A. Bonfiglio, M. Lomascolo, G. Traetta, R. Cingolani, A. Di Carlo, F. Della Sala, P. Lugli, A. Botchkarev, and H. Morkoc, "Well-width dependence of the ground level emission of GaN/AlGaN quantum wells," *Journal of Applied Physics*, vol. 87, no. 5, pp. 2289–2292, 2000.

[52] B. Roul, M. Kumar, M. K. Rajpalke, T. N. Bhat, and S. B. Krupanidhi, "Binary group III-nitride based heterostructures: band offsets and transport properties," *Journal of Physics D: Applied Physics*, vol. 48, no. 42, p. 423001, 2015.

[53] P. G. Moses and C. G. Van de Walle, "Band bowing and band alignment in InGaN alloys," *Applied Physics Letters*, vol. 96, no. 2, p. 021908, 2010.

[54] P. G. Moses, M. Miao, Q. Yan, and C. G. Van de Walle, "Hybrid functional investigations of band gaps and band alignments for AlN, GaN, InN, and InGaN," *The Journal of Chemical Physics*, vol. 134, no. 8, p. 084703, 2011.

[55] T. M. Okon and J. R. Biard, "The first practical LED." `https://edisontechcenter.org/lighting/LED/TheFirstPracticalLED.pdf`, 2015. Accessed: 2023-05-23.

[56] J. Shim and D. Shin, "Measuring the internal quantum efficiency of light-emitting diodes: towards accurate and reliable room-temperature characterization," *Nanophotonics*, vol. 7, no. 10, pp. 1601–1615, 2018.

[57] R. Finn and S. Schulz, "Impact of random alloy fluctuations on the electronic and optical properties of (Al,Ga)N quantum wells: Insights from tight-binding calculations," *The Journal of Chemical Physics*, vol. 157, no. 24, 2022. 244705.

[58] S. Schulz, M. A. Caro, L.-T. Tan, P. J. Parbrook, R. W. Martin, and E. P. O'Reilly, "Composition-dependent band gap and band-edge bowing in

AlInN: A combined theoretical and experimental study," *Applied Physics Express*, vol. 6, no. 12, p. 121001, 2013.

[59] J. Piprek, "Efficiency models for GaN-Based Light-Emitting Diodes: Status and Challenges," *Materials*, vol. 13, p. 5174, 2020.

[60] W. Shockley and W. T. Read, Jr, "Statistics of the recombinations of holes and electrons," *Phys. Rev.*, vol. 87, pp. 835–842, 1952.

[61] R. N. Hall, "Electron-hole recombination in germanium," *Phys. Rev.*, vol. 87, p. 387, 1952.

[62] D. A. Neamen, *Semiconductor physics and devices*. McGraw-Hill, New York, 4 ed., 2012.

[63] F. Zhao, M. E. Turiansky, A. Alkauskas, and C. G. Van de Walle, "Trap-assisted Auger-Meitner recombination from first principles." `https://doi.org/10.48550/arXiv.2211.08642`, 2022.

[64] D. Matsakis, A. Coster, B. Laster, and R. Sime, "A renaming proposal: "The Auger–Meitner effect"," *Physics Today*, vol. 72, no. 9, pp. 10–11, 2019.

[65] C. Weisbuch, M. Piccardo, L. Martinelli, J. Iveland, J. Peretti, and J. S. Speck, "The efficiency challenge of nitride light-emitting diodes for lighting," *physica status solidi (a)*, vol. 212, no. 5, pp. 899–913, 2015.

[66] Y. C. Shen, G. Mueller, S. Watanabe, N. F. Gardner, A. Munkholm, and M. R. Krames, "Auger recombination in InGaN measured by photoluminescence," *Appl. Phys. Lett.*, vol. 91, p. 141101, 2007.

[67] A. Nirschl, M. Binder, M. Schmid, I. Pietzonka, H. J. Lugauer, R. Zeisel, M. Sabathil, D. Bougeard, and B. Galler, "Towards quantification of the crucial impact of Auger recombination for the efficiency droop in (AlInGa)N quantum well structures," *Opt. Express*, vol. 24, p. 2971, 2016.

[68] M. Binder, A. Nirschl, R. Zeisel, T. Hager, H. J. Lugauer, M. Sabathil, J. Wagner, D. Bougeard, and B. Galler, "Identification of nnp and npp Auger recombination as significant contributor to the efficiency droop in (GaIn)N quantum wells by visualization of hot carriers in photoluminensce," *Appl. Phys. Lett.*, vol. 103, p. 071108, 2013.

[69] B. Galler, P. Dreschel, R. Monnard, P. Rode, P. Stauss, S. Froehlich, W. Bergbauer, M. Binder, M. Sabathil, B. Hahn, and J. Wagner, "Influence of indium content and temperature on Auger-like recombination in InGaN quantum wells grown on (111) silicon substrates," *Appl. Phys. Lett.*, vol. 101, p. 131111, 2012.

[70] P. Tian, J. J. D. McKendry, J. Hernsdorf, S. Watson, R. Ferreira, I. M. Watson, E. Gu, A. E. Kelly, and M. D. Dawson, "Temperature-dependent efficiency droop of blue InGaN micro-light emitting diodes," *Appl. Phys. Lett.*, vol. 105, p. 171107, 2014.

[71] S. K. Patra, *Electronic and optical properties of III-Nitride nanostructures*. PhD thesis, University College Cork, 2019.

[72] M. Á. Caro Bayo, *Theory of elasticity and electric polarization effects in the group-III nitrides*. PhD thesis, University College Cork, 2013.

[73] K. Y. Cheng, *III–V Compound Semiconductors and Devices*. Springer Cham, 2020.

[74] A. Kobayashi, O. F. Sankey, S. M. Volz, and J. D. Dow, "Semiempirical tight-binding band structures of wurtzite semiconductors: AlN, CdS, CdSe, ZnS, and ZnO," *Phys. Rev. B*, vol. 28, pp. 935–945, 1983.

[75] S. Schulz, *Electronic and Optical Properties of Quantum Dots: A Tight-Binding Approach*. PhD thesis, University of Bremen, 2007.

[76] H. Morkoç, *Handbook of Nitride Semiconductors and Devices*, vol. 1. Wiley-VCH Verlag, 2008.

[77] S. Pereira, M. R. Correia, E. Pereira, K. P. O'Donnell, E. Alves, A. D. Sequeira, and N. Franco, "Interpretation of double x-ray diffraction peaks from InGaN layers," *Applied Physics Letters*, vol. 79, no. 10, pp. 1432–1434, 2001.

[78] D. F. Feezell, M. C. Schmidt, S. P. DenBaars, and S. Nakamura, "Development of Nonpolar and Semipolar InGaN/GaN Visible Light-Emitting Diodes," *MRS Bulletin*, vol. 34, no. 5, p. 318–323, 2009.

[79] O. Ambacher, J. Majewski, C. Miskys, A. Link, M. Hermann, M. Eickhoff, M. Stutzmann, F. Bernardini, V. Fiorentini, V. Tilak, B. Schaff, and L. F. Eastman, "Pyroelectric properties of Al(In)GaN/GaN hetero- and

quantum well structures," *Journal of Physics: Condensed Matter*, vol. 14, no. 13, p. 3399, 2002.

[80] A. Zoroddu, F. Bernardini, P. Ruggerone, and V. Fiorentini, "First-principles prediction of structure, energetics, formation enthalpy, elastic constants, polarization, and piezoelectric constants of AlN, GaN, and InN: Comparison of local and gradient-corrected density-functional theory," *Phys. Rev. B*, vol. 64, p. 045208, 2001.

[81] B. P. Pandey, V. Kumar, and E. M. Proupin, "Elastic constants and Debye temperature of wz-AlN and wz-GaN semiconductors under high pressure from first-principles," *Pramana*, vol. 83, pp. 413–425, 2014.

[82] M. A. Caro, S. Schulz, and E. P. O'Reilly, "Theory of local electric polarization and its relation to internal strain: impact on the polarization potential and electronic properties of group-III nitrides," *Phys. Rev. B*, vol. 88, p. 214103, 2013.

[83] A. Zangwill, *Modern electrodynamics*, ch. Dielectric Matter. Cambridge University Press, 2013.

[84] J. D. Jackson, *Classical Electrodynamics*. John Wiley & Sons, Inc., 3 ed., 1999.

[85] F. Bernardini, V. Fiorentini, and D. Vanderbilt, "Spontaneous polarization and piezoelectric constants of III-V nitrides," *Phys. Rev. B*, vol. 56, pp. R10024–R10027, 1997.

[86] F. Bernardini and V. Fiorentini, "Spontaneous versus piezoelectric polarization in III–V nitrides: Conceptual aspects and practical consequences," *physica status solidi (b)*, vol. 216, no. 1, pp. 391–398, 1999.

[87] M. A. Migliorato, J. Pal, X. Huang, W. Hu, M. Willatzen, and Y. Gu, "Polarization in III-N semiconductors," in *Handbook of optoelectronic device modeling & simulation* (J. Piprek, ed.), vol. 1, CRC Press Taylor & Francis Group, 2017.

[88] A. Schliwa, G. Hönig, and D. Bimberg, "Electronic properties of III-V quantum dots," in *Multi-Band Effective Mass Approximations* (M. Ehrhardt and T. Koprucki, eds.), Springer International Publishing, 2014.

[89] D. S. P. Tanner, *A study of the elastic and electronic properties of III-nitride semiconductors*. PhD thesis, University College Cork, 2017.

[90] B.-T. Liou, C.-Y. Lin, S.-H. Yen, and Y.-K. Kuo, "First-principles calculation for bowing parameter of wurtzite $In_xGa_{1-x}N$," *Optics Communications*, vol. 249, no. 1, pp. 217–223, 2005.

[91] B. Jahnen, M. Albrecht, W. Dorsch, S. Christiansen, H. P. Strunk, D. Hanser, and R. F. Davis, "Pinholes, Dislocations and Strain Relaxation in InGaN," *MRS Internet Journal of Nitride Semiconductor Research*, vol. 3, no. 39, 1998.

[92] D. Holec, P. Costa, M. Kappers, and C. Humphreys, "Critical thickness calculations for InGaN/GaN," *Journal of Crystal Growth*, vol. 303, no. 1, pp. 314–317, 2007. Proceedings of the Fifth Workshop on Modeling in Crystal Growth.

[93] M. Leyer, J. Stellmach, C. Meissner, M. Pristovsek, and M. Kneissl, "The critical thickness of InGaN on (0001)GaN," *Journal of Crystal Growth*, vol. 310, no. 23, pp. 4913–4915, 2008. The Fourteenth International conference on Metalorganic Vapor Phase Epitaxy.

[94] F. Bernardini and V. Fiorentini, "Macroscopic polarization and band offsets at nitride heterojunctions," *Phys. Rev. B*, vol. 57, pp. R9427–R9430, 1998.

[95] J.-H. Ryou, P. D. Yoder, J. Liu, Z. Lochner, H. Kim, S. Choi, H. J. Kim, and R. D. Dupuis, "Control of Quantum-Confined Stark Effect in InGaN-Based Quantum Wells," *IEEE Journal of Selected Topics in Quantum Electronics*, vol. 15, no. 4, pp. 1080–1091, 2009.

[96] T. M. Smeeton, M. J. Kappers, J. S. Barnard, M. E. Vickers, and C. J. Humphreys, "Electron-beam-induced strain within InGaN quantum wells: False indium "cluster"' detection in the transmission electron microscope," *Appl. Phys. Lett.*, vol. 83, p. 5419, 2003.

[97] C. Frankerl, F. Nippert, A. Gomez-Iglesias, M. P. Hoffmann, C. Brandl, H.-J. Lugauer, R. Zeisel, A. Hoffmann, and M. J. Davies, "Origin of carrier localization in AlGaN-based quantum well structures and implications for efficiency droop," *Applied Physics Letters*, vol. 117, no. 10, p. 102107, 2020.

[98] T. P. Bartel, P. Specht, J. C. Ho, and C. Kisielowski, "Phase separation in $In_xGa_{1-x}N$," *Philosophical Magazine*, vol. 87, no. 13, pp. 1983–1998, 2007.

[99] D. M. Graham, A. Soltani-Vala, P. Dawson, M. J. Godfrey, T. M. Smeeton, J. S. Barnard, M. J. Kappers, C. J. Humphreys, and E. J. Thrush, "Optical and microstructural studies of InGaN/GaN single-quantum-well structures," *J. Appl. Phys.*, vol. 97, p. 103508, 2005.

[100] J. Singh and K. K. Bajaj, "Role of interface roughness and alloy disorder in photoluminescence in quantum-well structures," *Journal of Applied Physics*, vol. 57, no. 12, pp. 5433–5437, 1985.

[101] R. L. S. Devine, "Photoluminescence characterisation of InGaAs/GaAs quantum well structures," *Semiconductor Science and Technology*, vol. 3, no. 12, p. 1171, 1988.

[102] D. C. Bertolet, J. Hsu, K. M. Lau, E. S. Koteles, and D. Owens, "Exciton photoluminescence linewidths in very narrow AlGaAs/GaAs and GaAs/InGaAs quantum wells," *Journal of Applied Physics*, vol. 64, no. 11, pp. 6562–6564, 1988.

[103] D. T. S. Watson-Parris, *Carrier localization in InGaN/GaN quantum wells*. PhD thesis, University of Manchester, 2011.

[104] A. Aït-Ouali, R. Y.-F. Yip, J. L. Brebner, and R. A. Masut, "Strain relaxation and exciton localization effects on the Stokes shift in $InAs_xP_{1-x}$/InP multiple quantum wells," *Journal of Applied Physics*, vol. 83, no. 6, pp. 3153–3160, 1998.

[105] B. Damilano, N. Grandjean, J. Massies, L. Siozade, and J. Leymarie, "InGaN/GaN quantum wells grown by molecular-beam epitaxy emitting from blue to red at 300 K," *Appl. Phys. Lett.*, vol. 77, p. 1268, 2000.

[106] P. Lefebvre, A. Morel, M. Gallart, T. Taliercio, J. Allègre, B. Gil, H. Mathieu, B. Damilano, N. Grandjean, and J. Massies, "High internal electric field in a graded-width InGaN/GaN quantum well: Accurate determination by time-resolved photoluminescence spectroscopy," *Applied Physics Letters*, vol. 78, no. 9, pp. 1252–1254, 2001.

[107] A. Polimeni, A. Patanè, M. G. Alessi, M. Capizzi, F. Martelli, A. Bosacchi, and S. Franchi, "Stokes shift in quantum wells: Trapping versus thermalization," *Phys. Rev. B*, vol. 54, pp. 16389–16392, 1996.

[108] C. Delalande, M. H. Meynadier, and M. Voos, "Effect of temperature on exciton trapping on interface defects in GaAs quantum wells," *Phys. Rev. B*, vol. 31, pp. 2497–2498, 1985.

[109] M. Hetterich, M. D. Dawson, A. Y. Egorov, D. Bernklau, and H. Riechert, "Electronic states and band alignment in GaInNAs/GaAs quantum-well structures with low nitrogen content," *Applied Physics Letters*, vol. 76, no. 8, pp. 1030–1032, 2000.

[110] M. Colocci, M. Gurioli, and A. Vinattieri, "Thermal ionization of excitons in GaAs/AlGaAs quantum well structures," *Journal of Applied Physics*, vol. 68, no. 6, pp. 2809–2812, 1990.

[111] D. V. Talapin, R. Koeppe, S. Götzinger, A. Kornowski, J. M. Lupton, A. L. Rogach, O. Benson, J. Feldmann, and H. Weller, "Highly Emissive Colloidal CdSe/CdS Heterostructures of Mixed Dimensionality," *Nano Letters*, vol. 3, no. 12, pp. 1677–1681, 2003.

[112] Y.-H. Cho, G. H. Gainer, A. J. Fischer, J. J. Song, S. Keller, U. K. Mishra, and S. P. DenBaars, ""S-shaped" temperature-dependent emission shift and carrier dynamics in InGaN/GaN multiple quantum wells," *Applied Physics Letters*, vol. 73, no. 10, pp. 1370–1372, 1998.

[113] Y. Varshni, "Temperature dependence of the energy gap in semiconductors," *Physica*, vol. 34, no. 1, pp. 149–154, 1967.

[114] P. G. Eliseev, "The red σ^2/kt spectral shift in partially disordered semiconductors," *J. Appl. Phys.*, vol. 93, p. 5404, 2003.

[115] K. L. Teo, J. S. Colton, P. Y. Yu, E. R. Weber, M. F. Li, W. Liu, K. Uchida, H. Tokunaga, N. Akutsu, and K. Matsumoto, "An analysis of temperature dependent photoluminescence line shapes in InGaN," *Applied Physics Letters*, vol. 73, no. 12, pp. 1697–1699, 1998.

[116] Y. Narukawa, Y. Kawakami, M. Funato, S. Fujita, S. Fujita, and S. Nakamura, "Role of self-formed InGaN quantum dots for exciton localization in the purple laser diode emitting at 420 nm," *Applied Physics Letters*, vol. 70, no. 8, pp. 981–983, 1997.

[117] M. J. Galtrey, R. A. Oliver, M. J. Kappers, C. J. Humphreys, D. J. Stokes, P. H. Clifton, and A. Cerezo, "Three-dimensional atom probe studies of an $In_xGa_{1-x}N$/GaN multiple quantum well structure: Assessment of possible indium clustering," *Appl. Phys. Lett.*, vol. 90, p. 061903, 2007.

[118] L. Bellaiche, T. Mattila, L.-W. Wang, S.-H. Wei, and A. Zunger, "Resonant hole localization and anomalous optical bowing in InGaN alloys," *Applied Physics Letters*, vol. 74, no. 13, pp. 1842–1844, 1999.

[119] L.-W. Wang, "Calculations of carrier localization in $\mathrm{In}_x\mathrm{Ga}_{1-x}\mathrm{N}$," *Phys. Rev. B*, vol. 63, p. 245107, 2001.

[120] S. F. Chichibu, A. Uedono, T. Onuma, B. A. Haskell, A. Chakraborty, T. Koyama, P. T. Fini, S. Keller, S. P. DenBaars, J. S. Speck, U. K. Mishra, S. Nakamura, S. Yamaguchi, S. Kamiyama, H. Amano, I. Akasaki, J. Han, and T. Sota, "Origin of defect-insensitive emission probability in In-containing (Al,In,Ga)N alloy semiconductors," *Nature Mater.*, vol. 5, p. 810, 2006.

[121] J. A. Chan, J. Z. Liu, and A. Zunger, "Bridging the gap between atomic microstructure and electronic properties of alloys: The case of (In,Ga)N," *Phys. Rev. B*, vol. 82, p. 045112, 2010.

[122] M. Usman and E. P. O'Reilly, "Atomistic tight-binding study of electronic structure and interband optical transitions in $GaBi_xAs_{1-x}$/GaAs quantum wells," *Applied Physics Letters*, vol. 104, no. 7, p. 071103, 2014.

[123] R. W. Smith and G. S. Was, "Application of molecular dynamics to the study of hydrogen embrittlement in Ni-Cr-Fe alloys," *Phys. Rev. B*, vol. 40, pp. 10322–10336, 1989.

[124] D. Farkas, "Deformation behavior of a model high entropy alloy from atomistic simulations," *Materials Science and Engineering: A*, vol. 812, p. 141124, 2021.

[125] S.-H. Wei, L. G. Ferreira, J. E. Bernard, and A. Zunger, "Electronic properties of random alloys: Special quasirandom structures," *Phys. Rev. B*, vol. 42, pp. 9622–9649, 1990.

[126] S. Kalliakos, X. B. Zhang, T. Taliercio, P. Lefebvre, B. Gil, N. Grandjean, B. Damilano, and J. Massies, "Large size dependence of exciton-longitudinal-optical-phonon coupling in nitride-based quantum

wells and quantum boxes," *Applied Physics Letters*, vol. 80, no. 3, pp. 428–430, 2002.

[127] A. Morel, P. Lefebvre, S. Kalliakos, T. Taliercio, T. Bretagnon, and B. Gil, "Donor-acceptor-like behavior of electron-hole pair recombinations in low-dimensional (Ga,In)N/GaN systems," *Phys. Rev. B*, vol. 68, p. 045331, 2003.

[128] M. J. Galtrey, R. A. Oliver, M. J. Kappers, C. J. Humphreys, P. H. Clifton, D. Larson, D. W. Saxey, and A. Cerezo, "Three-dimensional atom probe analysis of green- and blue-emitting $In_xGa_{1-x}N/GaN$ multiple quantum well structures," *Journal of Applied Physics*, vol. 104, no. 1, p. 013524, 2008.

[129] D. Watson-Parris, M. J. Godfrey, P. Dawson, R. A. Oliver, M. J. Galtrey, M. J. Kappers, and C. J. Humphreys, "Carrier localization mechanisms in $In_xGa_{1-x}N/GaN$," *Phys. Rev. B*, vol. 83, p. 115321, 2011.

[130] D. S. P. Tanner, M. A. Caro, E. P. O'Reilly, and S. Schulz, "Random alloy fluctuations and structural inhomogeneities in c-plane $In_xGa_{1-x}N$ quantum wells: theory of ground and excited electron and hole states," *RSC Adv.*, vol. 6, p. 64513, 2016.

[131] R. T. Phillips, A. G. Steffan, S. R. Newton, T. L. Reinecke, and R. Kotlyar, "Exciton fine structure in interfacial quantum dots," *physica status solidi (b)*, vol. 238, no. 3, pp. 601–606, 2003.

[132] E. P. O'Reilly, *Quantum theory of solids*. Taylor & Francis, Taylor & Francis Group, 2002.

[133] M. Ueno, M. Yoshida, A. Onodera, O. Shimomura, and K. Takemura, "Stability of the wurtzite-type structure under high pressure: GaN and InN," *Phys. Rev. B*, vol. 49, pp. 14–21, 1994.

[134] H. Haug and S. W. Koch, *Quantum theory of the optical and electronic properties of semiconductors, third edition*. World Scientific Publishing Co. Pte. Ltd., 3 ed., 2001.

[135] P. Phillips, *Advanced Solid State Physics*. Cambridge University Press, 2 ed., 2012.

[136] M. Born and R. Oppenheimer, "Zur Quantentheorie der Molekeln," *Annalen der Physik*, vol. 389, no. 20, p. 457, 1927.

[137] E. Lipparini, *Modern many-particle physics*. 5 Toh Tuck Link, Singapore 596224: World Scientific Co. Pte. Ltd., 2 ed., 2008.

[138] F. Bloch, "Über die quantenmechanik der elektronen in kristallgittern," *Zeitschrift für physik*, vol. 52, no. 7-8, pp. 555–600, 1929.

[139] P. Hohenberg and W. Kohn, "Inhomogeneous electron gas," *Phys. Rev.*, vol. 136, pp. B864–B871, 1964.

[140] W. Kohn and L. J. Sham, "Self-consistent equations including exchange and correlation effects," *Phys. Rev.*, vol. 140, pp. A1133–A1138, 1965.

[141] T. Bredow and A. R. Gerson, "Effect of exchange and correlation on bulk properties of MgO, NiO, and CoO," *Phys. Rev. B*, vol. 61, pp. 5194–5201, 2000.

[142] J. Muscat, A. Wander, and N. Harrison, "On the prediction of band gaps from hybrid functional theory," *Chemical Physics Letters*, vol. 342, no. 3, pp. 397–401, 2001.

[143] E. Kioupakis, P. Rinke, K. T. Delaney, and C. G. Van de Walle, "Indirect Auger recombination as a cause of efficiency droop in nitride light-emitting diodes," *Appl. Phys. Lett.*, vol. 98, p. 161107, 2011.

[144] J. Heyd, G. E. Scuseria, and M. Ernzerhof, "Hybrid functionals based on a screened Coulomb potential," *The Journal of Chemical Physics*, vol. 118, no. 18, pp. 8207–8215, 2003.

[145] R. M. Martin, *Electronic structure: basic theory and practical methods*. Cambridge university press, 2020.

[146] J. P. Perdew, "Density functional theory and the band gap problem," *International Journal of Quantum Chemistry*, vol. 28, no. S19, pp. 497–523, 1985.

[147] A. J. Cohen, P. Mori-Sánchez, and W. Yang, "Challenges for density functional theory," *Chemical reviews*, vol. 112, no. 1, pp. 289–320, 2012.

[148] J. P. Perdew, K. Burke, and Y. Wang, "Generalized gradient approximation for the exchange-correlation hole of a many-electron system," *Physical review B*, vol. 54, no. 23, p. 16533, 1996.

[149] J. P. Perdew, K. Burke, and M. Ernzerhof, "Generalized gradient approximation made simple," *Phys. Rev. Lett.*, vol. 77, pp. 3865–3868, 1996.

[150] A. D. Becke, "A new mixing of Hartree–Fock and local density-functional theories," *The Journal of Chemical Physics*, vol. 98, no. 2, pp. 1372–1377, 1993.

[151] J. P. Perdew, M. Ernzerhof, and K. Burke, "Rationale for mixing exact exchange with density functional approximations," *The Journal of Chemical Physics*, vol. 105, no. 22, pp. 9982–9985, 1996.

[152] J. Paier, M. Marsman, K. Hummer, G. Kresse, I. C. Gerber, and J. G. Ángyán, "Screened hybrid density functionals applied to solids," *The Journal of Chemical Physics*, vol. 124, no. 15, p. 154709, 2006.

[153] J. Wróbel, K. J. Kurzydłowski, K. Hummer, G. Kresse, and J. Piechota, "Calculations of ZnO properties using the Heyd-Scuseria-Ernzerhof screened hybrid density functional," *Phys. Rev. B*, vol. 80, p. 155124, 2009.

[154] N. Marom, O. Hod, G. E. Scuseria, and L. Kronik, "Electronic structure of copper phthalocyanine: A comparative density functional theory study," *The Journal of Chemical Physics*, vol. 128, no. 16, p. 164107, 2008.

[155] T. Hornos, A. Gali, and B. G. Svensson, "Large-Scale Electronic Structure Calculations of Vacancies in 4H-SiC Using the Heyd-Scuseria-Ernzerhof Screened Hybrid Density Functional," in *Silicon Carbide and Related Materials 2010*, vol. 679 of *Materials Science Forum*, pp. 261–264, Trans Tech Publications Ltd, 2011.

[156] H. Wu, A. Stroppa, S. Sakong, S. Picozzi, M. Scheffler, and P. Kratzer, "Magnetism in C- or N-doped MgO and ZnO: A Density-Functional Study of Impurity Pairs," *Phys. Rev. Lett.*, vol. 105, p. 267203, 2010.

[157] K. T. Delaney, P. Rinke, and C. G. Van de Walle, "Auger recombination rates in nitrides from first principles," *Appl. Phys. Lett.*, vol. 94, p. 191109, 2009.

[158] A. Carvalho, A. Alkauskas, A. Pasquarello, A. K. Tagantsev, and N. Setter, "A hybrid density functional study of lithium in ZnO: Stability, ionization levels, and diffusion," *Phys. Rev. B*, vol. 80, p. 195205, 2009.

[159] A. Carvalho, A. Alkauskas, A. Pasquarello, A. Tagantsev, and N. Setter, "Li-related defects in ZnO: Hybrid functional calculations," *Physica B: Condensed Matter*, vol. 404, no. 23, pp. 4797–4799, 2009.

[160] D. S. Sholl and J. Steckel, *Density Functional Theory: A Practical Introduction*. Hoboken, New Jersey: John Wiley & Sons, Inc., 2 ed., 2009.

[161] M. A. Caro, S. Schulz, and E. P. O'Reilly, "Hybrid functional study of the elastic and structural properties of wurtzite and zinc-blende group-III nitrides," *Phys. Rev. B*, vol. 86, p. 014117, 2012.

[162] G. R. Schleder, A. C. M. Padilha, C. M. Acosta, M. Costa, and A. Fazzio, "From DFT to machine learning: recent approaches to materials science–a review," *Journal of Physics: Materials*, vol. 2, no. 3, p. 032001, 2019.

[163] J. C. A. Prentice, J. Aarons, J. C. Womack, A. E. A. Allen, L. Andrinopoulos, L. Anton, R. A. Bell, A. Bhandari, G. A. Bramley, R. J. Charlton, R. J. Clements, D. J. Cole, G. Constantinescu, F. Corsetti, S. M.-M. Dubois, K. K. B. Duff, J. M. Escartín, A. Greco, Q. Hill, L. P. Lee, E. Linscott, D. D. O'Regan, M. J. S. Phipps, L. E. Ratcliff, A. Serrano, E. W. Tait, G. Teobaldi, V. Vitale, N. Yeung, T. J. Zuehlsdorff, J. Dziedzic, P. D. Haynes, N. D. M. Hine, A. A. Mostofi, M. C. Payne, and C.-K. Skylaris, "The ONETEP linear-scaling density functional theory program," *The Journal of Chemical Physics*, vol. 152, no. 17, p. 174111, 2020.

[164] A. Nakata, J. S. Baker, S. Y. Mujahed, J. T. L. Poulton, S. Arapan, J. Lin, Z. Raza, S. Yadav, L. Truflandier, T. Miyazaki, and D. R. Bowler, "Large scale and linear scaling DFT with the CONQUEST code," *The Journal of Chemical Physics*, vol. 152, no. 16, p. 164112, 2020.

[165] D. J. Dugdale, S. Brand, and R. A. Abram, "Direct calculation of $\mathbf{k} \cdot \mathbf{p}$ parameters for wurtzite AlN, GaN, and InN," *Phys. Rev. B*, vol. 61, pp. 12933–12938, 2000.

[166] P. Löwdin, "A Note on the Quantum-Mechanical Perturbation Theory," *The Journal of Chemical Physics*, vol. 19, no. 11, pp. 1396–1401, 1951.

[167] S. L. Chuang and C. S. Chang, "k·p method for strained wurtzite semiconductors," *Phys. Rev. B*, vol. 54, pp. 2491–2504, 1996.

[168] C. R. Pidgeon and R. N. Brown, "Interband Magneto-Absorption and Faraday Rotation in InSb," *Phys. Rev.*, vol. 146, pp. 575–583, 1966.

[169] T.-J. Yang, R. Shivaraman, J. S. Speck, and Y.-R. Wu, "The influence of random indium alloy fluctuations in indium gallium nitride quantum wells on the device behavior," *Journal of Applied Physics*, vol. 116, no. 11, p. 113104, 2014.

[170] M. Piccardo, C.-K. Li, Y.-R. Wu, J. S. Speck, B. Bonef, R. M. Farrell, M. Filoche, L. Martinelli, J. Peretti, and C. Weisbuch, "Localization landscape theory of disorder in semiconductors. II. Urbach tails of disordered quantum well layers," *Phys. Rev. B*, vol. 95, p. 144205, 2017.

[171] Y.-R. Wu, R. Shivaraman, K.-C. Wang, and J. S. Speck, "Analyzing the physical properties of InGaN multiple quantum well light emitting diodes from nano scale structure," *Applied Physics Letters*, vol. 101, no. 8, p. 083505, 2012.

[172] M. O'Donovan, M. Luisier, E. P. O'Reilly, and S. Schulz, "Impact of random alloy fluctuations on inter-well transport in InGaN/GaN multi-quantum well systems: an atomistic non-equilibrium Green's function study," *Journal of Physics: Condensed Matter*, vol. 33, no. 4, p. 045302, 2020.

[173] M. Filoche and S. Mayboroda, "Universal mechanism for Anderson and weak localization," *Proceedings of the National Academy of Sciences*, vol. 109, no. 37, pp. 14761–14766, 2012.

[174] M. Filoche, M. Piccardo, Y.-R. Wu, C.-K. Li, C. Weisbuch, and S. Mayboroda, "Localization landscape theory of disorder in semiconductors. I. Theory and modeling," *Physical Review B*, vol. 95, no. 14, p. 144204, 2017.

[175] W. Wang and S. Zhang, "The exponential decay of eigenfunctions for tight-binding Hamiltonians via landscape and dual landscape functions," in *Annales Henri Poincaré*, vol. 22, pp. 1429–1457, Springer, 2021.

[176] D. Arnold, M. Filoche, S. Mayboroda, W. Wang, and S. Zhang, "The landscape law for tight binding Hamiltonians," *Communications in Mathematical Physics*, vol. 396, no. 3, pp. 1339–1391, 2022.

[177] D. Chaudhuri, J. C. Kelleher, M. R. O'Brien, E. P. O'Reilly, and S. Schulz, "Electronic structure of semiconductor nanostructures: A modified localization landscape theory," *Phys. Rev. B*, vol. 101, p. 035430, 2020.

[178] M. O'Donovan, D. Chaudhuri, T. Streckenbach, P. Farrell, S. Schulz, and T. Koprucki, "From atomistic tight-binding theory to macroscale drift–diffusion: Multiscale modeling and numerical simulation of uni-polar charge transport in (In,Ga)N devices with random fluctuations," *Journal of Applied Physics*, vol. 130, no. 6, p. 065702, 2021.

[179] C.-K. Li, M. Piccardo, L.-S. Lu, S. Mayboroda, L. Martinelli, J. Peretti, J. S. Speck, C. Weisbuch, M. Filoche, and Y.-R. Wu, "Localization landscape theory of disorder in semiconductors. III. Application to carrier transport and recombination in light emitting diodes," *Phys. Rev. B*, vol. 95, p. 144206, 2017.

[180] P. Rinke, M. Winkelnkemper, A. Qteish, D. Bimberg, J. Neugebauer, and M. Scheffler, "Consistent set of band parameters for the group-III nitrides AlN, GaN, and InN," *Physical Review B*, vol. 77, no. 7, p. 075202, 2008.

[181] J.-M. Jancu, F. Bassani, F. D. Sala, and R. Scholz, "Transferable tight-binding parametrization for the group-III nitrides," *Applied physics letters*, vol. 81, no. 25, pp. 4838–4840, 2002.

[182] J. C. Slater and G. F. Koster, "Simplified LCAO method for the periodic potential problem," *Physical review*, vol. 94, no. 6, p. 1498, 1954.

[183] S. Schulz, S. Schumacher, and G. Czycholl, "Tight-binding model for semiconductor quantum dots with a wurtzite crystal structure: From one-particle properties to Coulomb correlations and optical spectra," *Phys. Rev. B*, vol. 73, p. 245327, 2006.

[184] M. Luisier, A. Schenk, W. Fichtner, and G. Klimeck, "Atomistic simulation of nanowires in the $sp^3d^5s^*$ tight-binding formalism: From boundary conditions to strain calculations," *Physical Review B*, vol. 74, no. 20, p. 205323, 2006.

[185] M. López, A. Pecchia, M. Auf der Maur, F. Sacconi, G. Penazzi, and A. Di Carlo, "Atomistic simulations of InGaN/GaN random alloy

quantum well LEDs," *physica status solidi c*, vol. 11, no. 3-4, pp. 632–634, 2014.

[186] D. W. Jenkins and J. D. Dow, "Electronic structures and doping of InN, $\mathrm{In_xGa_{1-x}N}$, and $\mathrm{In_xAl_{1-x}N}$," *Phys. Rev. B*, vol. 39, pp. 3317–3329, 1989.

[187] T. Yang, S. Nakajima, and S. Sakai, "Electronic Structures of Wurtzite GaN, InN and Their Alloy $\mathrm{Ga_{1-x}In_xN}$ Calculated by the Tight-Binding Method," *Japanese Journal of Applied Physics*, vol. 34, no. 11R, p. 5912, 1995.

[188] E. O'Reilly, A. Lindsay, S. Tomić, and M. Kamal-Saadi, "Tight-binding and $\mathbf{k}\cdot\mathbf{p}$ models for the electronic structure of Ga (In) NAs and related alloys," *Semiconductor science and technology*, vol. 17, no. 8, p. 870, 2002.

[189] Z. Li and W. Pötz, "Electronic density of states of semiconductor alloys from lattice-mismatched isovalent binary constituents," *Physical Review B*, vol. 46, no. 4, p. 2109, 1992.

[190] T. B. Boykin, N. Kharche, G. Klimeck, and M. Korkusinski, "Approximate bandstructures of semiconductor alloys from tight-binding supercell calculations," *Journal of Physics: Condensed Matter*, vol. 19, no. 3, p. 036203, 2007.

[191] T. B. Boykin, G. Klimeck, R. C. Bowen, and F. Oyafuso, "Diagonal parameter shifts due to nearest-neighbor displacements in empirical tight-binding theory," *Phys. Rev. B*, vol. 66, p. 125207, 2002.

[192] Y. M. Niquet, D. Rideau, C. Tavernier, H. Jaouen, and X. Blase, "Onsite matrix elements of the tight-binding Hamiltonian of a strained crystal: Application to silicon, germanium, and their alloys," *Phys. Rev. B*, vol. 79, p. 245201, 2009.

[193] J.-M. Jancu, R. Scholz, F. Beltram, and F. Bassani, "Empirical $\mathrm{spds^*}$ tight-binding calculation for cubic semiconductors: General method and material parameters," *Phys. Rev. B*, vol. 57, pp. 6493–6507, 1998.

[194] M. Winkelnkemper, A. Schliwa, and D. Bimberg, "Interrelation of structural and electronic properties in $\mathrm{In_xGa_{1-x}N/GaN}$ quantum dots using an eight-band $\mathbf{k}\bullet\mathbf{p}$ model," *Phys. Rev. B*, vol. 74, p. 155322, 2006.

[195] S. Schulz, T. J. Badcock, M. A. Moram, P. Dawson, M. J. Kappers, C. J. Humphreys, and E. P. O'Reilly, "Electronic and optical properties of nonpolar a-plane GaN quantum wells," *Phys. Rev. B*, vol. 82, p. 125318, 2010.

[196] Q. Yan, P. Rinke, M. Scheffler, and C. G. Van de Walle, "Strain effects in group-III nitrides: Deformation potentials for AlN, GaN, and InN," *Applied Physics Letters*, vol. 95, no. 12, p. 121111, 2009.

[197] F. H. Stillinger and T. A. Weber, "Computer simulation of local order in condensed phases of silicon," *Physical review B*, vol. 31, no. 8, p. 5262, 1985.

[198] J. E. Jones and S. Chapman, "On the determination of molecular fields.—I. From the variation of the viscosity of a gas with temperature," *Proceedings of the Royal Society of London. Series A, Containing Papers of a Mathematical and Physical Character*, vol. 106, no. 738, pp. 441–462, 1924.

[199] M. Musgrave and J. A. Pople, "A general valence force field for diamond," *Proceedings of the Royal Society of London. Series A. Mathematical and Physical Sciences*, vol. 268, no. 1335, pp. 474–484, 1962.

[200] P. N. Keating, "Effect of invariance requirements on the elastic strain energy of crystals with application to the diamond structure," *Physical Review*, vol. 145, no. 2, p. 637, 1966.

[201] R. M. Martin, "Elastic properties of ZnS structure semiconductors," *Physical Review B*, vol. 1, no. 10, p. 4005, 1970.

[202] D. S. Tanner, M. A. Caro, S. Schulz, and E. P. O'Reilly, "Fully analytic valence force field model for the elastic and inner elastic properties of diamond and zincblende crystals," *Physical Review B*, vol. 100, no. 9, p. 094112, 2019.

[203] S. Schulz, M. A. Caro, C. Coughlan, and E. P. O'Reilly, "Atomistic anaylsis of the impact of alloy and well width fluctuations on the electronic and optical properties of InGaN/GaN quantum wells," *Phys. Rev. B*, vol. 91, p. 035439, 2015.

[204] A. P. Thompson, H. M. Aktulga, R. Berger, D. S. Bolintineanu, W. M. Brown, P. S. Crozier, P. J. in 't Veld, A. Kohlmeyer, S. G. Moore, T. D.

Nguyen, R. Shan, M. J. Stevens, J. Tranchida, C. Trott, and S. J. Plimpton, "LAMMPS - a flexible simulation tool for particle-based materials modeling at the atomic, meso, and continuum scales," *Computer Physics Communications*, vol. 271, p. 108171, 2022.

[205] C. Pryor, J. Kim, L. W. Wang, A. J. Williamson, and A. Zunger, "Comparison of two methods for describing the strain profiles in quantum dots," *Journal of Applied Physics*, vol. 83, no. 5, pp. 2548–2554, 1998.

[206] M. A. Caro, S. Schulz, and E. P. O'Reilly, "Effect of alloy fluctuations on the local polarization in nitride nanostructures," *physica status solidi (b)*, vol. 249, no. 3, pp. 526–530, 2012.

[207] G. L. G. Sleijpen and H. A. Van der Vorst, "A Jacobi-Davidson Iteration Method for Linear Eigenvalue Problems," *SIAM Review*, vol. 42, no. 2, pp. 267–293, 2000.

[208] B. K. Ridley, *Quantum processes in semiconductors*. Oxford University Press, Oxford, 4 ed., 1999.

[209] G. Grynberg, A. Aspect, C. Fabre, and C. Cohen-Tannoudji, *Introduction to Quantum Optics: From the Semi-classical Approach to Quantized Light*. Cambridge University Press, 2010.

[210] G. W. 't Hooft and C. van Opdorp, "Temperature dependence of interface recombination and radiative recombination in (Al, Ga)As heterostructures," *Appl. Phys. Lett.*, vol. 42, pp. 813–815, 1983.

[211] A. David, N. G. Young, and M. D. Craven, "Compensation between radiative and Auger recombinations in III-Nitrides: The scaling law of separated-wavefunction recombinations," *Appl. Phys. Lett.*, vol. 115, p. 193502, 2019.

[212] S. K. Patra, T. Wang, T. J. Puchtler, T. Zhu, R. A. Oliver, R. A. Taylor, and S. Schulz, "Theoretical and experimental analysis of radiative recombination lifetimes in nonpolar InGaN/GaN quantum dots," *Phys. Status Solidi B*, vol. 254, p. 1600675, 2017.

[213] N. Antoine-Vincent, F. Natali, M. Mihailovic, A. Vasson, J. Leymarie, P. Disseix, D. Byrne, F. Semond, and J. Massies, "Determination of the refractive indices of AlN, GaN, and $Al_xGa_{1-x}N$ grown on (111)Si

substrates," *Journal of Applied Physics*, vol. 93, no. 9, pp. 5222–5226, 2003.

[214] L. Rigutti, L. Mancini, D. Hernández-Maldonado, W. Lefebvre, E. Giraud, R. Butté, J. F. Carlin, N. Grandjean, D. Blavette, and F. Vurpillot, "Statistical correction of atom probe tomography data of semiconductor alloys combined with optical spectroscopy: The case of $Al_{0.25}Ga_{0.75}N$," *Journal of Applied Physics*, vol. 119, no. 10, p. 105704, 2016.

[215] A. David, N. G. Young, C. A. Hurni, and M. D. Craven, "Quantum Efficiency of III-Nitride Emitters: Evidence for Defect-Assisted Nonradiative Recombination and its Effect on the Green Gap," *Phys. Rev. Appl.*, vol. 11, p. 031001(R), 2019.

[216] P. Dawson, S. Schulz, R. A. Oliver, M. J. Kappers, and C. J. Humphreys, "The nature of carrier localisation in polar and nonpolar InGaN/GaN quantum wells," *J. Appl. Phys.*, vol. 119, p. 181505, 2016.

[217] C. Frankerl, F. Nippert, M. P. Hoffmann, H. Wang, C. Brandl, H.-J. Lugauer, R. Zeisel, A. Hoffmann, and M. J. Davies, "Strongly localized carriers in Al-rich AlGaN/AlN single quantum wells grown on sapphire substrates," *Journal of Applied Physics*, vol. 127, no. 9, 2020. 095701.

[218] C. Frankerl, F. Nippert, M. P. Hoffmann, C. Brandl, H.-J. Lugauer, R. Zeisel, A. Hoffmann, and M. J. Davies, "Carrier Dynamics in Al-Rich AlGaN/AlN Quantum Well Structures Governed by Carrier Localization," *physica status solidi (b)*, vol. 257, no. 12, p. 2000242, 2020.

[219] G. G. Zegrya and A. D. Andreev, "Mechanism of suppression of Auger recombination processes in type-II heterostructures," *Appl. Phys. Lett.*, vol. 67, p. 2681, 1995.

[220] A. D. Andreev and G. G. Zegrya, "Theoretical study of thresholdless Auger recombination in compressively strained InAlAsSb/GaSb quantum wells," *Appl. Phys. Lett.*, vol. 70, p. 601, 1997.

[221] F. Bernardini and V. Fiorentini, "Electronic dielectric constants of insulators calculated by the polarization method," *Phys. Rev. B*, vol. 58, pp. 15292–15295, 1998.

[222] W. Sheng, S. J. Cheng, and P. Hawrylak, "Multiband theory of multi-exciton complexes in self-assembled quantum dots," *Phys. Rev. B*, vol. 71, p. 035316, 2005.

[223] K. Schuh, S. Barthel, O. Marquardt, T. Hickel, J. Neugebauer, G. Czycholl, and F. Jahnke, "Strong dipole coupling in nonpolar nitride quantum dots due to Coulomb effects," *Appl. Phys. Lett.*, vol. 100, p. 092103, 2012.

[224] S. Barthel, K. Schuh, O. Marquardt, T. Hickel, J. Neugebauer, F. Jahnke, and G. Czycholl, "Interplay between Coulomb interaction and quantum-confinedStark-effect in polar and nonpolar wurtzite InN/GaNquantum dots," *Eur. Phys. J. B*, vol. 86, p. 449, 2013.

[225] N. Baer, S. Schulz, S. Schumacher, P. Gartner, G. Czycholl, and F. Jahnke, "Optical properties of self-organized wurtzite InN/GaN quantum dots: A combined atomistic tight-binding and full configuration interaction calculation," *Appl. Phys. Lett.*, vol. 87, p. 231114, 2005.

[226] M. Zieliński, "Multi-scale simulations of semiconductor nanostructures," *Acta Phys. Pol. A*, vol. 122, no. 2, pp. 312–315, 2012.

[227] E. Kioupakis, Q. Yan, and C. G. V. de Walle, "Interplay of polarization fields and Auger recombination in the efficiency droop of nitride light-emitting diodes," *Appl. Phys. Lett.*, vol. 101, p. 231107, 2012.

[228] S. Schulz, D. P. Tanner, E. P. O'Reilly, M. A. Caro, T. L. Martin, P. A. J. Bagot, M. P. Moody, F. Tang, J. T. Griffiths, F. Oehler, M. J. Kappers, R. A. Oliver, C. J. Humphreys, D. Sutherland, M. J. Davies, and P. Dawson, "Structural, electronic, and optical properties of m-plane InGaN/GaN quantum wells: Insights from experiment and atomistic theory," *Phys. Rev. B*, vol. 92, p. 235419, 2015.

[229] A. David, N. G. Young, C. Lund, and M. D. Craven, "Review—the physics of recombinations in III-Nitride emitters," *ECS J. Solid State Sci. Technol.*, vol. 9, p. 016021, 2020.

[230] G. Muziol, M. Hajdel, M. Siekacz, H. Turski, K. Pieniak, A. Bercha, W. Trzeciakowski, R. Kudrawiec, T. Suski, and C. Skierbiszewski, "III-nitride optoelectronic devices containing wide quantum

wells—unexpectedly efficient light sources," *Jpn. J. Appl. Phys.*, vol. 61, p. SA0801, 2022.

[231] M. Hajdel, M. Chlipała, M. Siekacz, H. Turski, P. Wolny, K. Nowakowski-Szkudlarek, A. Feduniewicz-Żmuda, C. Skierbiszewski, and G. Muziol, "Dependence of InGaN quantum well thickness on the nature of optical transitions in LEDs," *Materials*, vol. 15, p. 237, 2022.

[232] S.-H. Park and S.-L. Chuang, "Piezoelectric effects on electrical and optical properties of wurtzite GaN/AlGaN quantum well lasers," *Applied Physics Letters*, vol. 72, no. 24, pp. 3103–3105, 1998.

[233] T. R. Nielsen, P. Gartner, M. Lorke, J. Seebeck, and F. Jahnke, "Coulomb scattering in nitride-based self-assembled quantum dot systems," *Phys. Rev. B*, vol. 72, p. 235311, 2005.

[234] L. Rigutti, B. Bonef, J. Speck, F. Tang, and R. A. Oliver, "Atom probe tomography of nitride semiconductors," *Scripta Materialia*, vol. 148, p. 75, 2018.

[235] A. David, N. G. Young, and M. D. Craven, "Many-body effects in strongly-disordered III-nitride quantum wells: interplay between carrier localization and coulomb interaction," *Phys. Rev. Appl.*, vol. 12, p. 044059, 2019.

[236] A. David, N. G. Young, C. Lund, and M. D. Craven, "Thermal droop in high-quality InGaN LEDs," *Appl. Phys. Lett.*, vol. 115, p. 223502, 2019.

[237] B. Witzigmann, M. Tomamichel, S. Steiger, R. G. Veprek, K. Kojima, and U. T. Schwarz, "Analysis of gain and luminescence in violet and blue GaInN-GaN quantum wells," *IEEE J. Quantum Electron.*, vol. 44, p. 144, 2008.

[238] K. P. O'Donnell, R. W. Martin, and P. G. Middleton, "Origin of luminescence from InGaN diodes," *Phys. Rev. Lett.*, vol. 82, p. 237, 1999.

[239] G. M. Christian, S. Schulz, M. J. Kappers, C. J. Humphreys, R. A. Oliver, and P. Dawson, "Recombination from polar InGaN/GaN quantum well structures at high excitation carrier densities," *Phys. Rev. B*, vol. 98, p. 155301, 2018.

[240] B. Galler, H.-J. Lugauer, M. Binder, R. Hollweck, Y. Folwill, A. Nirschl, A. Gomez-Iglesias, B. Hahn, J. Wagner, and M. Sabathil, "Experimental Determination of the Dominant Type of Auger Recombination in InGaN Quantum Wells," *Applied Physics Express*, vol. 6, no. 11, p. 112101, 2013.

[241] D. J. Myers, A. C. Espenlaub, K. Gelzinyte, E. C. Young, L. Martinelli, J. Peretti, C. Weisbuch, and J. S. Speck, "Evidence for trap-assisted Auger recombination in MBE grown InGaN quantum wells by electron emission spectroscopy," *Appl. Phys. Lett.*, vol. 116, p. 091102, 2020.

[242] C. Haller, J.-F. Carlin, G. Jacopin, W. Liu, D. Martin, R. Butté, and N. Grandjean, "GaN surface as the source of non-radiative defects in InGaN/GaN quantum wells," *Applied Physics Letters*, vol. 113, no. 11, p. 111106, 2018.

[243] J.-X. Shen, D. Wickramaratne, C. E. Dreyer, A. Alkauskas, E. Young, J. S. Speck, and C. G. V. de Walle, "Calcium as a nonradiative recombination center in InGaN," *Applied Physics Express*, vol. 10, no. 2, p. 021001, 2017.

[244] C. G. Van de Walle and J. Neugebauer, "First-principles calculations for defects and impurities: Applications to III-nitrides," *Journal of Applied Physics*, vol. 95, no. 8, pp. 3851–3879, 2004.

[245] D. Florescu, J. Ramer, V. Merai, A. Parekh, D. Lu, D. Lee, and E. Armour, "AFM and temperature-dependent photoluminescence studies of the degree of localization induced by quantum-dot like states in InGaN single quantum well light emitting diodes grown by MOCVD on (0001) sapphire," *Journal of Crystal Growth*, vol. 272, no. 1, pp. 449–454, 2004. The Twelfth International Conference on Metalorganic Vapor Phase Epitaxy.

[246] D. Schiavon, M. Binder, M. Peter, B. Galler, P. Drechsel, and F. Scholz, "Wavelength-dependent determination of the recombination rate coefficients in single-quantum-well GaInN/GaN light emitting diodes," *Phys. Status Solidi B*, vol. 250, p. 283, 2013.

[247] A. Alkauskas, C. E. Dreyer, J. L. Lyons, and C. G. Van de Walle, "Role of excited states in Shockley-Read-Hall recombination in wide-band-gap semiconductors," *Phys. Rev. B*, vol. 93, p. 201304(R), 2016.

[248] R. M. Barrett, R. Ahumada-Lazo, J. A. Alanis, P. Parkinson, S. A. Church, M. J. Kappers, R. A. Oliver, and D. J. Binks, "Effect of Micron-scale Photoluminescence Variation on Droop Measurements in InGaN/GaN Quantum Wells," *J. Phys.: Conf. Ser.*, vol. 1919, p. 012011, 2021.

[249] J. Hader, J. V. Moloney, and S. W. Koch, "Influence of internal fields on gain and spontaneous emission in InGaN quantum wells," *Appl. Phys. Lett.*, vol. 89, p. 171120, 2006.

[250] C. Tan, W. Sun, J. J. Wierer, and N. Tansu, "Effect of interface roughness on Auger recombination in semiconductor quantum wells," *AIP Adv.*, vol. 7, p. 035212, 2017.

[251] S. Hammersley, M. J. Kappers, F. C.-P. Massabuau, S.-L. Sahonta, P. Dawson, R. A. Oliver, and C. J. Humphreys, "Effect of QW growth temperature on the optical properties of blue and green InGaN/GaN QW structures," *physica status solidi c*, vol. 13, no. 5-6, pp. 209–213, 2016.

[252] X. Li, E. DeJong, R. Armitage, A. M. Armstrong, and D. Feezell, "Influence of trap-assisted and intrinsic Auger–Meitner recombination on efficiency droop in green InGaN/GaN LEDs," *Applied Physics Letters*, vol. 123, no. 11, p. 112109, 2023.

[253] J. Piprek, F. Römer, and B. Witzigmann, "On the uncertainty of the Auger recombination coefficient extracted from InGaN/GaN light-emitting diode efficiency droop measurements," *Applied Physics Letters*, vol. 106, no. 10, p. 101101, 2015.

[254] F. Nippert, S. Karpov, I. Pietzonka, B. Galler, A. Wilm, T. Kure, C. Nenstiel, G. Callsen, M. Straßburg, H.-J. Lugauer, and A. Hoffmann, "Determination of recombination coefficients in InGaN quantum-well light-emitting diodes by small-signal time-resolved photoluminescence," *Japanese Journal of Applied Physics*, vol. 55, no. 5S, p. 05FJ01, 2016.

[255] T. J. Badcock, M. Ali, T. Zhu, M. Pristovsek, R. A. Oliver, and A. J. Shields, "Radiative recombination mechanisms in polar and non-polar InGaN/GaN quantum well LED structures," *Applied Physics Letters*, vol. 109, no. 15, p. 151110, 2016.

[256] R. M. Barrett, *Investigating Carrier Dynamics in InGaN/GaN Quantum Wells*. PhD thesis, University of Manchester, 2023.

[257] W. H. Press and S. A. Teukolsky, "Savitzky-Golay Smoothing Filters," *Computers in Physics*, vol. 4, no. 6, pp. 669–672, 1990.

[258] F. Piva, M. Pilati, M. Buffolo, N. Roccato, N. Susilo, D. Hauer Vidal, A. Muhin, L. Sulmoni, T. Wernicke, M. Kneissl, C. De Santi, G. Meneghesso, E. Zanoni, and M. Meneghini, "Degradation of AlGaN-based UV-C SQW LEDs analyzed by means of capacitance deep-level transient spectroscopy and numerical simulations," *Applied Physics Letters*, vol. 122, no. 18, 2023. 181102.

[259] M. Kneissl, "A brief review of III-Nitride UV emitter technologies and their applications," in *III-Nitride Ultraviolet Emitters: Technology and Applications* (M. Kneissl and J. Rass, eds.), pp. 1–25, Springer International Publishing, 2016.

[260] W. Y. Ching and B. N. Harmon, "Electronic structure of AlN," *Phys. Rev. B*, vol. 34, pp. 5305–5308, 1986.

[261] E. Ruiz, S. Alvarez, and P. Alemany, "Electronic structure and properties of AlN," *Phys. Rev. B*, vol. 49, pp. 7115–7123, 1994.

[262] F. Litimein, B. Bouhafs, Z. Dridi, and P. Ruterana, "The electronic structure of wurtzite and zincblende AlN: an ab initio comparative study," *New Journal of Physics*, vol. 4, no. 1, p. 64, 2002.

[263] C. Coughlan, S. Schulz, M. A. Caro, and E. P. O'Reilly, "Band gap bowing and optical polarization switching in AlGaN alloys," *physica status solidi (b)*, vol. 252, no. 5, pp. 879–884, 2015.

[264] R. Ishii, A. Yoshikawa, K. Nagase, M. Funato, and Y. Kawakami, "Temperature-dependent electroluminescence study on 265-nm AlGaN-based deep-ultraviolet light-emitting diodes grown on AlN substrates," *AIP Advances*, vol. 10, no. 12, 2020. 125014.

[265] H. Murotani, R. Tanabe, K. Hisanaga, A. Hamada, K. Beppu, N. Maeda, M. A. Khan, M. Jo, H. Hirayama, and Y. Yamada, "High internal quantum efficiency and optically pumped stimulated emission in AlGaN-based UV-C multiple quantum wells," *Applied Physics Letters*, vol. 117, no. 16, 2020. 162106.

[266] Y. Iwata, R. G. Banal, S. Ichikawa, M. Funato, and Y. Kawakami, "Emission mechanisms in Al-rich AlGaN/AlN quantum wells assessed by

excitation power dependent photoluminescence spectroscopy," *Journal of Applied Physics*, vol. 117, no. 7, 2015. 075701.

[267] G.-D. Hao, N. Tamari, T. Obata, T. Kinoshita, and S. Inoue, "Electrical determination of current injection and internal quantum efficiencies in AlGaN-based deep-ultraviolet light-emitting diodes," *Opt. Express*, vol. 25, no. 16, pp. A639–A648, 2017.

[268] J. Yun, J.-I. Shim, and H. Hirayama, "Analysis of efficiency droop in 280-nm AlGaN multiple-quantum-well light-emitting diodes based on carrier rate equation," *Applied Physics Express*, vol. 8, no. 2, p. 022104, 2015.

[269] M. Shatalov, J. Yang, W. Sun, R. Kennedy, R. Gaska, K. Liu, M. Shur, and G. Tamulaitis, "Efficiency of light emission in high aluminum content AlGaN quantum wells," *Journal of Applied Physics*, vol. 105, no. 7, 2009. 073103.

[270] S. Deng, Z. Chen, M. Li, M. Su, X. Zhu, K. Xiao, Y. Wang, J. Deng, and W. Sun, "Variable temperature thermal droop characteristics of 255 nm UV LED," *Applied Physics Letters*, vol. 121, no. 3, 2022. 031104.

[271] C. R. Haughn, G. Rupper, T. Wunderer, Z. Yang, N. M. Johnson, M. Wraback, and G. A. Garrett, "Highly radiative nature of ultra-thin c-plane Al-rich AlGaN/AlN quantum wells for deep ultraviolet emitters," *Applied Physics Letters*, vol. 114, no. 10, 2019. 102101.

[272] D. Chaudhuri, M. O'Donovan, T. Streckenbach, O. Marquardt, P. Farrell, S. K. Patra, T. Koprucki, and S. Schulz, "Multiscale simulations of the electronic structure of III-nitride quantum wells with varied indium content: Connecting atomistic and continuum-based models," *J. Appl. Phys.*, vol. 129, p. 073104, 2021.

[273] S. Y. Karpov, "Effect of Carrier Localization on Recombination Processes and Efficiency of InGaN-Based LEDs Operating in the "Green Gap"'," *Applied Sciences*, vol. 8, no. 5, 2018.

[274] J. Glaab, J. Ruschel, N. Lobo Ploch, H. K. Cho, F. Mehnke, L. Sulmoni, M. Guttmann, T. Wernicke, M. Weyers, S. Einfeldt, and M. Kneissl, "Impact of operation parameters on the degradation of 233 nm AlGaN-based far-UVC LEDs," *Journal of Applied Physics*, vol. 131, no. 1, p. 014501, 2022.

[275] N. Roccato, F. Piva, C. De Santi, M. Buffolo, M. Fregolent, M. Pilati, N. Susilo, D. H. Vidal, A. Muhin, L. Sulmoni, T. Wernicke, M. Kneissl, G. Meneghesso, E. Zanoni, and M. Meneghini, "Modeling the electrical degradation of AlGaN-based UV-C LEDs by combined deep-level optical spectroscopy and TCAD simulations," *Applied Physics Letters*, vol. 122, no. 16, p. 161105, 2023.

[276] M. O'Donovan, P. Farrell, J. Moatti, T. Streckenbach, T. Koprucki, and S. Schulz, "Impact of random alloy fluctuations on the carrier distribution in multicolor $(\mathrm{In},\mathrm{Ga})\mathrm{N}/\mathrm{GaN}$ quantum well systems," *Phys. Rev. Appl.*, vol. 21, p. 024052, 2024.

[277] C.-L. Nies, T. P. Sheerin, and S. Schulz, "Electronic and optical properties of boron-containing GaN alloys: The role of boron atom clustering," *APL Materials*, vol. 11, no. 9, p. 091119, 2023.

[278] S. Lee, L. Jönsson, J. W. Wilkins, G. W. Bryant, and G. Klimeck, "Electron-hole correlations in semiconductor quantum dots with tight-binding wave functions," *Phys. Rev. B*, vol. 63, p. 195318, 2001.

[279] S. Lee, J. Kim, L. Jönsson, J. W. Wilkins, G. W. Bryant, and G. Klimeck, "Many-body levels of optically excited and multiply charged InAs nanocrystals modeled by semiempirical tight binding," *Phys. Rev. B*, vol. 66, p. 235307, 2002.

[280] J. C. Slater, "Atomic shielding constants," *Physical Review*, vol. 36, p. 57, 1930.

[281] Y.-L. Xu, "Fast evaluation of the Gaunt coefficients," *Mathematics of Computation*, vol. 65, p. 1601, 1996.

[282] I. Schnell, G. Czycholl, and R. C. Albers, "Hubbard-U calculations for Cu from first-principle Wannier functions," *Phys. Rev. B*, vol. 65, p. 075103, 2002.

[283] P. R. C. Kent and A. Zunger, "Carrier localization and the origin of luminescence in cubic InGaN alloys," *Appl. Phys. Lett.*, vol. 79, p. 1977, 2001.

Appendices

Appendix A

Determination of on-site energies

In this appendix we provide further information on the Coulomb matrix element calculations and the impact of the on-site energy, W_0, on the Auger rates. In the following we focus our attention on the general form of the Coulomb matrix elements,

$$M = \frac{e^2}{4\pi\epsilon_0\epsilon_r}\int\int d^3\tilde{r}' d^3\tilde{r}\frac{\psi_1^*(\tilde{\mathbf{r}}')\psi_2(\tilde{\mathbf{r}}')\psi_3^*(\tilde{\mathbf{r}})\psi_4(\tilde{\mathbf{r}})}{|\tilde{\mathbf{r}}-\tilde{\mathbf{r}}'|}\ . \tag{A.1}$$

Here, each $\psi(\tilde{\mathbf{r}})$ is a TB wave function, which are given by Eq. (3.13), i.e., by linear combinations of localised, atomic-like orbitals, $\phi_{\mathbf{R},\sigma}(\tilde{\mathbf{r}})$, $\sigma = \{s, p_x, p_y, p_z\}$, located at the lattice sites, $\mathbf{R}$. In the following we make the two-centre approximation discussed in detail in Ref. [183], so that the Coulomb matrix element, M, becomes:

$$\begin{aligned} M \ &\approx \ \frac{e^2}{4\pi\epsilon_0\epsilon_r}\sum_{\mathbf{R},\mathbf{R}'}\sum_{\alpha,\beta,\gamma,\delta} c^*_{\mathbf{R}',\alpha}c_{\mathbf{R}',\delta}c^*_{\mathbf{R},\beta}c_{\mathbf{R},\gamma} \\ &\quad\times\int\int d^3r' d^3r\frac{\phi^*_{\mathbf{R}',\alpha}(\mathbf{r}')\phi_{\mathbf{R}',\delta}(\mathbf{r}')\phi^*_{\mathbf{R},\beta}(\mathbf{r})\phi_{\mathbf{R},\gamma}(\mathbf{r})}{|\mathbf{R}+\mathbf{r}-\mathbf{R}'-\mathbf{r}'|}\ . \end{aligned}$$

Here, we have decomposed the positions $\tilde{\mathbf{r}}$ and $\tilde{\mathbf{r}}'$ into the positions $\mathbf{R}$ and $\mathbf{R}'$ of the lattice sites and the positions $\mathbf{r}$ and $\mathbf{r}'$ inside the local tetrahedron of the lattice site. Due to the localised nature of the atomic-like orbitals, $\phi_{\mathbf{R},\sigma}(\mathbf{r})$, when the lattice sites at which the orbitals are localised are far apart, the exact structure of these s- and p-like orbitals is of secondary important. In doing so, one ends up with the approximation given in Eq. (3.12).

However, when the situation $\mathbf{R} = \mathbf{R}'$ arises, this on-site energy needs to be

treated carefully. In principle, the specific form of the atomic like basis states needs to be known. To this end, we now employ the often used approach [278, 279] to approximate $\phi_{\mathbf{R},\sigma}(\mathbf{r})$ via Slater orbitals [280], which can be written, in general, as:

$$\phi_n(\mathbf{r}) = R_n(r)Y_n(\theta,\phi) \ , \tag{A.2}$$

where the index n denotes the orbital type, $Y_n(\theta,\phi)$ are spherical harmonics, and $R_n(r) = Dr^a e^{-br}$ are the radial parts; the constants a and b are given by Slater's rules [280] and D is a normalisation constant. Given that we are evaluating on-site energies, and without loss of generality, we assume $\mathbf{R} = \mathbf{R}' = \mathbf{0}$. Equipped with these orbitals, in this second step, we expand the Coulomb potential in spherical harmonics [84]:

$$\frac{1}{|\mathbf{r}-\mathbf{r}'|} = \sum_{l=0}^{\infty} \frac{4\pi}{2l+1} \frac{r_<^l}{r_>^{l+1}} \sum_{m=-l}^{l} Y_{lm}^*(\mathbf{r}')Y_{lm}(\mathbf{r}) \ .$$

Here, $r_>$ ($r_<$) are the length of the larger (smaller) of the vectors $\mathbf{r}$ and $\mathbf{r}'$. Using the above, and Eq. (3.13), the Coulomb matrix element, M, becomes, for the case of $\mathbf{R} = \mathbf{R}' = \mathbf{0}$:

$$\begin{aligned} M &= \frac{e^2}{4\pi\epsilon_0} \sum_{l,\{n\}} c_{n_1}^* c_{n_2} c_{n_3}^* c_{n_4} \int dr' \int dr r'^2 R_{n_1}(r') R_{n_2}(r') r^2 R_{n_3}(r) R_{n_4}(r) \\ &\quad \times \frac{r_<^l}{r_>^{l+1}} \frac{4\pi}{2l+1} \sum_{m=-l}^{l} K_{n_1,n_2,l,m} K_{n_3,n_4,l,m} \ . \end{aligned}$$

The coefficients $K_{n,n',l,m}$ are the so-called Gaunt coefficients [281]. We define now:

$$\begin{aligned} M &= \sum_{\{n\}} c_{n_1}^* c_{n_2} c_{n_3}^* c_{n_4} \sum_l \mathcal{K}_{n_1,..,n_4}^l \times \mathcal{I}_{n_1,..,n_4}^l \\ &= \sum_{\{n\}} c_{n_1}^* c_{n_2} c_{n_3}^* c_{n_4} W_0 \ . \end{aligned}$$

with

$$\mathcal{K}_{n_1,..,n_4}^l = \frac{4\pi}{2l+1} \sum_{m=-l}^{l} K_{n_1,n_2,l,m} K_{n_3,n_4,l,m} \ , \tag{A.3}$$

and

$$\mathcal{I}_{n_1,..,n_4}^l = C \int dr' r'^2 R_{n_1}^*(r') R_{n_2}(r') \int dr r^2 R_{n_3}^*(r) R_{n_4}(r) \frac{r_<^l}{r_>^{l+1}} \ , \tag{A.4}$$

with $C = e^2/(4\pi\epsilon_0)$. The values for $\mathcal{K}^l_{n_1,..,n_4}$, Eq. (A.3), can be obtained from the properties and values of the Gaunt coefficients. The radial part, Eq. (A.4), can be evaluated by integrating over a sphere of radius s, that has the same volume as a local tetrahedron in the wurtzite crystal [282]:

$$\begin{aligned}\mathcal{I}^l_{n_1,..,n_4} =& C\left(\int_0^s dr(r)^{l-1}R^*_{n_3}(r)R_{n_4}(r)\int_0^r dr'(r')^{2+l}R^*_{n_1}(r')R_{n_2}(r')\right.\\ &\left.+\int_0^s dr(r)^{2+l}R^*_{n_3}(r)R_{n_4}(r)\int_r^s dr'(r')^{l-1}R^*_{n_1}(r')R_{n_2}(r')\right) .\end{aligned}$$

We note that based on the Slater rules [280] and the fact that we are considering wave functions at the same lattice site, the radial part will be identical for the four wave functions involved in the above integral [183].

This derivation for evaluating the on-site Coulomb energies allows us to now proceed as follows. Given that the underlying TB framework is an sp^3 TB model, and that when using Slater orbitals the radial function of the localised orbitals is the same, we restrict the spherical expansion to $l = 0$ (s-like) contributions. Furthermore, we assume that the wave functions are constant over the sphere around the considered lattice site. In doing so, we find that

$$W_0 = \frac{e^2}{4\pi\epsilon_0}\frac{9}{s}\frac{2}{15} .$$

Evaluating W_0 for InN, we find that $W_0^{\text{InN}} \approx 16.5$ eV, while for GaN, given the smaller lattice constant compared to InN, we find $W_0^{\text{GaN}} \approx 18$ eV. While further refinements can be made in the evaluation of the on-site energies, these numbers are in good agreement with other calculations of unscreened on-site Coulomb matrix elements [282].

The above numbers for the on-site energy are determined for pure InN and GaN. In an (In,Ga)N/GaN QW, due to alloy fluctuations and strain effects, the volume of the local tetrahedron will vary. To test the impact of the on-site energy on the Auger rate, we have performed calculations using W_0^{InN} and W_0^{GaN} at low (T = 10 K) and high temperatures (T = 300 K). These test calculations revealed that the eeh Auger coefficient increases by less than 3% at temperatures of 10 K and 300 K when using W_0^{GaN} instead of W_0^{InN}; the hhe Auger coefficient increases by less than 13% at the same temperatures again when using W_0^{GaN} instead of W_0^{InN}. This analysis shows that precise knowledge of the on-site energy is of secondary importance and that the Auger rates are primarily affected by the long range character of the Coulomb interaction. For

all calculations in the main part of the manuscript we have used W_0^{InN}, given that hole wave functions are strongly localised near In-N-In chains [283]. Furthermore, the value W_0^{InN} is expected to represent a lower bound on the on-site energies and thus also for the Auger rates. Larger W_0 values will, in general, result in a larger Auger rate compared to values obtained in the main text.